PRECISION ENGINEERING CENTER

2006 ANNUAL REPORT
VOLUME XXIV
March 2007

Sponsors:

3M Corporation
Electro-Optics Center at Pennsylvania State University
Lexmark International, Inc.
Missile Defense Agency
National Science Foundation
Optical Research Associates
Panasonic Boston Laboratory
Sandia National Laboratory
Vistakon, Johnson & Johnson Vision Care Inc.

Faculty:

Thomas Dow, Editor
Greg Buckner
Jeffrey Eischen
Dieter Grifis
Paul Ro
Ronald Scattergood

Graduate Students:

David Brehl
Qunyi Chen
Karalyn Folkert
Timothy Kennedy
D. Lucas Lamonds
Arun Veeramani
Nadim Wanna
Robert Woodside
Yanbo Yin

Staff:

Kenneth Garrard
Donna Irwin
Alexander Sohn

Consultants:

Karl Falter
David Youden

TABLE OF CONTENTS

SUMMARY

The goals of the Precision Engineering Center are: 1) to develop new technology in the areas of precision metrology, actuation, manufacturing and assembly; and 2) to train a new generation of engineers and scientists with the background and experience to transfer this technology to industry. Because the problems related to precision engineering originate from a variety of sources, significant progress can only be achieved by applying a multidisciplinary approach; one in which the faculty, students, staff and sponsors work together to identify important research issues and find the optimum solutions. Such an environment has been created and nurtured at the PEC for over 25 years and the 100+ graduates attest to the quality of the results.

The 2006 Annual Report summarizes the progress over the past year by the faculty, students and staff in the Precision Engineering Center. During the past year, this group included 7 faculty, 9 graduate students, 2 full-time technical staff members and 1 administrative staff member. This diverse group of scientists and engineers provides a wealth of experience to address precision engineering problems. The format of this Annual Report separates the research effort into individual projects but there is significant interaction that occurs among all of the faculty, staff and students. Weekly seminars by the students and faculty provide information exchange and feedback as well as practice in technical presentations. Teamwork and group interactions are a hallmark of research at the PEC and this contributes to both the quality of the research as well as the education of the graduates.

The summaries of individual projects that follow are arranged in the same order as the body of the report, 1) design, 2) fabrication, 3) metrology, 4) actuation and 5) optics.

1) DESIGN

The emphasis of the metrology projects has been to develop new techniques that can be used to predict surface shape as well as measure important parameters such as tool force.

Software Tools for Freeform Optics

Freeform optical surfaces are defined as any non-rotationally symmetric surface or a symmetric surface that is rotated about any axis that is not its axis of symmetry. These surfaces improve the packaging efficiency and dramatically improve image quality. Unfortunately, these systems are more difficult to design, manufacture and measure than those with rotationally symmetric surfaces. Software tools have been developed to enhance the design process.

Design of Reflective TMA

The optical and opto-mechanical design of two systems were studied: a two mirror Ritchey-Chrétien telescope and a Three Mirror Anastigmat (TMA). The two mirror Ritchey-Chrétien telescope used rotationally symmetric hyperbolic surfaces and was designed and built. The TMA achieves better performance because of the addition of a third mirror. New fabrication and fiducial features were developed using off-axis conic sections and freeform mirrors. The results were impressive with errors less than 2% of the RC design

Modeling of Vibration and Dithering in SPDT

The objective of this work is to develop a model to simulate the effects of vibration on the surface finish of single-point diamond turned parts. This model can be used to optimize cutting conditions for best surface finish and to predict geometric characteristics of the surface beyond the conventional rules of thumb. In addition to small-amplitude oscillations due to machine vibration in the normal direction, purposely induced large-amplitude vibrations in the lateral direction to reduce coherent scatter in the finished part were modeled.

2) FABRICATION

Fabrication of precision components is an emphasis area for the PEC. Current projects include machining of freeform optics, MEMS devices and single crystal silicon.

Fast Long Range Actuator - *Flora*

To produce optical quality freeform surfaces, a Fast Long Range Actuator (FLORA) is being developed with a target range of motion of ±2 mm at 20 Hz. This design uses a 50 mm stroke linear motor, air bearing supported lightweight triangular piston and a glass-scale linear encoder. Changes to the encoder, amplifier and controller and the resulting improvements in performance are reported. Both simulations and experimental results are presented to evaluate the performance of the existing design and determine the direction for a new system design.

Design and Fabrication of an Optical Assembly Test

A simple test system has been designed to identify the error sources in the machining and assembly of optical systems. Using simple geometries, it can be used to test different aspects of the machining and assembly process and allow error sources to be identified. Ultimately, the test will be used to compare assembly techniques such as the current pin/slot assembly method and a new quasi-kinematic assembly technique using features machined with a fast-tool servo.

Elliptical Vibration-Assisted Machining (EVAM)

The Ultramill EVAM tool has been used to machine MEMS scale features with complex 3-D geometry. Test parts were machined using tools with both round-nose and sharp-nose geometry.

Because round-nosed tools can only make low aspect-ratio structures with shallow curved sidewalls, sharp-nosed tools were used to overcome these limitations and make 80 μm tall trihedrons and small (< 15 μm wide) groove structures featuring sculpted 3-D geometry. Suggestions for improving sharp-nose tool geometry were developed.

3) METROLOGY

Metrology is at the heart of precision engineering – from measuring fabricated parts to calibration artifacts to dynamic system characterization.

Metrology Artifact for Dynamic Performance Evaluation

Part acceptance based on dimensional inspection can be influenced by the static and dynamic errors in the CMM inspection instrumentation. Traditional calibration artifacts are used to determine static influences due to machine geometry. A new artifact is proposed that will test a CMM both statically and dynamically. The artifact is a ring gauge with sinusoidal features (5μm amplitude) whose wavelength varies linearly between 6.4 mm and 0.4 mm. Using this gage, an operator can devise a measurement strategy that does not exceed the dynamic range of the CMM.

Metrology of Reflective Optical Systems

An accurate metrology process must be available to measure the performance of a telescope and its relationship to the design specifications. A Ritchey-Chretién with diamond-turned hyperbolic mirrors was measured using a variety of techniques. The secondary mirror had a form error near λ/4 but the primary mirror had a large non-rotationally symmetric form error of 3λ. The system had 1.5 μm of wavefront error at, spot sizes 2x the magnitude predicted by the Code V model and the MTF values were approximately 10-20% of the theoretical values.

TEM and Raman Spectroscopic Analysis of Diamond Turned Single Crystal Silicon

Single point diamond machining, using both a lathe and a fly cutting, was performed on Si using both -30° and -45° diamond tools with federate from 1 to 5 μm/rev. Dislocation loops and slip planes were found at depths up to 250 nm on the lathe samples but this amorphous layer was not always created during fly cutting depending on tool edge design. Different conclusions were drawn from the Raman spectra and cross sectional TEM images of the diamond turned silicon surfaces. The relationship between feed rate and the depth of the amorphous layer is discussed.

Fresnel Lenses for Scanning Systems

The use of Fresnel lenses in scanning systems can have performance and manufacturing benefits. Thinner Fresnel lenses are more economical to injection mold and reduce dispersion in the material. However, designing and fabricating such lenses presents some unique challenges.

Design issues are addressed by evaluating possible geometries and simple designs. Manufacturability is the next challenge due to the special requirements for scanning systems. Concepts and strategies for addressing all these issues are explored.

1 SOFTWARE TOOLS FOR FREEFORM OPTICS

Kenneth Garrard
Precision Engineering Center Staff

Freeform optical surfaces are defined as any non-rotationally symmetric surface or a symmetric surface that is rotated about any axis that is not its axis of symmetry. These surfaces offer degrees of freedom that can be used to improve the packaging properties of an optical system and dramatically improve image quality. Unfortunately, optical systems with freeform surfaces are more difficult to design, manufacture and measure than those with rotationally symmetric surfaces. Software tools have been developed to enhance the infrastructure of the PEC with respect to fabrication and metrology of freeform optics as well as the development of design and assembly tolerances.

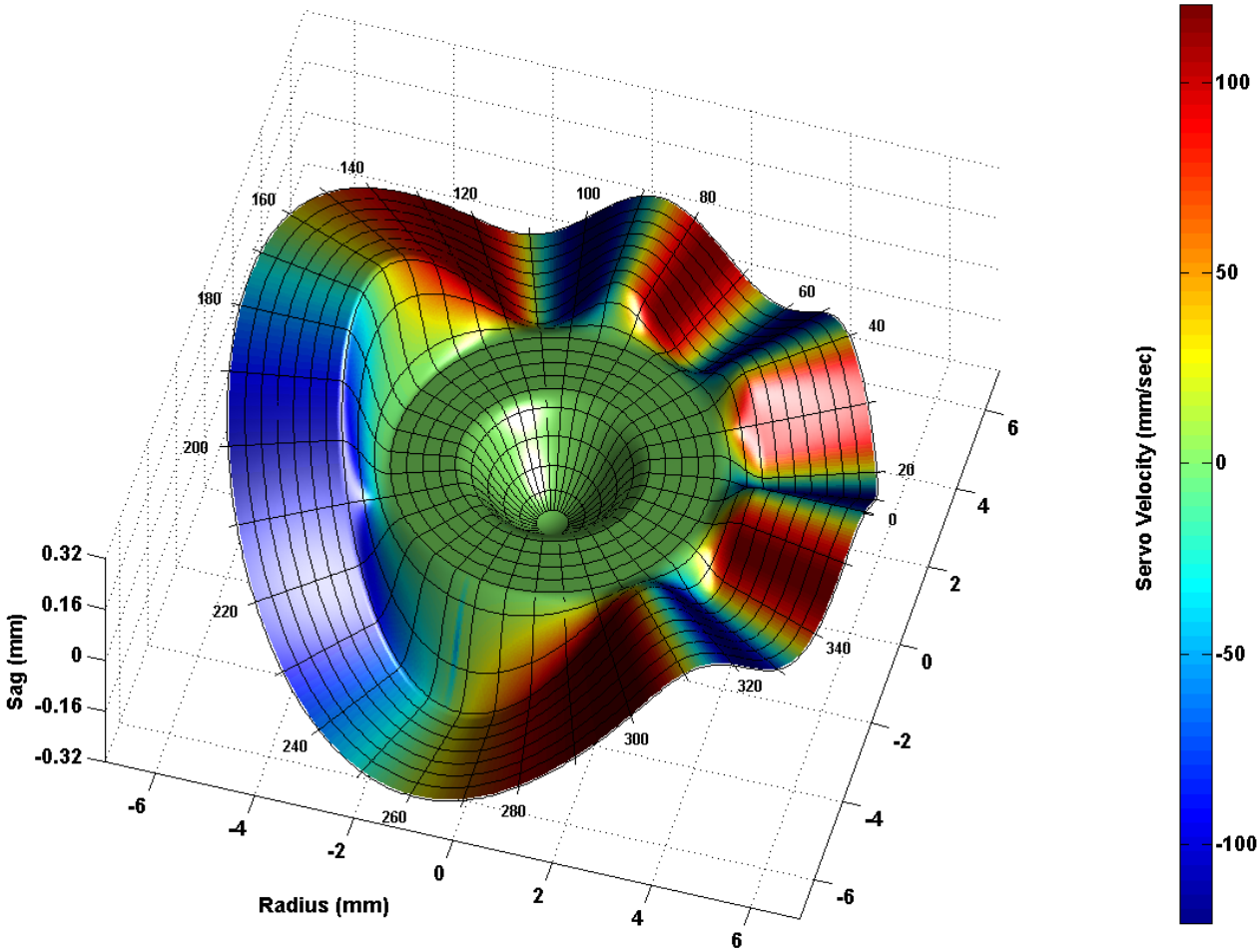

1.1 INTRODUCTION

Software tools for the efficient design, fabrication and metrology of freeform optics have been constructed. Last year a project with Optical Research Associates integrated both a freeform fabrication cost metric and a fabrication error simulation into CODE V™ [1]. Recent work has concentrated on four additional areas: surface tolerance specification, enhancements to the ASG 2500 DTM control system, a comprehensive solution to the motion planning problem for non-rotationally symmetric (NRS) surfaces and analysis of surface metrology data. These four topics are discussed below. Further details can be found in [2].

1.2 SURFACE TOLERANCING

A critical step in the design of an optical system is the definition of a fabrication and assembly error budget that enables the accurate prediction of the as-built system performance. Since no system component will be manufactured perfectly, the tolerance with which each lens, mirror, mounting surface and detector must be built and assembled is an important component of the overall cost estimate of the system. Tolerance analysis can also identify the most effective compensators that should be included in the optomechanical design. For example, focus is a common and effective compensator for on-axis, rotationally symmetric lens systems, particularly those with large f-number. Off-axis systems such as Three Mirror Anastigmats (TMAs) and fast systems with highly curved surfaces may require one or more tilt compensators to meet performance requirements with reasonable fabrication and assembly cost. A complete analytical treatment of the third order wavefront aberrations resulting from perturbations in the shape and location of both surfaces in two mirror telescopes is found in Majahan [3]. For more complex systems, sensitivity to small perturbations in surface parameters is less obvious and must be simulated over a range of tolerance combinations.

1.2.1 CODE V

The tolerancing process is supported by the CODE V optical design software with three types of automatic features: finite differencing (TOLFDIF), monte carlo simulation (TOLMONTE) and wavefront differential analysis (TOR,TOD and TOL) [4,5].

The finite differencing approach modifies system variables one at a time, constrains those variables and re-evaluates the optical system with respect to the desired performance criteria. For large parameter variations this provides accurate results and parameter sensitivity information, but can be very time consuming for complex systems and does not include cross-term interactions. The monte carlo approach varies all parameters randomly and includes variable interactions, but provides no information on individual parameter sensitivity. Re-

analysis of the system after each random trial may also be very slow. Wavefront differential tolerancing is unique to CODE V. It provides individual parameter sensitivity, includes cross-term variations and does not require re-analysis of the system. However there are two assumptions that affect the accuracy of the results. First is that optical path differences are a linear function of parameter variation. This is typically valid only for small tolerance ranges. Also, the technique assumes that overall system performance follows a Gaussian probability distribution. This means that each tolerance parameter contributes similar performance degradation over its range. Wavefront differential tolerancing is only available for predefined tolerance types. These include curvature, thickness, refractive index, tilt, decenter, wedge, cylinder power and the Zernike polynomial coefficients.

When the assumptions of the wavefront differential approach are not valid or a tolerance parameter (e.g., conic constant variation) is difficult to quantify in terms of a particular fabrication error (e.g., phase lag), the parameter variation must be simulated and manually included in the system analysis. CODE V provides an interferometric deformation and intensity apodization feature that allows an externally generated wavefront error file to be attached to any surface in the system. This can be from a real measurement of a surface or a simulation of a surface shape due to dynamic loading, stress birefringence modeling, fabrication dynamics, assembly tilt or alignment errors, etc. Matlab™ has been used to simulate the effects of uncorrected actuator dynamics on fabrication and the results imported into CODE V as an apodization file. Subsequent analysis revealed the effect on system wavefront error [1].

1.2.2 FABRICATION TOLERANCES

While it is essential to produce a realistic tolerance for each parameter of an optical design, it is not always apparent how the tolerance is related to an actual fabrication error. For example, it is unlikely that a conic mirror would be diamond turned with the correct vertex radius, but have an incorrect eccentricity. The small amplitude, low frequency error motions of the axes of a machine tool are largely independent of the shape of the machined part, but are dependent on its aperture. They contribute to the form error in a nonlinear way and thus are difficult to quantify in terms of a percentage error in radius of curvature or conic constant or variations in Zernike polynomial coefficients.

The sag over a conic, biconic and polynomial surface is nonlinear with respect to its shape parameters (i.e., curvatures, eccentricities, Zernike coefficients) and its aperture. The parameters also have different units or are dimensionless and may be difficult to compare or analyze with respect to sensitivity. For example, the effect on surface sag of a percentage change in one of the conic constants of a biconic surface is unbounded without knowing the values of the other parameters and it also varies nonlinearly with aperture. A wide range of multiple parameter

variations for a surface may result in the same overall form error, but do not necessarily give the same overall system wavefront error for the complete optical system. For example, as the aperture and/or curvature decrease, a prolate ellipsoid can be closely approximated by a hyperboloid.

1.2.3 ZERNIKE POLYNOMIALS

Zernike polynomials are widely used for interpretation of optical surface data and are readily derived from a wavefront measurement [6]. The Zernike polynomials are the only polynomials in cylindrical coordinates (ρ, θ) that are orthogonal when normalized over a unit circle, complete, and invariant with respect to rotation about the origin. Completeness and orthogonality mean that adding or deleting terms does not affect the value of the remaining coefficients. Also the polynomials are minimized with respect to the rms departure from a reference surface. This means that the Zernike coefficients can be determined for a given data set with a least squares fit and the fit error is the rms of the difference between the polynomial representation of the data and the actual data. Furthermore, since the polynomials form a linearly independent basis each coefficient represents the standard deviation of the corresponding aberration term across the circular aperture.

The mathematical description of a continuous surface is given by Equation (1) where ρ and θ are radial and azimuthal variables, A_{nm} and B_{nm} are Zernike coefficients and n and m are radial and circumferential wave numbers.

$$Z(\rho,\theta) = A_{00} + \sum_{n=2}^{\infty} A_{n0} R_n^0(\rho) + \sum_{n=1}^{\infty}\sum_{m=1}^{n} R_n^m\left[A_{nm}\cos(m\theta) + B_{nm}\sin(m\theta)\right] \tag{1}$$

The radial dependence function, R_n^m, is defined by Equation (2) over a normalized unit radius for positive integer wave numbers n and m such that $n \geq m$ and $n+m$ is even.

$$R_n^m(\rho) = \sum_{s=0}^{(n-m)/2}\left[\frac{(-1)^s (n-s)!\,\rho^{(n-2s)}}{s!\left(\frac{n+m}{2}-s\right)!\left(\frac{n-m}{2}-s\right)!}\right] \tag{2}$$

For a rotationally symmetric (i.e., even) surface the B_{nm} coefficients are all equal to zero. The orthogonality condition for the set of Zernike functions is satisfied only if the area of the product over the unit circle of any pair of functions, Φ_1 and Φ_2, is zero. This condition is given by Equation (3).

$$\int_0^1 \int_0^{2\pi} \Phi_1 \Phi_2 \rho \, d\Phi \, d\rho = 0 \tag{3}$$

For non-circular apertures the orthogonality condition is lost since the radial and azimuthal integration limits in Equation (3) will include undefined values of functions Φ_1 and Φ_2. For some shapes (e.g., an annulus) there are alternative formulations of the Zernike polynomials [7,8] or other orthogonal polynomial sets (e.g., Legendre polynomials for rectangular apertures, Legendre-Fourier polynomials for cylindrical optics). The Gramm-Schmidt orthonormalization process can be used to construct orthogonal polynomials for more general aperture shapes such as sectors and segments of circles [9,10].

Commercial software packages such as MetroPro™ use the smallest circle that inscribes the data set, interpolating through missing regions of the aperture. The magnitude of reported aberration error can be determined by comparing the values of the Zernike coefficients when fit with different maximum orders. If the values change significantly then the Zernike expansion is not orthogonal and the coefficients may not accurately represent the magnitude of the associated aberrations.

The Zernike polynomials are also not orthogonal for discretely sampled data, which is always the case when analyzing interferograms. For discrete data Equation (3) is evaluated as,

$$\sum_k \Phi_{1k} \Phi_{2k} A_k = 0 \tag{4}$$

where A_k is the area associated with the k^{th} pixel. As the number of pixels imaging a given aperture are increased (and the normalized area represented by each pixel decreases) the residual error is minimized. As with non-circular apertures the degree of non-orthogonality can be checked. Also certain fabrication errors (e.g., ogive error due to tool alignment in diamond turning) cannot be adequately described by the Zernike polynomials with a reasonable number of terms [11,12].

Fitting Zernike polynomials to surface data (measured or calculated) can be performed using a standard least squares technique. First an error function is defined over a grid of data,

$$E = \sum_k W_k \left(\delta_k - Z_k \right)^2 \tag{5}$$

where the k^{th} data point, δ_k, is a computed or measured sag, Z_k, is the value of the Zernike polynomial and W_k is a weighting function proportional to the area represented by the point. The

weighting function is a fraction of the total normal or projected surface area. The Zernike polynomial approximation of the surface sag for coefficients, c_j and polynomial terms Φ_{kj} is given by Equation (6).

$$Z_k = \sum_j c_j \Phi_{kj} \tag{6}$$

Substituting Equation (6) into Equation (5) yields a least squares error function,

$$E = \sum_k W_k \left(\delta_k - \sum_j c_j \Phi_{kj} \right)^2 \tag{7}$$

Equation (7) can be minimized with respect to the Zernike coefficients by taking the derivative of the error function with respect to each coefficient and setting it equal to zero.

$$\frac{\partial E}{\partial c_j} = 2 \sum_k W_k \left(\delta_k - \sum_j c_j \Phi_{kj} \right) \Phi_{kj} = 0 \tag{8}$$

Equation (8) is a linear matrix which can be easily solved for the Zernike coefficients using QR decomposition [13]. The rms fit error can be computed as the rms difference between the polynomial representation, Z_k, and the discrete data, δ_k.

1.3 RESEARCH DIAMOND TURNING CONTROLLER

The control system for the Precision Engineering Center's ASG 2500 Diamond Turning Machine was designed and built in the early 1990s using a rack-mount PC-AT, ISA bus digital and analog I/O boards and a 68020 co-processor card with dual-port RAM. The control software was written in primarily in C. Custom drivers for the I/O boards, timer chip, video card and keyboard were coded in assembly language to meet a performance target of 1 kHz servo loop closure. The control software is very flexible and has provided a platform for control algorithm development, cutting mechanics and material science studies and freeform optics fabrication. The goal of this task was to replace the aging hardware with faster more reliable computer while retaining compatibility with the control software. Numerous updates and feature enhancements to the control system have been delayed over the past decade due to performance limitations of the 80286 and 68020 CPUs.

1.3.1 PERFORMANCE LIMITATIONS

The architecture of the control system was state-of-the-art in 1989. The PC-AT is responsible for user interface tasks and I/O and the 68020 co-processor was used for real-time servo loop timing, feedback control calculations and trajectory generation. The two CPUs are synchronized via a semaphore mechanism implemented in the 68202's dual-port memory. The 68020 has no direct access to the I/O boards connected to the machine. It would be ideal to replace the entire system with a new computer and compatible I/O boards. However the software for the dual-processor architecture cannot be simply re-compiled for a new system. The bulk of the code deals with the user interface and can be ported to another system with minimal change. The servo loop processing and I/O processing code is architecture, processor and in some cases compiler dependent. It was decided to incrementally replace the hardware to minimize machine down-time during software redeployment.

1.3.2 HOST PC REPLACEMENT

The PC-AT was replaced with a rack mount system from Advantech that includes ISA bus slots for compatibility with the existing Burr-Brown I/O cards and the Definicon 68202 co-processor card. This was essentially a plug-and-play replacement requiring only the recompilation of the user interface code. However the ISA cards that were migrated to the new PC are limited in their address capabilities so specific requirements were placed on the memory space usage of the new system. Unfortunately, this task proved to be experimental even for an experienced vendor and multiple motherboard and chip set configurations were tried before a successful combination was found. The 68020 co-processor and I/O cards were moved to the new rack mount PC and the software was installed. The new system was tested and used to machine the Ritchey-Chretien telescope mirrors. Performance is still limited, but now by the I/O cards and the 68020 instead of the 82086 CPU.

1.3.3 SOFTWARE ENHANCEMENTS

The performance bottleneck of the original controller software design was the need to perform all real-time I/O with the 80286 host processor. The newer Intel CPU (2 GHz Pentium 4) is limited by the response of the analog I/O channels and the ISA bus. The ISA bus is also used to communicate with the 68020 which is still performing trajectory and servo loop calculations. The migration of all calculation functions to the Intel CPU and the implementation of a real-time interrupt handler to drive servo calculations will allow the 68020 to be removed. Further improvement can then be gained by replacing the ISA I/O boards with functionally equivalent PCI boards. The hardware is also appropriate for a migration path to a dedicated DSP controller

such as a Delta Tau or PMDi, retaining only the newly purchased host PC and eliminating all of the original computer system components.

The control software has been recoded to eliminate several obsolete features, improving performance and simplifying the processor-to-processor synchronization code. The ordering of bytes within multi-byte words of data on the two processor system is different. (The Motorola convention is "big-endian" or most significant byte first and the Intel convention is "little-endian" or least significant byte first.) Every numeric piece of information passed between the two processors must have its bytes reordered by one of them. This process was performed on the 68020 in the original software since that was the faster processor. The speed advantage of the newer Intel chip is significant so this low level function is now implemented on the host PC.

1.3.4 AXIS TRACKING

Machining of a non-rotationally symmetric surface with the DTM augmented with an auxiliary fast tool servo axis requires synchronization of the motion of the auxiliary axis with the spindle and at least one of the DTM axes (usually the radial cross-feed axis). The high bandwidth motion is required of the FTS is beyond the capability of the axes controller so it has its own DSP control system operating at a minimum frequency of 20,000 Hz. This controller needs axis and spindle position information in real-time to generate motion commands for the FTS. The square wave quadrature signal from the spindle encoder is easily interfaced to multiple controllers since it requires no synchronization or handshaking signals. However, the position of each DTM axis is tracked by a Zygo Axiom laser interferometer and stored in a 32-bit accumulator. The controller can only read these accumulators if it follows a strict synchronization protocol with the Axiom measurement electronics. If two controllers both need the position information their access protocols must be synchronized.

For most feasible machining scenarios, the slope of the FTS motion with respect to spindle rotation will be high and the rate of change with radial axis position will be low. The radial axis motions are typically slow, producing a high quality surface finish. Thus it is possible read the axis laser data with the slower DTM axes controller which then sends the current position to the FTS controller. Many configurations are possible using either analog or digital signals. Digital signals are preferred as they have both lower latency and lower noise. At least two bits of information are required to track both motion and its direction. Both pulse and direction and synthetic square wave quadrature have been implemented in the DTM controller software. They are described below.

An encoder square wave quadrature signal consists of two 50% duty cycle TTL square waves separated in time by one quarter of a wave period (i.e., 90° phase offset). The DTM controller

maintains a 32-bit position accumulator for each machine axis with a least significant bit value of 2.5 nm. Since the accumulator is a 2's complement binary integer, the n^{th} bit of the accumulator represents twice as much axis distance as the next lower bit and half as much distance as the next higher bit and it changes state whenever the axis has moved an integer multiple of 2^{n-1} laser counts. If the axis position is tracked by examining the n^{th} and $(n-1)^{th}$ bits on each controller cycle, then the maximum axis velocity that can unambiguously tracked is equal to the product of the tracking width (2^{n-1} laser counts) and the cycle time in Hz. This means that if the state of the n^{th} bit changes from one cycle to the next, it could not have happened more than once.

The axis controller implements pulse-direction or quadrature tracking for the x and z axes. Pulse and direction axis tracking is implemented by simply routing the n^{th} bit of the absolute laser data to a digital output (where the closest boundary greater than the desired tracking width is 2^{n-1} laser counts) and toggling another digital output whenever the axis changes directions between cycles. The receiving DSP must count state changes of the pulse signal; adding or subtracting according to the state of the direction signal. On-chip counter/timer circuits are embedded in most DSPs and are easily programmed to process pulse-direction counting at very high bandwidths. Quadrature tracking is implemented by setting two digital outputs according to the four possible state combinations of the n^{th} and $(n-1)^{th}$ bits. One signal, A, is set to the value of the n^{th} bit. The other signal, B, is set to the complement of the exclusive-OR of the two adjacent bits. That is, B is set to zero if the two adjacent bits are the same; otherwise B is set one. As with pulse and direction, the quadrature tracking width (i.e., effective count resolution in the DSP controller) constrains the maximum axis velocity. For the current controller servo cycle frequency of 750 Hz, an axis velocity of 7.2 mm/min can be tracked with a resolution of 160 nm.

1.4 NRS MOTION PLANNING

A new technique has been developed for fabrication of non-rotationally symmetric or freeform optical surfaces on a diamond turning machine. This technique involves mounting a mirror blank on-axis and programming the DTM to follow a best-fit rotationally symmetric (RS) cross-section (spherical, conic or aspheric) while an auxiliary axis such as a fast tool servo (FTS) rapidly moves the tool to alter the shape of the resulting surface. By synchronizing the axes, spindle and FTS motions the desired non-rotationally symmetric surface is efficiently produced.

Surfaces of revolution are succinctly represented as a two dimensional cross sectional path in any plane that includes the axis of rotation. These representations include RS-274 G-codes, functional representations in Cartesian or polar coordinates and parametric representations. Freeform surfaces and symmetric surfaces rotated about a machine axis that is not coincident with their axis of symmetry (e.g., an off-axis conic segment rotated about the center of its aperture) require a complete three dimensional description rather than a cross-sectional path.

In the past, freeform surfaces were dealt with on an ad hoc basis and a specific solution was produced for each machining operation that depended on a variety of parameters such as the part fixture and part location on the fixture; machine geometry; tool geometry; fast axis orientation, bandwidth and range; and the original specification of the surface to be produced as illustrated in Figure 1 with an off-axis biconic mirror. Currently there is no standard way to decompose an arbitrary freeform surface into motion commands for the axes of a machining center. The surface may be expressed as an explicit or implicit 3D function in one of several coordinate systems or as a collection of vectors (i.e., data points and direction cosines). It is apparent that any of the functional forms can be used to generate such a point cloud in any coordinate system desired and at the density necessary to accurately represent the surface.

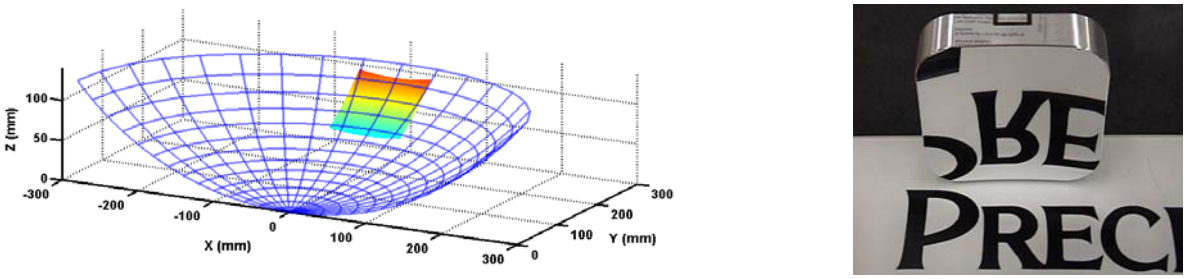

a) Off-axis biconic mirror segment

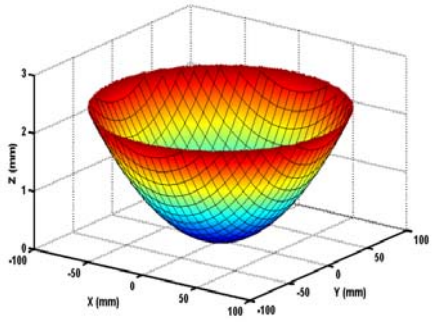

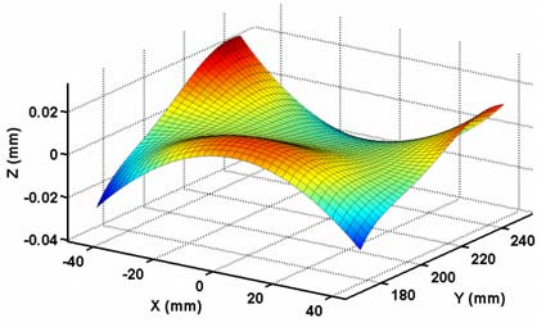

b) Rotationally symmetric component of mirror c) NRS component of the mirror

Figure 1. Decomposition of a biconic mirror surface (a) into symmetric (b) and non-symmetric (c) components for on-axis fabrication.

Motion planning for fabrication of a freeform or non-rotationally symmetric surface with diamond turning consists of four steps. Each of these steps is discussed in the following sections.

1) Decomposition of the surface shape into rotationally symmetric (X, Z DTM axes) and non-rotationally symmetric (FTS) components.
2) Description of the RS and NRS motion paths. This could be a functional description, but a 3D sag table over a polar grid (R,θ,z) is needed for the NRS path and 2D half-meridian cross-section (R,z) RS path is needed.
3) Compensation of the motion commands for the tool shape and radius.
4) Deconvolution of the NRS tool path to pre-compensate FTS actuator dynamics.

1.4.1 DECOMPOSITION OF FREEFORM SURFACES

Off-axis Conics

An analytic solution for the optimal decomposition of an off-axis segment of a conic surface into a rotationally symmetric component and a non-rotationally symmetric residual was developed for the Oak Ridge Y-12 Optics Modil in the early 1990s [14]. The algorithm was optimized for execution speed and coded in C for real-time generation of the command signals needed to drive a diamond turning machine and a fast tool servo to fabricate an NRS optical surface. The result is a functional description of the conic surface translated on axis and tilted, along with coefficients to a radial polynomial that is the "best-fit" asphere minimizing the NRS sag.

The NRS component is the difference between this function and the asphere. A C decomposition program, **nrsgen**, creates a sag table for the entire surface, the asphere or the NRS component over the specified aperture in either cylindrical or Cartesian coordinates. The aperture can be circular or square and the distribution of data points over the aperture can be evenly spaced in X and Y (plaid), spaced at equal angles on concentric radii (polar) or at equal angles and linearly decreasing radii (spiral). This program can be used to generate sag tables describing mirror surfaces for non-rotationally symmetric machining. Table 1 shows the decomposition parameters and results for an off-axis conic, three mirror anastigmat (TMA) described in [2]. Note that the best-fit asphere is almost a parabola for all three mirrors (i.e., the quadratic radial coefficient, A2, is at least five orders of magnitude larger than the other coefficients). The NRS shape is described in cylindrical coordinates by substituting the NRS coefficients from Table 1 into Equation 9. The derivation of this equation and C code for the automatic decomposition of off-axis conic surfaces can be found in [15].

$$z(\rho,\theta)_{NRS} = d_1 + d_2\rho\cos(\theta) - \sqrt{d_3 + d_4\rho\cos(\theta) + d_5\rho^2 + d_6\cos^2(\theta)} \qquad (9)$$

The difference between Equation 9 and the best-fit asphere is the required fast tool servo motion for any given radial position, ρ, and spindle angle, θ. The asphere error values in Table 1 give an estimate of the maximum sag difference between the true best-fit asphere and surface generated

by connecting the points of the asphere grid sag table with straight lines. It can be used as a guide to generating a table dense enough to meet error tolerances. The table was generated using a 400 x 400 square grid enclosing the circular aperture of each mirror.

Table 1. Off-axis conic TMA decomposition.

	Off-Axis Conic TMA		
	M1	**M2**	**M3**
R (1/curvature)	-1000.000000	-587.151127	-939.432788
K (conic constant)	-1.754657	-5.801289	-5.197043
Aperture Radius	70.000000	38.500000	35.000000
Decenter (Y)	220.242790	105.991898	79.181555
NRS Sag	0.186543	0.183477	0.023528
Tilt (YZ)	0.212285	-0.164886	0.082592
Decenter (Z)	24.035459	-9.219260	3.312460
Asphere Sag	2.350159	-1.152737	0.639387
Asphere Error	0.000004	0.000002	0.000001
Asphere Coefficients			
A2	4.800E-04	-7.809E-04	5.227E-04
A4	-7.484E-11	2.212E-09	-5.942E-10
A6	2.334E-17	-1.253E-14	1.351E-15
A8 (A10 to A16 omitted)	-9.097E-24	8.877E-20	-3.841E-21
NRS Coefficients			
D1	-1.539E+03	1.378E+02	-2.299E+02
D2	-5.340E-01	2.022E-01	-1.027E-01
D3	2.369E+06	1.900E+04	5.284E+04
D4	1.646E+03	5.614E+01	4.733E+01
D5	1.478E+00	2.153E-01	2.403E-01
D6	1.701E-01	7.244E-03	2.042E-03

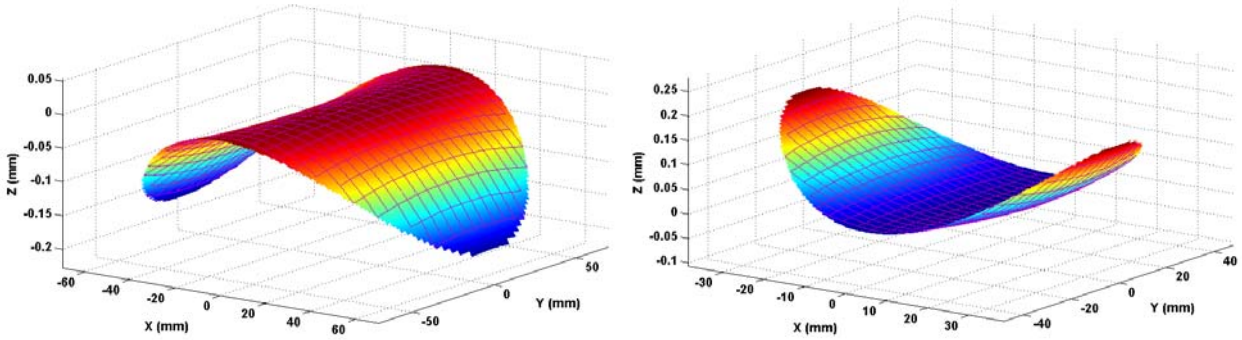

Figure 2. NRS component of off-axis conic TMA mirrors M1 (left) and M2 (right).

The shapes of the NRS components of the primary (M1) and secondary (M2) are shown in Figure 2 (the tertiary (M3) is similar to M1 with 1/8 the sag). For all three mirrors the FTS will reverse directions twice per spindle revolution. The maximum velocity of the Variform FTS is 140 mm/sec. By calculating the maximum slope in the circumferential direction along each surface and dividing these quantities into 140, the maximum rotational speed for machining can

be determined. For all three mirrors the slopes are less than 2 mm/sec. So the Variform velocity limit is not reached until the spindle speed exceeds 4200 rpm (140/2*60), which is more than twice as fast as the maximum ASG 2500 spindle speed. A similar calculation can be made for other actuators and other constraints (e.g., acceleration limits).

On-axis Zernike Polynomials

An on-axis Zernike polynomial TMA, also described in [2] was analyzed using two methods. Examination of the fabrication table output of CODE V revealed a maximum sag difference from a base radius sphere and for each mirror surface of no more than 184 μm. One option would be to machine this base radius sphere into each mirror while simultaneously moving the FTS to make up the sag difference. However smaller servo excursions generally produce better surface finishes so the mirror shapes were studied in more detail. The shape and location parameters of the three mirrors are given in Table 2. Each mirror is a hyperboloid deformed by Zernike coefficients 4 through 26. The "Tilt (YZ)" angle specifies the pointing angle of the normal vector from the vertex of each mirror surface in the YZ plane.

Table 2. Zernike polynomial TMA decomposition.

	Zernike Polynomial [ORA]		
	M1	**M2**	**M3**
R (1/curvature)	-946.952538	-489.108365	-875.359850
K (conic constant)	-1.679276	-5.703053	-3.850754
Aperture Radius	72.510880	32.581828	34.824238
Decenter (Y)	121.059700	145.843230	225.663140
Zernike Coefficients			
Z4 (Z1=Z2=Z3=0)	-1.065E-005	-1.323E-005	8.162E-006
Z5	8.564E-007	-8.314E-005	-6.505E-005
Z6	1.087E-008	5.704E-008	-1.152E-008
Z7	-4.661E-012	-8.385E-011	-4.515E-011
Z8	-1.244E-012	-1.742E-011	2.274E-012
Z9	4.151E-008	2.352E-007	-3.270E-008
Z10 (Z11 to Z26 omitted)	-7.659E-009	-1.696E-007	-7.481E-008
NRS Sag	0.152000	0.184000	0.164000
Tilt (YZ)	0.221632	-0.266386	0.177875
Sphere Radius	-946.952538	-489.108365	-875.359850
NRS Sag (optimized)	0.138000	0.048000	0.020000

Fitting an asphere (radial polynomial) to each surface reduces the NRS sag to a maximum of 138 μm for M1. Figures 3 and 4 show the NRS component remaining after removal of the best-fit asphere from each surface. Additional tilt of the mirrors may further reduce the NRS sag (especially for M2). This would change the mounting plane angle with respect to the optical housing by an equal amount.

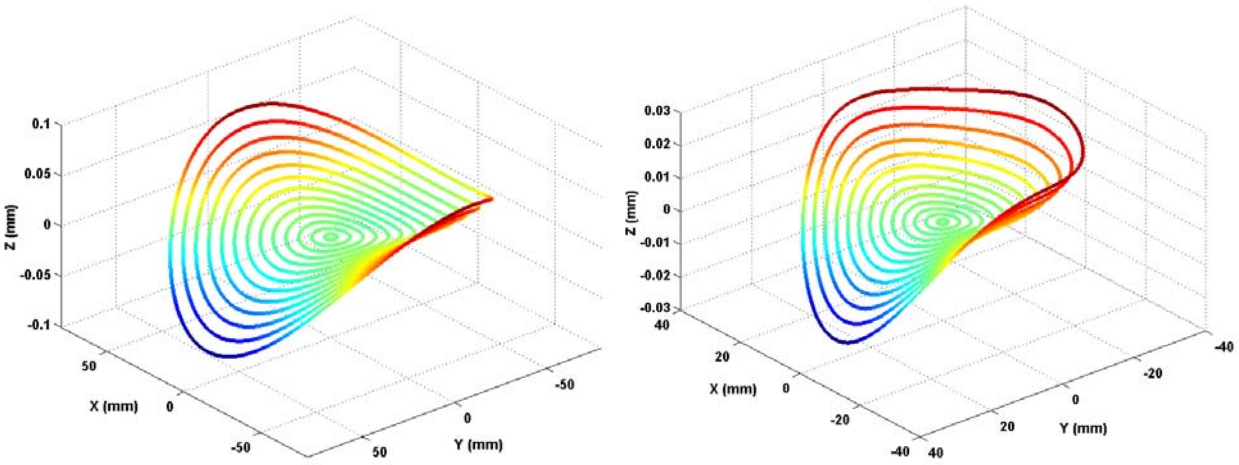

Figure 3. NRS component of Zernike polynomial TMA mirrors M1 (left) and M2 (right).

Generalized NRS Decomposition Algorithm

The technique used to generate the optimized NRS sag values for the Zernike polynomial TMA mirrors by fitting an asphere is quite simple and can be applied to any surface described by a function or a grid sag table that is to be machined about the center of its aperture.

1) Generate sag values along concentric radii about the center of rotation either by direct evaluation of the surface function or interpolation of a sag table.
2) Fit a least squares plane to the sag data.
3) Rotate the data to remove this plane. Note the XY and YZ tilt angles of this plane for design of a mounting surface.
4) At each radius,
   a) Find the mean sag value.
   b) The "best-fit" asphere at this radius must pass through the mean sag.
   c) For each angular location at this radius, the residual sag is the NRS surface.

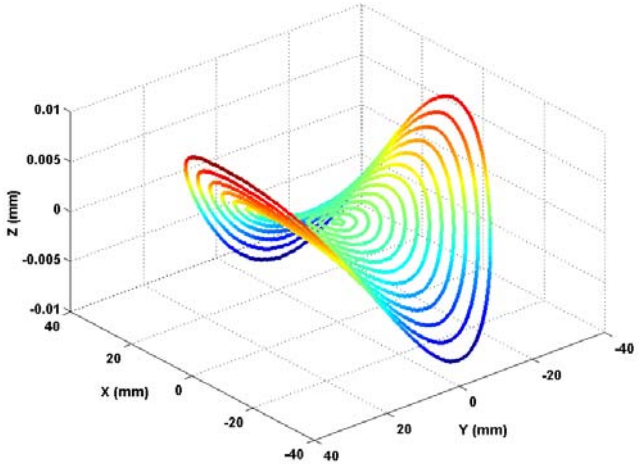

Figure 4. NRS component of Zernike polynomial TMA mirror M3.

In this way, both the best-fit asphere (ρ,z) and the NRS surface (ρ,θ,z) can quickly be constructed point-by-point as a 1D table (step 4b) and a 2D table (step 4c), respectively. The procedure is optimal in that it minimizes the NRS sag. Steps 2 and 3 can be skipped or modified to use the largest of the two tilt angles if a compound tilt in the mounting surface is undesirable. A sphere

instead of an asphere may be easily fit to the data so that the rough machined surfaces will be easier to evaluate. In this case a least squares sphere with its center constrained to lie along the spindle centerline is fit to the 3D sag table data. It is also possible to fit a circle to the (ρ,z) columns of the 3D sag table (ignoring θ). If the circle center is constrained to the spindle centerline the results will be identical to the spherical fit. All three methods have been coded in Matlab. If the sag table is arranged such that each row is a concentric ring (or equivalently each column is a meridian), then the asphere fit and tool radius compensation operations described below can be fully vectorized in Matlab.

1.4.2 REAL-TIME MOTION PATH

The rotationally symmetric component of the surface is described to the DTM controller as a (ρ,z) toolpath, usually from the edge of the part to the center for on-axis turning of a circular aperture. The exact command format depends on the controller, but usually follows the RS-274 G-code format. For an asphere the path consists of closely spaced points and an interpolation method for moving between points. The **nrsgen** program or the point-by-point algorithm discussed above can be used to generate the asphere and estimate the error due to linear interpolation, which should yield a worst case result.

To find the FTS locations at each point on the mirror surface during machining a bilinear interpolation algorithm over a grid of (ρ,θ,z) machine axis locations is used. The interpolation is expressed in polar coordinates since the DTM cross-feed axis (X) and spindle (θ) define a cylindrical coordinate system. The interpolation table is easily managed by the FTS control system and can yield a toolpath with residual errors smaller than the positioning accuracy of the actuator if the tabulated values are closely spaced relative to the surface curvature. The basic idea of multi-dimensional interpolation is to find the neighborhood of an un-tabulated value in the table and construct a weighted average of the values of nearby points as an estimate of the unknown value. For a two dimensional table, there are four nearest points to consider. A linear estimator uses the product of the distance ratios from the un-tabulated point to the grid lines intersecting each neighbor point in each dimension as the weighting factor for that tabulated neighbor point. Higher order estimators that use cubic functions, splines or a table of derivatives can produce smoother, more accurate interpolators; all at the cost of longer computation time and more memory.

Bilinear Interpolation

The interpolation grid covers an area somewhat larger radial area than the aperture of the mirror to avoid edge discontinuities that induce vibrations and degrade surface finish. Bilinear interpolation begins by finding the two rows and columns that bound an input (ρ,θ) data point.

Saturation instead of extrapolation at the table boundaries accomplishes the objective of having the tool position not change as a function of spindle rotation outside the aperture of the mirror. This also allows angular subapertures (useful for off-axis machining) to be easily implemented. For an equally spaced rectangular grid (in polar coordinates) the indices of the nearest neighbor tabulated points to *(ρ,θ)*, can be found by calculating,

$$ri = \left\lfloor \frac{\rho - r_{\min}}{r_{delta}} \right\rfloor \qquad \text{and} \qquad ti = \left\lfloor \frac{\theta - \theta_{\min}}{\theta_{delta}} \right\rfloor \tag{10}$$

where r_{delta} and θ_{delta} are the radial and angular grid spacing and r_{min} and θ_{min} are the lower boundaries of the interpolation table, respectively. The four nearest points are located at [row, column] positions: *[ri, ti]*, *[ri+1, ti]*, *[ri, ti+1]*, and *[ri+1, ti+1]*. Weighting factors for the radial and angular dimensions are,

$$w_r = \frac{(\rho - Vr_{ri})}{r_{delta}} \qquad \text{and} \qquad w_t = \frac{(\theta - Vt_{ti})}{\theta_{delta}} \tag{11}$$

where *Vr* and *Vt* are vectors of the radius and angle values defining the row and column coordinates of the interpolation grid. The FTS position is estimated as,

$$z_{FTS} = w_r \cdot w_t \cdot Mz_{ri+1,ti+1} + w_r \cdot (1 - w_t) \cdot Mz_{ri+1,ti} + (1 - w_r) \cdot w_t \cdot Mz_{ri_i,ti+1} + (1 - w_r) \cdot (1 - w_t) \cdot Mz_{ri_i,ti} \tag{12}$$

where *Mz* is the two dimensional interpolation table of exact tool locations. If the grid is not uniformly spaced Equation (10) must be replaced with a search procedure to find *ri* and *ti*. This need not be time consuming since on any given control cycle the search can start at the grid location of the last cycle. The weighting factors in Equation (11) will also have to be modified since are r_{delta} and θ_{delta} become constant vectors instead of scalars.

The two toolpaths, RS and NRS, are followed independently by the two control systems, but are synchronized by the common feedback signals from the machine axes. The spindle encoder and X axis (radial direction) laser interferometer data must be available to both controllers in real-time.

1.4.3 TOOL RADIUS COMPENSATION

Since the tool has a finite shape (usually a circular radius) in the XZ plane of motion, the contact point between the tool edge and the work surface changes as a function of the slope of that surface. For RS machining with circular tools the required compensation is easily implemented by offsetting the tool path by the radius of the tool in a direction normal to the surface.

For example, a circular segment of a concave sphere of radius R_S can be machined with a tool of radius R_T by moving the tool through a path from the edge to the center of the aperture along a circular path of radius (R_S - R_T). For other shapes the change in slope is not constant, requiring computation of the gradient of the surface either analytically or numerically. For a surface normal angle, φ, measured with respect to a vector from the center to the apex of the tool the corrections are,

$$x_{delta} = R_T \sin(\varphi) \qquad \text{and} \qquad z_{delta} = R_T \cos(\varphi) \tag{13}$$

For a non-rotationally symmetric surface, the normal angle, φ, is dependent on both the radial and angular location of a point on the surface (i.e., the surface is three dimensional). Thus the normal vector cannot be found from a single cross-section nor is the normal always in the plane of the cutting tool.

Normal Vectors

If the surface is described by parameters to a function (e.g., a biconic or polynomial expansion), then it may be convenient to generate tool radius compensation values analytically. For any continuous, differentiable surface a normal line is perpendicular to any two tangent lines that intersect at a right angle. In particular, the tangent lines that lie in the XZ and YZ planes define a plane tangent to the surface and can be used to find the normal. Parametric expressions for these two lines tangent to F of length u are,

$$L_{XZ}(u,x,y) = \left[x+u, y, F(x,y) + u \cdot \left(\frac{\partial F}{\partial x} \right)(x,y) \right] \tag{14}$$

$$L_{YZ}(u,x,y) = \left[x, y+u, F(x,y) + u \cdot \left(\frac{\partial F}{\partial y} \right)(x,y) \right] \tag{15}$$

The normalized cross product of unit length tangent lines, L_{XZ} and L_{YZ}, evaluated at any (x,y) defines a normal to the surface at (x,y) as shown in Equation (16).

$$NL(x,y) = \left\| \left[L_{XZ}(1,x,y) - L_{XZ}(0,x,y) \right] \times \left[L_{YZ}(1,x,y) - L_{YZ}(0,x,y) \right] \right\| \tag{16}$$

A parametric function that gives the coordinates of the endpoints of a normal line of length u can be defined as,

$$PNL(u,x,y) = \left[x + u \cdot NL(x,y)_1, y + u \cdot NL(x,y)_2, F(x,y) + u \cdot NL(x,y)_3 \right] \tag{17}$$

Substituting the Cartesian function defining surface sag for F in Equation (17) and evaluating it for each point ($x, y, F(x,y)$) and the length, u, yields the coordinates (x', y', z') of the other end of the vector.

If F is described by a grid sag table, interpolation must be used to find the sag for untabulated (x,y) points. Finite difference methods can be used to find the partial derivatives required to evaluate Equations (14) and (15) if analytic expressions are not known. However, in this case, the 3D radius compensation method described in the next section may be simpler to implement.

After generating a new data set (or functional description) offset by the tool radius in the surface normal direction using Equation (17), a projection into the cutting plane (typically XZ) is required to obtain the final corrected toolpath. The correct orthographic projection is simple since the XZ and YZ tangent lines were used to derive Equation (17). The result is given in Equation (18).

$$QNL(u,x,y) = \left[x + u \cdot NL(x,y)_1, F(x,y) + u \cdot NL(x,y)_3\right] \tag{18}$$

Alternatively, since discrete data points must eventually be generated the projection can be expressed as a homogeneous transformation matrix. If the corrected data set from Equation (17) is the (n by 4) matrix M, then the orthographic projection given by Equation (19) produces the radius compensated data set P projected into the XZ plane.

$$[P] = \begin{bmatrix} 1 & 0 & 0 & 0 \\ 0 & 1 & 0 & 0 \\ 0 & 0 & 0 & 0 \\ 0 & 0 & 0 & 1 \end{bmatrix} \times [M] \tag{19}$$

3D Radius Compensation

For tool radius compensation of an NRS surface, the normal vectors can be determined analytically or estimated numerically from a grid sag table, but they must be projected into the plane of the tool (XZ). The tool offsets for a given point are then the x and z components of that projected vector. If the radial spacing of the original tool path is to be retained, then the x correction must be zero and the z correction is adjusted proportional to the cosine of the projected normal vector.

The tool compensation procedure described is straightforward to implement with an algebraic programming language such as Maple, but is difficult to implement in a procedural programming

language such as C or Matlab. As an alternative, consider the 3D radius compensation problem as a series of 2D problems; one for each angular position of the spindle. If the surface data is expressed in cylindrical coordinates, a collection of half-meridian paths (radial lines from edge to part center) can be individually corrected for tool radius giving a corrected path for each spindle angle. A complete cylindrical 3D grid sag table for the NRS surface can be built in this way with any angular resolution. This is equivalent to the vector projection technique discussed above but is much simpler to implement. For large apertures the number of meridians needed to adequately describe the surface may be large since the surface area represented by each point on an equiangular gird increases with radius. Matlab code has been developed that implements this 3D tool radius compensation algorithm. The half-meridians are extended a short distance past the center and outer edge of the aperture since slope estimation using finite differences is inaccurate at the endpoints of a curve. The redundant data points are discarded after compensation.

1.4.4 DECONVOLUTION OF ACTUATOR DYNAMICS

Synchronization between the DTM axes and the FTS is critical if the correct NRS shape is to be produced. While the machine axes follow a low frequency trajectory to create a rotationally symmetric (RS) component, the FTS moves at high temporal and spatial frequency to produce an NRS feature within one revolution of the part. An example is the fabrication of a toric lens, which has two different radii of curvature in orthogonal directions. There is an average radius that can be cut by the slow speed machine axes, but an FTS is needed to add features twice per revolution to create the smaller radius at one location and the larger radius 90 degrees later. The synchronized motions of the machine axes and the FTS combine to create the desired geometric surface. However, the dynamic behavior of the axes, particularly the FTS, can influence the commands, delaying the motion of the tool and creating errors in the resulting surface. The phase errors of the base machine axes can usually be ignored as the axis accelerations are moderate and velocity is low. However, even a small lag time associated with a FTS will result in poor form fidelity and improper placement of NRS surface features with respect to the base surface and any fiducials on the part. The errors caused by the FTS dynamics can be corrected if they are known, repeatable and used to modify the input command to the actuator.

Actuator Phase Lag

Figure 5 illustrates the delayed and attenuated response of the Variform FTS. In this example, the phase angle is less than one degree; however the effect of phase lag scales with radius and results in significant form error (6.28 mm at 600 rpm and 100 mm radius) unless the actuator is operated at a frequency substantially below its bandwidth (by a factor of 100 or at about 3 Hz).

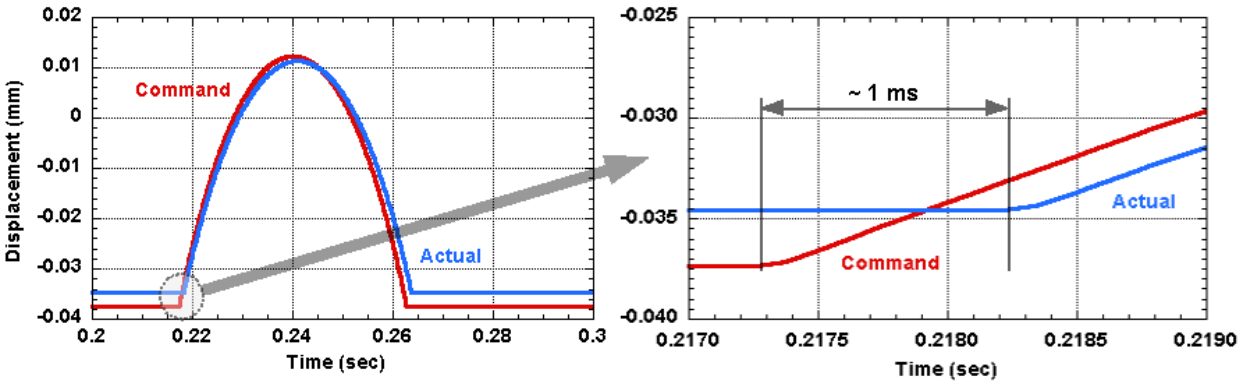

Figure 5. Response of the Variform to an input command.
Actuator motion is delayed about 1 msec and attenuated by about 8%.

Convolution

The response of a dynamic system to an applied signal is a function of the frequency of that signal. In general, the response results in an attenuated and delayed motion of the output with respect to the input signal. When the system is a fast tool servo and the dynamic input signal is made up of a variety of frequencies, the result is form error in the machined surface. If the input contains multiple frequencies, the corresponding output can be determined using the principle of superposition; that is, the input signal can be uniquely decomposed into single-frequency components each of which will be individually attenuated and delayed.

The response of the system is the sum of these frequency components. To machine a desired surface profile with high fidelity, the amplitude attenuation and phase related delay must be eliminated. To achieve this, the input signals are modified prior to applying them to the system such that the attenuation is canceled and the phase is compensated. A technique for system identification and an input signal modification algorithm have been developed and applied to several fast tool servos to produce the desired output response for high frequency inputs [16].

Deconvolution

The effect of a dynamic system on an input signal of length N can be determined by applying the convolution operation to the input $x[n]$ and the impulse response $h[n]$ of the system. The convolution operation describes how a linear filter (an actuator) modifies a given input signal (command) to produce an output signal (motion). Each value in the convolved output signal $y[n]$ can be calculated with the summation in Equation (20), where M is the length of the impulse response. The length of $y[n]$ is $N+M-1$. Convolution is mathematically equivalent to polynomial multiplication and can be directly (and inefficiently) calculated from Equation (20) in the time

domain. If the discretely sampled input and impulse response signals are transformed to the frequency domain, convolution becomes a straightforward element-by-element, complex multiplication of two vectors. The discrete Fourier transform (DFT) is commonly implemented by the fast Fourier transform (FFT) algorithm which exploits the symmetries in Equation (20) to accelerate this calculation. Equation (20) can thus be restated in the frequency domain using an FFT operator as shown in Equation (21). The inverse FFT operation can then be used to find *y[n]*.

$$y[k] = \sum_{m=0}^{M-1} h[m] \times x[k-m] \tag{20}$$

$$\mathbf{FFT}(x[n]) \times \mathbf{FFT}(h[n]) = \mathbf{FFT}(y[n]) \tag{21}$$

Deconvolution is the inverse of convolution and can thus be used to find *x[n]*, given an actuator impulse response *h[n]* and a desired motion $y_d[n]$. Rearranging Equation (21) gives Equation (22). Note however that $y_d[n]$ and *h[n]* must be the same length and sampled at the same frequencies for the division operation to be carried out.

$$x[n] = \mathbf{FFT}^{-1}\left(\frac{\mathbf{FFT}(y_d[n])}{\mathbf{FFT}(h[n])} \right) \tag{22}$$

Application of the inverse FFT operation then yields a signal that should exactly counteract the actuator dynamics so that it follows the desired trajectory, eliminating steady-state following error. This technique critically depends on knowledge of the actuator dynamics as embodied in the impulse response and requires the complete desired motion profile.

Experimental Verification

The algorithm has been validated for the Variform FTS. The response of this actuator is predominately second order although nonlinearities are present for large amplitude command signals. Figure 6 shows the path error associated with a 160 μm command signal that is the sum of 100 Hz and 300 Hz sine waves. The response of the actuator to the 300 Hz sinusoid is 140 degrees out of phase and attenuated 2.5 dB resulting in a very large (200 μm PV) error. The deconvolution algorithm calculates a new command signal that effectively pre-compensates for these effects individually at each constituent frequency. The following (or tracking) error is reduced by about 3 orders of magnitude. The response shows virtually no delay from the desired excursion after a startup interval lasting approximately 4 ms. In practice, this startup period will occur before machining begins and thus will not affect the fidelity of a surface.

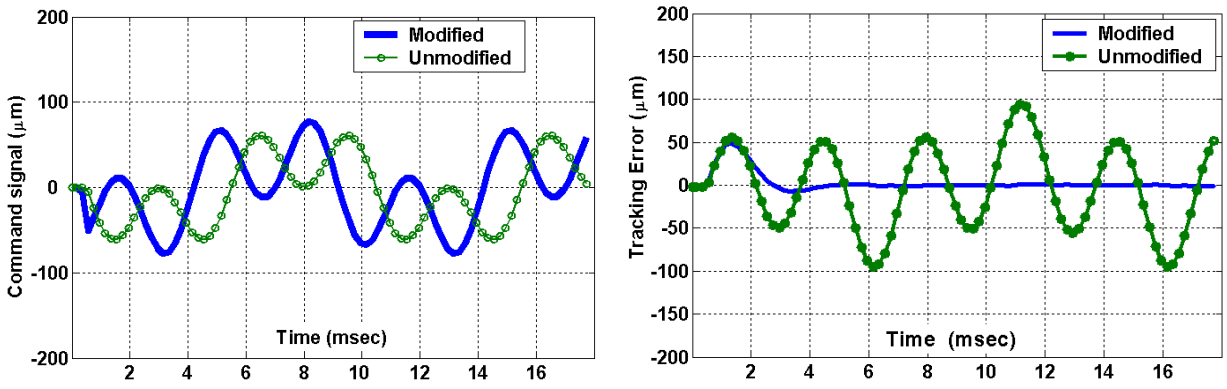

(a) Command signals (b) Acutator tracking error

Figure 6. Deconvolution experiment for a high frequency command signal.

Implementation

The deconvolution algorithm described by Equation (22) has been coded in Matlab and generalized for use with any surface described as a time-based path. A direct implementation of this equation encounters several obstacles. These include sampling frequency and sampling duration mismatch in $h[n]$ and $y_d[n]$, noise amplification by the vector division operation, frequency bin leakage due to imperfect sampling of $h[n]$ and computational round-off from the FFT operations. These problems were overcome with two innovations to the standard frequency domain deconvolution technique. First, by inverting $h[n]$ and re-sampling the result so that its resolution and duration match $y_d[n]$ an overlap-add block convolution algorithm can be used. In other words, the deconvolution operation is replaced with convolution of the command signal with the inverse dynamic response of the actuator. It is also possible to measure the inverse dynamics directly with a spectrum analyzer by reversing the roles of the input (or excitation) signal and the output (or actuator response) signal. Frequency leakage from the dynamic response causes the inverse FFT to produce a complex result. Clearly the time-domain trajectory command sent to the actuator controller cannot be complex. Simply discarding the imaginary part of each value or taking the absolute value is incorrect. The second innovation was the implementation of an inverse FFT algorithm that always returns a correct real result.

To pre-compensate a fast tool servo shape for diamond turning, the spindle speed must be selected so that a time-based spiral path can be generated that represents the FTS actuator motion. Then deconvolution in the frequency domain can generate a compensated tool path (also a spiral). Finally the spiral data can be transformed back into the time domain and overlaid into a polar grid for the FTS controller bilinear interpolation routine. This process has been automated for several types of freeform surface descriptions including those described in this report.

Group Delay

The concept of phase in the frequency domain is closely related to symmetry in the time domain. This is because the phase information locates the constituent sinusoids of a transformed signal in time; that is, phase tells us when something happens. The term group delay is used in signal processing to quantify the temporal distortion of a waveform within a frequency band as it passes through a filter, for example an audio signal through a speaker. Group delay is defined as the rate of change of total phase shift with respect to angular frequency and has units of seconds. If this quantity is a constant then the phase of the filter it constant and all parts of the waveform passing through it are time shifted by the same amount (the group delay), but not distorted.

Time shifting a waveform results a change in the slope of the phase when the waveform is transformed to the frequency domain. Thus if the slope of the phase is constant, that is, the phase plotted using linear (not logarithmic or dB) axes is a straight line, then all frequencies shift in time by the same amount. Therefore an actuator with linear phase acts as a filter with a perfectly symmetric impulse response and changes all input frequencies in the same way. In fact this change is distortion free and is simply a time shift between the input and output. Except for this time shift and an amplitude change if the gain ratio is not unity, the commanded motion and actual motion will be identical. Furthermore correcting any gain mismatch by applying a multiplicative factor to the input (i.e., command a larger or smaller signal to get the desired response) is independent of the phase shift.

Linear phase is thus a highly desirable characteristic since without it the actuator acting as a filter temporally "smears" its input command resulting in a distorted motion profile. The deconvolution process and software discussed above corrects this behavior by shifting each frequency component by a different amount. However, if the phase response is nearly linear then the distortion is minimal. Everything simply happens later than desired. The result is a "clocking" of all spindle angle dependent features machined by the fast tool servo with respect to any previously machined part feature or fiducial that was angularly aligned with the zero meridian. This effect can be easily compensated by clocking the part in the opposite direction on the chuck.

The phase linearity of two actuators, the FTS-1000 and the Variform, are shown in Figures 7 and 8. The FTS-1000 phase deviates from a straight line by ±0.5° and the Variform phase is within 5° of being linear over its useable frequency range.

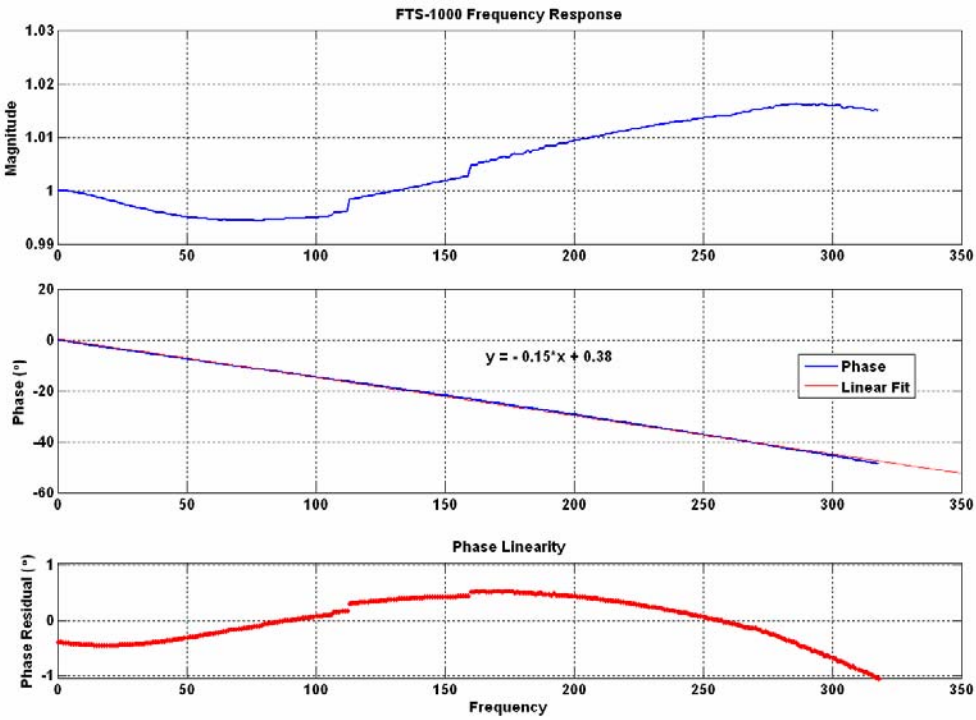

Figure 7. Normalized average frequency response of the FTS-1000.
The lower plot shows ±0.5° phase deviation from a constant group delay of 0.15° per Hz.

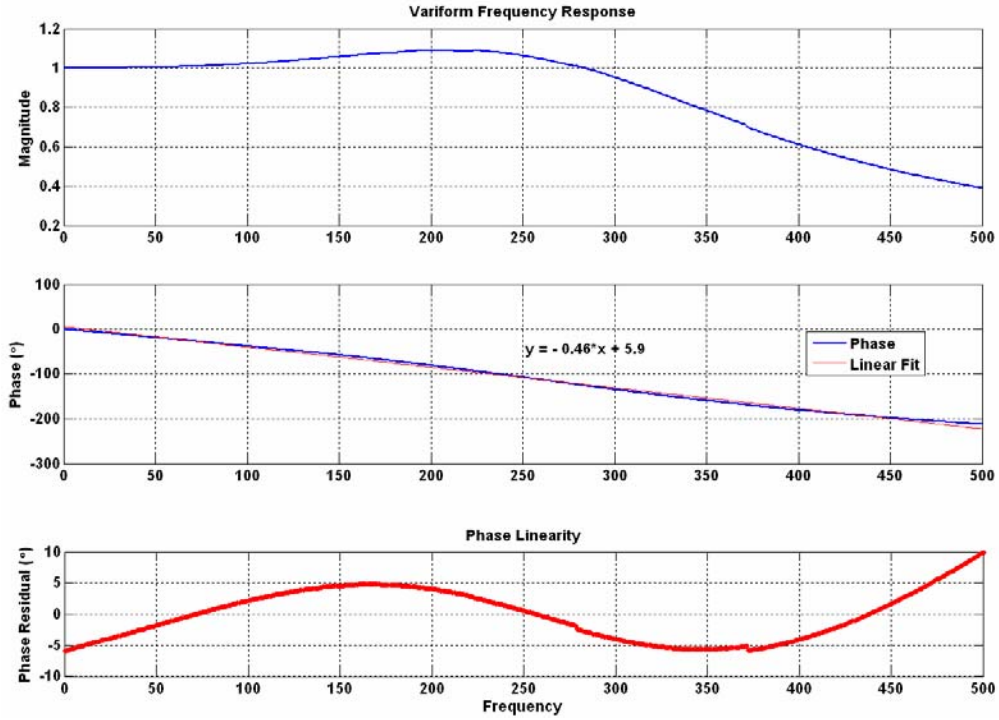

Figure 8. Normalized average frequency response of the Variform.
The lower plot shows ±5° phase deviation from a constant group delay of 0.46° per Hz.

Phase Lead Phase lag in an actuator can be canceled by introducing phase lead into the machining operation. Four techniques to accomplish this are listed below.

1) Rotate the part relative to the chuck in the direction opposite to spindle rotation during machining. This can be done by moving either the part or the chuck.
2) Offset encoder readings in the machine tool controller before they are used to determine the real-time commands set to the actuator.
3) Time shift the stream of position commands going into the controller.
4) Modify the part description by circularly shifting meridians of data.

The fourth technique is mathematically equivalent to the deconvolution of a time-based motion trajectory with an ideal actuator having unity gain and linear phase shift. The first three methods are simple and fast for production machining, but may require modification of the machine tool control software.

1.5 METROLOGY

The Zygo GPI-XP interferometer and the Taylor Hobson Form Talysurf profilometer are widely used for form metrology of optical and bearing surfaces. However, both instruments have limited capabilities for characterizing aspheric and non-rotationally symmetric surfaces. With a hologram or custom reference elements and appropriate fixtures a wide variety of mirrors and lenses can be characterized with an interferometer. But the reference elements are costly, come with their own surface deformations and their setup is both time consuming and error prone. The wavefront errors due to incorrect alignment of reference elements may also be indistinguishable from common fabrication errors.

A two dimensional profilometer can measure a cross-section of any surface within its vertical and horizontal traverse area subject to its probe slope limitations. However, registration of a trace with respect to the geometry of the surface is difficult if the optical axis (or other axis of symmetry) does not intersect the measurement plane. Measurement data from on-axis rotationally symmetric surfaces such as conics and aspheres may be incorrectly interpreted due to out of plane tilt of the surface. If the apex or "crown" of the part is inaccessible (e.g., an off-axis conic segment) or virtual (e.g., an annular surface) the difficulties increase. Freeform surfaces without an axis of symmetry can be measured, but a single 2D cross-section through an arbitrary region of the surface may be of little value other than determining a lower bound on the peak-to-valley error of the part. The problem is that even though a least squares fit with a 3D model can be performed with data from a single 2D trace, multiple traces cannot be used to derive the overall form error of the surface unless all the data is transformed to the same coordinate system origin.

To analyze profilometer and interferometer data tools other than the equipment vendor software are needed. Utilities for conversion of MetroPro and Talysurf data files from the proprietary vendor format to a text format that is easily imported into Matlab were developed. 2D and 3D least squared procedures (linear and nonlinear) and a graphical utility to extract a 2D slice of data from a 3D Cartesian data set using Matlab have also been written.

1.5.1 TALYSURF DATA CONVERSION

The Taylor Hobson Form Talysurf software includes a command line utility program, conv_dep, to convert a saved binary data file into an ASCII text format. The correctness of its output has been verified, but it frequently fails to produce an output file. A systematic investigation of measurement and analysis combinations failed to indicate a particular set of reliable options. Taylor Hobson no longer supports this utility, but did provide a newer program, talyconverter. Unfortunately, this program only converts raw measurement data and has been demonstrated to produce incorrect results when applying arcuate correction (i.e., probe radius and stylus swing) to a calibration sphere measurement data set. Fitting a desired curvature profile to measured data using Matlab is straightforward; however there is little point in doing so without arcuate correction. Probe radius is easily compensated, but the algorithm used by the Taylor Hobson software to compensate for stylus swing from calibration data is not available. It is also not known if the instrument software corrects for non-spherical probe shape or other errors evaluated during calibration. A simple, reliable procedure for saving and converting Talysurf measurement data for off-line analysis is as follows.

1) **Datum** should be selected from the **Form Options Menu**
2) Save the data with the **Modified Profile** option selected from the **Saving Data Menu**
3) Delete the header and trailer from the resulting binary data file. Currently this is done with the Vedit text editor. The header and trailer are delimited with easily identified tag strings. The size of the trailer is fixed, but the header length is variable.
4) Convert the edited binary file to ASCII with a C utility program *bdtoa*.

1.5.2 METROPRO DATA CONVERSION

The Zygo MetroPro software saves interferometer data files in a binary raw data format that includes all instrument settings needed for data analysis. A command line C program, *metropro*, was written to read a file of this format and produce a 3D Cartesian data set in one of several text formats. Table 3 shows the invocation options for *metropro*.

The default options will produce a matrix of sag values in a text file with a single header line as shown in Table 3. Tilt is not removed from the data unless the '-r' option is specified. To import

a MetroPro data file directly into the Matlab workspace a function was written that calls the metropro program. A default set of options returns a matrix of Z sag values, two vectors containing Y (row) and X (column) labels, and a header information structure. The Matlab function template for *import_metropro* is shown in Table 4.

Table 3. Metropro data conversion utility options.

```
metropro  [-bapimlrqszudnwhkv]  input_file  output_file
   b   binary metropro input file
   a   ascii  metropro input file
   p   extract phase     matrix (micrometers)
   i   extract intensity matrix (normalized to 0..1)
   m   matrix output  (rows and columns, z values in um)
   l   linear output  (x,y,z (mm,mm,um))
   r   remove least squares plane from data
   q   don't remove least squares plane from data
   s   scale output values  (x:mm,y:mm,z:um or 0..1)
   z   suppress scaling of  (x,y)   output values, scale z
   u   suppress scaling of  (x,y,z) output values
   d   use '.'   for missing z output values
   n   use 'NaN' for missing z output values
   w   don't output xyz data with missing z values
   h   print all metropro header fields
   k   quiet operation, no console output
   v   verify file format (no data output)

   b, p, m, q, s and n are default options,
   input_file  is the name of a zygo metropro data file and
   output_file is the name of the output text file

   output file header format:
       #cols  #rows  col_offset  row_offset  xy_res  z_res
```

Table 4. Metropro data import function specification.

```
  Import a metropro binary data file
     [zz,y,x,hdr] = import_metropro(fn,opts)
  Input
     fn     metropro binary data file
     opt    option string passed to metropro.exe
  Output
     zz     surface data matrix      (n x m) (um)
     y      vector of row    values  (n x 1) (mm)
     x      vector of column values  (1 x m) (mm)
     hdr    structure containing column, row, offset and resolution
            values

  The program metropro.exe is invoked to convert a metropro data file into
  a matrix of sag values.  If omitted as an input argument, the default
  option string'-bpmqsnk' is passed to metropro.exe and binary phase data
  is converted to a scaled sag matrix, zz, and two vectors, x and y,
  denominating the column and row extent of zz.  NaNs are used to represent
  missing data values in zz.
```

For example, a measurement of a scribed PMMA sample with the Zygo NewView white light interferometer can be imported into the Matlab workspace as follows,

```
>> [zz,y,x,hdr]=import_metropro('pmma08.dat','-bpmrsnk');
>> hdr
hdr =
         ncols: 640
         nrows: 480
    col_offset: 0
    row_offset: 0
      xy_scale: 0.0011
       z_scale: 1.0000e-005
```

A 3D surface plot of the imported data can be generated with the Matlab function call, **mesh(x,y,zz)**, as shown in Figure 9. Note that an explicit options list was given in the call to *import_metropro* so that tilt would be removed from the data. An *export_metropro* function was also written to export surface height data into the phase matrix of a binary data file for analysis with MetroPro.

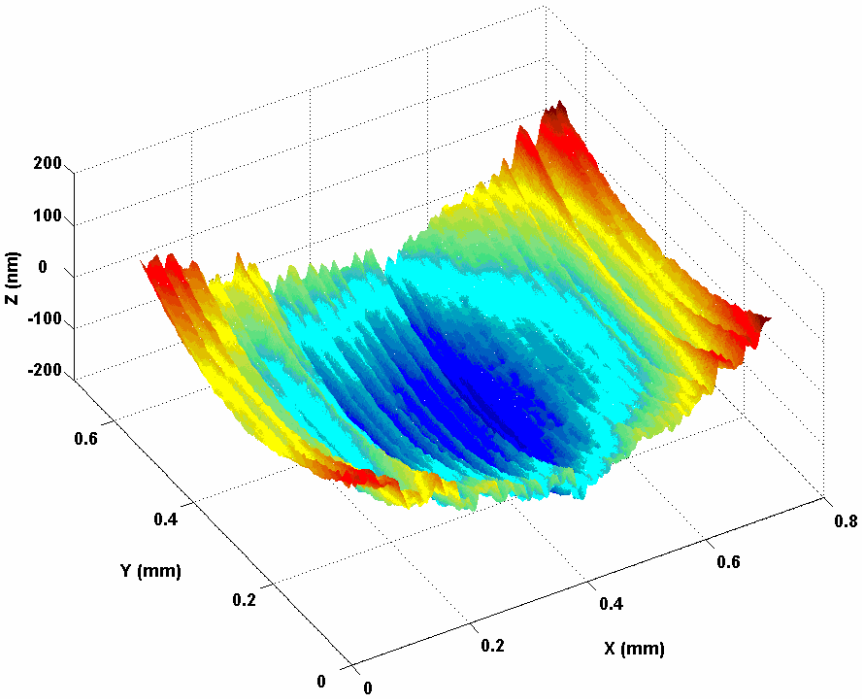

Figure 9. MetroPro surface data imported into Matlab.

2D Cross-Sectioning

A frequently used feature of the MetroPro interferogram analysis software is the profile plot of a slice through a filled contour. The accompanying analysis features have proven very useful for visualizing both surface finish and form features. Unfortunately, the 2D data slices selected by the user cannot be individually exported into data files. Thus it is difficult to quantitatively compare data slices from multiple measurements.

A profile sectioning application was written using the Matlab graphical user interface environment, GUIDE. This application, *slicer*, consists of a single window with two graphs (a filled contour of a surface and a 2D profile slice) and a small set of UI components. These include slider bars for positioning the data slice; push buttons to update plots and export data; data entry fields for mesh size, number of sliced data points and the name of the exported data structure and text fields with profile statistics (Rt, Rq and Ra). Figure 10 shows the *slicer* application window after importing the example data set shown in Figure 9.

The XL, YL, XR and YR slider bars control the horizontal and vertical positions each end of the sectioning slice. The X, Y and Z pull-down lists are filled with all current workspace variables when *slicer* is started. The variables selected may be vectors or matrices. They must all have the same dimensions or X and Y may be vectors matching the row and column dimensions of the matrix Z. Since a slice that is not horizontal or vertical will not intersect the input data grid, cubic polynomial interpolation is used to find Z values along the profile.

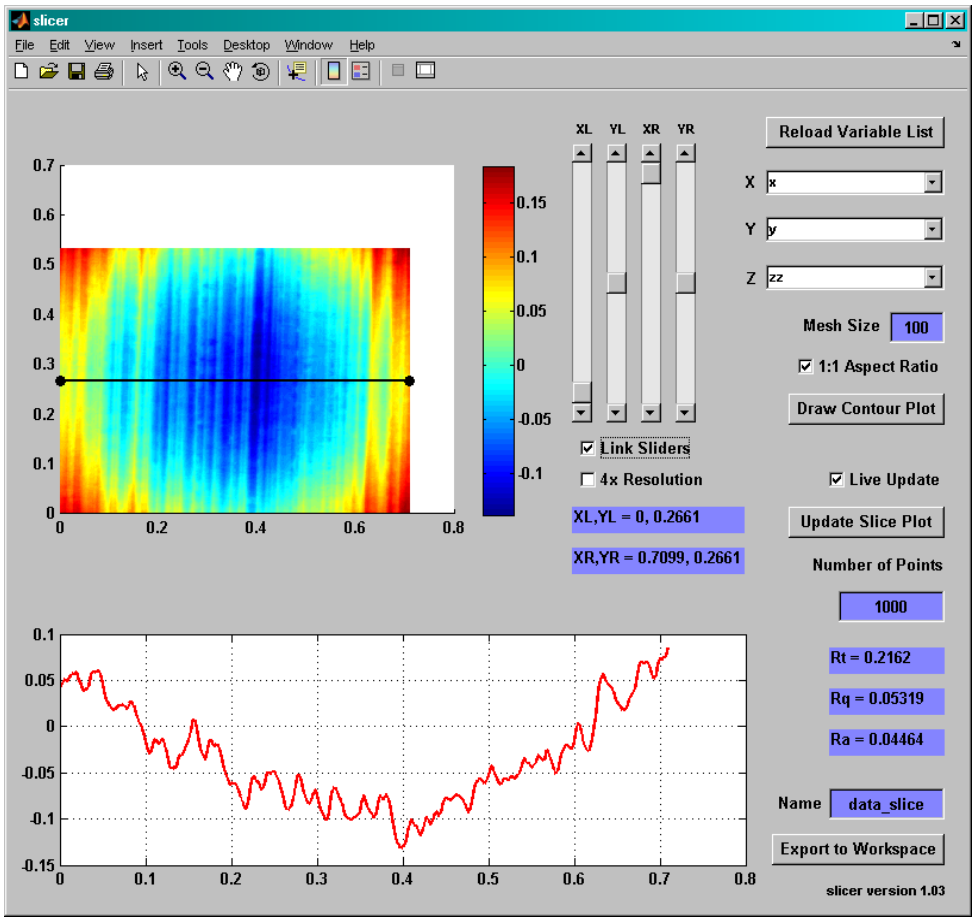

Figure 10. *Slicer* application window showing surface data and a cross-section profile.

For the data in Figure 10, pressing the **Export to Workspace** button results in a structure named *data_slice* being created in the current Matlab workspace. This structure contains the following fields,

```
>> data_slice
data_slice =
     N: 1000
     x: [1000x1 double]
     y: [1000x1 double]
     d: [1000x1 double]
     z: [1000x1 double]
    Rt: 0.2162
    Rq: 0.0532
    Ra: 0.0446
```

The structure elements d and z contain the ordinate and abscissa values of the 2D profile plot and the x and y vectors are the location of the slice in the original data set. The metrology statistics Rt, Rq and Ra are along the 2D profile.

1.6 CONCLUSIONS AND FUTURE WORK

Metrology data import procedures (TalySurf) and code (MetroPro) have been developed and a visualization tool for 3D surface data slices was written in Matlab. A function was also written to allow data to be put back into MetroPro for analysis. This data could be from simulation of a fabrication process or from an optical design tool (e.g., CODE V).

Matlab codes have also been developed for the decomposition of an arbitrary surface into RS and NRS motion paths for fabrication via diamond turning. The RS motion path is in the form of a 2D point-to-point asphere, the coefficients of a best fit radial polynomial or a circular cross-section. The NRS motion path is a 3D cylindrical coordinate lookup table or the coefficients of a functional representation in the case of off-axis conics. A general purpose tool shape compensation algorithm for NRS surfaces has also been developed. These new functions produce output data files that are easily exported to the DTM controller (RS), the PEC deconvolution software (NRS) and the FTS controller.

Presently, the decomposition and tool shape compensation code assumes that the part will be machined with the spindle axis aligned with the z axis of the defining coordinate system. That is, the aperture is centered on the spindle and the workpiece tilted in the XZ plane. Future work will remove this limitation and allow rotation about any axis including one that may not intersect the aperture. The objective is to automatically find the optimal location and direction for the axis of rotation vector.

REFERENCES

1. K. Garrard, T. Bruegge, J. Hoffman, T. Dow and A. Sohn. Design tools for freeform optics. SPIE 5874, 95-105, (2005).
2. T. Dow, K. Garrard, A. Sohn, Final Report to the Navy ElectroOptics Center on FOCUS, Freeform Optics Center of the US, (2006).
3. V.N. Mahajan. Optical Imaging and Aberrations, Part I Ray Geometric Optics. SPIE Press, Bellingham, Washington (1998).
4. CODE V Electronic Document Library, Volume II, Chapter 8, Defining Tolerances, Optical Research Associates, Version 9.6, (2005).

5. CODE V Electronic Document Library, Volume III, Chapter 20, Tolerancing, Optical Research Associates, Version 9.6, (2005).
6. K.B. Doyle, V.L. Genberg and G.J. Michels. Integrated Optomechanical Analysis. SPIE Press, Bellingham, Washington (2002).
7. V.N. Mahajan. Optical Imaging and Aberrations, Part II Wave Diffraction Optics. SPIE Press, Bellingham, Washington (1998).
8. V.N. Mahajan. Exploring optical aberrations. SPIE Short Course Notes SC560 (2005).
9. R. Upton and B. Ellerbroek. Gram-Schmidt orthogonalization of the Zernike polynomial on apertures of arbitrary shape. Optics Letters, 29, 24, 2840-2842 (2004).
10. W. Swantner and W.W. Chow. Gram-Schmidt orthonormalization of Zernike polynomials for general aperture shapes. Applied Optics, 33, 10, 1832-1837 (1994).
11. M. Gerchman. Optical tolerancing for diamond turning ogive error. Reflective Optics II, Dietrich G. Korsch (ed), SPIE 1113, 224-230 (1989).
12. J.C. Wyant and K. Creath. Applied Optics and Optical Engineering, Volume XI, Chapter 1, Basic Wavefront Aberration Theory for Optical Metrology, Academic Press, (1992).
13. W.H. Press, S.A. Teukolsky, W.T. Vetterling, B.P. Flannery. Numerical Recipes in C, 2nd edition. Cambridge University Press, (1999).
14. W.D. Allen, R.J. Fornaro, K.P. Garrard, L.W. Taylor. A High Performance Embedded Machine Tool Controller, Microprocessors and Microprogramming, 40, 179-191, (1994).
15. T. Bruegge, J. Hoffman, T. Dow, A. Sohn and K. Garrard. Advanced Design Tools for Freeform Optics. Final Report to the U.S. Army Space and Missile Defense Command, STTR Contract W9113M-04-P-0149, (2005).
16. W. Panusittikorn. Error Compensation Using Inverse Actuator Dynamics. PhD Dissertation, North Carolina State University, (2004).

2 DESIGN OF REFLECTIVE TMA

Nadim Wanna
Graduate Student
Mechanical and Aerospace Engineering
T.A. Dow
Duncan Professor of Mechanical Engineering and Director, PEC

The primary objective of this research is to develop optical and opto-mechanical design procedures for reflective optical systems. Challenges in fabrication, metrology and assembly have limited the surfaces used in such systems to rotationally symmetric surfaces. Freeform surfaces or non-rotationally symmetric surfaces can significantly increase the performance for a fixed volume or keep the same performance with 20% less volume. To gain familiarity with optical and opto-mechanical design techniques, two systems were studied: a two mirror Ritchey-Chrétien telescope and a Three Mirror Anastigmat (TMA). The two mirror Ritchey-Chrétien telescope using rotationally symmetric hyperbolic surfaces was designed and built. The opto-mechanical design incorporated an external tube to align the primary and secondary mirrors in the axial, radial and tilt directions. The TMA achieves better performance because of the addition of a third mirror. Both off-axis conic sections and freeform mirrors were considered in the design. The opto-mechanical design developed the telescope frame and the fiducial surfaces that relate the optical surfaces to each other and to the detector. The TMA exhibited impressive performance (< 2% of the error in the RC telescope) using freeform surfaces.

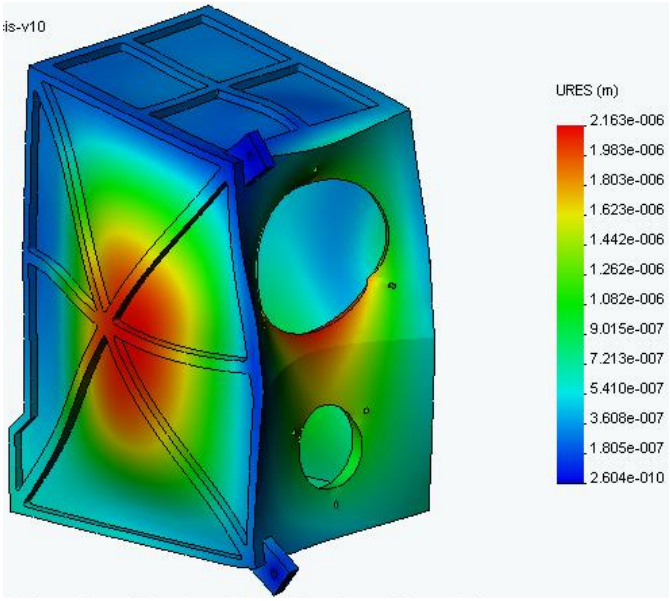

2.1 INTRODUCTION

Optical systems play a crucial role in a wide variety of products from camera phones to seeker missile guidance systems to free-space optical interconnects on computer chips. The field is divided into two major categories: Geometrical Optics is the study of light without diffraction or interference and Physical Optics expands the scope to include diffraction effects. Whereas some optical systems use reflective, refractive and diffractive elements, the emphasis in this project will be on reflective systems that can be operated multiple wavelengths. This is important for defense systems that use the optical system with different sensors to provide the desired information.

Optical systems have been around since early 17th century. Galileo is credited for building the first telescope in 1609 for astronomical purposes using convex object lens and concave eye lens. The early history, from 1608 up to 1672, is particularly instructive because the basic theory of reflecting telescopes and their basic forms were explored. Optical theory of compound telescopes consisting of two curved mirrors was developed through the work of Descartes, Mersenne, Gregory, Newton and Cassegrain. Through the period between 1672 and 1840, intensive development of the refractor was accomplished and complemented by major improvements in manufacturing capabilities [6]. A refracting telescope is another type of optical telescope that refracts or bends light at each end utilizing lenses. Due to aperture size limits, reflective telescopes gained popularity over refractive telescopes.

This project addresses the need for high-performance reflecting telescopes for defense applications such as optics for missiles guidance systems. A two mirror Ritchey-Chrétien telescope with an aperture of 150 mm, a *f#* of 5.73 and a focal length 859 mm was designed and built using rotationally symmetric hyperbolic surfaces. The performance of two mirror telescopes are limited by optical aberrations especially at high field angles (±0.5º for this design). In addition, locating the mirrors in a tube over-constrained the components and distorted the optical surfaces.

Three Mirror Anastigmat (TMA) optical designs use the third mirror to realize improved performance compared to a two-mirror design. This section will describe TMA design using both off-axis conic sections of a rotationally symmetric surfaces and freeform shapes. Opto-mechanical design will address the distortion of the optical surfaces by kinematically supporting the mirrors. Design of the optical frame that supports the mirrors will be addressed in light of the magnitude and frequency of the loading typical of missile designs.

2.2 THREE MIRROR ANASTIGMAT (TMA) – OPTICAL DESIGN

For rotationally symmetric systems, there is no astigmatism for the on-axis field. As the field angle moves further from the axis, the amount of astigmatism linearly increases. To avoid astigmatism at an off-axis field angle, two unobstructed three mirror telescopes were investigated. First, a traditional Three Mirror Anastigmat (TMA) with a single axis of symmetry was designed using off-axis sections of rotationally symmetric conic surfaces. An alternative design was also investigated using freeform surfaces, where the surfaces are converted to Zernike surfaces.

The Three Mirror Anastigmat (TMA) designs have an *f#* of 6.139 with an unobstructed entrance pupil diameter of 140 mm, a 1° circular field of view and an effective focal length of 859.5 mm. These specifications are close to the two mirror telescope discussed in Section 8. The entrance pupil diameter (EPD) was reduced from 150 mm to 140mm to allow the fiducial ring to be measured in the laser interferometer. The interferometer can accommodate flat parts with aperture diameter up to 150 mm.

2.2.1 TMA USING CONIC SURFACES

Size and Shape of Conic Surfaces The TMA system was designed to improve on the performance of the two mirror telescope. The primary mirror is the corner stone of the design and its radius of curvature is set at 1000 mm. The state of the art is a primary mirror with an f-number between 0.75 and 1.25. The conic constant is set to -1 (parabola) in the initial layout, shown in Figure 1, but it was allowed to vary in the optimization. The entrance pupil diameter (stop surface) was decentered by 220 mm, setting the *f#* of the primary mirror in the range specified.

The secondary mirror shares the same optical axis as the primary mirror. The distance between the primary and the secondary is 260 mm, ensuring the incoming rays are unobstructed. The radius of curvature is initially set at 400 mm, but allowed to vary in the optimization. Following the initial specifications, the conic constant was initially set to -2 (hyperbolic) and allowed to vary.

The tertiary mirror is placed coplanar with the primary mirror. This could be an advantage if the primary and tertiary mirror were machined from the same blank. The radius of curvature is calculated in Code V by the YZ paraxial marginal exit angle. The conic constant is initially set at -2 (hyperbola) and allowed to vary in the optimization. The distance from the tertiary mirror to the image plane is determined by the paraxial image distance solve. This option sets the

distance to the image surface such that the paraxial marginal rays or rays parallel to the optical axis intersect the image plane at the center.

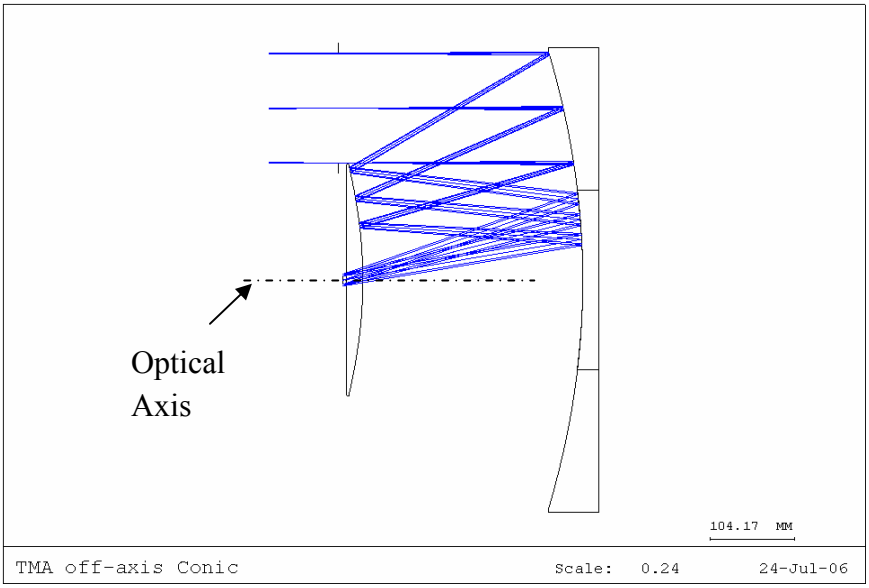

Figure 1. TMA using conic sections layout

Detector The Canon digital camera with a CMOS detector was used to capture the images produced by the two mirror telescope. The detector is 44 mm behind the lens mounting flange in the camera. Since the image is located behind the primary mirror, the camera is mounted co-axially to the system with enough space for the housing. For the TMA optical system, the image is below the secondary mirror and slightly behind it. Due to geometrical constraints, the detector's location with respect to the mounting flange and the lack of focus shift with the lens mounting flange, an astronomical camera was chosen for the TMA. The Starlight Xpress SXV-M25 has a high resolution, 6-megapixel CCD sensor with USB interface, single cable control. The detector is a 23.4 mm by 15.6 mm sensor with a square pixel size of 7.8 μm. The CCD detector has very similar specification to the Canon CMOS detector. The camera is mounted on the telescope structure using a T-42 thread mount with the advantage of linear translation of the detector, or focus compensation.

Optimization of Conic Surfaces The purpose of optimization is to generate the best optical design within a given set of physical and other constraints. The error function combines image error data into a single number that is minimized in the optimization routine. Code V provides four error function types, wavefront error variance is chosen in this case since the system performance will be measured using dual pass interferometry.

The image plane position is constrained to be behind the secondary mirror by at least 25 mm for mounting clearance of the Starlight detector. The effective focal length and f-number of the

system are calculated by the paraxial marginal exit angle reflected from the third mirror. For this system, the detector and entrance pupil diameter set the f-number at 6.139 and the effective focal length at 859.5 mm. All specifications not explicitly selected are allowed to vary during optimization.

The optimization process produces a telescope with improved system performance. The system is evaluated using the field map option. This option presents various analysis results as a grid of field points, helping to visualize the variation of performance across the field of view or image format [3]. Plotting the wavefront polynomial fit for coma and spherical aberration, shows a node for each option that is above the center of the field. A node or an aberration node, in the field of view represents a point where the particular aberration plotted is zero. The wavefront polynomial fit plot for astigmatism shows a node very close to the center. For optical systems without symmetry, Thompson [4] shows that two nodes exist in the astigmatism plot; the other node is outside the field of view. Constraints are added to the system by targeting the single coma and spherical aberration nodes on-axis and targeting the astigmatic nodes to the top and bottom of the field. Running the optimization routine, with the added constraints, does not improve the optical performance of the system due to the lack of variables in the conic surfaces.

The 2-D plot of the three mirror anastigmat is shown in Figure 2, for the parent system in (a) and for the apertures used in (b). The optical specifications of the three mirrors are tabulated in Table 1. Distance between the primary-secondary and secondary-tertiary is set to 270 mm for clearance of incoming beams. The decenter and aperture of each surface is solved for in Code V real ray tracing data. The image plane is 294.860 mm away from the tertiary mirror where the chief ray has a zero height. To minimize the wavefront error over the field of view, the image plane is linearly translated to the best focus position. The distance between the tertiary mirror and the image plane best focus position is 295 mm, different from the on-axis focus position given in Table 1. The effective focal length of the finalized system is 859.5 mm.

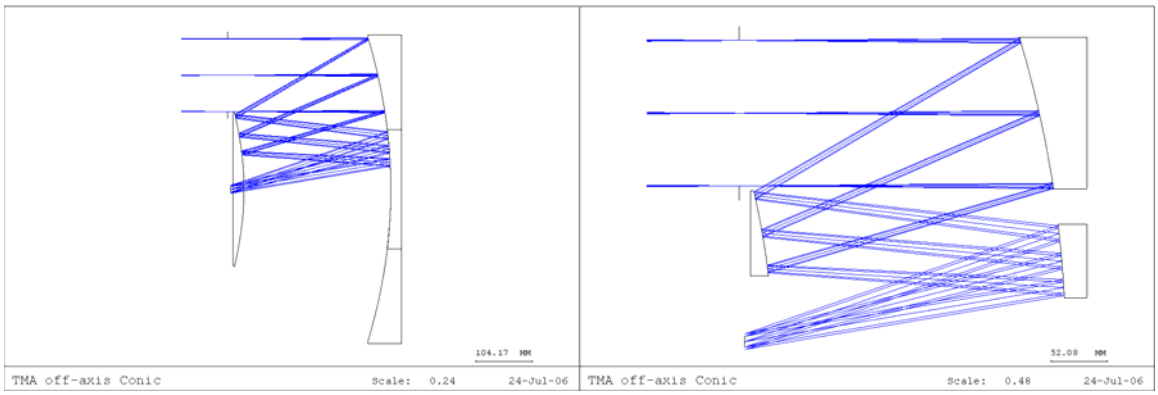

a) Parent system b) Used apertures only

Figure 2. TMA using rotationally symmetric conic surfaces

Table 1. Off-axis conic optical system specifications

	Radius of curvature (mm)	Conic Constant	Aperture Diameter (mm)	Surface decenter (mm)	Distance to next surface (mm)
Primary	-1000	-1.755	140	220	270
Secondary	-587.151	-5.801	79.5	104.409	270
Tertiary	-939.433	-5.197	68	77.508	294.86

2.2.2 TMA USING ZERNIKE SURFACES

Size and Shape of Freeform Surfaces An alternative design for the three mirror anastigmat using freeform surfaces is shown in Figure 3. This design maintains the f-number, field of view, entrance pupil diameter, and focal length of the conic TMA. The optical surfaces in this design are converted to on-axis Zernike polynomial surface types. The Zernike surface is a 10th order standard Zernike polynomial added to a base conic and the equation used is the following:

$$z = \frac{cr^2}{1+\sqrt{1-(1+k)c^2r^2}} + \sum_{j=1}^{66} C_{j+1} Z_j \tag{1}$$

Where z is the sag of the surface parallel to the z-axis
c is the vertex curvature
k is the conic constant
Z_j is the j-th Zernike polynomial (range of j: 1 to 66)
C_{j+1} is the coefficient for Z_j

Using the TMA off-axis conic design as a baseline, entrance pupil diameter decenter is deleted leading to an on-axis rotationally symmetric system. Then, surface properties of the three mirrors are changed from conical surfaces to freeform surfaces or Zernike polynomial surfaces keeping the same radius of curvatures and conic constant values. Zernike polynomial coefficients (C_{j+1}), 4th to 26th terms, are set to variable. Primary and secondary mirrors radii of curvature are set as variable, while the tertiary mirror's radius of curvature is solved by the paraxial marginal exit angle to set the f-number of the system at 6.139 and the EFL at 859.5 mm.

To realize an unobstructed telescope design, the mirrors are tilted about their optical axis. "Decenter and Bend" option in Code V tilts the optical components about their optical axis with the new optical axis collinear with the normal vector at the vertex of the surface [5]. Positive α-tilt is rotation about the x-axis in the counter-clockwise direction. First, the primary mirror is

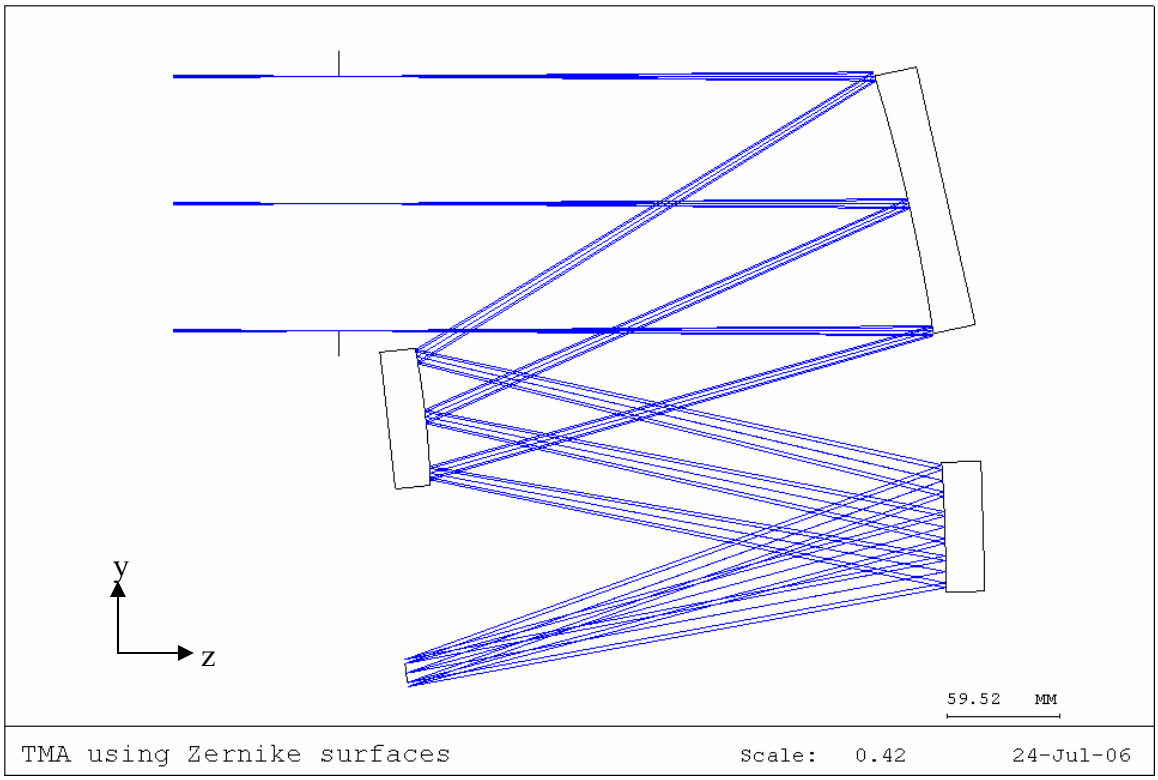

Figure 3. TMA using on-axis Zernike surfaces

tilted by 12.7°, placing the secondary mirror below the entrance pupil. Next, the secondary mirror is titled by -15.3°, placing the tertiary mirror below the primary mirror. Finally, the tertiary mirror is tilted by 10.2°, placing the image below the secondary mirror. The image plane α-tilt is set as variable to solve for the best orientation minimizing the wavefront error in the optimization routine. Distance between primary-secondary and secondary-tertiary mirrors is set to 280 mm. Distance between tertiary mirror and image is variable.

Optimization of Freeform Surfaces The starting point of each optical design is a design goal and initial specifications set prior to running an optimization routine. The off-axis conic TMA design is used as a starting point with the changes to on-axis freeform surfaces to optimize the TMA using Zernike surfaces. Of the four error function types provided by Code V, wavefront error variance is chosen as the optimization parameter since the system is diffraction limited.

The system is optimized by minimizing the wavefront error and geometrically constraining the vertical distance between the secondary mirror and the entrance pupil diameter to be at least 10 mm. The field map option, in Code V, is used to evaluate the system at the image plane. The wavefront polynomial fit for spherical aberration displays a node located on the horizontal axis. The polynomial fit for coma shows a node located below the axis at (-0.1°, 0.2°) field angle. Polynomial fit for astigmatism displays two nodes [4] for non-rotationally symmetric systems.

The two nodes are in the field of view and are located on the horizontal axis at (±0.2°, 0°). To minimize these optical aberrations thus the wavefront error, further optimization is executed with additional constraints applied to the system.

To improving the performance of the TMA, more constrains were added to the optimization routine. To minimize the coma and spherical aberration over the field of view, the coma node is constrained to be at the origin of the circular field of view. This also constrains the spherical aberration node to be at the center of field. Astigmatic nodes are shifted from their original location to (±0.35°, 0°) on the horizontal axis. Astigmatism increases radially outwards from both nodal positions. Placing the nodes at this intermediate position decreases the astigmatic average over the field of view while placing the nodes at the edge increases the average.

The 3-D wireframe plot of the optimized TMA using on-axis freeform optics is shown in Figure 4. Optical specifications of the system are tabulated in Table 2. The primary and secondary base optical surfaces are hyperboloids while the tertiary mirror base is an ellipsoid. Distance between tertiary mirror and the image plane on-axis focus position is 294.453 mm. To minimize the wavefront error over the field of view, the image plane is linearly translated to the best focus position. Distance between the tertiary mirror and the image plane best focus position is 294.596 mm, different from the on-axis focus position given in Table 2. The mirror tilts are also shown in Table 2 where the image is tilted by -9.574° to compensate for optical aberrations.

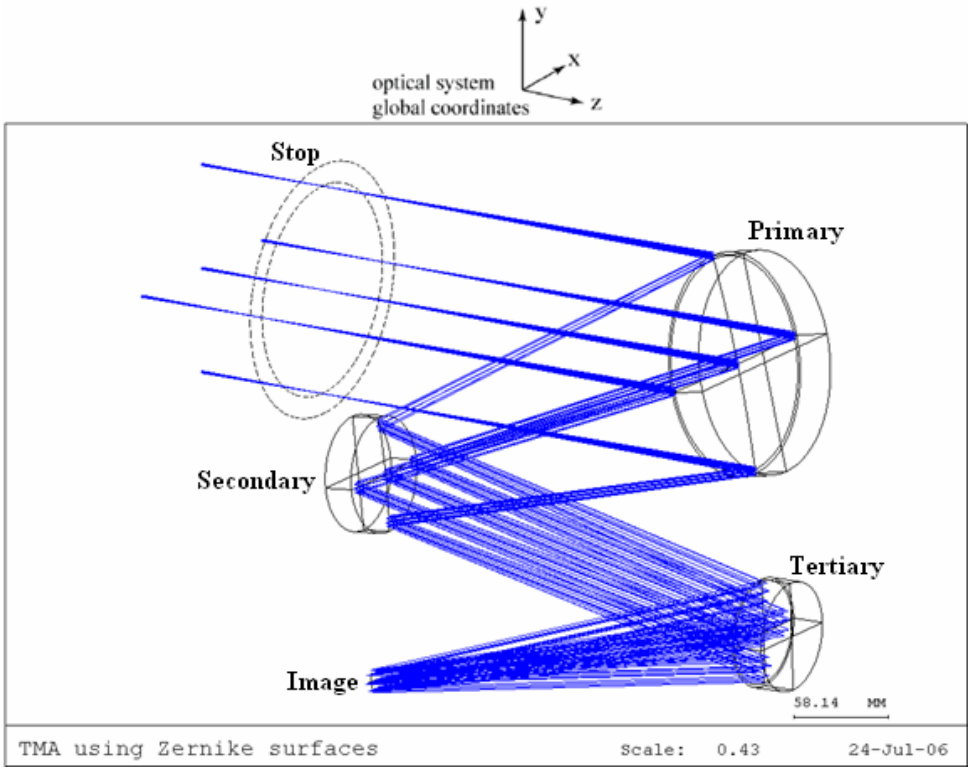

Figure 4. TMA using Zernike surfaces optical system

Table 2. TMA using Zernike surfaces optical system specifications

	Radius of curvature (mm)	Conic Constant	Aperture Diameter (mm)	Distance to next surface (mm)	α-tilt (°)
Primary	-1003.328	-1.613	140	280	12.374
Secondary	-556.276	-5.769	72	280	-18.646
Tertiary	-865.999	1.399	68	294.453	14.184
Image	-	-	15.1	-	-9.571

2.3 WAVEFRONT ANALYSIS - CONIC AND FREEFORM SYSTEMS

2.3.1 WAVEFRONT ERROR

Wavefront error plot for Zernike polynomial TMA over the full field of view, shown in Figure 5, gives the best description of the performance of the system. Wavefront error is a combination of the errors as the light moves through the system from stop surface to the image plane. Minimum error is 0.003 waves located at (±0.4°, 0°) near the location of astigmatic nodes. Error increases from these points inward, towards the center of the field, and outwards away from both field points. The error at the worst point in the field is 0.011 waves at the center of the field, with an average of 0.0063 waves over the field of view.

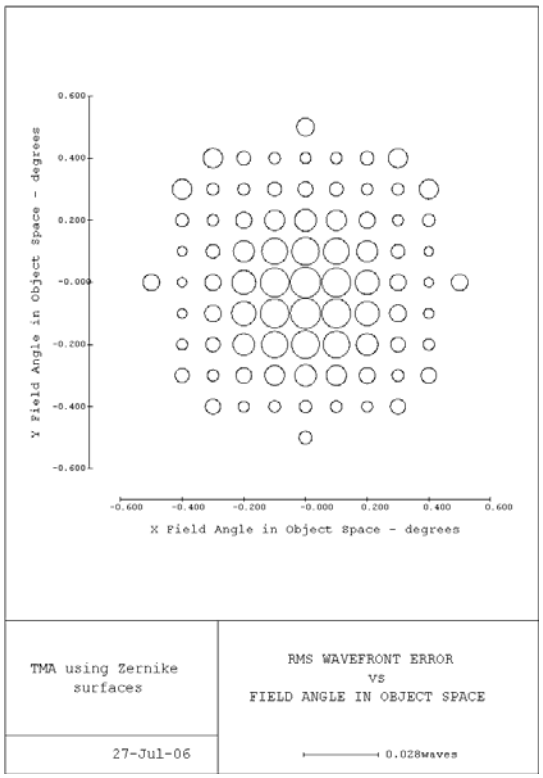

Figure 5. RMS wavefront error for Zernike TMA across the field of view

The wavefront error over the full field of the two TMA systems is compared in Figure 6 with both plots having the same scale. The diameters of the circles indicated the magnitude of the error at each field location. For the off-axis conic TMA, wavefront error is shown in Figure 6(a). The smallest error occurs in the center of the field at (0°, 0.2°) and the minimum error is 0.032 waves. The location of the minimum error is due to the system being off-axis where the different aberration nodes for this system are located above the optical axis. The error increases radially

outwards to reach a maximum of 0.242 waves at -0.5°. The average wavefront error over the field of view is 0.134 waves. Compared to the on-axis Zernike system, average wavefront error over the field of view is 0.0063 waves or 21 times improvement over the off-axis conic TMA. This is noticed in Figure 6, where at the common scale, wavefront error magnitudes of freeform design are nearly invisible.

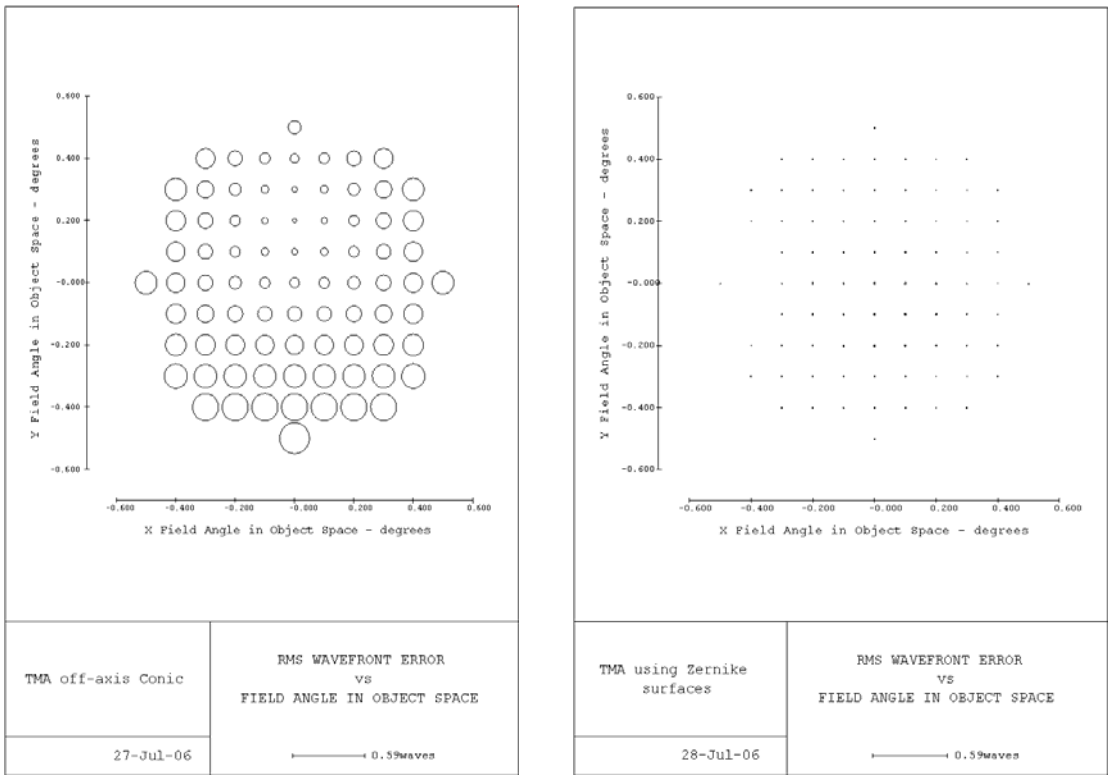

(a) Off-axis conic TMA (b) On-axis Zernike polynomial TMA

Figure 6. RMS wavefront error as field angle over the aperture of the telescope

2.3.2 MODULATION TRANSFER FUNCTION

Modulation Transfer Function (MTF) is another measure of the performance of optical systems consisting of a series of alternating light and dark bars [6]. The MTF plot gives a modulation value for contrast with 1.0 being perfectly black and white boundaries and 0.0 being totally gray as a function of the spatial frequency. Diffraction is an optical effect that limits the resolution or optical performance of a system and is plotted as the right-most dotted line in Figure 7. The off-axis conic system MTF plot is shown in Figure 7(a) and the best performance is the center of the field where it is almost diffraction limited, or 96 cycles/mm at 50% modulation. Other field angles in the system do not exhibit a sudden drop-off in modulation found in the two-mirror design. The lowest MTF is at the 0.5° field angle showing 33 cycles/mm at 50% modulation. The Starlight Xpress CCD detector threshold or Nyquist frequency (64 cycles/mm) is determined

by dividing twice the pixel size by 1. Nyquist frequency is the highest resolution the CCD sensor can detect. At this frequency, modulation varies between 23% for the worst field (0.5°) to 67% at the best field (0°) for the off-axis conic TMA system.

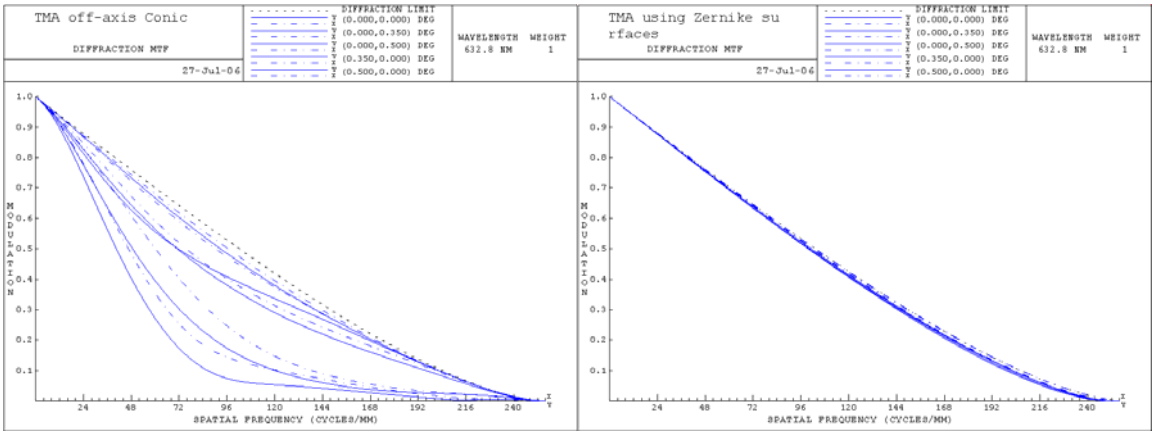

(a) Off-axis conic TMA (b) On-axis Zernike polynomial TMA

Figure 7. MTF for both TMA optical systems

The on-axis Zernike polynomial system MTF plot is shown in Figure 7(b). Performance is essentially perfect; even at the worst location in the field it is diffraction limited. At 50% modulation, system frequency varies between 99 – 104 cycles/mm. At the Nyquist frequency of the detector (64 cycles/mm), modulation varies between 68% and 69%. Compared to the off-axis conic system, the on-axis Zernike system MTF shows an impressive improvement in overall performance.

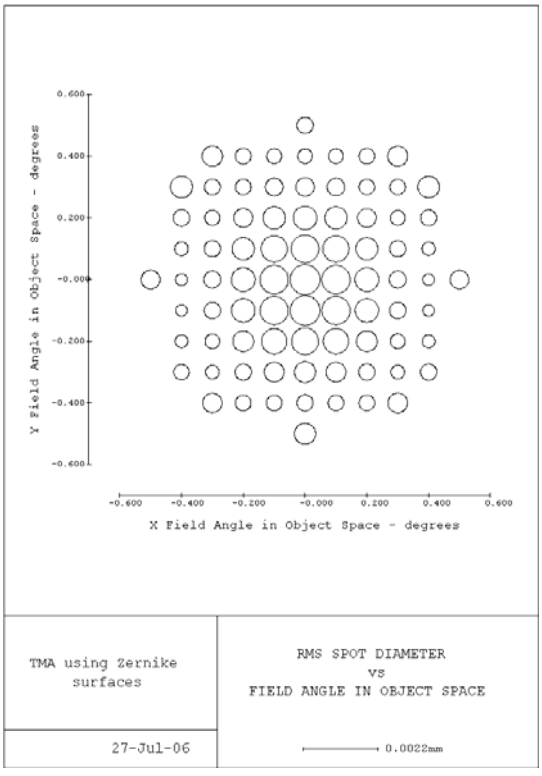

Figure 8. RMS spot diagram for the Zernike polynomial system

2.3.3 SPOT DIAGRAM

The spot diagram shows the dispersion of rays at different field angles on the image plane. The spot diameter gives a visual impression of image quality for each field angle. Image quality is related to the spot size at a particular field angle where the smaller the spot diameter the better image quality. The spot diagram of the on-axis Zernike polynomial TMA at best focus position is shown in Figure 8. The smallest RMS spot diameter is 0.336 μm at (±°0.4, 0°) field angles in the field of view,

coincident with the location of the minimum wavefront error. The RMS spot size is highest at the center of the field, 0.876 μm, with an average of 0.551 μm over the field of view.

RMS spot diagram for both TMA systems is compared in Figure 9, using the same scale. The on-axis Zernike polynomial system shows smaller spot diameters compared to the off-axis conic system demonstrating an improved system performance. Spot diagram of the off-axis conic system at best focus position is shown in Figure 9(a). The smallest RMS spot diameter is 2.5 μm at the location of the best focus (0°, 0.2°), and it increases radially outward to reach a value of 18.8 μm the bottom of the field (-0.5°). The average spot diameter over the field of view is 9.4 μm compared to 0.551 μm for the on-axis Zernike polynomial system.

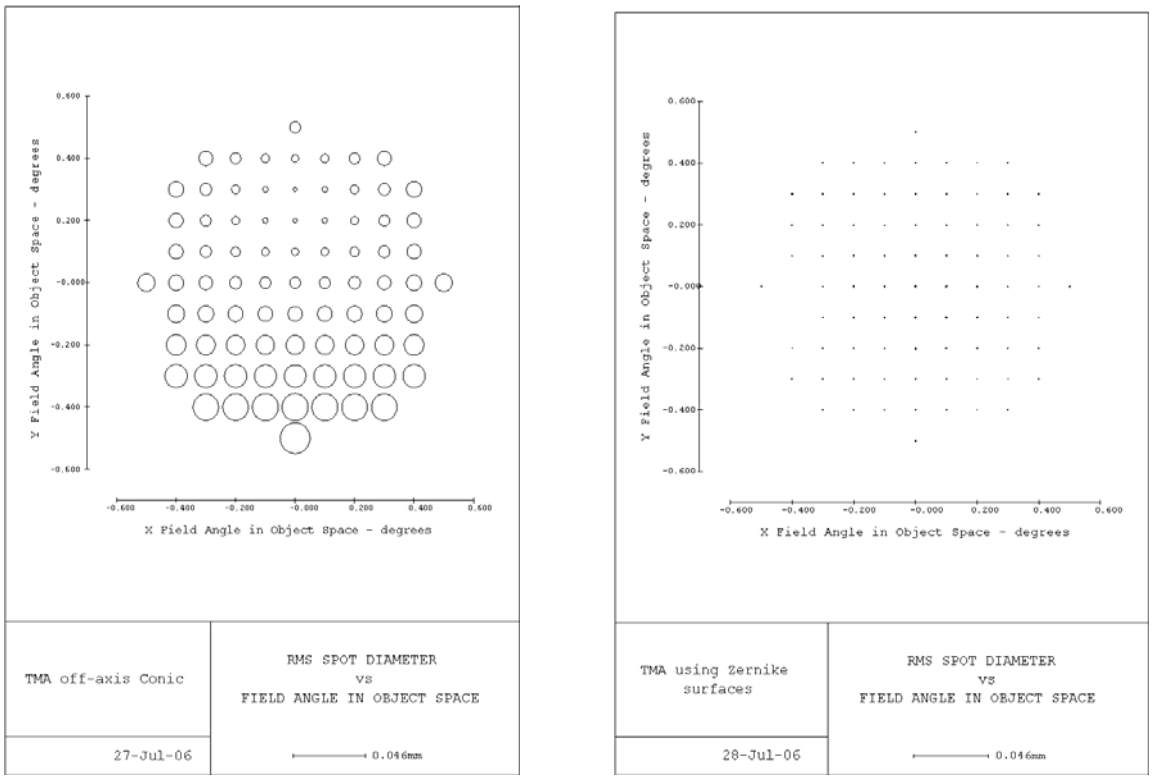

(a) Off-axis conic TMA (b) On-axis Zernike polynomial TMA

Figure 9. RMS spot diagram for both TMA systems plotted using the same scale

2.3.4 COMPARISON OF CONIC AND FREEFORM TMA SYSTEMS

The eccentric conic TMA has the advantage that its surfaces may be tested with the laser interferometer, using relatively simple test configurations. The on-axis Zernike polynomial freeform surfaces require a computer generated hologram (CGH) to be tested using interferometric equipment. Stylus profilometer or an ultra-precision CMM can measure freeform

surfaces, provided machines have sufficient accuracy. Freeform surfaces present a more challenging task to measure than off-axis conics.

Both TMA systems optical surfaces can be machined on the diamond turning machine with a Fast Tool Servo (FTS) to compensate for the sag difference. Fast tool servos that have a small range produce better surface finish over the same range than using a FTS with a longer range. On-axis Zernike polynomial surfaces require smaller servo excursions (110 μm) than the off-axis conical surfaces (191 μm). In addition, performance of the on-axis Zernike TMA shows impressive improvement over the off-axis conic TMA. Although, sensitivity analysis shows the on-axis Zernike system is more sensitive to fabrication errors, overall performance is remarkably better. Therefore, the opto-mechanical TMA design was directed towards designing the structure that maintains the alignment of the optical elements during ground tests and launch for the on-axis Zernike polynomial system.

2.4 THREE MIRROR ANASTIGMAT – OPTO-MECHANICAL DESIGN

Non-rotationally symmetric optical surfaces for telescope objectives have been shown to produce remarkable improvements in performance over off-axis conic sections and rotationally symmetric surfaces. However, non-rotationally symmetric surfaces add complexity to the opto-mechanical design because of the added degree of freedom over rotationally symmetric two mirror systems that come with performance gain.

The opto-mechanical details are based on the on-axis Zernike polynomial optical design. The goal is a snap-together design for the three mirror telescope with diamond machined optical surfaces and special emphasis on the component orientation and assembly. The opto-mechanical design specifications are based on a missile application and must withstand vibration and high acceleration loading. Standard methods use pins, holes, slots and machined flats to locate the optical component on an intermediate plate. Flexure mounts integrated in the component mount the optical structure onto the housing [7].

2.4.1 MATERIAL

Similar to the two-mirror telescope, components of the TMA system are to be machined from aluminum 6061-T6 alloys. Aluminum alloys are lightweight, strong and are widely used in optical instrument structures [8]. This material presents a balanced compromise between material strength necessary for structural rigidity and material properties to create surface finishes adequate for infrared imaging. Optical and fiducial surfaces are machined utilizing diamond turning process capable of producing high fidelity optical surfaces in many non-ferrous materials. The potential surface finish of 6061 Aluminum is not as good as Aluminum

electrodeposited plated surfaces but is acceptable for the infrared needs of this telescope [9]. Fabrication of mirrors and telescope frame from 6061-T6 aluminum allows system expansion and contraction proportionally with a temperature gradient. Thus, thermal instability does not affect the optical performance of the system.

2.4.2 MIRROR STRUCTURE

Lightweight Design for Fabrication The design of the mirror structure is crucial in achieving a snap-together telescope. Each of the three mirrors is designed to incorporate the same fiducial and mounting features. The thickness of each mirror structure is based on the aspect ratio; that is, the ratio of the mirror diameter to the thickness. Using the aspect ratio simulation conclusions discussed in the two-mirror optomechanical Section 3.4.2, a part with an aspect ratio between 3 and 4 provides minimal distortion values when mounted on the vacuum chuck for machining. Distortions of the optical surfaces can occur when the mirror component is mounted on the vacuum chuck of a diamond turning machine for fabrication. The aspect ratio is reduced from 6 to 3 by using a 75 mm raised mounting plane, for a 25 mm thick part, instead of the whole aperture. Figure 10 shows a comparison between a 25 mm thick primary mirror using its full aperture (150 mm) mounted on the vacuum chuck and a 75 mm diameter region. Optical surface distortion is reduced from 891 nm to 99.7 nm respectively.

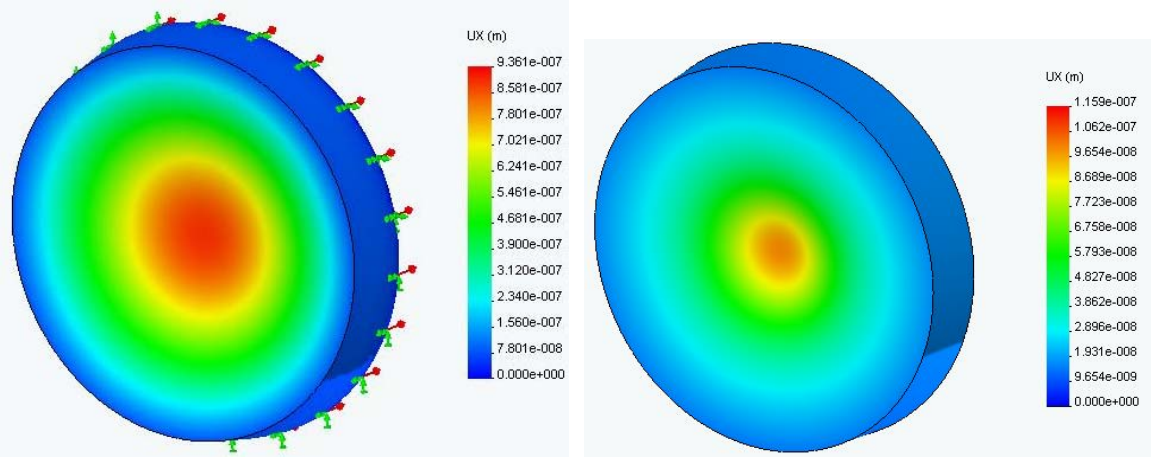

Figure 10. Distortion of the optical surface when the entire back is used (left) and when only a region is used (right) to mount onto the vacuum chuck

Figure 11 shows the primary mirror structural design. The part is 150 mm in diameter and 25 mm thick at the center and increases to reach a maximum thickness of 27.45 mm at the edge. The raised mounting plane is 75 mm in diameter. Light-weighting the part reduces the mass and therefore the deflection due to gravitational loading. Radial struts connect the outer fiducial ring to the inner mounting plane. Two different thickness struts are used; the 10mm thick strut provides support for the mounting clamp contact area.

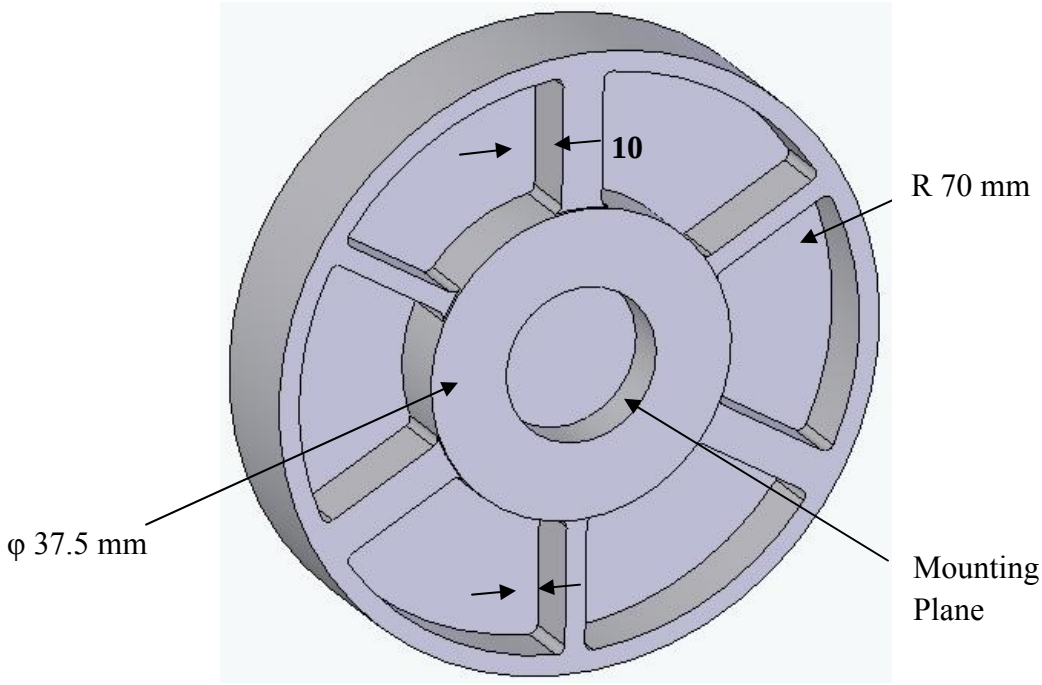

Figure 11. Lightweight primary mirror

2.4.3 FIDUCIALIZATION TECHNIQUES

For a rigid body, six degrees of freedom must be constrained by no more than six forces or these additional forces will distort the optical surfaces. Therefore, six forces are employed to constrain each mirror. The two mirror optical system only requires five forces due to the rotational symmetry. Rotation about the optical axis, or z-axis, does not need to be constrained. If the surfaces are not rotationally symmetric, the final degree of freedom, rotation about the z-axis must be constrained. The following sections discuss techniques to locate the mirror components onto an optical housing with the proper orientation.

Pin/Slot/Hole The conventional technique involves locating the mirrors on a planar surface on the face of the housing using the reference fiducial surfaces machined onto the face of the mirror and a pair of pins that fit into a hole and a slot on the telescope frame. For the on-axis Zernike polynomial optical design, the optical axis of each mirror is normal to the surface at the center along the z-direction as shown in Figure 12. The fiducial surface creates a plane that mates to the plane created on the telescope frame through contact pads and positions the optical axis of the mirror in the correct direction with respect to the other mirrors in the system. The fiducial plane constrains the optical component in three degrees of freedom but will allow translation in the x and y directions and rotation about the z axis. These degrees of freedom are constrained by the pair of pins protruding from the fiducial plane on the mirror. One pin will fit into a pin hole

constraining linear translation of the mirror in the x and y directions. The other pin will fit into a slot constraining the mirror from rotating about the z-axis, thus all six degrees of freedom of the mirror are constrained. Orientation of each optical surface depends on the orientation of the fiducial plane on the telescope frame and the location of the hole and slot in the contact pads. Fabrication of the optical surface will be created with respect to the fiducial plane and the location of the two pins.

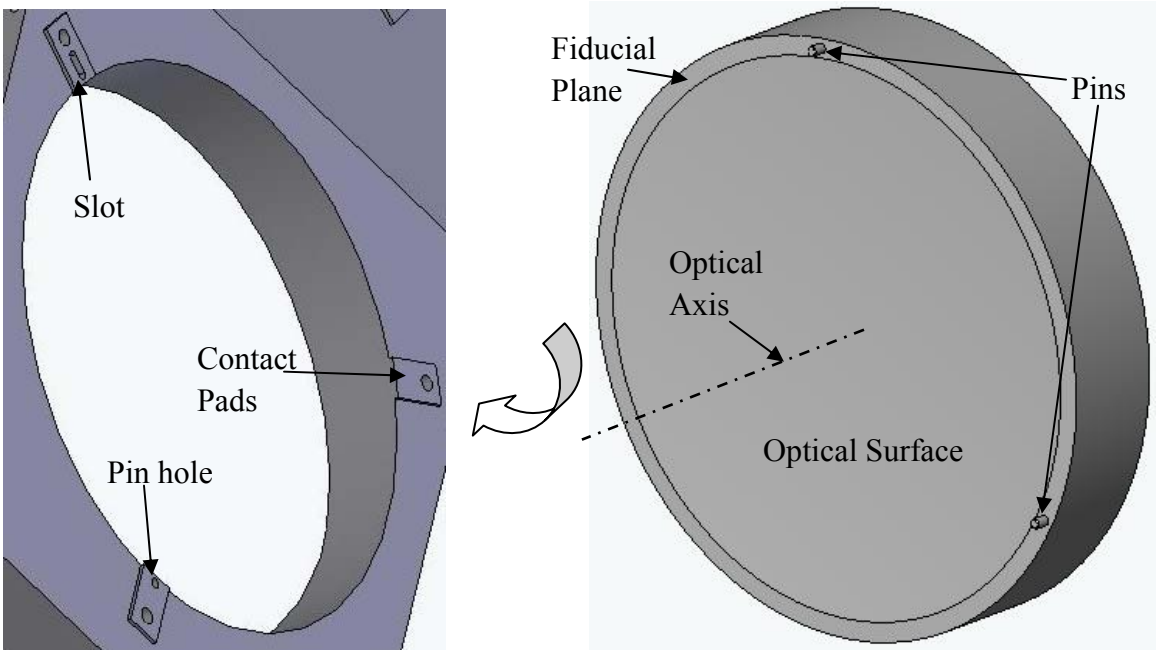

Figure 12. Mirror blank with pins installed in the fiducial plane that fit into a pin hole and slot on the telescope frame

Kinematic Coupling Kinematic or Kelvin coupling provides deterministic location in all six degrees of freedom of two components in relation to each other without over-constraining them. Avoiding over-constrain is necessary since it causes stress in the structural component that results in optical surface distortion and non-repeatable location [10]. Ideally, three points on a structure that are rigidly coupled to each other locate with six planes rigidly connected on another component. Ignoring contact stress, this locating technique provides a unique and critical constraint with respect to both mating components.

An example of a kinematic coupling is shown at right. Spheres attached on the bottom component mate with a three V-grooves on the top. Components are kept in contact through gravitational force or an external force applied through flexures or clamping components together. Contact stress inherent

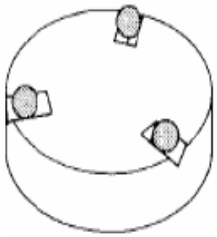

in kinematic design is a concern due to the significant influence on the placement of the components or plastic deformation of the mating surfaces. Figure 13 shows an example of ball features machined on the surface of the optic. These alignment features would be machined at the same time as the optical shape guaranteeing alignment.

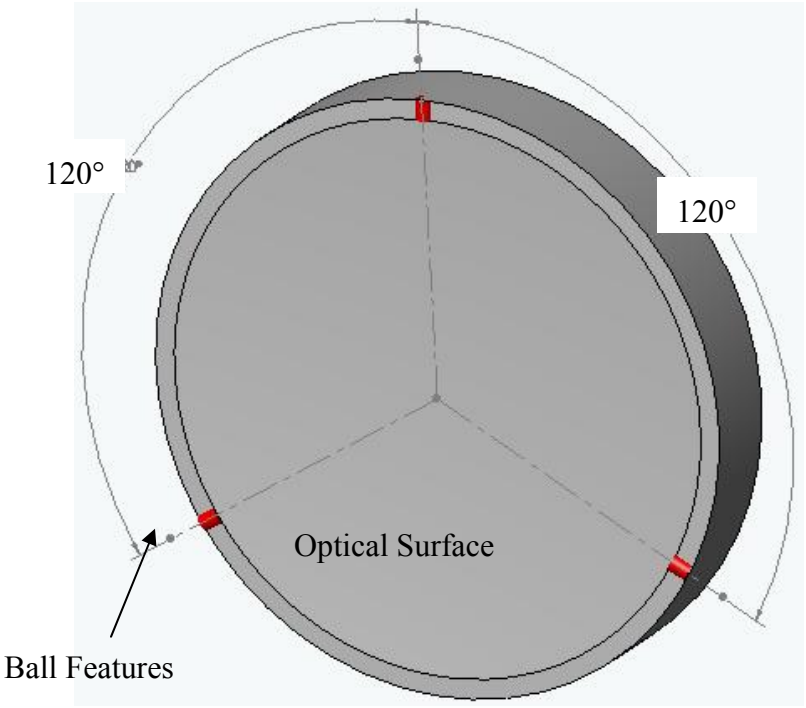

Figure 13. Sketch of the mirror surface showing the ball features machined on the outside fiducial ring

Figure 14 shows the detailed shape of the ball features. The optical surface is machined using the FTS to generate both the NRS optical surface and the alignment ball features. The ball features have a height of only a few hundred micrometers. These features can be created using the Variform FTS which has a 400 μm range of motion at 140 mm/sec maximum speed. The same tool will be used for the optical surface and fiducials to guarantee relative placement. The housing V-groove surfaces will be machined using a flycutter and a dead sharp diamond tool. Using a modeled load equivalent to ten times the weight of the primary mirror, the maximum stress does not exceed the bearing yield stress of the 6061-T651 aluminum material.

The conventional pin-hole-slot locating method limits the optical performance of the system to the predicted wavefront error described in the sensitivity analysis. This limit in optical performance is due to the inaccuracy of locating the optical surface with respect to the pins while machining, in addition to the clearance tolerance between the pins and the holes and slots. Utilizing the fast tool servo to machine the fiducial features and the optical surface during the

same setup should significantly improve assembly tolerances to less than 2 μm and is limited by the machine resolution to less than 1 μm, thus increasing the optical performance.

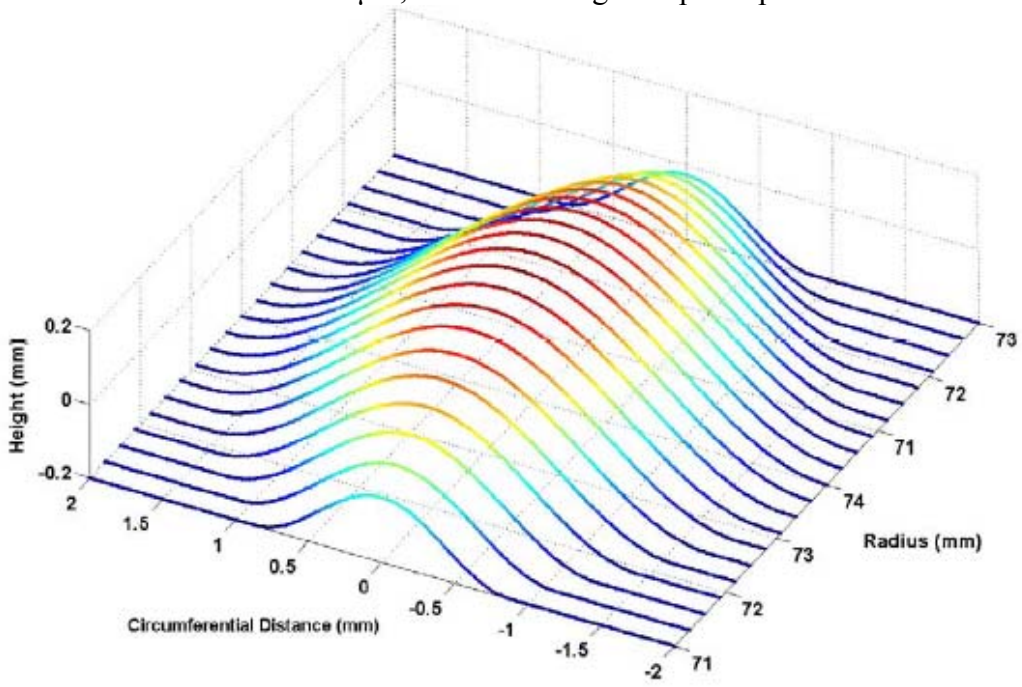

Figure 14. Details of the three ball features on the mirror fiducial surface

2.4.4 MOUNTING CLAMPS

The mounting flexures or clamps are designed to meet the following criteria:

- Clamping force of 30 N for the primary mirror and 10 N for the secondary and tertiary mirrors
- Machined from 6061-T6 Aluminum (yield strength = 276 MPa)
- Maximum stress not to exceed 50% of yield strength
- Deflection at least 10 times the fabrication tolerance (12 μm)

Each mirror is held in place using three clamps. For each clamp, the mounting load is applied directly over the fiducial pad, eliminating the moments that cause distortion of the optical surface. The clamp design for the primary is shown in Figure 15 with a 10 mm radius contact region. The clamp has two flexures in series, 4.5 mm top and 3.5 mm thick bottom, making the clamp more compliant to the mounting loads. M4 socket head cap screws are utilized to apply the axial clamping load and a lip at the bottom prevents rotation of the post. The clamps will be fabricated using wire EDM technology.

Modeling the clamp stress and deflection was performed in Solidworks/Cosmos, where the base of the post is fixed and a uniform load of 30 N applied to the radius contact surface in the vertical

direction. Figure 15 shows the displacement plot (left) and stress distribution (right) for the clamp. Displacement at the radius contact point is 125 μm and this represents at least 10 times the tolerance for wire EDM. Having the contact radius displacement be at least 10 times the fabrication tolerance ensures that the mounting load is applied and will sustain 10 times gravitational acceleration. Maximum stress of 122.1 MPa occurs at the bottom flexure or 44% of the yield stress of 6061-T6 Aluminum, satisfying the stress criterion.

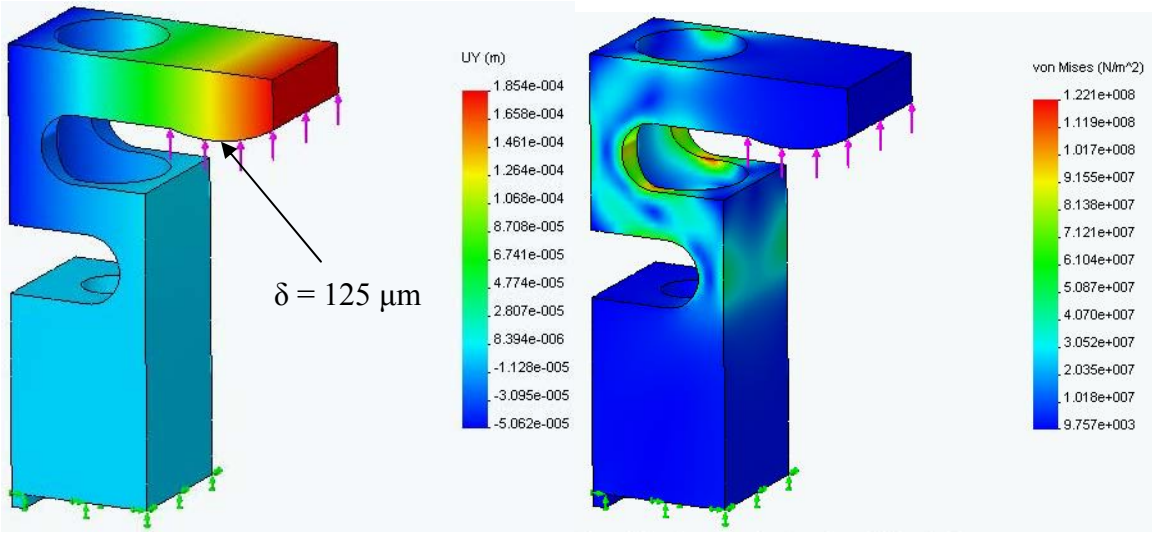

Figure 15. Deflection of the mounting tab (left) and the stress distribution (right)

The effect of clamping force on the optical surface of the lightweight primary mirror, shown in Figure 16, was simulated by restraining the optical structure in 6 degrees of freedom through the fiducial features. Clamping force, equivalent to 30 N, was applied opposing the fiducial features assuming a circular contact region 10 mm in diameter. Optical surface distortion is a maximum of 95 nm. Eliminating the moments created by the flexural mounting tabs and applying the mounting load co-linear with the fiducial contact tabs reduces the optical surface distortion.

2.4.5 TELESCOPE FRAME

To support the mirrors in space, a telescope frame is fabricated to support each optical element in the correct orientation with the other elements without distorting the optical surfaces. The frame facilitates mounting the telescope structure onto an optical bench for testing or to an anti-ballistic missile structure. The TMA optical system consists of on-axis Zernike polynomial surfaces as described in the optical design Section 2.2.2 and the support and orientation of the mirrors will be discussed in this section.

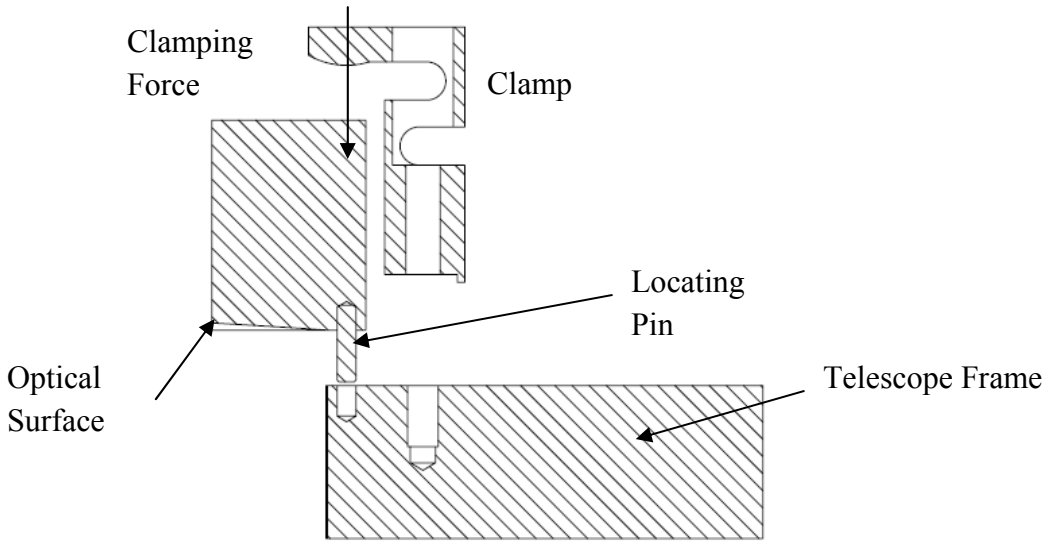

Figure 16. Schematic of locating and mounting mirror on the telescope housing

Structure The frame is a lightweight aluminum structure with mounting surfaces for the three mirrors and the detector. The frame incorporates the mirror and detector tilt angles with respect to the vertical axis. A solid block of 6061-T6 Aluminum will be used for the main structure and wire EDM or water-jet machining will be used to eliminate most of material in the center of the optical frame. Side view of the frame is shown in Figure 17 with the primary and tertiary locating and mounting planes. The optical component mounting surfaces consist of three fiducial contact tabs that create the plane that locates the mirrors on the housing frame in three degrees of freedom. The tabs incorporate a hole and slot where two pins protruding from the mirror fiducial ring locate the mirrors in the correct orientation about the optical axis constraining the mirror in six degrees of freedom as described in the conventional fiducialization technique. Three clamps apply the mounting load through the threaded holes to hold the mirrors in place and sustain 10 times the gravitational acceleration.

Side plates of the housing will be fabricated as solid plates and bolted to the housing using M3 socket head cap screws around the periphery of the frame as shown in Figure 17. Side plates are mounted on the frame using pins and bolts to increase the structural integrity. Assembly of the side plates onto the telescope frame must be carefully conducted to ensure that no permanent distortion of the frame occurs after bolting the parts together [20]. The telescope frame can be mounted to an optical bench for testing or to a missile structure through the three outer tabs using three M6 socket head cap screws and three spherical washers.

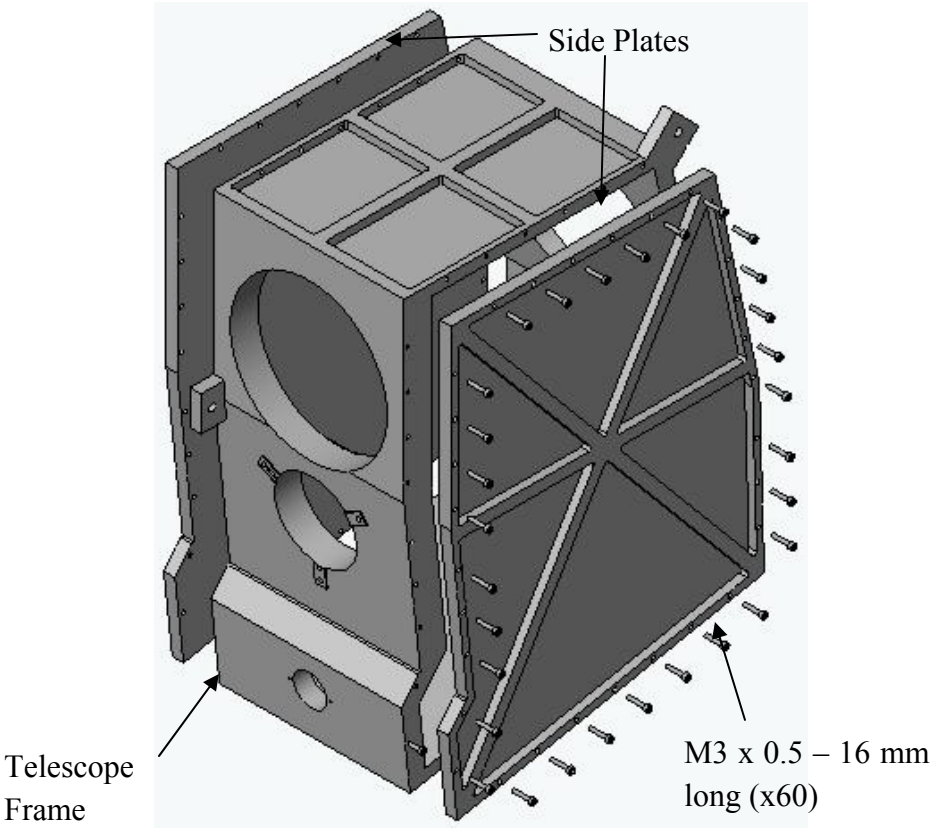

Figure 17. Telescope frame with side plates

2.4.6 FRAME STRUCTURAL ANALYSIS

Launch Acceleration The telescope frame was modeled to optimize the wall thicknesses and minimize mass to support the missile launch specifications. A wall thickness of 15 mm was chosen for mirror and detector mounting surfaces and 10 mm was used for non-mounting surfaces. The FE model was used to minimize the mirror contact tabs distortion using the following loading-restraint conditions. The frame was constrained in six degrees of freedom using the three outer tab mounting holes. Launch acceleration or ten times gravitational acceleration is applied in the z-direction, perpendicular to the entrance aperture (vertical axis). On each mirror mounting surface, clamping load is applied on the threaded holes (30 N for primary mirror and 10 N for secondary and tertiary mirror). Mirror contact pads are loaded with a normal force equivalent to 10 times the mirror weight in addition to the clamping force (58.5 N for primary, 16.5 N for secondary and 15.5 N for tertiary mirror). The detector mounting holes are loaded with 10 times the detector weight (50 N). The outer mounting tabs are located at the edge of the frame, as shown in Figure 17, to support the telescope frame with the three mirrors and the detector. Multiple tab positions were modeled to find the tab location where minimum mounting surface distortion under gravitational loading occurred.

Multiple secondary mirror wall thicknesses were simulated to reduce the mounting surface distortion below the 2 μm tolerance. Distortion of the final implementation of the frame is shown in Figure 18 and mirror mounting plane displacements are tabulated in Table 3. The table also includes the maximum optical surface displacement results for the three mirror components under launch acceleration requirements. Each mirror component is constrained in six degrees of freedom at the pin hole edges with ten times gravitational loading in the z-direction in addition to the clamping force discussed earlier in this section. Total displacement of each mirror component is included in Table 3 which is addition of the mounting tab and the maximum optical surface displacement. The total displacement does not exceed the 2 μm tolerance specified in the sensitivity analysis Section 4.4. Non-mounting plates are lightweight to reduce the mass of the frame from 11.035 kg (24.328 lbs) to 7.148 kg (15.76 lbs) or 35 % reduction without any significant effect on the mounting planes.

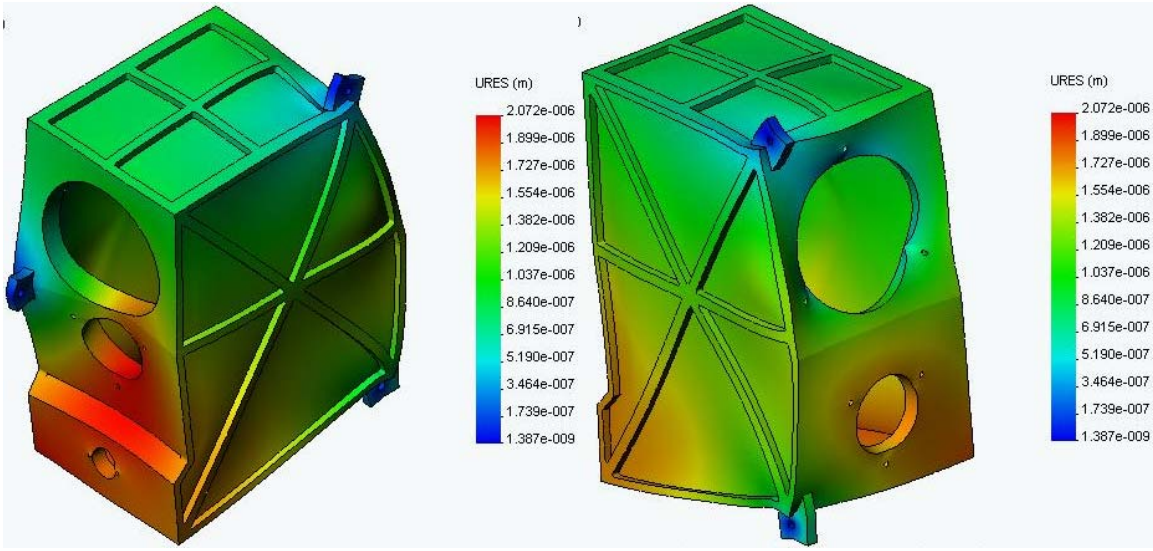

Figure 18. Frame displacement with the final mounting surface wall thicknesses

Table 3. Mirror mounting tab and optical surface displacement results (μm)

	Primary	Secondary	Tertiary
Mounting Plane	0.627	1.844	1.689
Optical Surface	-0.330	0.141	-0.021
Total Displacement	0.297	1.985	1.668

Gravity Loading The frame gravity loading condition is simulated using the loading-restraint specifications except that (1g) gravitational acceleration is applied in three directions rather than the launch loads. Distortion of the frame is shown in Figure 19 with 1.85 μm displacement at the primary mirror mounting plane, 0.403 μm at the secondary mirror and 1.43 μm at the tertiary mirror.

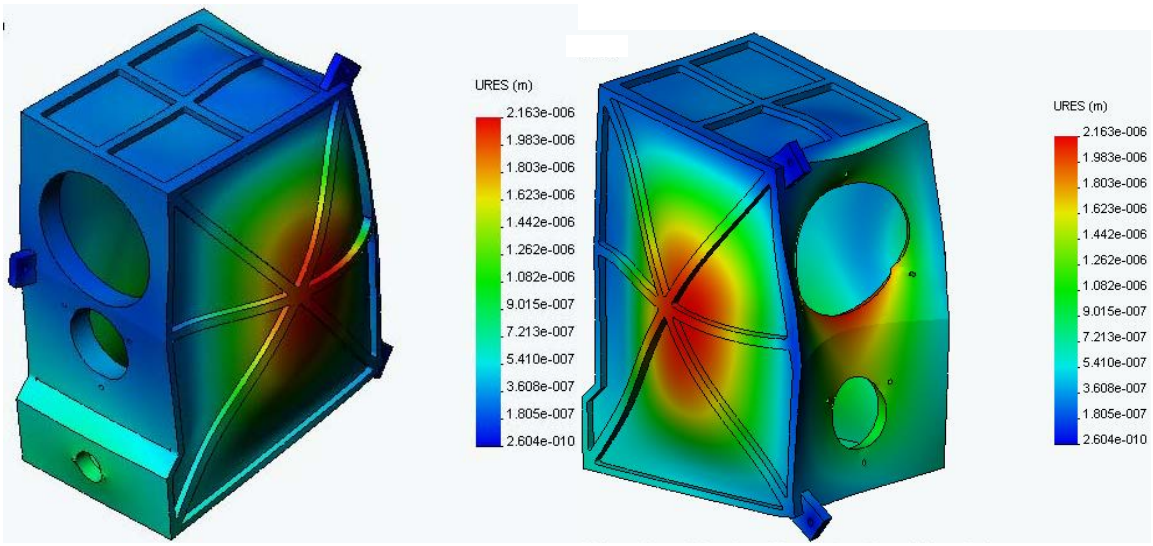

Figure 19. Frame displacement due to weight of components in different directions

Modal Analysis Finite element analysis was used to evaluate the vibration modes of the mirror components and the telescope frame structure. The first mode shape of the telescope structure is 575 Hz which is higher than the missile launch excitation peak frequency of 400 Hz. The results of the simulation are tabulated in Table 4.

Table 4. First mode frequencies for the components and frame structure

	1st Mode
Primary Mirror	1579.7 Hz
Secondary Mirror	3488.5 Hz
Tertiary Mirror	3641.4 Hz
Telescope Frame	575 Hz

Manufacturing Feasibility Fabrication of the TMA telescope could be carried out at the Precision Engineering Center (PEC) using the Rank Pneumo ASG 2500 and the Nanoform 600 Diamond Turning Machines. The three optical surfaces as well as the fiducial ring on each mirror component will be diamond turned in one setup utilizing the Fast Tool Servo. The freeform optical surfaces have been decomposed into rotationally symmetric and non-rotationally symmetric shapes to determine if the equipment available are capable of fabricating the mirror surfaces by using surface decomposition. The Variform fast tool servo with 400 μm range has the capacity to machine the freeform optical surfaces on the DTM. The telescope frame will be machined on the Nanoform 600 3-axis diamond turning machine. The frame will be mounted on the positioning spindle that is equipped with a high-torque motor and an angular encoder that can place it at a specific angular location. A diamond flycutter is mounted on a vertical y-axis that is mounted on the z-axis that moves along the spindle axis. The axis of the

flycutter is along the x-axis direction. The fiducial mounting surfaces on the telescope frame will be diamond flycut by moving the flycutter across the face of the frame, then the frame is rotated to the appropriate location and the next mounting surface is machined. The telescope frame is finished in one machining setup to ensure accurate location of the optical surfaces and the detector with respect to each other.

Overall Assembly The overall dimensions of the Three Mirror Anastigmat are 190 mm x 281 mm x 385 mm with a total weight of 8.404 kg (18.528 lbs). A final assembly isometric view and dimensions is shown in Figure 20.

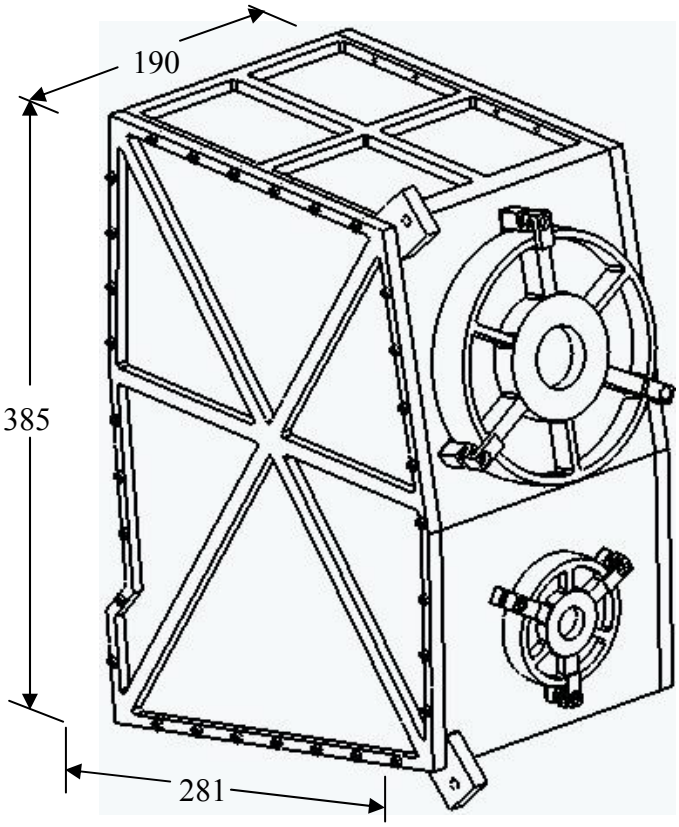

Figure 20. Final telescope assembly and telescope frame dimensions (in mm)

2.5 CONCLUSIONS

Optical performance is improved with the addition of a third mirror. The first Three Mirror Anastigmat (TMA) optical system is designed using off-axis conic sections of rotationally symmetric surfaces.

- The off-axis conic TMA optical design follows similar specifications as the RC system with a 15 mm diameter image, 1° circular field of view and an effective focal length of 859.5 mm.

- Optical performance of the off-axis conic TMA is 2.7 times better than the RC system but limited aberration node control due to the lack of variables.
- Average RMS wavefront error is 0.134 waves over the field of view.

A TMA optical system using freeform surfaces is designed following the same specifications as the off-axis conic TMA.

- Freeform surfaces introduce additional variables to the system that can be manipulated in the optimization routine. Average RMS wavefront error is 0.0063 waves over the field of view.
- Aberration nodal control achieved with freeform surfaces shows 21 times optical performance improvement over the off-axis conic TMA and 58 times improvement over the RC system.

Optical surfaces were decomposed into a rotationally symmetric component (machined by the DTM) and a non-rotationally symmetric component (machined by the FTS) to check the surface fabrication with capabilities available at the PEC and provide feedback to the optical designer.

- On-axis freeform surfaces are machined on-axis utilizing the FTS and require smaller servo excursions (110 μm) to machine the NRS component.
- Ability to integrate freeform surfaces in an optical design with optical surface fabrication feedback to the designer is a great advantage.

Opto-mechanical design of the TMA focuses on simplifying manufacturing and snap-together assembly processes for freeform optical systems while improving optical performance.

- Mirror components are lightweight structures with a low aspect ratio reducing optical surface distortion below 100 nm while machining.
- Conventional fiducialization techniques were evaluated using pins in holes and slots. Clearance between the pins and the mating hole and slot limit assembly tolerances.
- Integrating the fabrication of kinematic fiducials with freeform optical surfaces using a fast tool servo permits tolerances less than 1 μm.
- Application of the mounting forces through independent clamps directly over the fiducial contact pad eliminates the moment and reduces the optical surface distortion to 95 nm.
- Mirror mounting surface and optical surface distortions are lower than the 2 μm fabrication tolerance under high gravitational loading (ten times gravitational acceleration) and gravity loading.

REFERENCES

1. Wanna, Nadim and Dow, T.A., *Design of Reflective Optical Systems*. PEC 2005 Annual Report , 27-48.

2. Schroeder, Daniel J., *Astronomical Optics*. San Diego: Academic Press, 1-6, (2000).
3. Irving, B., *Code V, Introductory User's Guide*. ORA, 44-51, (2004).
4. Thompson, K., *Description of the Third-Order Optical Aberrations of Near-Circular Pupil Optical Systems without Symmetry*. Optical Society of America, 1389-1401, July (2005).
5. Bruegge, T., Corn, E., Hasenauer, D., Kuper, T., Reid, D., Rimmer, M., Stone, B., *Code V Application Programming Reference Guide*. Pasadena, California: ORA, (2005).
6. Smith, Warren J., *Modern Optical Engineering*. 3rd Ed., SPIE Press, McGraw Hill, New York, NY, 22, 62-71,152, 355, 366-383, (2000).
7. Cohen, E.J., Hull, A.B., Escobedo-Torres, J., Barber, D.D., Johnston, R.A., Small, D.W., Prata, A.J., Freniere, E.R., Butcher, H.R., *Optical Design of the Ultra-Light-Weight FIRST Telescope*. Proceedings of SPIE, Munich, Germany, 4015, 559-566, (2000).
8. Yoder, Paul R., *Opto-Mechanical Systems Design*. 3rd Ed., Boca Raton, FL: CRC Press, 124-129, 272-288, (2006).
9. Schaefer, J.P., *Progress in Precision – Single Point Diamond Turning (SPDT) of Optical Components*. Presented at ASPE 2002 Spring Tropical Meeting on Progress in Precision. Raleigh, NC, (2002).
10. Solcum, A.H., *Precision Machine Design*. Prentice Hall, Englewood Cliffs NJ, 401-412, (1992).
11. Hegge, M.J., Baer, J.W., Hardaway, L.M.R., Taudien, G., Sabatke, D.S., Shidemantli, S.R., *Diamond Turned, Light Weight, Athermal, Visible TMA Telescope for the Planned New Horizons Mission to Pluto*. Proceedings of SPIE, Ed. Alson Hatheway, Bellingham, WA, (2005).
12. Roark, R. and Young, W., *Formulas for Stress and Strain*. McGraw Hill, 362, (1975).

3 MODELING OF VIBRATION AND DITHERING IN SPDT

Lucas Lamonds
Graduate Student
Alex Sohn
Kenneth Garrard
Precision Engineering Center Staff

The objective of this work is to develop a model to simulate the effects of vibration on the surface finish of single-point diamond turned parts. This model can be used to optimize cutting conditions for best surface finish and to predict geometric characteristics of the surface beyond the conventional rules of thumb. In addition to small-amplitude oscillations due to machine vibration in the normal direction, purposely induced large-amplitude vibrations in the lateral direction to reduce coherent scatter in the finished part were modeled.

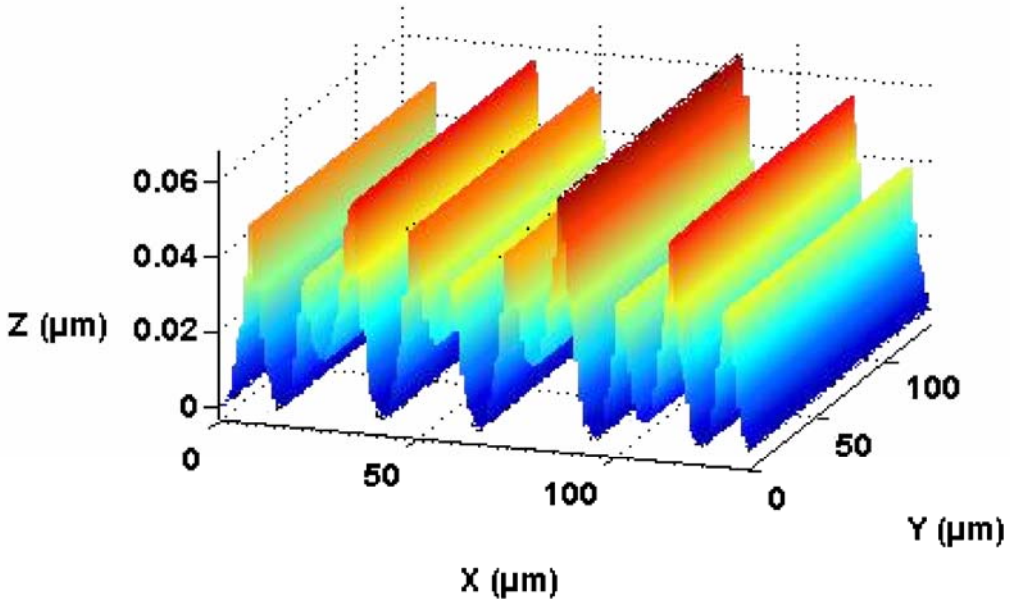

3.1 INTRODUCTION

Surface finish in single-point diamond turning is primarily influenced by four factors: Geometry, vibration, material properties, and tool edge quality. The first-order geometric model using the parabolic approximation gives the peak-to-valley roughness which is determined solely by the crossfeed (f), and the tool radius (R).

$$PV = \frac{f^2}{8R} \tag{1}$$

This approximation is often used as the sole determiner for choosing radius and feedrate even though at large radii and small feeds, the predicted finish is not achievable.

3.1.1 VIBRATION

Assuming suitable materials are selected and the tool edge quality is high, vibration is typically the next largest factor in determining surface finish. The origin of this vibration can be from a number of sources, although the axes of the machine or the spindle are the most likely candidates. The ASG 2500 Diamond Turning Machine at the Precision Engineering Center suffers mainly from a 65 Hz vibration of the Z-axis which has a magnitude of about 30 nm. This amplitude can vary slightly depending on spindle rpm and balance. Either of these can increase this vibration. For the purposes of the following discussions and examples, the vibration of the ASG 2500 Z-slide will be used as the source of the vibration, though the technique can be applied to any source.

The impact of vibration on a diamond-turned surface is generally to degrade the surface finish. In its simplest form, a sinusoidal vibration in the normal direction would degrade RMS surface finish proportional to the amplitude of the vibration. It would seem that the surface finish could never be improved beyond this value and there would be no point in slowing the feedrate or using a larger radius tool. This assumption is, however, incorrect due to interaction between neighboring grooves at small feedrates. By modeling the surface produced by a vibrating tool, it can be shown that the surface finish is no longer limited by the vibration amplitude but can be improved by moving to finer feedrates.

Initial surface finish tests were conducted at machining rates where the parabolic approximation should accurately predict peak-to-valley surface finish. These tests were designed to check for surface finish dependence on cutting depth, surface speed, and cross feed-rate. Results indicated that finish was dependant on cross feed-rate but that there were other factors causing increased roughness. Further examination of the results showed that machine vibration and minimum chip thickness (a variable dependant on tool edge sharpness) were adding to roughness. A model was created to predict surface roughness influenced by machine vibration and experiments to prove

the model used a freshly sharpened tool. The model results predicted that surface finish can be improved beyond the vibration amplitude of the machine as did the experimental results. The model was expanded to further improve the finish quality by dithering the tool in cross feed direction such that diffraction patterns from diamond turned cusps were smooth rather than periodic.

3.2 BACKGROUND

The research done at the PEC by Drescher [1] and Arcona [2] was used as a baseline for repeated experiments in a regime where the first-order effects of feed rate and tool radius accurately predict roughness. The goal was to machine in a regime where the parabolic approximation discussed earlier can predict surface finish. Depth of cut was varied to test the effects of cutting and thrust forces on roughness. A tool servo was used to quickly change the depth of cut so that a large portion of the cutting window remained after machining and could be compared with a theoretical profile from the theoretical nose radius. Cutting speed was also varied by machining with the same feed-rate at different radii on the workpiece to verify that speed had little effect on the surface finish in this regime.

Quick depth changes provided the ability to observe a large section of the tool edge as it advanced thought the work piece and its relationship to the previous passes. An example of the quick depth change is seen in Figure 1 where the lower set of grooves were cut 1 μm deeper than the upper grooves. It shows a large portion of the cutting window so interactions between the tool edge and the material that was removed could be examined. This is interesting because the leading section of the tool is much deeper in the workpiece than the trailing section (the trailing section is responsible for the residual grooves that determine surface roughness). Test measurements were then easily matched to theoretical tool paths for analysis of desired and undesired features. In the event that the curvature of the cups did not match the tool radius, the large section of the edge could have been used to verify the radius or align the cusps with a theoretical profile.

3.2.1 SURFACE FINISH VARIABLES

Diamond tool geometry has two main variables that influence surface roughness: nose radius and edge radius. The nose radius of a diamond tool leaves a circular cusp in the workpiece that has a width equal to the cross-feed. As the cross-feed is linearly reduced, cusp spacing becomes proportionally narrower; however, the RMS cusp height decreases by the square – see Equation 1. This is the basis for the first-order model discussed where large tool radii and fine cross-feeds

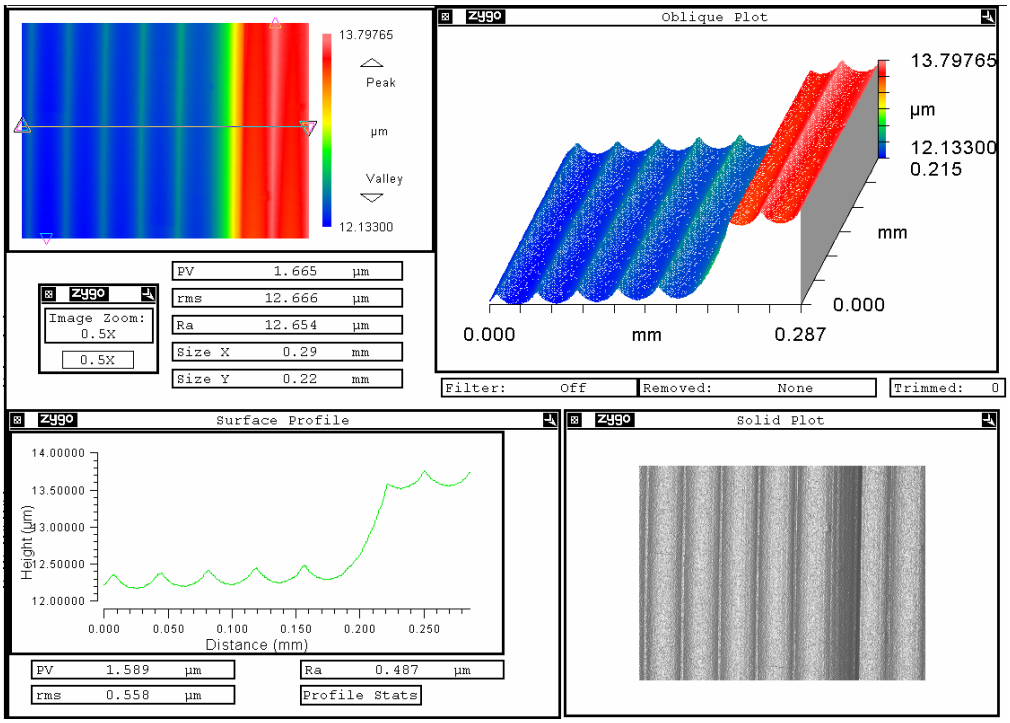

Figure 1. Transition from 2 µm cutting depth to 1 µm at 37.7 µm/rev feed rate, and m/s surface speed in electroplated copper with a .75 mm radius tool.

should produce a surface contour with a very small PV roughness. For the tests described here, a smaller nose radius of 750 µm was used such that the cusps were easily identified in the surface profiles at both coarse and fine cross-feeds. For a given feed rate, a smaller nose radius tool will produce a rougher surface with large cusp heights. Thus the first order approximation can predict surface finish at a relatively low slide speed (~2 mm/min with a spindle speed of 500 rpm).

The edge radius of the diamond tool is a measure of its "sharpness." As the edge wears, the radius becomes larger and the tool becomes "duller". Others [2] have shown that cutting and thrust forces increase with edge wear, as does the effect of minimum chip thickness as shown in Figure 2. Because the chip thickness cannot be zero (due to the diamond tool edge radius), a certain amount of material is elastically deformed into the workpiece as the tool passes. Once the tool has left the area, the deformed material springs back leaving a thicker section at the trailing edge (also called spanzipfel) where the cutting depth should theoretically be zero. The result is a portion of the residual cusp rises above the expected round cusp shape thereby increasing the surface roughness. The influence of a minimum chip was undesired in these tests so the 750 µm tool used was sharpened in anticipation of this experiment to minimize the presents of material spring back.

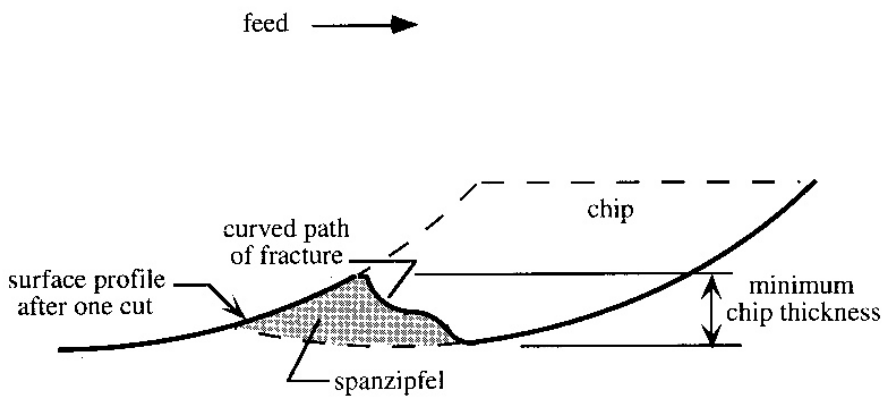

Figure 2. Second-order effect of minimum chip thickness caused by a large edge radius [2].

Electroplated copper made it an ideal material choice for this experiment because of its high microhardness, small grain structure (~10 nm), lack of ductility and lack of second-phase particulates. The microhardness of electroplated copper has been shown near the pure copper limit. As seen by the diamond tool, this material is homogenous. When using a tool with a sharp edge, surface profiles produced in this material have sharp cusp corners and smooth up-feed grooves.

Depth of cut directly affects both cutting and thrust forces by changing the area of the rake face that is removing material [2]. The area of the rake face used is enclosed by the uncut surface, the radius left by the previous pass, and the edge of the tool that is cutting as seen in Figure 2. Depth of cut was varied between sets of machining passes in this section with a tool servo. The servo retracted the tool from the workpiece at high velocity so a deeper groove was left for almost an entire revolution of the workpiece. The section of the tool edge that is higher than the cusps seen in Figure 3 could then be matched to the residual cusps or examined independently to check for other features.

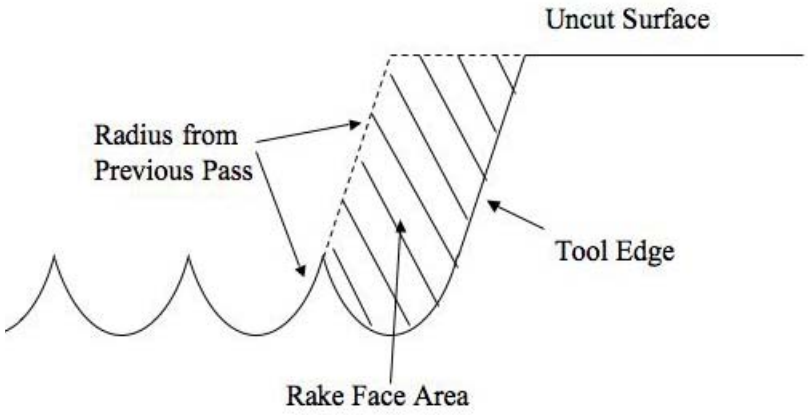

Figure 3. Rake face area enclosed by the previous pass, tool edge and uncut surface. The aspect ratio in this drawing was set to resemble Figure 1.

In lathe-based rotational machining, the surface speed of the work piece relative to the tool changes linearly as the radius of the part changes. The changing surface speed dictates that material removal rate and cutting speed change linearly over the duration of a cut. Others have shown that the effect of surface speed is insignificant at the cutting velocities used in this experiment [2]. The tests were performed at several radii on the workpiece to verify these results.

Cross-feed rate of the diamond tool through the workpiece sets the cusp spacing and, combined with the tool nose radius through the parabolic approximation, will determine the cusp height. The largest cross-feed was set so a coarse surface with relatively large cusps was produced. This coarse surface presented the opportunity to match large cusps to a theoretical tool edge and align them with the large step remaining after the depth of cut was quickly changed. Since the goal, again, was to machine in a regime where the parabolic approximation can predict the roughness of a surface profile, the smallest cross-feed was set such that the profile exhibited regularly spaced cusps at that cross-feed.

3.2.2 EXPERIMENTAL SETUP

A fast tool servo (FTS) was mounted to the ASG-2500 diamond turning machine (DTM) as seen in Figure 4 to facilitate instant depth of cut changes. The FTS axis of motion was orthogonal to both the spindle face and the experimental surface. The FTS was mounted on the micro-height adjuster for adjustability in the vertical (Y-axis) direction. This allows precise (< 1 μm) positioning of the diamond tool relative to the spindle centerline. To cool and lubricate the material removal process, petroleum oil cutting fluid (Mobilmet Omicron®) was sprayed onto the tool. The cutting fluid was manually sprayed onto the tool (from directly above with a squirt bottle) because experiments conducted in the preceding weeks had ridges in the cusps from a nicked tool edge that may have been damaged by contamination in the ASG-2500 lubrication system.

The servo was designed and built at the PEC and a great deal of research has been dedicated to measuring the dynamic response, developing closed loop control schemes, and novel applications of this auxiliary axis. It consists of a threaded housing that sets a preload on a tubular piezoelectric stack (PZT) stack through annular flexures. A capacitance (cap) gage is situated inside the PZT stack and measures the position of the back face of the tool holder. Positive input voltages to the PZT result in a displacement of the tool holder toward the part, which is opposite the flexure force direction. The cap gage output provides position feedback for closed loop control of the tool position (depth of cut). For closed loop feedback control discussions, it is position commanded with position feedback.

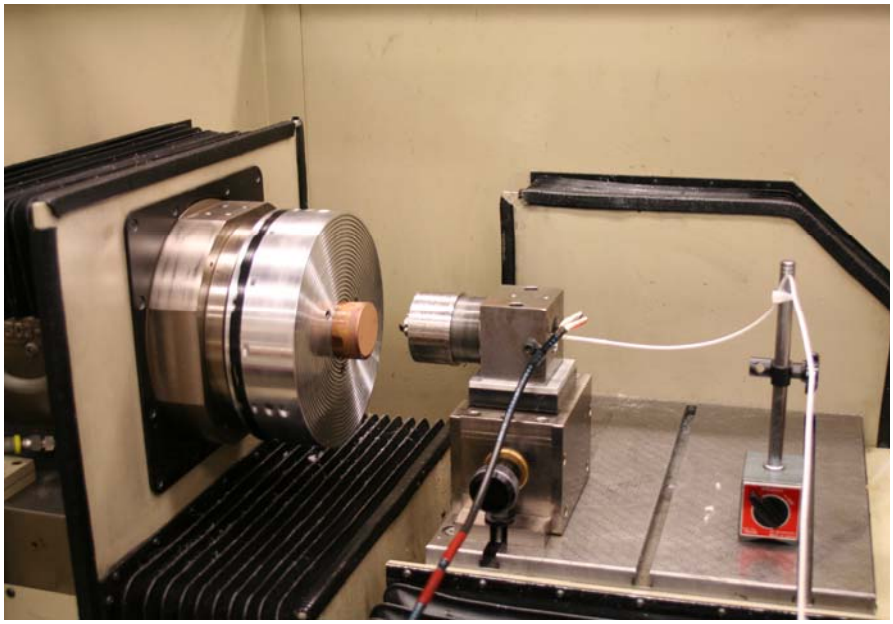

Figure 4. Diamond Turning Machine with FTS for instant depth of cut change nicked tool edge that may have been damaged by contamination in the ASG-2500 lubrication system.

Depth of Cut Changes with Fast Tool Servo

The Fast Tool Servo (FTS) was used to instantly change the depth of cut during each of the machining programs discussed later in this section. Each program had only one cross-feed rate and calculations were performed to produce 10 passes at each depth of cut. The first set of 10 was the deepest and the FTS moved the tool out of the workpiece for each successive depth of cut. Figure 5 shows an instance on the part where the depth of cut is changed with the FTS.

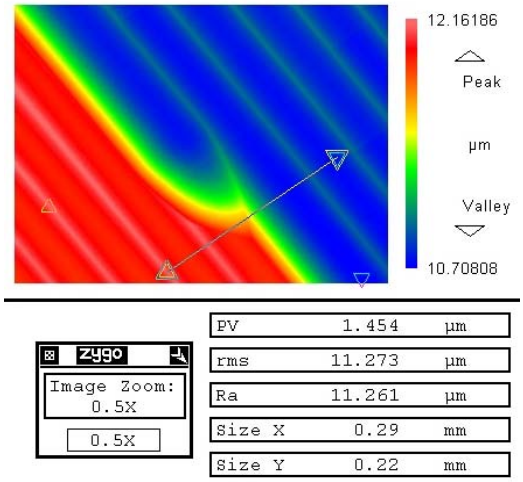

Figure 5. 1 µm cutting depth change command at a circumference of 125mm. Rise time is 5.3 ms.

Fast Tool Servo Setup

A 40 mm long PZT stack was used in the FTS and it provided a displacement of 40 µm. A cap gage with a 20 µm range provided position feedback for closed loop control of tool position and to eliminate errors such as hysteresis effects. The difference in range between the PZT and the cap gage was accounted for by mechanically setting the gage to null with the servo extended half of its range or 20 µm. This practice keeps the PZT in the center of its mechanical and electrical range during closed loop operation.

Tool Path

The DTM plunged the tool into the part and then moved the tool across the face of the workpiece (perpendicular to the spindle face) at a constant velocity while the FTS instantly stepped the tool to a new, shallower cutting depth. The plunge depth was 10 µm into the work piece at an outer radius and the tool was moved towards the spindle centerline to an inner radius. The FTS stepped the tool out of the work piece after 10 grooves at each cutting depth were created. The step sizes were 5 µm, 3µm, 1 µm and 3 µm. This yielded depths of 10 µm, 5 µm, 2 µm, and 1 µm. The final step of 3 µm removed the tool from the work piece and held it 2 µm above the original surface. An example of a continuous cut with all depth of cuts represented and the original surface and is seen in Figure 6.

Machining Plan

A total of seven continuous cutting passes were performed. The first three tests are named 1, 2 and 3 while the last four are 4A, 4B, 4C, and 4D. Tests 1, 2, and 3 had identical feed rates and spacing, but were performed at different radii on the work-piece to test the effects of surface speed. Tests 4A-4D were at increasing slower feed rates and were at intermediate radii on the workpiece. These tested for any combined effect from depth of cut and feed rate.

Tests 1, 2, and 3 were performed at feed rate of 37.7 µm/rev. Test 1 started at a work-piece radius of 20 mm and completed at a radius of 18.1 mm, Test 2 from 6 mm to 4.1 mm, and Test 3 from 2 mm to 0.1 mm. The speeds at the start of each cut were 1.1, 0.3 and 0.1 m/s, respectively. The change in radius from Test 1 to 2 results in a 70% decrease in cutting speed, 1 to 3 results in a 90% decrease. The final revolution in Test 3 is 90% slower than the first revolution. Theoretical PV roughness was 231 nm and RMS roughness was 69 nm.

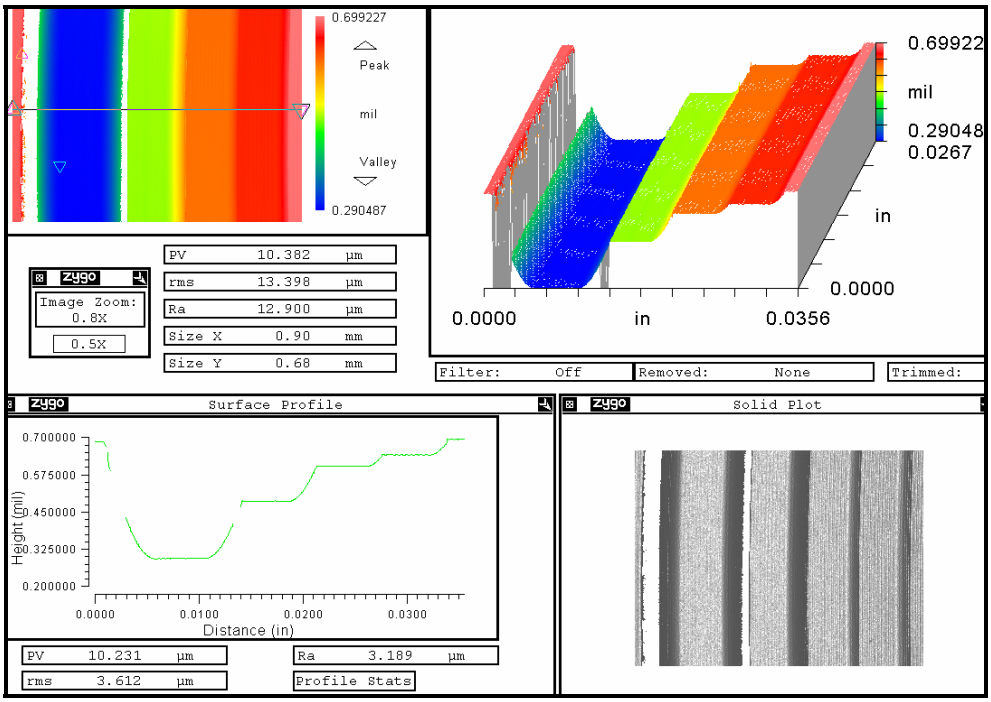

Figure 6. Example tool path with instant depth of cut changes. The original surface is seen at far left and right of the profile. The deepest cut on the left is 10 µm and was performed first with the 5 µm, 2 µm and 1 µm following.

Tests 4A-4D ranged from a work piece radius of 17 mm to 9 mm with a spacing of 2 mm between the starting radii. The changes in feed rate were determined by reductions in the theoretical PV roughness from the first three tests. Order of magnitude decreases in surface finish were initially desired but the final reductions were 1/2, 1/5, 1/10, and 1/50 to allow for intermediate roughness and to ensure that cusps were still visible at the lowest feed rate. The details for Tests 1-4 are in Table 1.

Table 1. Layout of tests on copper workpiece.

Test	Radius Begin (mm)	Radius End (mm)	Feed Rate (µm/rev)	PV-Theory (nm)	RMS-Theory (nm)
1, 2, 3	20, 6, 2	18.1, 4.1, 0.1	37.7	231	69.1
4A	17	15.67	26.7	115	34.5
4B	15	14.07	16.86	46.2	13.8
4C	13	12.26	11.9	23.1	6.9
4D	11	10.53	5.33	4.6	1.4

3.2.3 SURFACE SPEED EFFECTS

The results of Test 1, 2, and 3 were measured to assess the surface finish effects. A Zygo NewView 5000 Scanning White Light Interferometer produced 3D profiles of the machined surface and was able to easily resolve the diamond tool grooves. A sample measurement of the surface for Test 1 at 5 µm cut depth is seen in Figure 7. From this 3D data, a 2D trace was produced in the cross feed direction.

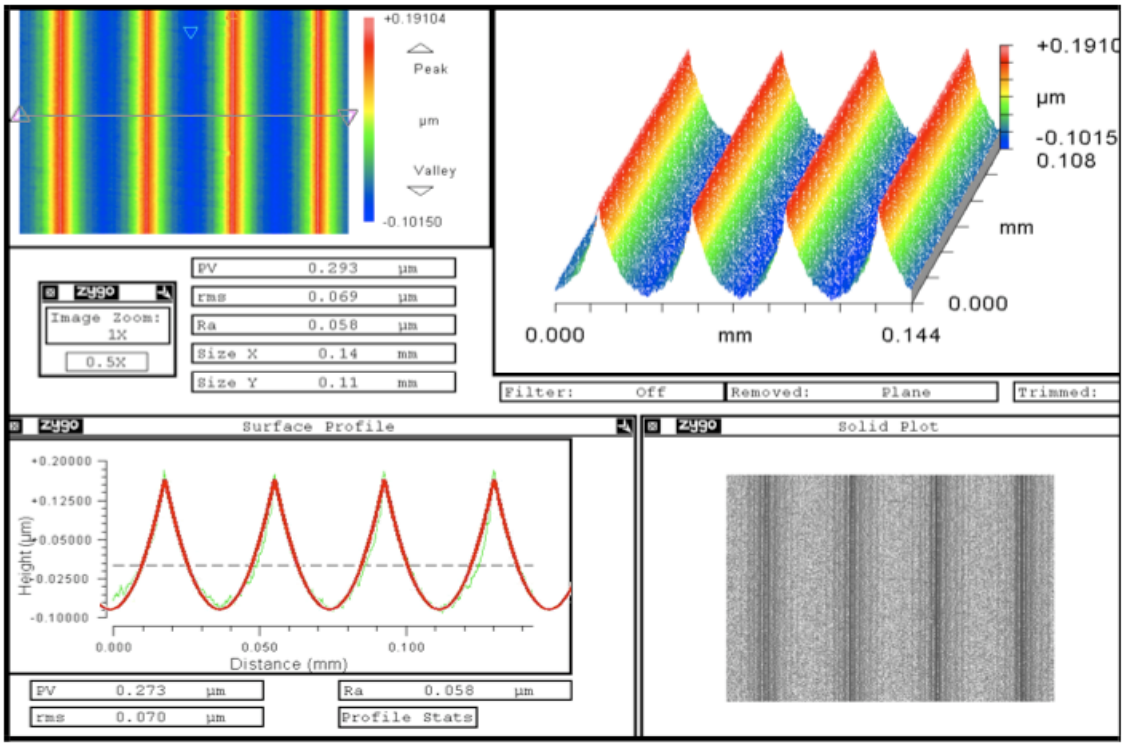

Figure 7. Sample New View Scan. Test 1 at the 5 µm DOC, cross-feed: left to right, up-feed: bottom to top. Dark line is theoretical tool overlaid on surface trace.

Roughness measurements from Tests 1, 2 and 3 (all depths of cut included) were compiled into Figure 8 for evaluation of surface speed effects. Surface speeds of 0.1, 0.3 and 1.1 m/s at 530 RPM correspond to respective workpiece radii of 2, 6 and 20 mm. The PV and RMS roughness for each of the three surface speeds have similar means and variation. For each surface speed, there were four cutting depths, thus four data points at each speed. Trends between cutting depths were examined with respect to surface speed but no similarity was seen. The slowest speed has a couple of points with lower PV than the other two speeds, but by less than 20 nm. Both actual PV and RMS have higher means than the theoretical values and the increases appear consistent across the different speeds. This suggests that roughness is independent of surface

speed for range typically seen in diamond turning operations, which is consistent with conclusions made in the previous research [1, 2].

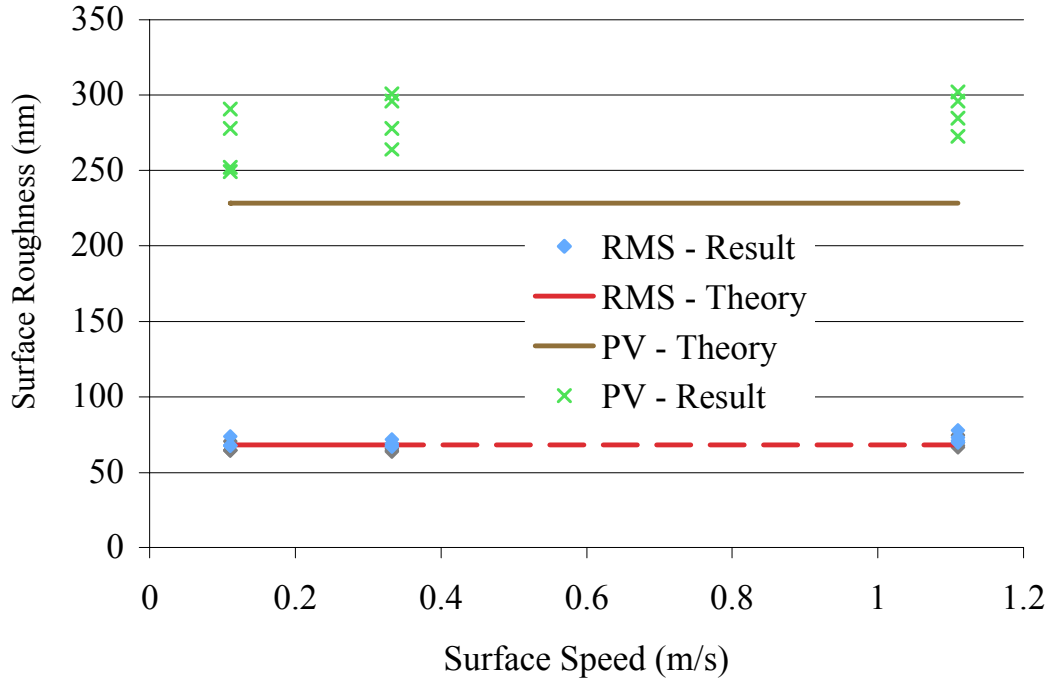

Figure 8. Surface speed effects on roughness with data compiled from all tests.

3.2.4 Depth of Cut Effect

Measurements of Tests 1, 2, and 3 show there is little in this experiment indicating that roughness is a function of cutting depth. Because Tests 1, 2, and 3 also showed no trend when compared by surface speed (as calculated with workpiece radius and spindle speed), the entire set of data points was grouped together as the 37.7 µm/rev feed rate for the depth of cut plot in Figure 9. For comparison, horizontal lines in the plot show the theoretical PV and RMS surface roughness. The data spread is fairly consistent for each cut depth and there is little variation from depth to depth. The separation in PV roughnesses is about 60 nm but, when grouping the rest of the data together in the next section, the spread is just over 50 nm. When comparing the PV and RMS theoretical values to the actual data, the actual data are consistently higher (similar to the surface speed comparisons).

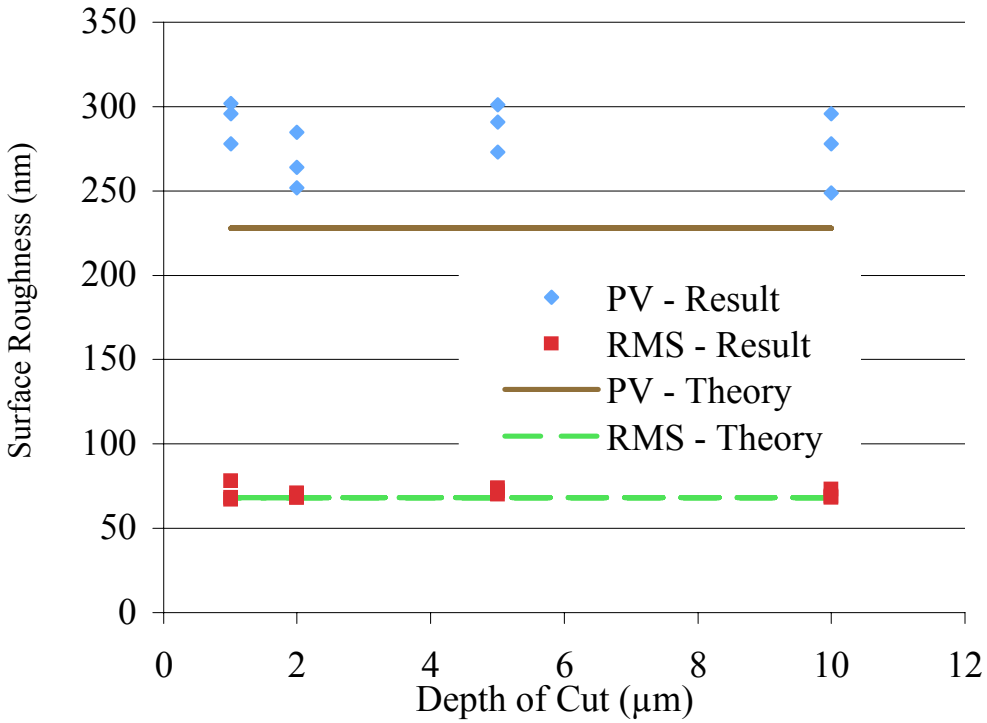

Figure 9. Surface Finish vs. Depth of Cut for Test 1-3. f = 37.7 µm/rev.

Tests 4A-D showed similar a result to Tests 1-3: a generally uniform PV and RMS when comparing different depth of cuts. The complied results are presented in Figures 10 to 13 where PV and RMS roughnesses are plotted for each cut depth with horizontal lines to represent the theoretical PV and RMS roughnesses. For each feed rate, the actual roughness is consistently higher than the theoretical, although the difference is much less of a factor in the higher feed rate tests than in the lower. Closer examination reveals that the actual PV is 30 nm to 50 nm larger than the theoretical for all feed rates. This suggests that another variable (second order effect such as machine vibration, tool sharpness or tool radius measurement) has an influence on PV and RMS roughness that is independent of feed rate.

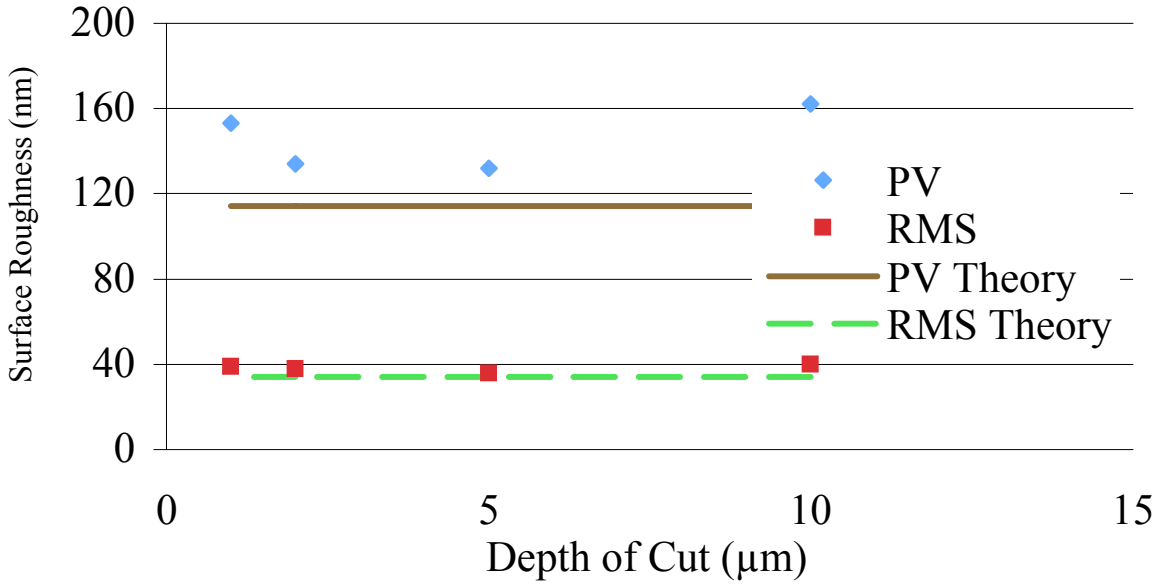

Figure 10. Test 4A. f = 26.7 µm/rev.

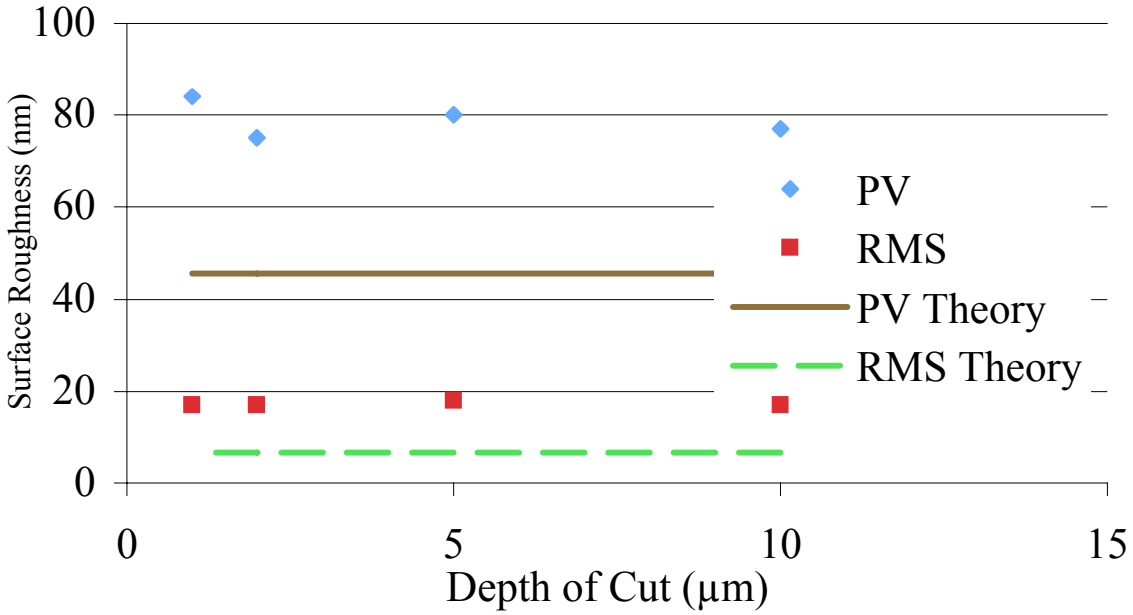

Figure 11. Test 4B. f = 16.9 µm/rev.

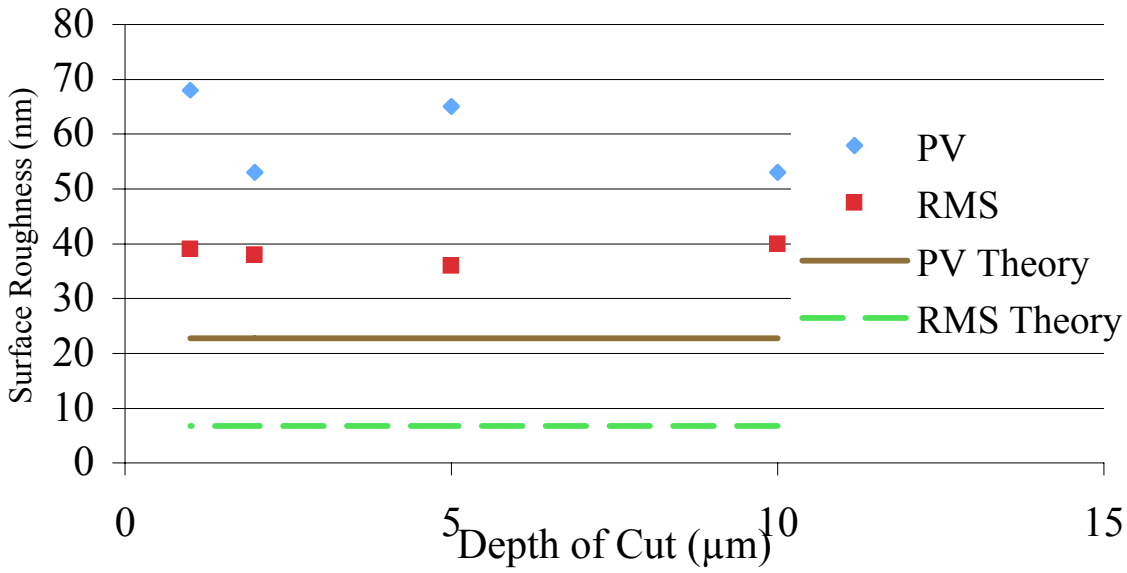

Figure 12. Test 4C. f = 11.9 µm/rev.

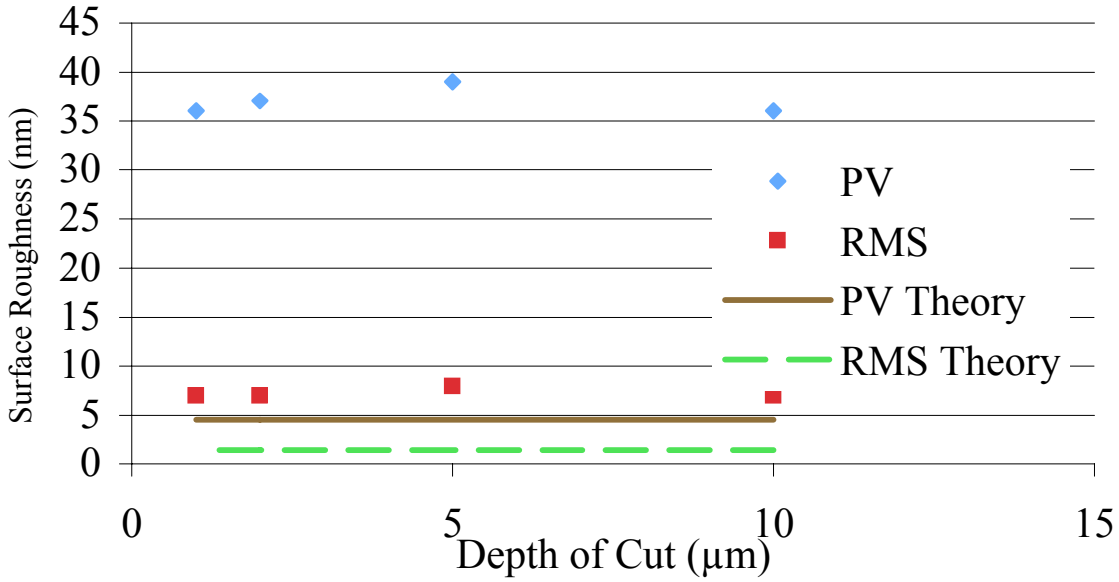

Figure 13. Test 4D. f = 5.34 µm/rev.

3.2.5 CROSS-FEED RATE EFFECT

Measurements from all experiments were complied into a single data set to compare feed rate affects on surface roughness. Plots of this data with respect to cross-feed rate are found in Figure 14 for RMS roughness. The plot has a line to represent the theoretical value and a series of points that represent different cutting depths and workpiece radii for each data point.

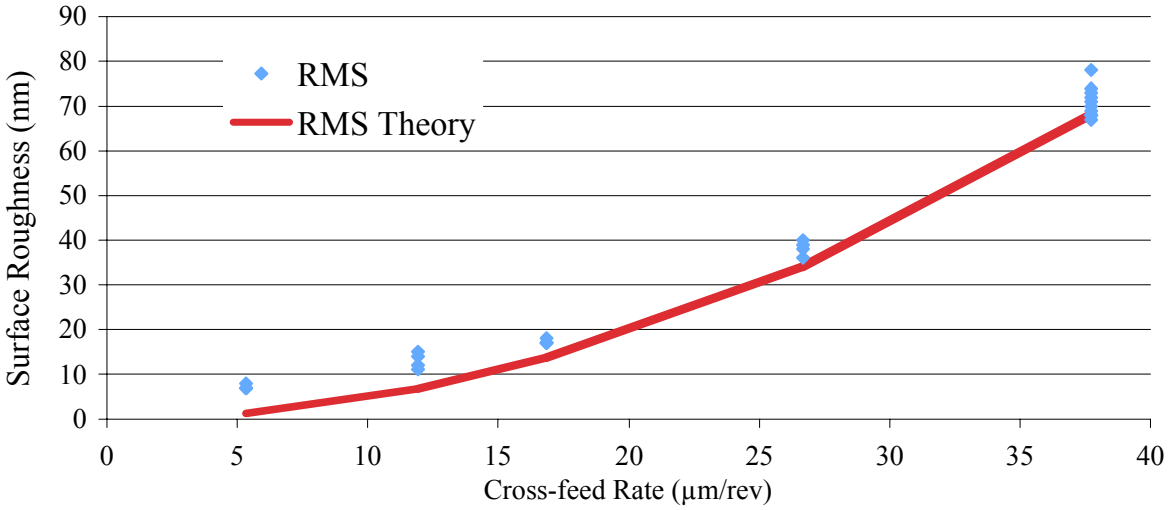

Figure 14. Feed rate effects on RMS surface roughness.

The RMS roughness data both demonstrate trends that follow the theoretical predictions. The mean of the RMS roughness measurements were consistently 5 to 8 nm larger than the theoretical value, again implying that this measurement is affected by an independent variable (such as machine vibration, tool sharpness or tool radius measurement) that remains constant with respect to feed rate. The RMS roughness appears consistently larger as well.

Further investigation of the measured cross-feed traces revealed the features causing the increase to PV and RMS roughness as discussed in the next section.

3.2.6 Groove Comparison with Instant Depth of Cut Change

Figure 5 showed an example of an instant depth change while machining at a large feed rate (37.7 µm/rev) and, for contrast, Figure 15 shows the same depth change (1 µm) while machining at a the lowest feed rate in the test (5.33 µm/rev). At the low feed rate the cusp features are barely discernable when compared to the 1 µm step change while the high feed rate they are readily distinguishable.

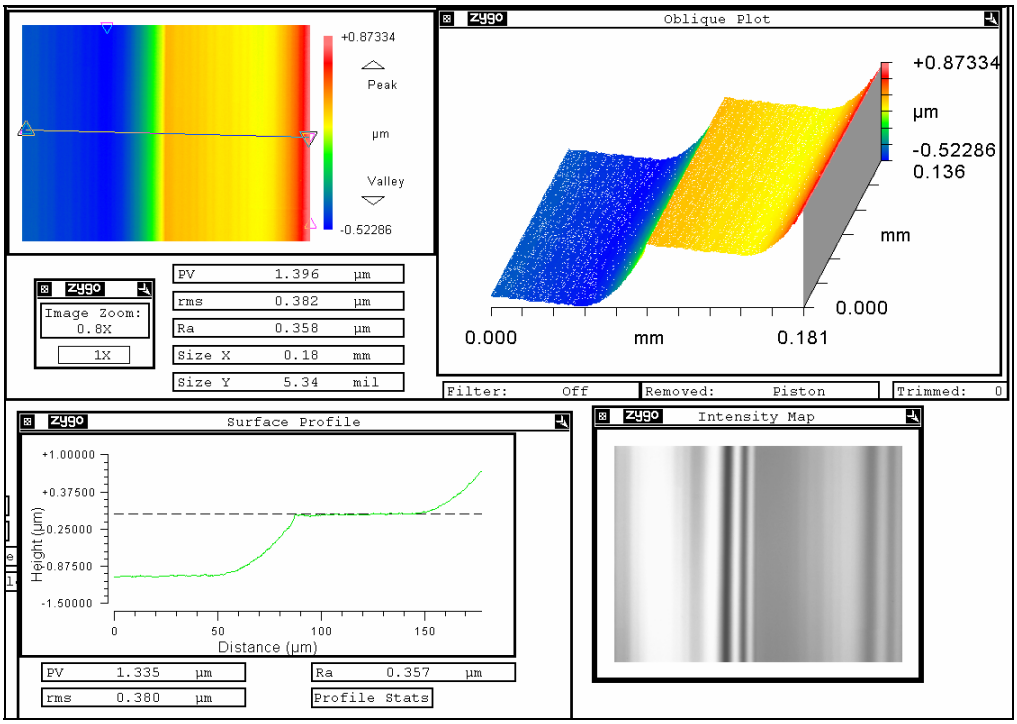

Figure 15. 1 µm depth of Cut change for 5.33 µm/rev feed rate.

The large radius left by the step change was compared to the remaining cusps. Figure 16 shows a surface profile of several cusps leading up to a cutting depth change and the theoretical tool shape at the prescribed feed rate. When comparing features at this level, it is difficult to discern much other than the fit between the theoretical cusp spacing and the actual cusp spacing. Figure 17 shows a comparable plot at a feed rate of 5.33 µm/rev where it is more difficult to match the theoretical cup spacing and the step profile to the actual surface contour. At this fine of a cross feed, the contribution to roughness has less to do with the cross feed rate and more to with secondary effects. These secondary effects are the cause of the increase to PV and RMS roughness as seen in the previous sections.

Two separate mechanisms caused larger surface roughness than the parabolic approximation (PV and RMS) for a round nose tool predicted. One was minimum chip thickness: a function of tool edge radius or sharpness. All tools have some edge radius after sharpening and, as they wear, this radius becomes larger. According to work done by Arcona [2], even a freshly sharpened tool (<50 nm edge radius) will cause elastic deformation as the tool moves through the workpiece. The elastic rebound, when cutting with a sharp tool round nose tool in electroplated copper, was approximately equal to the edge radius. With elastic rebound present in the cutting conditions, some minimum chip thickness was seen in the surface profile. By placing a theoretical tool path against the trace, the uncut material was observed and can be seen as the

small hump at the intersection of adjacent tool passes. Figure 18 is an example from Test 1 (37.7 µm/rev) at 5 µm depth of cut. Also, Figure 19 shows Test 4C (11.9 µm/rev) at 5 µm depth of cut

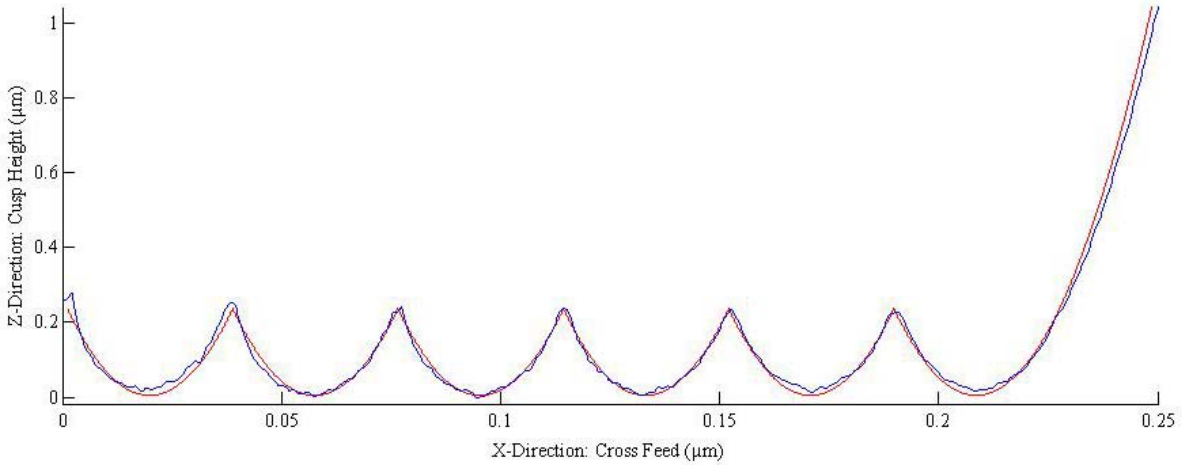

Figure 16. 37.7 µm/rev (Test 1) feed rate with cutting depth change compared to theoretical profile (smooth line).

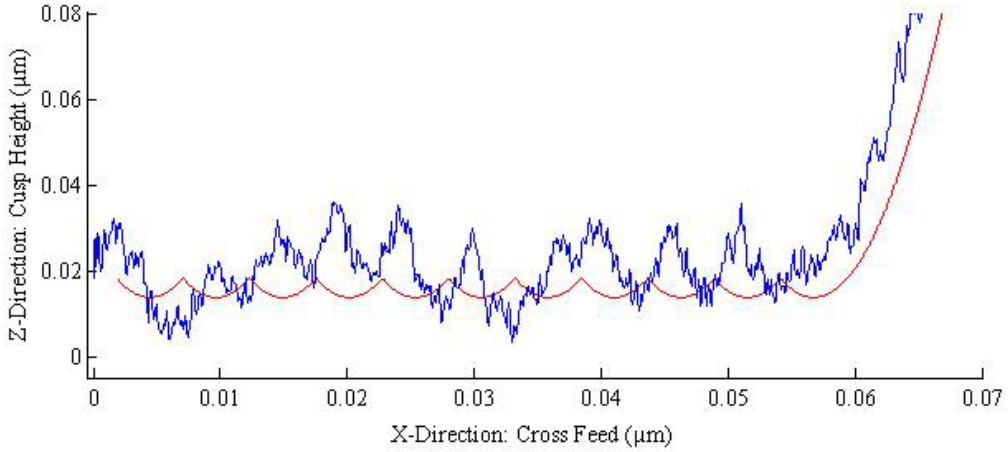

Figure 17. 5.33 µm/rev (Test 4D) feed rate with cutting depth change compared to theoretical profile (smooth line).

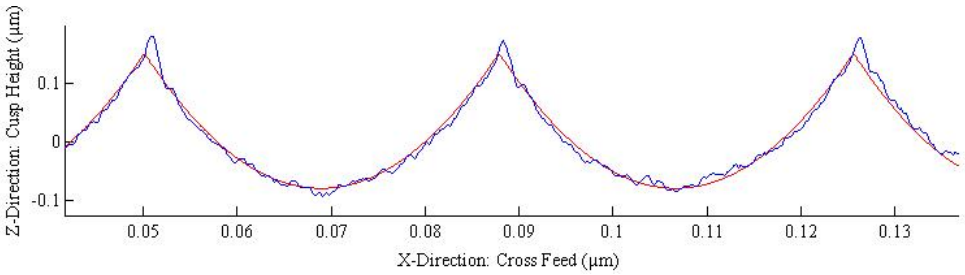

Figure 18. 37.7 µm/rev feed rate (Test 1) zoomed to show only a few cusps and compared to theoretical (smooth line). Feed direction left to right.

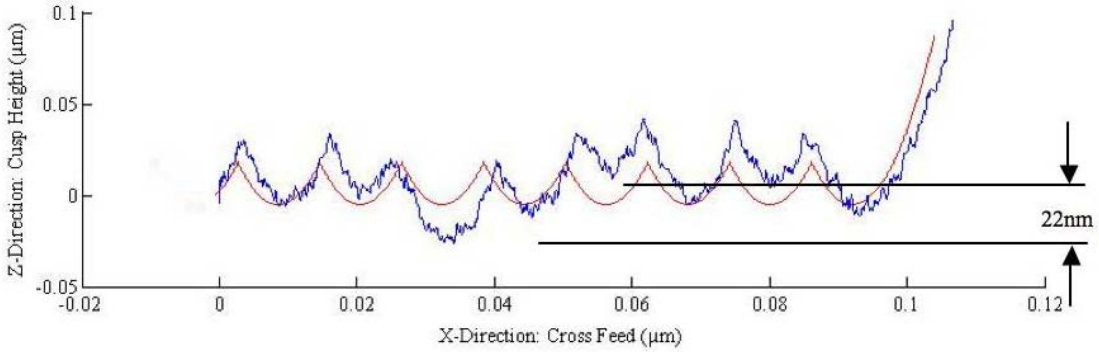

Figure 19. 11.9 µm/rev feed rate (Test 4C) with cutting depth change compared to theoretical profile (smooth line). Asynchronous vibration caused valley-to-valley variation of 22 nm. Feed direction left to right.

where the minimum chip thickness is more dominating because the smaller feed rate creates a smaller cusp. This is best seen in the first two cusps (left side) where the theoretical profile is closely aligned on the leading edge of the theoretical tool, but is separated from the trailing edge of the theoretical tool. The second mechanism is asynchronous spindle vibration and is best seen in Figure 19 because, again, the cusp height is lower. Each pass occurs at different depth where the range of depths closely matches the previously reported vibration of the Z-axis and spindle with full amplitude of 30 nm [12].

3.3 MACHINE VIBRATION

Optical quality surface roughness in single-point diamond turning, as observed in the previous section, is primarily influenced by four factors: cross-feed geometry, material properties, tool edge quality and machine vibration. As with the previous section, lubrication for chip removal is essential to low roughness. The first-order geometric model using the parabolic approximation

gives the peak-to-valley (PV) and is determined solely by the cross feed (f), and the tool radius (R) as shown in Equation 1. This approximation is often used as the sole determiner for choosing radius and feed rate even though for large radii and small feeds, the predicted finish is not achievable. This effect is observed in experiments (more obvious at lower feed rates) where a virtually homogenous material, a recently lapped tool with a high quality edge, and a small cross-feed produced a PV of more than 50 nm while theoretical was 23 nm (Test 4C). Figure 19 shows a relatively large variation in cusp valley depth that partly caused an increase in surface roughness beyond theoretical and can be attributed to machine vibration. As discussed previously, elastic rebound on trailing edge of the cusp due to minimum chip criterion also contributed to the surface roughness increase.

The impact of machine vibration on a diamond-turned surface is generally to degrade the surface finish. The vibration can also have a significant impact on optical surfaces that operate in the visible range by introducing coherent scatter that produces the familiar "rainbow" appearance of diamond turned surfaces in white light. In a simple assumption, a sinusoidal vibration in the normal direction would degrade RMS surface finish proportional to the amplitude of the vibration. It would seem that the surface finish could never be improved beyond this value and there would be no point in slowing the feed rate or using a larger radius tool. To test this assumption, a model was developed to simulate the interaction between successive tool passes when the tool is vibrating relative to a single-point diamond turned workpiece. The model was designed to draw successive cusps left in the surface by cross feeds (in 2D and 3D) so surface roughness statistics could be calculated. Variables in the model were cross-feed rate, tool nose radius, frequency of sinusoidal machine vibration, and amplitude of machine vibration.

3.3.1 ASG 2500 Z-AXIS VIBRATION MOTION

The origin of machine vibration motion can be from a number of sources, although the axes hydrostatic ways or the air bearing in the spindle are the most likely candidates because these interfaces are more compliant than the steel structures or granite base of a DTM. Drescher [4] addressed the surface finish capabilities of the ASG-2500 and the relationship between tooling forces, machine vibration, tool edge quality and surface finish. It was found that the motion between the tool and spindle was caused by the Z-axis. The only way to eliminate this motion was to shut off the oil flow to the Z-slide to let it rest on the machine base and turn off the Z-axis controller. Only then was the predictive model accurate.

Most optical workpieces are fabricated with the surface normal nearly parallel to the Z-axis and it has also been shown that roughness is most sensitive to disturbances in this direction [5]. For the following discussions and examples, the vibration of the ASG 2500 Z-slide will be used as the source of the vibration, though the technique can be applied to any source. This amplitude

can vary slightly depending on spindle rpm and balance. Changes to either of these can result in amplitude increases.

Z-axis motion from the spiral groove at workpiece center

Characteristics of the of the Z-slide dynamic motion were determined by measuring the features left in the center a copper workpiece. For those tests, the tool was centered with respect to the spindle centerline within 1 µm. The spiral created after the final centering adjustment is found in Figure 20. It was measured with the NewView white light interferometer and imported into MATLAB for analysis. A MATLAB script was written to align a spiral trace to the data and perform interpolation along the trace. The number of interpolated points was calculating by taking the circumference (c) at the largest trace radius of 22.4 µm and equating this to the grid sample density found in the NewView data of 0.11 µm/sample as:

$$\#\ of\ samples = (c = 2*\pi*22.4 = 140\ \mu m) / 0.11\ \mu m/sample = 1270 \qquad (2)$$

A plot of the spiral fit to the tool path is in Figure 21 where the dark line represents the series of points taken to form the groove trace. The spindle speed for this cut was 530 rpm and with 1270 samples per revolution, the trace sample frequency is 11 kHz. The highest un-aliased frequency component is half the sample rate, or 5.5 kHz. The expected Z-axis vibration frequency is less than 100 Hz so the trace data has more than enough information. A plot of the interpolated tool height along the spiral trace is in Figure 22.

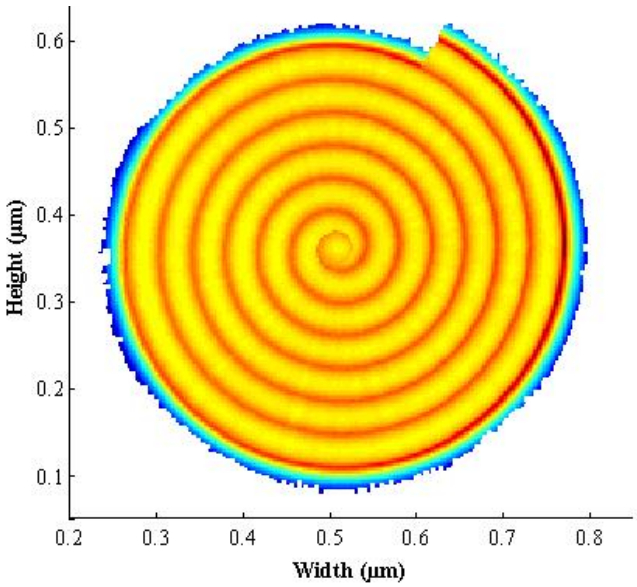

Figure 20. Spiral found at center of workpiece after last tool centering adjustment.

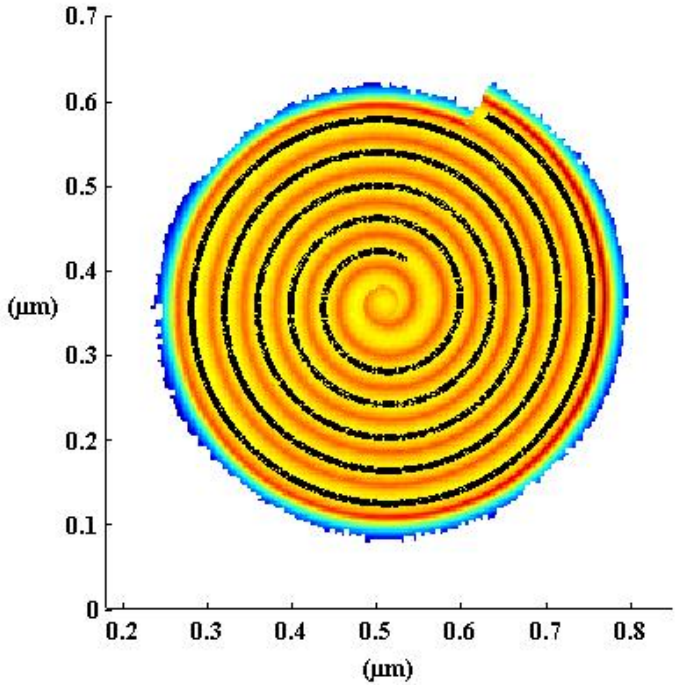

Figure 21. Center feature found in Figure 20 with a spiral trace aligned to the groove bottoms.

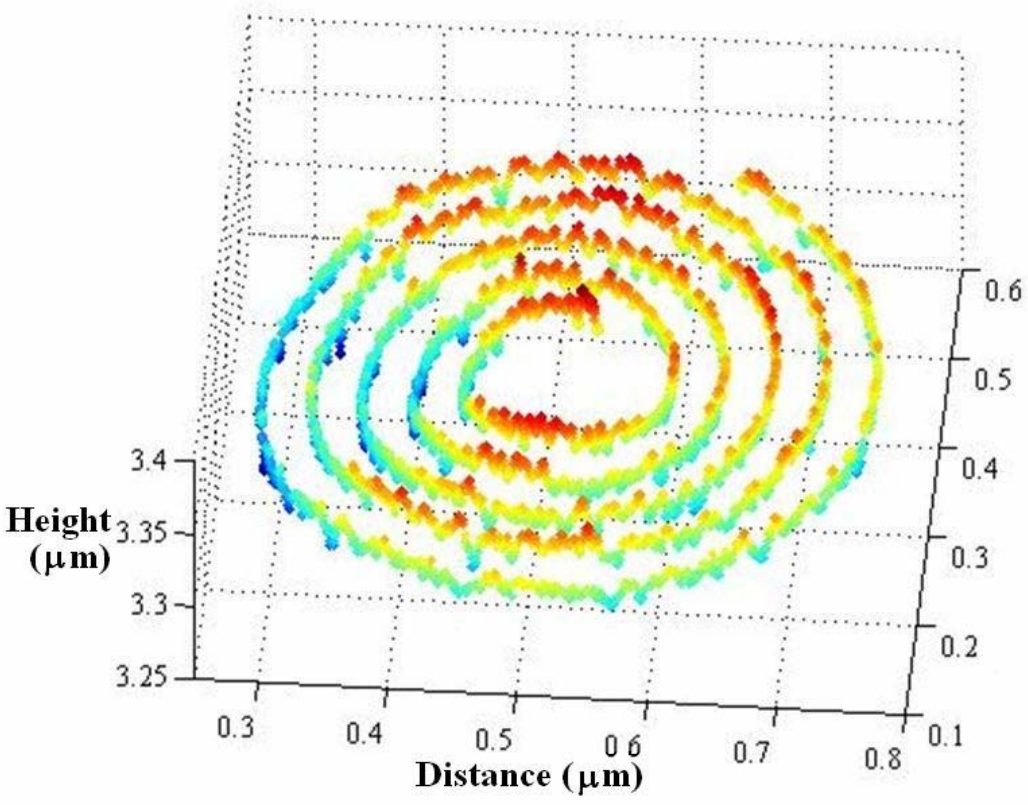

Figure 22. 3D plot of interpolated points from the spiral trace in Figure 21.

Frequency response of spiral groove at workpiece center

The spiral trace was analyzed for frequency content and the result is found in Figure 23. The first four peaks represent 0.5, 1, 2, and 3 times the spindle speed (530 rpm = 8.833 Hz) or peak 1 = 4.42 Hz, 2 = 8.83 Hz, 3 = 17.7 Hz, and 4 = 53.0 Hz. These points represent synchronous motions of the Z-axis and are most likely a combination of form error, tilt in the measurement, and Fourier transform of a data set that contains incomplete waves. Synchronous motions at low frequencies have no effect on surface finish because the height of the tool for a given profile is the same from one revolution to the next. The second (once per revolution) and third (twice per revolution) are largest because the synchronous motions of the spindle are largest. The first asynchronous frequency is the fifth peak at 63.6 Hz. This was assumed to be the first natural frequency of the Z-axis in the Z-direction. Because the hydrostatic bearing slide-way in the Z-axis is intended to move freely in the Z-direction, the stiffness in that direction is determined by the decoupling flexures that attach it to the ball screw slide-way and by the ball screw itself. The flexure stiffness design is a compromise between the undesired motions of a ball screw drive and the stiffness of the axis in the direction of motion. A stiffer axis results in increased form error due to the influence of a screw shaft that can never be perfectly straight.

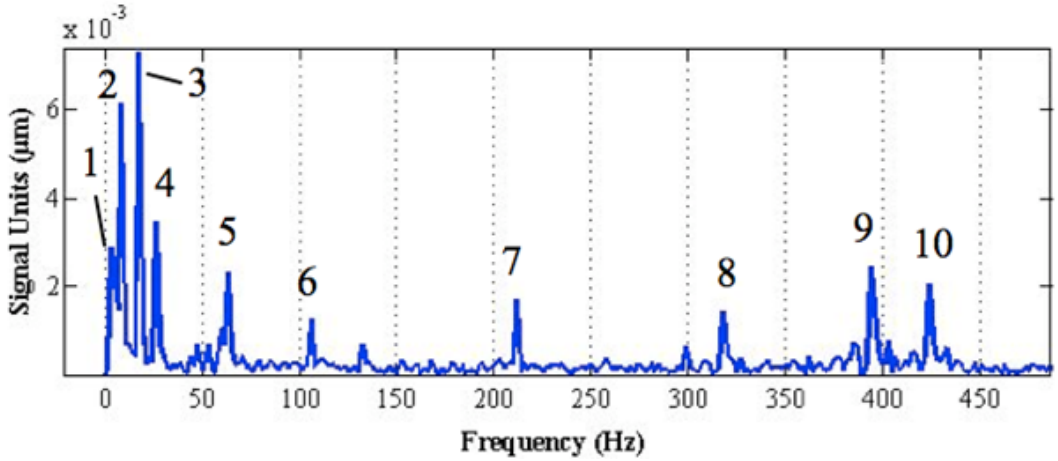

Figure 23. Frequency response of spiral profile seen in Figure 22.

An experiment was conducted using a capacitance gage to measure the closed loop response of the Z-axis when subjected to an impulse. A silicon wafer was vacuumed to the chuck and the cap gage clamped to a tool holder that was bolted to the X-axis. The cap gage was aligned perpendicular to the silicon wafer and the Z-axis was jogged towards the cap gage with open loop commands to the cap gage null position (output = 0 volts). The voltage output of the cap gage was fed into an oscilloscope, which was then configured to calculate frequency. Closed loop control was initiated to hold the null position. A rubber hammer was used to tap the Z-axis

table in the Z-direction to create an impulse disturbance. The oscilloscope output the settling frequency of 64 Hz and confirmed the frequency analysis describe above.

The sixth, seventh, eighth, and tenth peak in the data represent 12, 24, 36, and 48 times the spindle speed or 106, 212, 318, and 424 Hz. The sixth is caused by ASG 2500 air-bearing spindle because it has twelve air pads and the seventh, eight, and tenth are harmonics of the marks caused by the 12 pads. The features caused by the pads have been measured and are small. The ninth peak at 394 Hz and the high frequency peaks are insignificant in terms of machine vibration because the Z-axis will respond at its first mode of 64 Hz when excited [23].

Vibration Amplitude from Workpiece

The amplitude of Z-axis vibration was found by analyzing the surface profiles from the experiments conducted for Figure 14. Several sets of traces were examined and the maximum trough-to-trough separation of 22 nm was set as the vibration magnitude. This traced showed significant separation while still clearly demonstrating the expected number of cusps. At lower cross-feeds, the cusps were less obvious and it was difficult to discern the trough locations.

3.4 SURFACE FINISH MODEL WITH VIBRATION

A number of points along the edge of the tool are calculated for each x-position in increments of the crossfeed. The depth of cut changes around the periphery of the part with the vibration environment. After multiple profiles are generated, redundant points in the overlapping regions are eliminated and only the point with the largest depth at each x-coordinate is retained. Individual cross-traces at different rotational positions of the spindle can then also be assembled into 3D profiles.

3.4.1 MODEL DEVELOPMENT

The variables used to model surface finish with machine vibration are cross-feed rate, tool nose radius, and the motion parameters of the ASG-2500 as discussed earlier. Like the parabolic rule-of-thumb in equation 1, the model assumes ideal cusps created by a round nose tool with perfect edge sharpness and homogenous materials that are appropriate for diamond turning. The model is independent of surface speed or depth of cut, as the results in Figure 8 show. Also, the assumed location of the simulated surface profile was at a large radius on the workpiece (all simulations used 20 mm) so the diamond turned grooves would appear straight. At the large radius, the circumferential distance between points was assumed equal at every radius.

The surface profile was formed by calculating a rectangular grid of tool center positions, solving the tool height for each point in the grid, solving for the two dimensional profiles in the cross-feed direction (profiles along meridians), and then stacking the cross-feed traces in the up-feed direction which generated a three dimensional profile. The first step in the program was to input the machining parameters: feed rate, spindle RPM, tool nose radius, machine vibration frequency, and machine vibration amplitude. Then the number of data points in the cross-feed direction and the number of tool passes across the profile were input.

Tool Tip X and Z Position

The tool tip locations were calculated from the input variables. The spacing of the tool tip between passes in the cross feed direction was set by multiplying the number of passes by the cross-feed rate. The spacing of the tool tip in the up-feed direction was set by dividing the length of the cross-feed profile by the number of data points for the cross-feed profiles; this was done to make data point density in the final three-dimensional profile equal in both up-feed and cross-feed. With the tool tip spacing known, tool center vectors were calculated for the X and θ directions. In order to take advantage of the vectorization (simplified and efficient coding designed to eliminate programming loops) routines in MATLAB, the center vectors were expanded to matrices. The tool center vectors were input to a function that catenated each vector with itself (one vector was catenated horizontally and the other vertically) such that rectangular tool center matrices of equal size for the X and θ direction were created (number of tool passes wide, number of points tall).

The tool center matrices were input to a formula that would calculate the tool depth at each tool tip location. The result was a third matrix (same dimensions as the tool tip matrices) that contained the tool tip depths. The depth of cut changes around the periphery of the part with the vibration environment in the following formula:

$$depth = A \cdot \sin\left(\frac{\omega x}{\Omega f}\right) \tag{3}$$

where A is the vibration amplitude, ω is the vibration frequency of the tool, x is the radial position of the tool center and Ω is the vibration frequency of the spindle. Because the tool center matrices were in the X and θ-directions and tool depth was only a function of the radial X-position, the θ-position was converted into a X-position increment ((ΔX = (θ/360º) * cross-feed) and summed with the X-position when input to Equation 3.

Surface Profiles

The surface profiles were calculated in the cross-feed direction (along radial lines from the spindle centerline with equal angular spacing referred to as meridians) because the variation in height of adjacent tool passes potentially caused each cusp to have a different influence on the final profile as seen in Figure 24. The shape of the cusps the appeared in the final profile were calculated with the Cartesian formula of a circle:

$$(x - x_0)^2 + (z\text{-}z_0)^2 = R^2 \tag{4}$$

where x is the vector of evenly spaced x-positions, x0 is the vector of cross-feed tool centers taken from the X tool-center matrix, z is the vector of z-positions, z0 is the vector of tool tip depth taken from the matrix calculated with Equation 4, and R is the tool nose radius. A set of z values was calculated for all tool tip locations (x0 , z0) for each x in the vector of x-positions. The minimum z for each x in the x-position vector was retained, thus producing the lowest point in the profile for each x-position. The final product was a pair of equal length x-position and z-position vectors, which describe a surface that only displays the residual cusps. Also, this gives a final surface profile with constant sample density in the x direction.

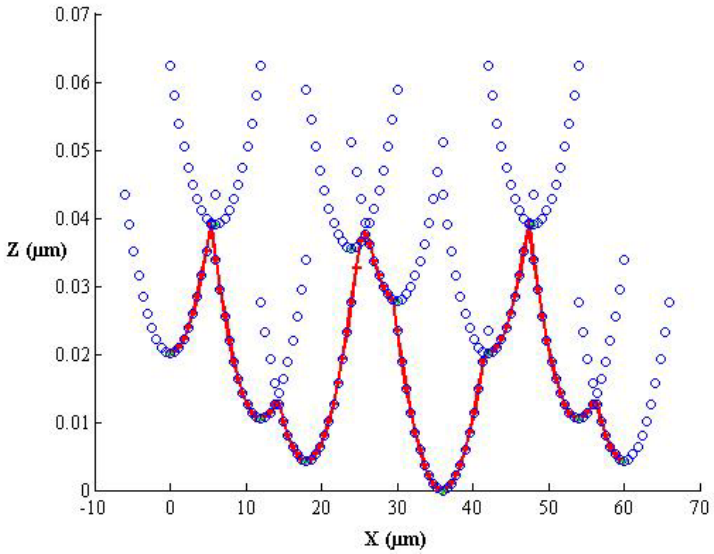

Figure 24. Certain points from multiple tool cups (circles), at varying depths due to vibration, produce a finished surface contour (line).

As shown in Figure 24 where complete tool edges from adjacent cusps have been generated (circles), the redundant points in the overlapping regions do not appear in the final surface contour (line). Individual cross-traces at different rotational positions of the spindle can then also be assembled into 3D profiles as shown in Figure 25. When creating the 3D profile, the

number of traces in the Y direction is equal to the number of points per trace in the X direction allowing a sample with a uniformly spaced grid of samples.

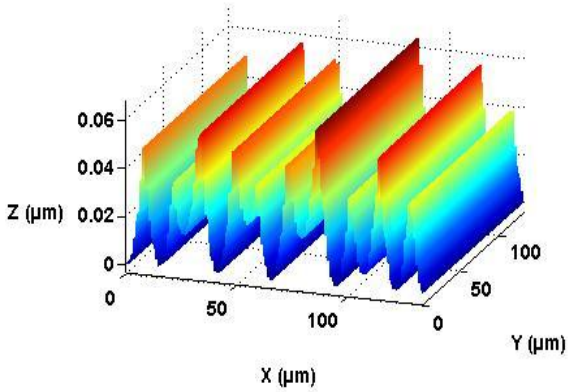

Figure 25. Consecutive surface contours in the cross-feed direction (X) were stacked in the up-feed direction (Y) into a 3-D surface.

Fine Cross-feed Rates

It is at lower feed rates that the effects of tool vibration on a diamond-turned surface become interesting as seen in Figure 26. The plot shows the surface profile for a small cross-feed rate while the crosshairs show the apex of tool for each pass. A number of passes are completely absent from the finished surface, leaving only the most extreme passes and, hence, a smoother surface than would be expected with machine vibration.

Figure 27 shows the relationship between the theoretical RMS finish and the finish model with vibration. The figure indicates that as the theoretical RMS surface finish calculated with the parabolic approximation decreases, the effects of machine vibration on RMS roughness are reduced. Finer cross-feed rates, with a constant tool radius, reduce the roughness data in Figure 26. At the higher theoretical roughness of 20 nm (large cross feeds) the effect of vibration adds only a couple nanometers (10%) to the modeled roughness. As the theoretical RMS roughness decreases to 3 nm, the vibration influences double the RMS, indicating a profile shape similar to Figure 24 where all pass are represented but the height difference between cusps is large. However, once the theoretical falls below this point, certain tool passes are absent from the final profile and the modeled RMS starts to decrease rapidly.

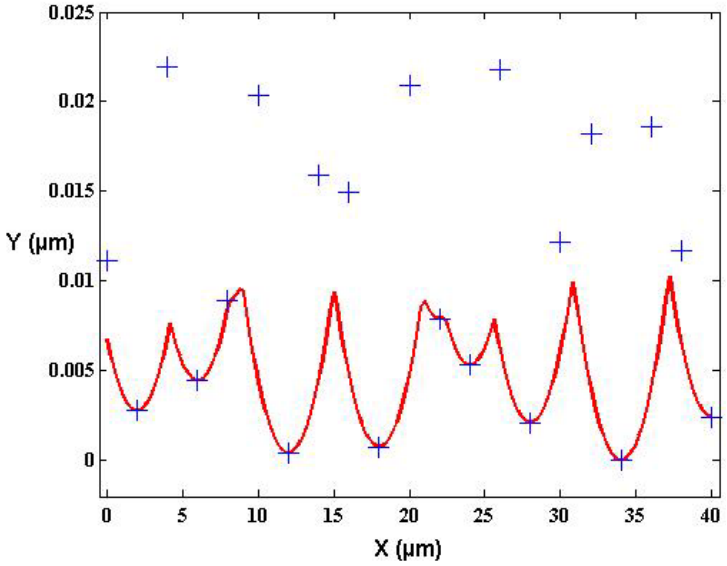

Figure 26. At fine cross-feed rates, some passes of the tool (+) are not represented in the finished surface. This produces a better finish than would be expected from the RMS of the vibration alone.

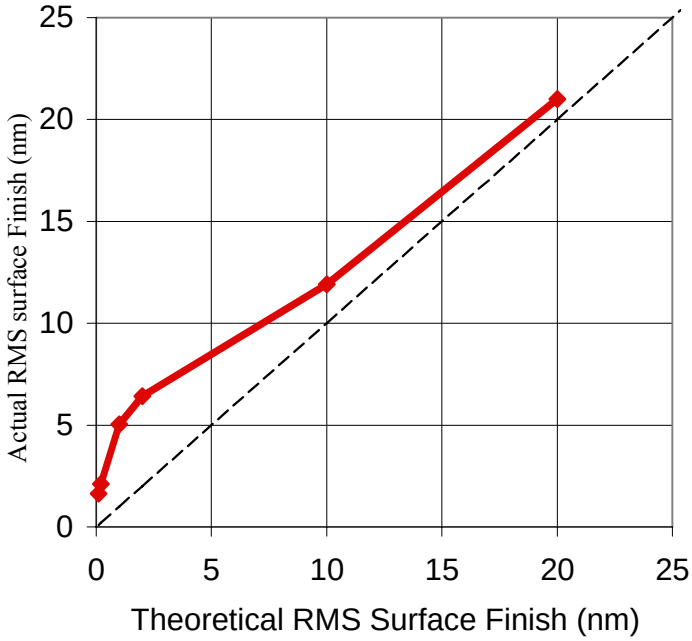

Figure 27. As theoretical surface finish decreases, the effects of machine vibration on surface finished are reduced. Vibration magnitude PV = 22 nm and RMS = 7.7 nm.

3.4.2 EXPERIMENTAL RESULTS

An electroplated copper sample was machined with the same feed rates used in the model. The machining experiments were performed on an ASG-2500 DTM with a 500 rpm spindle speed and a 480 µm radius, zero degree rake angle single-crystal diamond tool. Special care was taken

when setting up this experiment such that the freshly sharpened diamond had almost no cutting exposure before the test was run. The laboratory temperature was controlled to 20 ±0.05°C. Cutting fluid (Mobilmet Omicron®) was sprayed from a PEC custom-built system for lubrication and chip removal. The tool moved across the part from OD to ID.

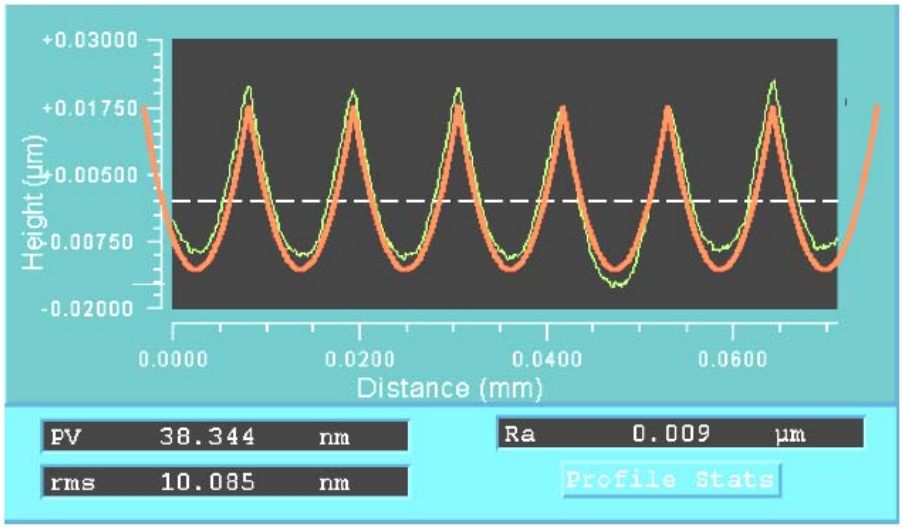

Figure 28. Typical surface profile measurement illustrating the depth change as a result of vibration with large feed rate of 11.3 µm/rev. Theoretical PV = 33 and Theoretical RMS = 10 nm drawn with bold line.

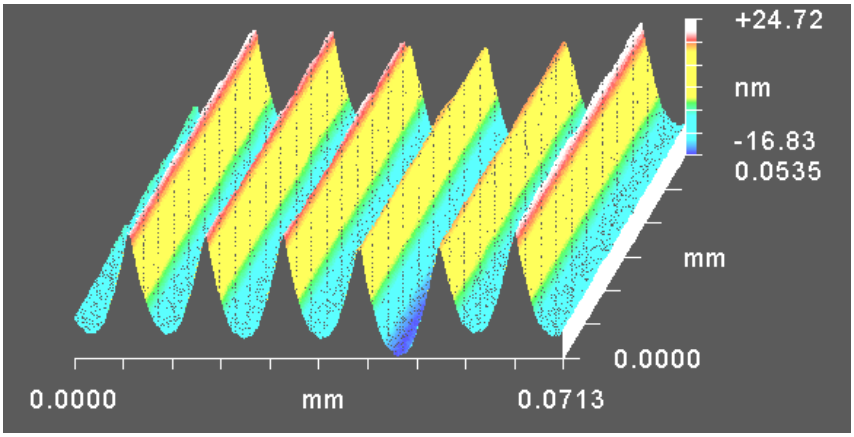

Figure 29. Typical measurements result in oblique plot form. This is the same surface shown in Figure 28.

Eight 2 mm wide bands were machined on the 50 mm diameter sample with cross feeds of 1.13, 1.60, 3.58, 5.06, 11.3, and 16.0 µm/rev. The surface was cleaned by spraying it with (in order)

Mineral Spirits, Acetone, Methanol and an industrial-grade degreasing soap diluted with de-ionized water. Optical grade wipes were used to gently scrub (no direct pressure) the surface and it was rinsed with de-ionized water before another wipe was used to absorb the water standing on the surface. It was then measured on a Zygo NewView 5000 Scanning White-Light Interferometer (SWLI) using 50X & 100X magnification. The measurement area was 108 µm tall by 144 µm wide or 55 µm tall by 72 µm wide. Figures 27 and 28 show the typical profile measurement result. The effects of vibration on groove depth (~7.5 nm) are seen in the profile at this large feed rate. The depth varies with no repetitive cycle as the tool traverses the part. Note that the cusps are free of any repeated features and that they have smooth shapes.

The results for a series of simulations and cuts performed are shown in Figure 30, which exhibits the RMS of machine vibration (7.7 nm), the theoretical RMS roughness from the parabolic approximation (curved solid line), and a dashed line for the model predicted RMS trend. The

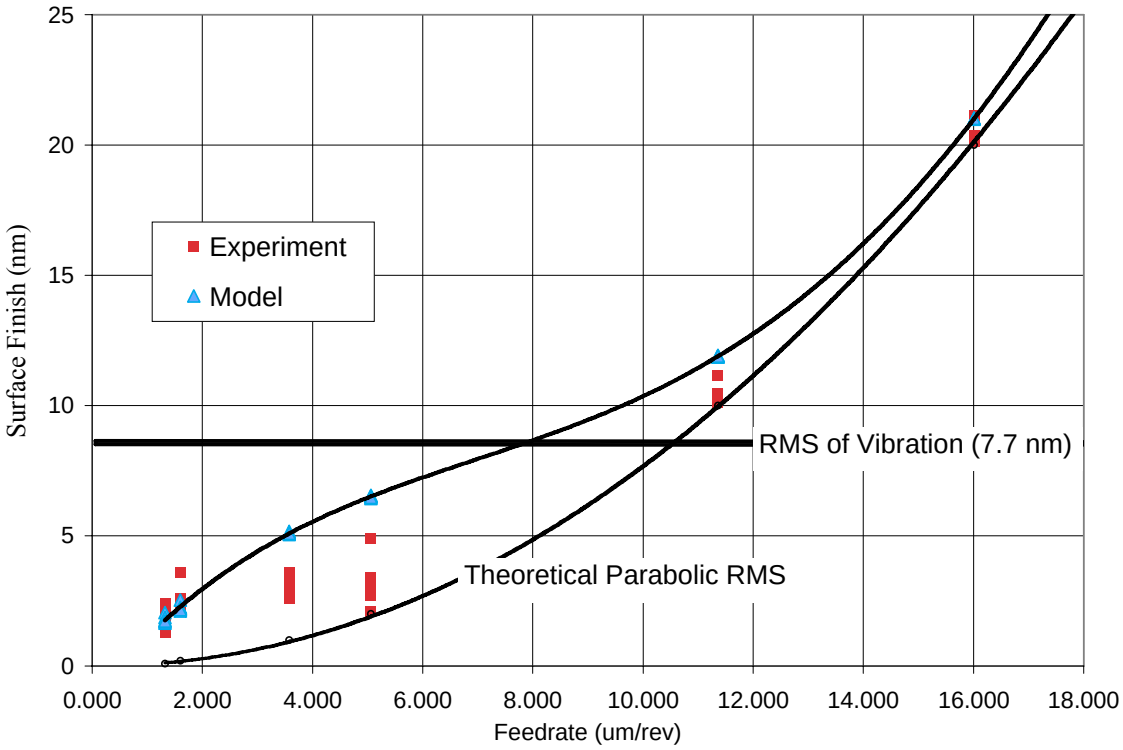

Figure 30. Results from experimental and model data with threshold of RMS Z-axis vibration, a curve to represent the theoretical parabolic RMS surface roughness and a dashed line to represent model prediction.

theoretical RMS roughness for the parabolic surface where f is the cross-feed rate in µm/rev and R is the tool radius (480 µm) as shown in Equation 1. For each feed rate there are 5 modeled roughnesses and 5 experimental roughnesses (in both cases, found by moving around the

workpiece at the same radius). Clearly, the surface finish can improve significantly beyond the RMS 7.7 nm limit of a simple sinusoidal vibration. The finish also continues to improve with finer feed rates, where RMS roughness was measured between 2 and 5 nm, when they already deviate significantly from the theoretical parabolic approximation. The shape of the deviation is similar to the shape of the model in Figure 26. The mean of the measured RMS roughness for each feed rate follows the predicted shape and, while larger than theoretical RMS, is smaller than the modeled roughness for the feed rates larger than 2 μm/rev. This would suggest that the simulated asynchronous sinusoidal vibration is slightly smaller than that described earlier. At feed rates lower than 2 μm/rev the model more closely matches the experimental values but other effects, such as material anisotropies, most likely increased the RMS to above 2 nm and are discussed in the following sections. These effects are also the cause of the large spread seen in the data at the 3.08 and 5.06 μm/rev feed rates.

3.5 CROSS-FEED TOOL DITHERING TO REDUCE COHERENT SCATTER

The precisely controlled cross-feed rate of the tool in a diamond turning process produces a surface that has periodic cusps. The regularly spaced cusps act like a diffraction grating when light waves are incident to the surface, resulting in a reflection that exhibits a diffraction interference pattern. Also, the range of wavelengths found in white light are affected differently by the grating and will produce differing scatter patterns for each wavelength that cause the "rainbow" of diamond turned surfaces. This diffraction effect traditionally limits diamond turned optics to infrared and near infrared wavelengths [6] that are large in comparison to the shallow, narrow grooves in a diamond turned surface. By dithering the tool in the cross-feed direction, the regular spacing of the cusps can be reduced and therefore smooth the inference pattern from an evenly spaced grating (intense, discrete points) to a random grating pattern (smooth, continuous line).

3.5.1 OPTICAL SCATTERING IN DIAMOND TURNING

For discussions of scattering from diamond turned surfaces, the evenly spaced cusps of a diamond turned surface can be thought of as a summation of sinusoidal components calculated through Fourier transformation of the surface profile [7]. Each sinusoid found in the Fourier transform will create a diffraction pattern as described by the sinusoidal grating diffraction equation [7]:

$$\sin\theta_n = \sin\theta_i + nf\lambda \tag{5}$$

where n is the diffraction order (n = ± 1, ± 2, ± 3…), θ_n is the angle of each order with respect to the surface normal, θ_i is the incident light angle with respect to the surface normal, f is the sinusoid spatial frequency (1/wavelength) of the surface, and λ is the incident light wavelength. Figure 31 shows the positions of the diffracted modes relative to the surface normal. The incident light beam is reflected about the surface normal.

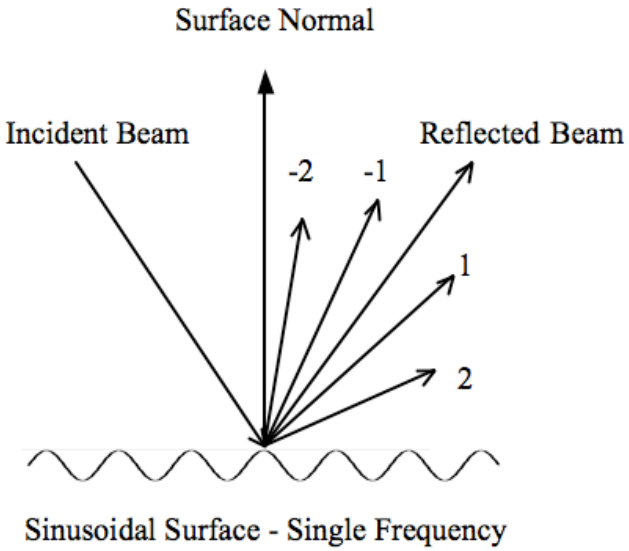

Figure 31. Diffraction pattern from a sinusoidal surface.

The diffraction patterns created by each sinusoid are then summed to form the diffraction pattern created by the surface. The sinusoidal grating diffraction equation (Equation 5) predicts that scatter angles for different orders will differ with light wavelength so white light, which contains all wavelengths between ultra-violet (λ =390 nm) to near infrared (λ =780), will yield a different pattern for each wavelength prescribed. This is the diffraction effect that can separate white light into the colors of a rainbow. Table 2 gives examples of the diffraction angles found from four wavelengths spread over the white light spectrum with $\theta_i = 0^o$ (parallel to surface normal) and f = 0.3 μm^{-1} (3.33 μm wavelength) for the first four diffraction modes. The relationship between light wavelength and scatter-mode angle is linear so, for a given angle of incidence, the difference in angular spacing between two wavelengths is proportional to the ratio of the two wavelengths. This can be seen in Table 2 where the first mode of λ = 780 nm light is reflected at an angle equal to the second mode of λ = 380 nm light (790:380 = 2:1) so for every mode of 780 nm light, there will be two modes of 380 nm light. As the surface spatial frequency increases, the angle of each diffraction order increases until they become larger than 90º, at which point they diffract into the sample and contribute to absorption. Also, the spot diameter of the incident beam must be larger than the spatial wavelength (1/f).

Table 2. Angles of Diffraction for the first four diffraction orders and four wavelengths of light over visible spectrum. Incident light is parallel with the surface normal ($\theta_i = 0^o$) and the surface spatial frequency is 0.3 1/μm (or 3.33 μm sinusoid wavelength).

Diffraction Order	1	2	3	4
Light Wavelength (μm)	Angle of Diffraction Order from Surface Normal (°)			
0.78	14	28	45	69
0.6328	11	22	35	49
0.5	9	17	27	37
0.38	7	13	20	27

Finally, Figure 32 shows the scatter pattern found on a diamond turned surface which is a combination of 32c, d and e.

3.5.2 CROSS FEED DITHER MODEL

With the knowledge that an actual diamond turned surface has residual cusps left by a round-nose tool, some spatial frequency content that represents the cusp spacing and a lower limit of finish quality as discussed in the vibration section; a model was created to reduce the discrete scatter points to a continuous pattern of mild points by randomizing the spacing of the residual grooves. Assuming that the tool edge radius was sharp and the edge quality was perfect, the random one-dimensional contribution in Figure 32d was introduced by machine vibration and could be optimized by manipulating the cross feed spacing of the cusps.

The Z-axis vibration model was expanded to accommodate varying the movement of the tool in the X-direction (cross feed). The spacing of each cross feed was moved from its evenly spaced X-coordinate in a positive or negative direction. Figure 33 shows the center of each cross feed with a crosshair and resultant surface trace without the effects of Z-axis vibration. While the height of each apex is at zero, the cross feed is no longer periodic and the residual cusps are no longer uniform heights and widths. The assumptions in this model were the same as with the vibration model: ideal cusps created with a sharp tool and a homogenous material compatible for diamond turning.

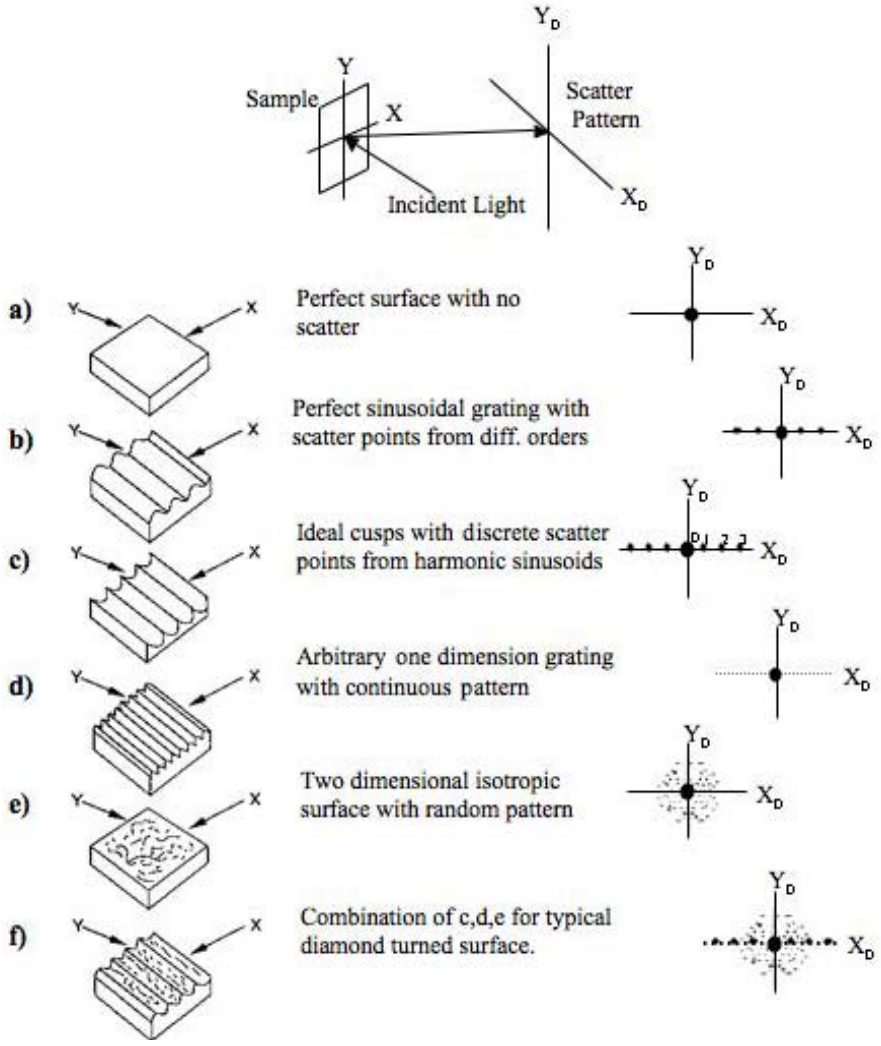

Figure 32. Scatter patterns for various surface profiles.

Figure 33 also demonstrates that any change from perfectly spaced cups when using a round nose tool will increase the theoretical surface roughness; the theoretical PV without dither is 5.5 nm and RMS is 1.6 nm compared to the 10 nm PV and the 2.4 nm RMS in the figure. Realizing that change from evenly spaced cusps increases roughness, the dithering amplitude must be selected so the cross-feed cusp spacing is only changed enough to randomize periodicity. A Gaussian distribution was selected for generating the cross-feed variations. Several standard deviations (σ) and cross-feed rates were modeled. Standard deviation was calculated using +/- 3σ distributions with a spreads equal to half, once, and twice the cross feed rate. Because cross-feed dithering has a negative effect on surface finish, dithering rates were kept low enough that individual grooves show little variation in the up-feed direction for surface profile of typical length and width. A 3D profile with dithering and machine vibration is shown in Figure 34.

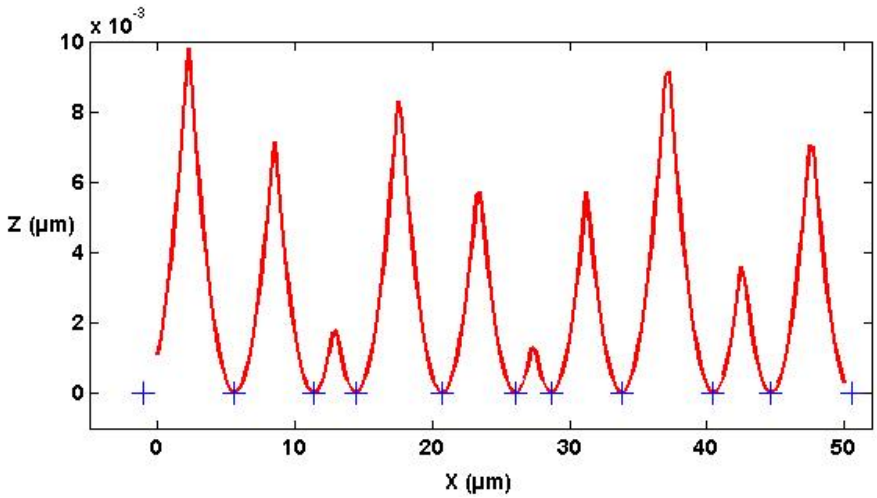

Figure 33. Example of dither concept (without machine vibration disturbing the cusps in the Z-direction) showing apex of tool (+) moved from regularly spaced intervals (cross-feed) and resultant contour of circular cusps. A 570 µm nose radius tool was used with a 5 µm/rev cross feed. PV = 10 nm and RMS = 2.4 nm.

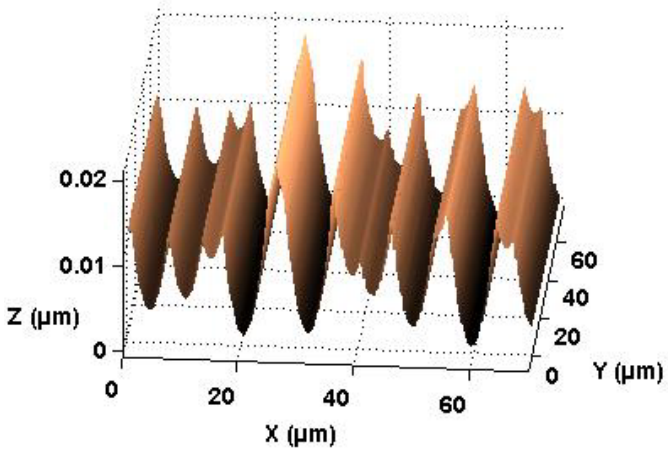

Figure 34. Sample 3D surface profile with cross feed dithering (motion along the X-axis) and Z-axis machine vibration.

3.5.3 Analytical Model Analysis

To evaluate the spatial repetitiveness of the surface, the autocovariance function [8] was applied to each trace generated by the model. It was selected because it is an excellent indicator of repetitive features in the surface. PSD was not used because the harmonics of diamond turned cusps will always show up as peaks in the PSD plot.

The autocovariance function (G(z)) is the product of two copies of the same surface contour as one is shifted (lag length) relative to the other. The formula for autocovariance is found in this equation:

$$G(l) = \frac{1}{N}\sum_{i=1}^{N-l} z_i \cdot z_{i+1} \qquad l = 0, 1, 2, \ldots N\text{-}1 \tag{6}$$

where l is the integer corresponding to lag length, N is the total number of data points in the data set, and z is a point in the data set. It has units of height squared and the first point (G(0)), where the lag length equals zero, is the square of RMS roughness. Lag increments are equal to the spacing between data points or samples. It is important that the profile be quantized with at a constant sample rate. A highly positive value of G(z) at a certain lag length will indicate that the surface has correlating features for that length. Also, the mean of the surface must be zero for the first point in the autocovariance (G(0)) to equal the square of RMS roughness.

A surface with ideal cusp spacing (Figure 35) and uniform height will then alternate between positive (peak aligned to peak) and negative (peak aligned to trough) when evaluated with the autocovariance function as seen in Figure 36. For reference, a perfectly flat surface will result in a straight line along with G(z) = 0. Also, a random surface (isotropic with a Gaussian distribution) will start at G(z) = RMS^2, decay immediately to G(z) = 0, and randomly oscillate about G(z) = 0 through the remaining lag length.

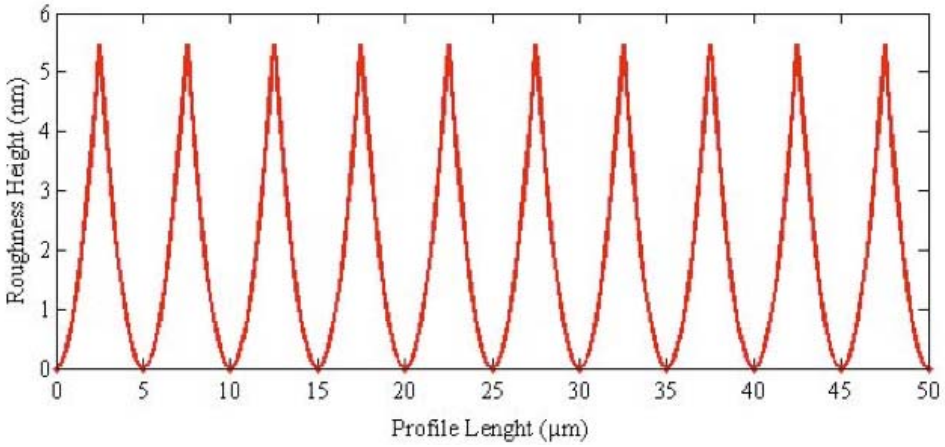

Figure 35. Surface Profile for autocovariance seen in Figure 36.
f = 5 µm/rev and R = 570 µm.

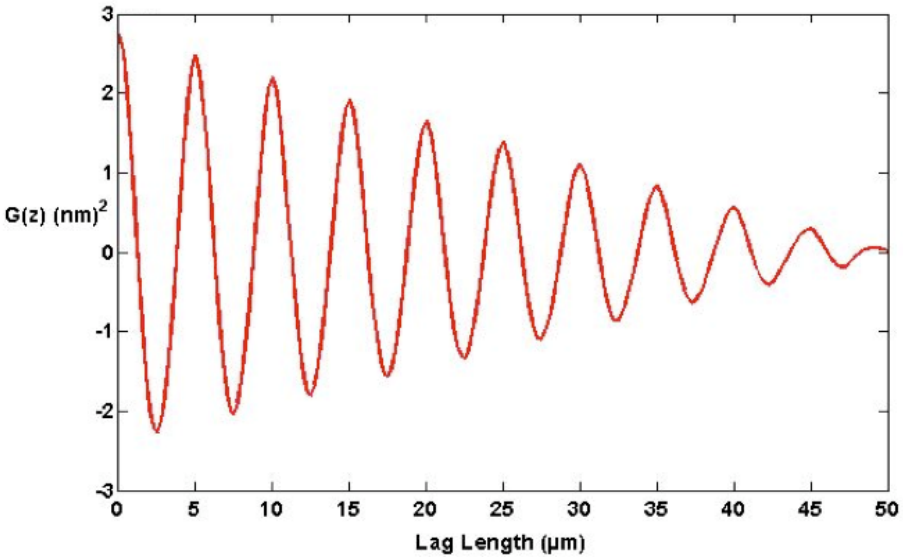

Figure 36. Autocovariance of theoretical profile in Figure 35 where f =5 μm/rev, R = 570 μm, PV =5.5 nm, RMS = 1.6 nm, G(0) = RMS^2 = 2.56 nm^2.

3.6 CONCLUSIONS

Understanding surface finish in diamond turning is pivotal in properly applying diamond turning. New insights into finish aspects of the diamond turning process can lead to improvements and further implementation in new areas. Traditional rules of thumb such as the parabolic approximation work well until low federates are encountered. With the inclusion of the effects of vibration on diamond turning, more efficient federates can be chosen to achieve a desired surface finish. Interestingly enough, until material limitations become important, the influence of vibration when coupled with tool geometry produces better results than one would intuitively expect. Finally, intentionally induced vibrations parallel to the surface appear to reduce the coherence of the groove spacing on surfaces, though this gain appears to be more than offset by an associated worsening of the RMS surface finish. Further experimentation may reveal qualitative advantages for visible optics, but the currently available quantitative results show that the technique provides no real gain.

REFERENCES

1. Drescher, J.D., *Tool Force, Tool Edge, and Surface Finish Relationships in Diamond Turning*. Ph.D. Thesis, North Carolina State University, (1991).
2. Arcona, C., *Tool Force, Chip Formation, and Surface Finish in Diamond Turning*. PhD Thesis, North Carolina State University, (1996).
3. Moriwaki, T., Okuda, K., *Machinability of Copper in Ultra-Precision Micro Diamond Cutting*. Annual of the CIRP, Vol. 38, No. 1, 115-118, (1989).

4. Drescher, J. and Dow, T., *Tool Force and Surface Finish Aspects in Diamond Turning of Ductile Metals*. Precision Engineer Center 1991 Annual Report, 9, 109-138, (1991).
5. Thrane, N., Wismer, J., Konstantin-Hanson, H., and Gade, S., *Practical use of the "Hilbert transform"*. Brüel & Kjær, Denmark, http://www.bksv.com/pdf/Bo0437.pdf.
6. Schaefer, J.P., *Progress in Precision – Single Point Diamond Turning (SPDT) of Optical Components*. Presented at ASPE 2002 Spring Topical Meeting on Progress in Precision, (2002).
7. Stover, J.C., *Optical Scattering : Measurement and Analysis*. McGraw-Hill, Inc., New York, New York, (1990).

4 FAST LONG RANGE ACTUATOR - *FLORA*

Qunyi Chen
Graduate Student
Thomas Dow, Gregory Buckner
Kenneth Garrard, Karl Falter, David Youden, and Alex Sohn
Faculty, Staff and Consultants, PEC

The goal of this project is to develop a Fast Long Range Actuator (FLORA) to produce optical quality freeform surfaces. The target range of motion of ±2 mm at 20 Hz creates a challenging problem and will require innovation in design, fabrication and control. This report discusses the performance of the first prototype – FLORA I – built in conjunction with Precitech on a small-business grant funded by NASA and the extension of that prototype to FLORA II over the past year. These designs use a 50 mm stroke linear motor, air bearing supported lightweight triangular piston and a glass-scale linear encoder. Changes to the encoder, amplifier and controller and the resulting improvements in performance are reported. Both simulations and experimental results are presented to evaluate the performance of the existing design and determine the direction for a new system design. Significant improvements in following error (value) and disturbance rejection (value) have resulted in the changes incorporated in FLORA II. In addition, more general design philosophies for this application are discussed including the effect of moving mass, motor power, sampling rate and physical damping.

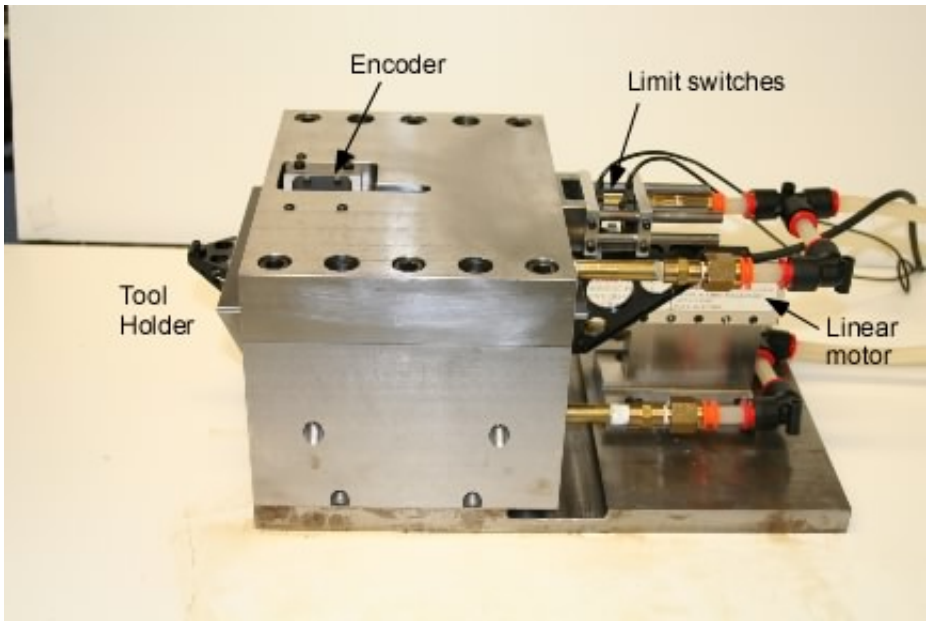

4.1 INTRODUCTION

Diamond turning (DT) has revolutionized the fabrication of optical surfaces for consumer, defense and science applications such as contact lenses, forward-looking infrared radar and infrared spectrometers. It has made this impact not only because it can accurately and rapidly fabricate diffractive, refractive and reflective optical surfaces, but also because it can create reference features tied to the optical surfaces to assist in the assembly process.

The original application of DT in the 70s was spherical shells but it rapidly expanded to other applications such as flat aluminum substrates for magnetic hard disks, hard contact lenses and eyeglasses. In the early 80s, the idea of making Non-Rotationally Symmetric (NRS) surfaces was proposed and the piezoelectric Fast Tool Servo (FTS) was born [1]. This was initially designed to correct spindle errors on the but was quickly expanded to produce biconic contact lenses for correcting astigmatism and zone plates for optical applications [2].

The problem with piezoelectric servos is their lack of stroke. A stack of piezoelectric (PZT) disks produces a strain of 0.1% or 1 μm per mm of length. The PEC made a system for Oak Ridge in the mid-80s with a 100 mm hollow stack that had 100 μm of range – called the MAC 100 [3 patent]. Shortly thereafter, systems that used mechanical and hydraulic amplification of the PZT motion were developed. Kinetic Ceramics produced the Variform with 400 μm of stroke using a lever amplifier and a flexure-based tool holder. They also produced a longer range version (Varimax) with 600 μm stroke. These commercial units are marketed for the contact lens industry by Sterling UltraPrecision in Tampa FL.

One outcome of the stroke limitation of tool servos was the development of decomposition algorithms by the PEC and others [4-6]. In this case, the surface shape is divided into rotationally and non-rotationally symmetric components. The axis of the DT machine are used to create the spheric or aspheric component and the FTS is used to add the NRS component. Off-axis conic sections are often used in three mirror telescopes for defense applications and the decomposition technique can be used to create these NRS surfaces in the same time as the parent conic surface.

Another event that overcame the limitations of PZT servo was the adoption of linear motors for DT machine slide drives to replace ball screws. This change allowed more flexibility in the motion of the slide without damage to the ball screw. NRS surfaces can now be machined by coordinating the motion of all of the axes (including the spindle) using a process called slow slide servo machining. In this case, the spindle speed is reduced to the point where the heavy slides can follow the position commands. This leads to long fabrication times and the potential for thermal drift. Reducing the mass of the slide to improve its bandwidth is the aim of the LRS

but this makes it more susceptible to disturbances from controller noise, vibration and cutting force variations.

Other long range fast tool servos have been designed to increase the range of motion. The use of a linear motor and air-bearing slide as the basis for a fast tool servo was proposed by Spivey Douglas at Y12 in Oak Ridge in 1983 [7]. The application was to machine off-axis sections of parabolic mirrors on axis. More recently, voice coil driven long range servos have appeared on the market. One is marketed by Sterling UltraPrecision and built by John Hoogstrate and Nick Page in Keene, NH and the second was recently introduced by Moore Nanotech. Little technical information is available on the design or performance of these devices.

The goal of this project is to develop the mechanical design of a fast tool servo along with a control system that can be used to make high quality optical surfaces whose shape is not rotationally symmetric. This device will utilize new and existing technologies (air bearings, linear motors, high-resolution encoders and real-time control) to create a moving tool holder. The result will be a high-bandwidth, high-resolution, long-stroke machine that can reduce fabrication time and cost for freeform surfaces.

4.2 TECHNICAL CHALLENGES

The goal of the LRS is to create optical quality surfaces (RMS surface < 2 nm) while moving the tool over a range of ± 2 mm at a frequency of 20 Hz which creates a maximum acceleration of 32 m/s^2 (~3 Gs) and a maximum velocity of 250 mm/s. To achieve this goal, a number of technical challenges must be overcome.

Form Error Diamond turning machines can achieve excellent form fidelity because of their stiff, straight, slow linear slides and accurate air-bearing spindles. This process is ideally suited (and was developed) for rotationally symmetric surfaces such as spheres or rotationally-symmetric aspheres. Moving the slides of these machines to create NRS surfaces at typical spindle speeds would be well beyond the bandwidth limits of the large, heavy axes. The goal is to create a lightweight design that will reduce the machining time while retaining the form accuracy of current DTMs.

Surface Finish Simple theoretical relationships between machining parameters (spindle speed, axis velocity) and tool geometry can be used to predict surface finish; however, the actual surface will be degraded by tool imperfections (waviness, wear, damage) and workpiece material properties. For the dynamic conditions envisioned, machine vibrations and dynamic forces can exacerbate the problem and result in unacceptable surfaces.

Motion Planning and Control To reduce machining time, advanced algorithms must be developed to decompose the freeform surface geometry into the synchronized, motion

commands for fast and slow machine axes. A fast, robust control system must also be developed to implement these commands and create the desired shape.

Damping Mechanical damping (in addition to derivative control action) has been deemed a desirable property for a fast tool servo [8]. The amount needed and how it is added to the actuator design needs to be addressed.

Disturbances Internal and external disturbances can degrade the surface finish during machining. This noise may be mechanical or electrical and can originate inside or outside the system.

Counter-balance Force As the moving mass of the actuator grows in size, the inertial forces related to its motion and their effect on the DTM to which it is attached become more significant. The goal of this project is to address these technical challenges. The result will be an ultra-precision servo drive and control systems that can quickly create optical quality freeform surfaces.

4.3 DESIGN SPACE

The design of a long range servo for machining applications requires that it track the desired trajectory with little following error and reject disturbances from internal and external sources. To evaluate the influence of primary or critical variables in the design space, three variables were modeled and changed to see their influence on the performance of the servo.

4.3.1 MODEL PERFORMANCE

Tracking Error, ER One common test performed with a fast tool servo is to create a tilted flat. If done correctly, a flat surface will be created by driving the tool in a sine wave motion with amplitude growing as a linear function of the radius. One parameter for evaluating system performance is the tracking error; that is, the ability of the tool to follow the command with minimum amplitude attenuation and phase lag. The most extreme operating condition for the LRS is a 20 Hz sine wave with amplitude of 2 mm (4 mm PV).

Disturbance Rejection, ED During the machining operation, small changes in the depth of cut will change the force on the tool and introduce a disturbance to the positioning system. Vibration of the LRS structure can also create forces disturbances. Disturbance rejection is an important characteristic of a motion control system. Disturbances result not only from the cutting force variations but also from electrical noise in the controller and the amplifier. These disturbances result in poor surface finish. The disturbance of interest was defined as a sinusoidal cutting force disturbance with 0.025 N amplitude and a frequency of 54.849 Hz.

The computed tracking errors and disturbance amplitudes using an optimized PID feedback algorithm are given in Table 1. For each case, the optimized controller gains were selected by minimizing the following error using the sine wave profile. Using these gains, the simulated disturbance was introduced and the resulting amplitude at that frequency was calculated.

Table 1. Simulated control performance for different selections of physical parameters

Case	Motor Force, N	Mass, Kg	Sample Freq, KHz	Tracking, μm	Disturbance, nm
1	84	0.5	2.5	1.507	7.7
2	336	0.5	2.5	1.507	7.7
3	84	2	2.5	2.116	3.2
4	336	2	2.5	1.507	2.3
5	84	0.5	40	0.242	1.4
6	336	0.5	40	0.242	1.4
7	84	2	40	0.242	0.6
8	336	2	40	0.242	0.6
			Mean	0.950625	3.1125

The first two cases illustrate the influence of the motor force on the low mass system at low sampling frequency. In these cases, the power available from the small motor is sufficient to move the piston at the desired rate and additional power does not improve tracking error or disturbance rejection. Slow sampling rate reduces the gain for the control system and the position is more influenced by the disturbance. Cases 3 and 4 illustrate the change in the motor force at the large piston mass and slow feedback rate. The tracking error is larger for the smaller motor but the larger motor can provide enough force to improve the tracking error to that of the first 2 cases. However, the increased mass of the piston helps to reduce the effect of the disturbance. Cases 5 and 6 illustrate the improvement in both tracking performance and disturbance rejection if the sample time in increased from 2.5 KHz to 40 KHz. The previous experiments on the LRS used the slower feedback rate and the new system uses the faster rate. The tracking error is reduced by a factor of 6 and the disturbance position error is only about 20% of the slower system. The larger motor does not help the performance. The final two cases illustrate the faster cycle time combined with the larger mass. Here the tracking error is the same as the lighter mass but because of the increased inertia, the system is less influenced by the force disturbance.

The results of this simulation can also be viewed by fitting a curve to the data assuming a linear relationship between the tracking performance or disturbance rejection and the three variables: motor force, moving mass and sampling rate. The general expression is:

$$Response = Mean + K_1 * Motor\ Power + K_2 * Mass + K_3 * Sampling\ rate \quad (1)$$

The coefficients (K_1, K_2, $K3$) for the variables of each response (tracking performance and disturbance rejection) are given in Figure 1 for the experiments of Table 1. This plot illustrates the coefficients from Equation (1) as the parameters are changed from their low value to their high value. If the coefficient is negative, the response is reduced as the parameter goes from low to high. The sample rate has the biggest impact on both the tracking error and disturbance rejection. But the larger piston mass significantly reduces the effect of cutting disturbances while only having a minor effect on tracking error. The increased mass is counter to most design goals and will be investigated in future designs.

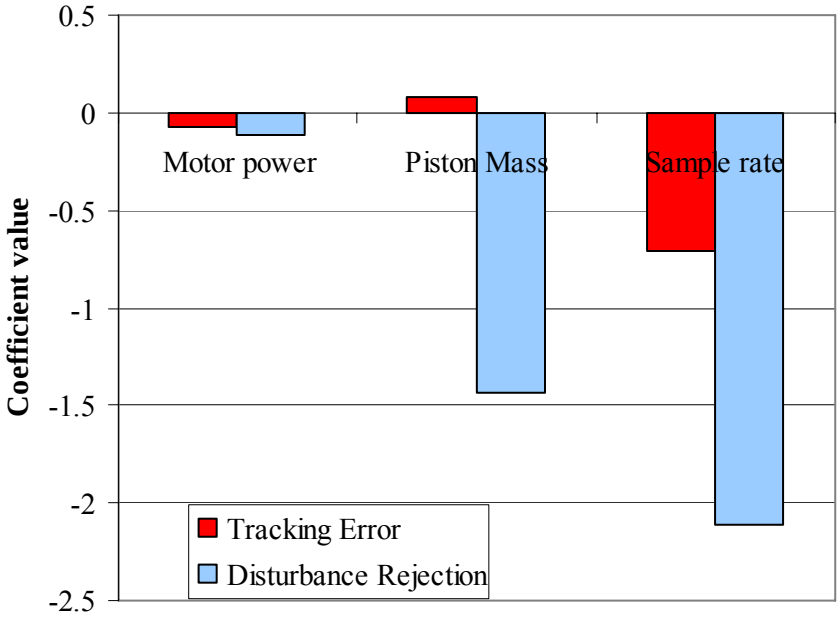

Figure 1. Coefficients for variable response in model of tool servo

4.3.2 DAMPING FOR SERVO SYSTEMS

One factor that was not included in this matrix is physical damping in the actuator. Controlling an undamped servo system using discrete-time algorithms can be complicated by several factors. Fixed sampling rates, bandwidth restrictions in the amplifier and actuator and computational issues limit the amount of damping that can be introduced in the control system. The resulting servo can exhibit oscillations, overshoot and reduced stability margins. Incorporating physical damping has been shown to improve the stability, robustness, and performance of lightly-damped servo systems. Determining the optimal damping level needed to realize the requisite bandwidth and surface finish will be investigated.

4.4 FLORA II

The first prototype servo was built during 2004 in a NASA supported small business collaborative project with Precitech. This system called *FLORA I*, shown in Figure 2, was used to machine flat and tilted flat specimens on plastic and metal substrates. The surface finish was 14 nm Ra for a plated copper flat and 20 nm Ra for a 1 mm amplitude, 5 Hz (300 rpm) tilted flat on an aluminum substrate. The form error for the flat surface was about 10 µm compared to the best fit flat surface. This new system, *FLORA II*, was built over the past year with a higher resolution encoder, a linear amplifier, and a dedicated, high-speed control computer. In addition, structural and control studies have been undertaken to evaluate the performance of the improved prototype.

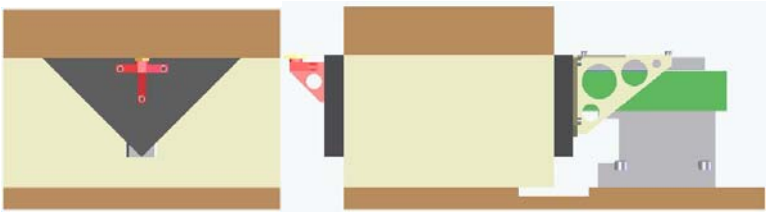

Figure 2. Front and side view drawings of the *FLORA II* and a photograph of the finished system

4.4.1 PISTON AND AIR BEARING

The aluminum honeycomb, triangular piston used for the first prototype with its air bearing were retained for the experiments described here. This piston was fabricated using sheets of aluminum honeycomb for each face and the first natural frequency was above 3500 Hz. The triangular cross-section is 140 mm wide and 70 mm high with a mass of 517 grams.

The piston is supported by a 90º v-block base assembly and a flat top as shown in Figure 2. The air bearing was designed by Precitech and incorporates innovations in both design and fabrication. The bearings in the base assembly were optimized for stiffness and damping in frequency range of the first dominant vibration mode (3400 Hz vertical and 1900 Hz tilt). Static stiffness measurements were made by loading the piston in the vertical direction (300 N/µm) and at one edge (0.2 Nm/µ rad).

4.4.2 LINEAR AMPLIFIER

The Pulsed Width Modulated (PWM) amplifier from the original prototype was replaced with a linear amplifier (Aerotech BL10-80A) to drive the linear motor. The rational was to reduce the high-frequency noise associated with a PWM and its influence on the control system. The linear amplifier provides sinusoidal motor commutation in a dual-phase command configuration. The dual-phase inputs (i.e., Phase A and B) are sinusoidal and are 120º out of phase from each other; the third phase (i.e., Phase C) is internally generated by the amplifier. By setting the amplifier's trans-conductance DC gain to 1, a 1 volt input signal for a phase would produce a 1 amp output in that phase.

Table 2 shows the actual and expected voltage on each phase of the WYE-connected motor with a static test using a 0.5 amp command. Notice that the actual voltages do not sum to zero as expected and that there is noise on each phase. In the control system, the output of Phase A and B can be biased to remove these offset values. However, only two analog outputs are used and therefore the output bias in Phase C cannot be removed directly. Future control systems will have additional analog outputs to address this problem.

Table 2. Amplifier phase output voltage and errors for 0.5 amp command

	Theoretical value (Volt DC)	**Measured value** (Volt)	
		Average	P-P Noise
Phase A	0	-0.0015	0.1086
Phase B	3.8105	3.8090	0.3320
Phase C	-3.8105	-3.6641	0.6955
Sum	0.0	0.1434	

Frequency analysis of the noise is shown in Figure 3. Each phase reveals 60 Hz noise along with its odd harmonics. Additional shielding and a three-phase command configuration will be implemented with a new PMDi based control system platform to remove output signal bias and reduce the noise level.

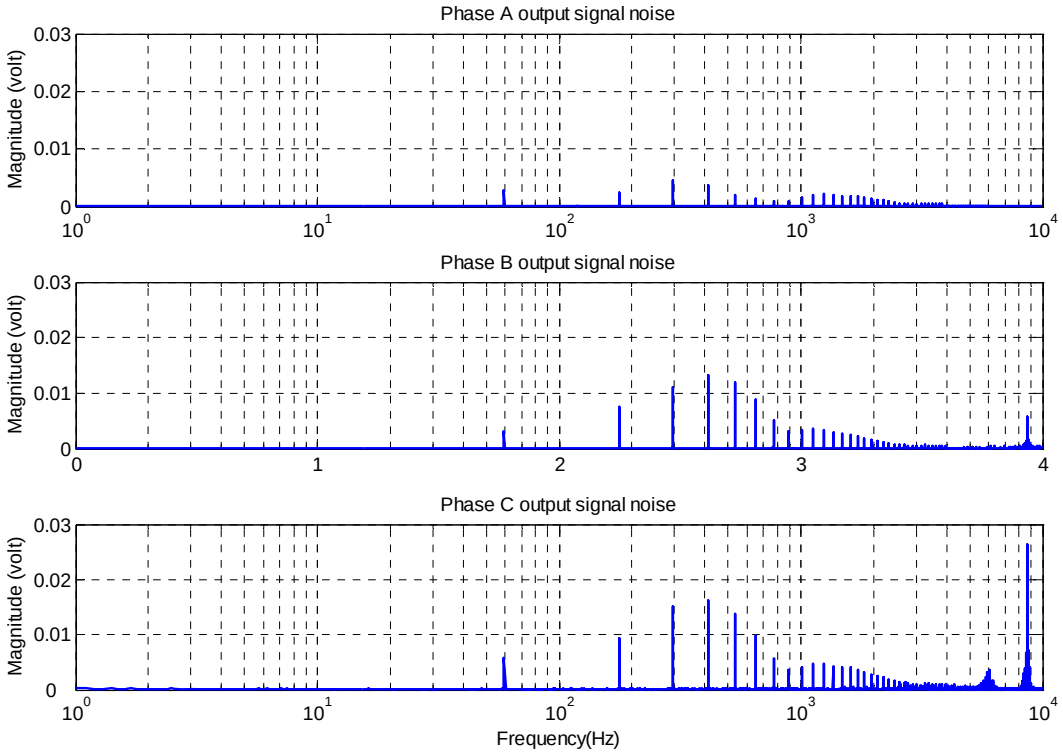

Figure 3. Frequency analysis of noise in amplifier output voltage

4.4.3 LINEAR MOTOR

The same brushless three-phase linear motor chosen for its fast response and smooth motion characteristics was retained. Table 3 lists the electrical characteristics for the motor (Airex P12-1). The aircore forcer design eliminates cogging and magnetic attraction. However, even with sinusoidal commutation, the force delivered by the motor may not be perfectly smooth due to variations in the magnets, mismatch between coil pitch and non-uniformity in air gap along the range of travel. A three-phase command configuration will minimize the impact of these factors and will be added in the future.

Table 3. Airex P12-1 linear motor specifications

	Resistance R (Ohms)	**Inductance** L (mH)	**Force constant** K_f (N/amp)	**Back EMF constant** K_e (V/m/s)	**Peak current** I_p (Amp)
Per coil	8.7	1.9	8.4	8.4	10.06

The effective motor constant (ratio between the controller current command and the motor force output) for the motor/linear amplifier in Wye connection is 12.6 N/A and the peak current is 5.81

A. The amplifier has a built-in PI controller to regulate the current loop. Equation (2) is the transfer function supplied by Aerotech between the commanding current to the resulting current on a per phase basis (Phase A and Phase B only) resulting from the block diagram in Figure 4. L refers to the line-to-neutral inductance, 1.9 mH; R refers to the line-to-neutral resistance, 8.7 Ohms; m refers the moving mass, 0.665 Kg; B refers to the damping; K_f refers to the motor force constant in WYE connection and K_e is the back emf.

$$G_I = \left[\frac{6.622}{L}\right] * \frac{s + 15151.52}{s^2 + s\left[\frac{0.0033\times10^{-6} * R + 2.193\times10^{-8}}{0.0033\times10^{-6} * L}\right] + \frac{100666.67}{L}} \tag{2}$$

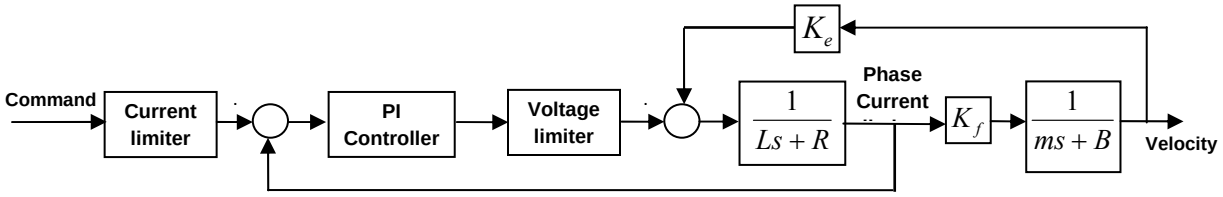

Figure 4. Block diagram of the system current control loop

Figure 5 is the bode plot of Equation (1). Due to the current loop PI controller gain settings, the magnitude starts to rise above 0 dB at 100 Hz, peaks around 800 Hz, and drops to -3 dB at 1543 Hz. The current control loop introduces a maximum of 102º phase lag at 3000 Hz where the output is 20% of input.

4.4.4 LINEAR ENCODER

To improve the position measurement accuracy, a glass scale Heidenhain encoder (LIP 401R) replaced the Renishaw metal scale encoder from the original prototype. This Heidenhain encoder has 2 μm signal period. After signal interpolation, it has 5 nm resolution and its noise level remains within 5 nm and the maximum speed is 20 mm/sec. At the 20 KHz sampling rate for the control system, the velocity estimation resolution is 0.1 mm/sec. The calibration chart provided by Heidenhain indicated the LIP 401R has measurement error due to the glass scale grating error. This uncertainty can be taken as an accumulated measurement error in a slope of 6nm per 1mm measurement length with respect to the encoder index point.

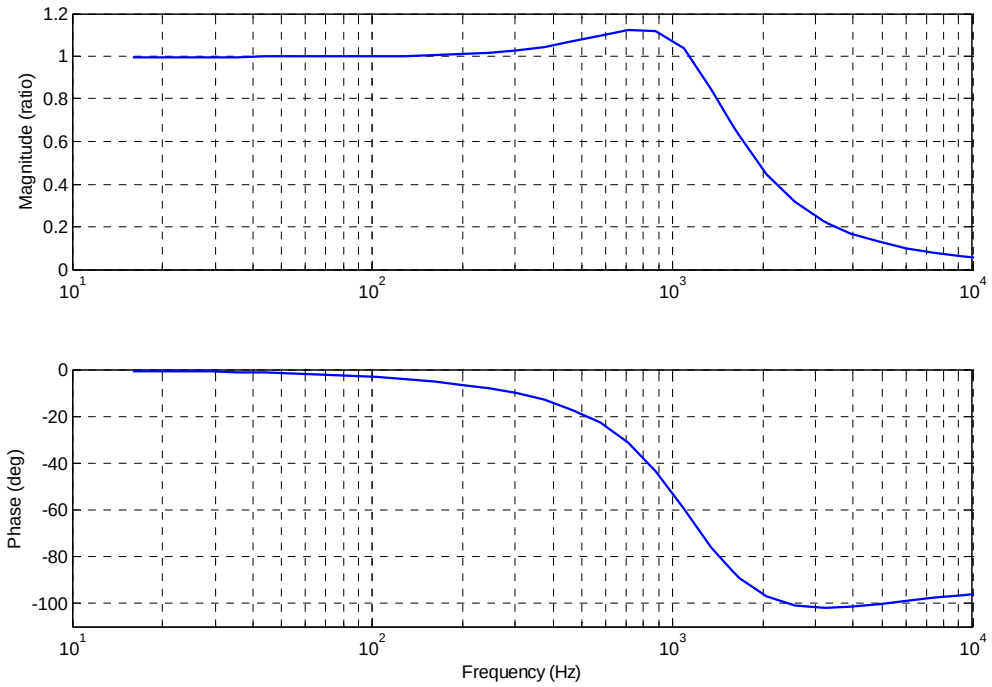

Figure 5. Transfer function between commanded current and the current on each phase of motor.

In addition to the encoder quantization error and the scale grating error, there is interpolation periodic position error occurring within one signal period of the encoder's output signals. This interpolation error is caused by encoder signal quality and is typically 1% to 2% of the signal period. Figure 6 shows the XY representation of two sinusoidal encoder signals with 90º phase shift on an oscilloscope. Ideal output signals appear as a circle. The size of the circle, which

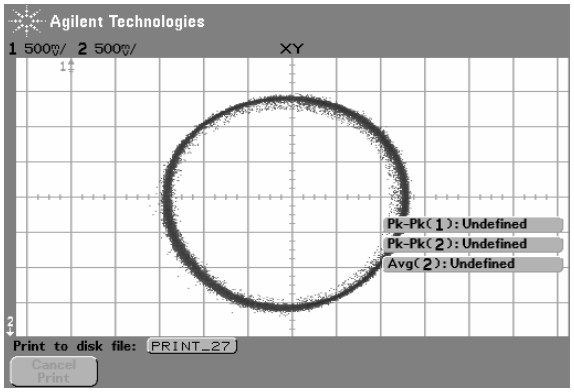

Figure 6. Oscilloscope XY representation of two encoder sinusoidal signals

corresponds to the amplitude of output signals, can vary within certain limits without influencing the measuring accuracy. However, any deviations in the circular form caused by position error within one signal period will go directly into the result of the measurement. Non-perfect mounting alignment between the encoder scanning head and the glass scale, and insufficient signals conditioning can lead to the signals deviating from the ideal sinusoidal shape as shown in Figure 7.

A comparison of position measurement by the encoder and a capacitance gage (LION, C2-B) in Figure 7 clearly shows the existence of this periodic spatial error in the encoder measurement. The vertical axis in Figure 7 is the difference between the encoder and the cap gage measurement. The dots are the original measurement difference; the thick line is the trend line. The P-P amplitude of the error is about 40 nm with a period of 1 μm.

High-resolution, interferometric encoders are sensitive to external disturbances. As a result, the 5 VDC power supply source for the sensor and the interpolation electronics must be clean and stable. Shielding and grounding practices recommended in the specification and manual must be followed and the encoder housing, the cables, the interpolation cards/box and control card must have the same ground potential.

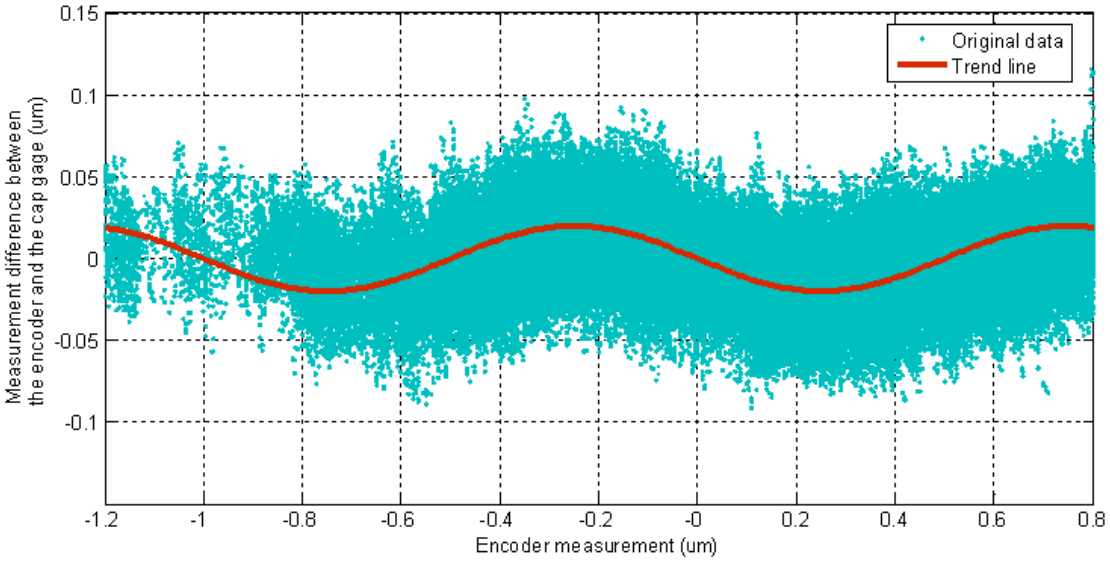

Figure 7. Encoder periodic spatial errors in the position measurement

4.4.5 REAL-TIME CONTROL SYSTEM IMPLEMENTATION

The DeltaTau UMAC controller used for the *FLORA I* system has been replaced with a MATLAB xPC Target development environment in *FLORA II*. The DeltaTau controller was limited to 2500 Hz sampling time. In the xPC Target environment, a desktop PC is used as the

host running MATLAB, Simulink, Stateflow and Real Time Workshop to create and simulate a control algorithm via Simulink block diagrams. Once the simulation is complete and the results are acceptable, executable code is created and downloaded to a second "target" PC running the xPC Target real-time kernel. After downloading, the target application can be run in a stand-alone, real-time mode. The xPC Target control development and rapid prototyping system integrate the entire development cycle into a single environment so simulations and experiments can be run and rerun. However, this flexibility has its cost – overhead time. Measurements of the cycle time for a simple test with one analog input and one analog output revealed a 20 μs overhead task execution time. This time stayed constant as more complicated computational tasks were added so that for a typical control algorithm, the total execution time may be on the order of 30 μs resulting in a maximum sample frequency of 33 KHz. In the coming year, the control system will be switched to a PMDi platform.

4.5 OPEN LOOP SYSTEM PERFORMANCE

In open loop motion control, the position of the piston is dependent only on current commands to the amplifier, not on position measurements. The values of the Phase A and B commands must always be 120º apart. These commands are physically converted into low power voltage signals through Phase A and B DAC outputs at a rate of 20 KHz and applied to the amplifier. There are two modes for open loop operation: non-commutated and commutated.

4.5.1 NON-COMMUTATED OPEN LOOP OPERATION

In this mode, the piston is forced (or driven) by the motor with no position feedback. This mode allows the functionality of the encoder, amplifier, motor and controller dual DAC outputs to be verified and the commutation parameters determined.

Distance of a commutation cycle The travel distance of the piston in one commutation cycle of the linear motor is measured by applying voltages at phase values ranging from 0º to 360º at a small constant current command (i.e., 0.5 A). The measured value for one cycle is 30.5 mm or about half the range of motion of the motor.

Zero phase detent position Zero phase detent position is one of the many locations where an electro-magnetic field of a permanent magnet and the motor coil are aligned. By applying zero phase command (0 to Phase A and 120º to Phase B) at small current command (i.e., 0.5), the piston will finally settle at the position -10.731 mm from the encoder reference mark. This position measurement provides an offset value to obtain the relative piston displacement $x(t)$ with respect to the zero phase detent position. Motor phase $\varphi(t)$ is generated at any time instant for commutation purpose as shown by Equation (3).

$$\varphi(t) = \frac{x(t)}{30.5} * 2\pi \tag{3}$$

Figure 8 shows the change of the motor actuation force (F_{OL1}) around the detent position governed by Equation (4) where K_f is the motor force constant in WYE connection, I is the amplitude of applied current command, K_f=12.6 N/amp and I = 0.5 amp

$$F_{OL1} = -K_f \cdot I \cdot \sin(\varphi(t)) \tag{4}$$

When the piston is in close proximity to the detent position, it oscillates like linear spring. Incorporating physical damping into the system will help it to settle to the detent position .

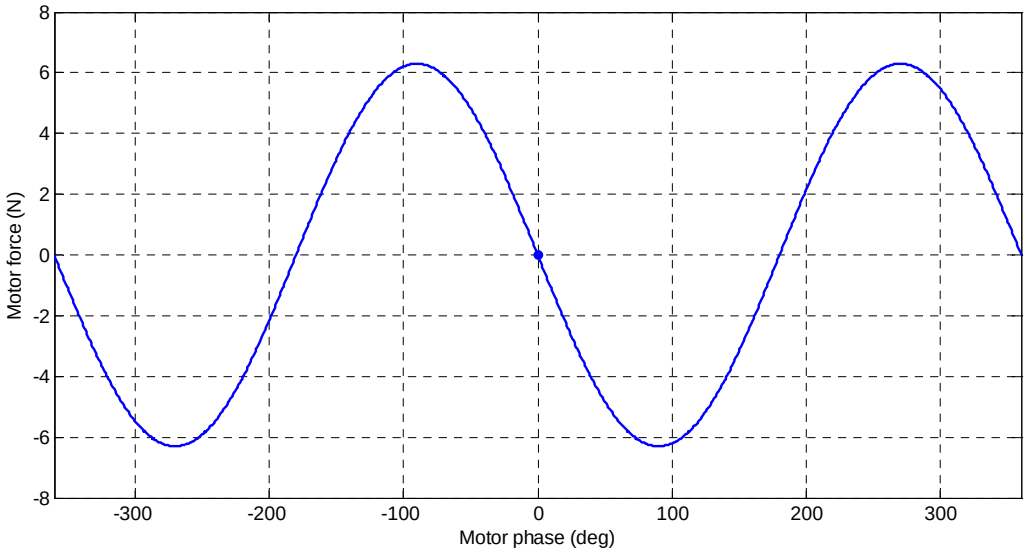

Figure 8. Variation of motor actuation force in non-commutated operation

4.5.2 COMMUTATED OPEN LOOP OPERATION

Software based sinusoidal commutation uses feedback position data from the encoder to update the phase command at 20 KHz with the measured motor phase $\varphi(t)$. Furthermore, the commutation angle is offset by an additional 90º so that the magnetic vector of the permanent magnet remains 90º phase ahead of the magnetic vector of the coil. As a result, the motor force output is maximized during the commutated operation. A test of open loop system dynamics in commutated operation would include all the system components at shown in Figure 9.

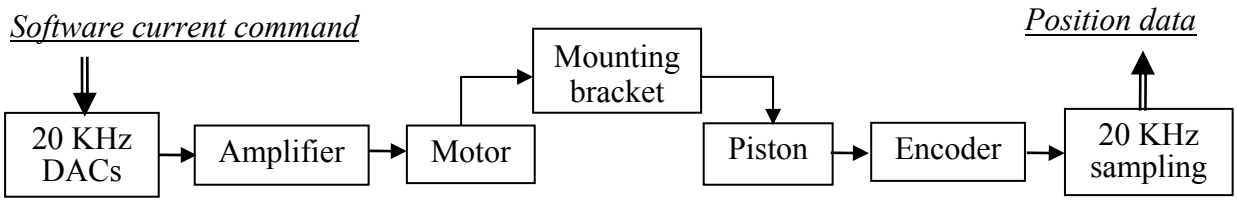

Figure 9. Schematic system flow diagram for open loop operation

Excitation command procedure Since the piston has nothing but inertia to hold it in position, the excitation command for the open loop tests must be carefully selected to keep the piston from hitting the end of travel. The following procedures were developed.

- Use a cosine current command to avoid drift of the driven mass. The applied force and acceleration is a negative cosine wave and position response is a sine wave.
- Switch the cosine current command to new frequency at its peak value; that is, when the piston is stationary. This creates a smooth transition between different frequencies.
- Start the test sequence at low frequency so that the current commanding sequence increases from zero for smooth operation.
- Select command amplitudes I and frequencies ω based on the Equation (5) to make the position response amplitude A remain at the same level.

$$A = \frac{K_f I}{m\omega^2} \tag{5}$$

- Command amplitudes I and frequencies ω are limited by the continuous peak current requirement of the motor, 2.6 amp; the speed shall be smaller than 20 mm/sec due to the frequency limit of the encoder interpolator. For noise reasons, the command amplitude I should be larger than 0.001 amp.

Figure 10 shows the selection of test points (in dots) in three test groups. Corresponding current command amplitude will be calculated from Equation (5) to obtain 0.02mm position response amplitude for Group 1, 0.001mm for Group 2, and 0.0001mm for Group 3. The arrows in the Figure 11 indicate the frequency increasing sequence in the execution. Figure 11(A) shows the increasing current command to keep 0.02mm position response amplitude for test Group 1. Figure 11(B&C) are expanded views of the command and the response. The 8 Hz excitation signal starts at 59.90845 second and the time duration for each frequency is 2 seconds.

Test method The testing code is developed with Simulink block diagram in MATLAB xPC Target real time environment. Additional measures are taken to achieve smooth position response during the test:

- The applied current command is set as zero before and after the excitation command sequence.
- The motor is operated in commutated mode even before the excitation signal is activated.
- The driven mass is loosely held in place by a rubber band.

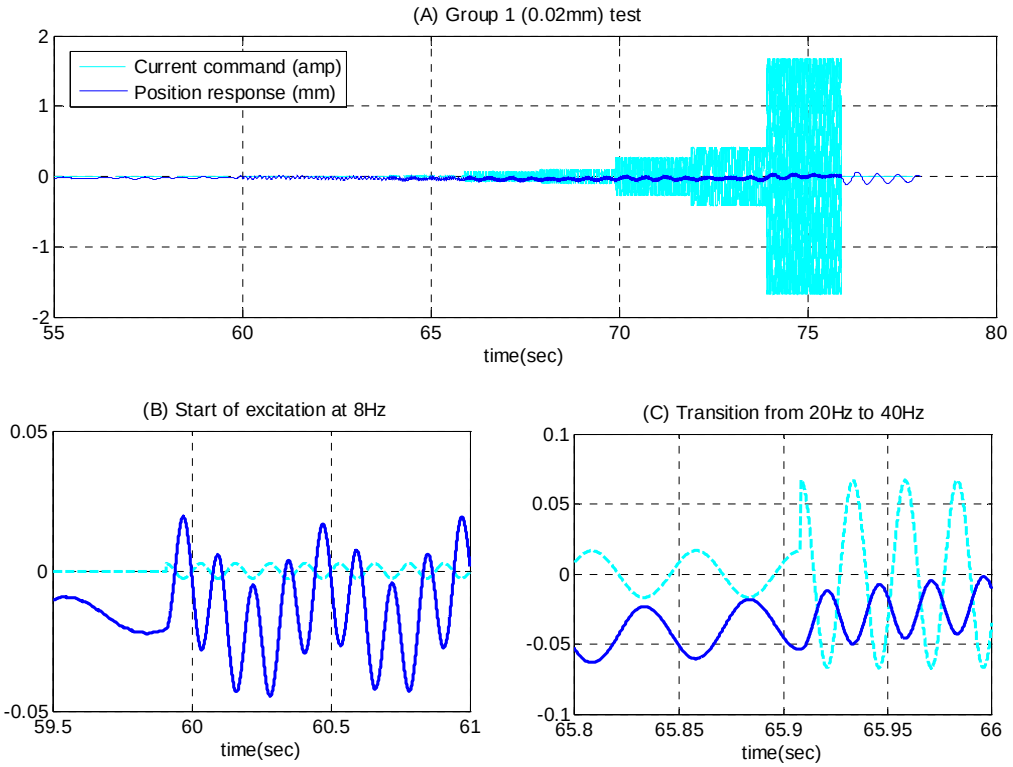

Figure 10. Open loop frequency response test points selection

Data processing The application of systematic techniques to process the raw data is critical to generating valid open loop frequency response plots. The following process was developed:
Apply a high pass filter to remove the low frequency position oscillation, for example, the 2 Hz natural frequency introduced by the rubber band used to hold the piston near center.

- Locate the time instant when the excitation command at a frequency is applied, take the response position data from that time instant. There is totally 40000 data points for each frequency level (2 seconds in 20 KHz sampling rate).
- Apply FFT of the 40000 data points to obtain magnitude and phase information at each excitation frequency level.
- Compare response with equivalent position commands: 0.02 mm position response amplitude for test Group 1, 0.001 mm for Group 2, and 0.0001 mm for Group 3, 180º phase for all three groups. Take average values at the overlapping test points, the magnitude (in ratio) and phase frequency response to obtain as shown in Figure 12.

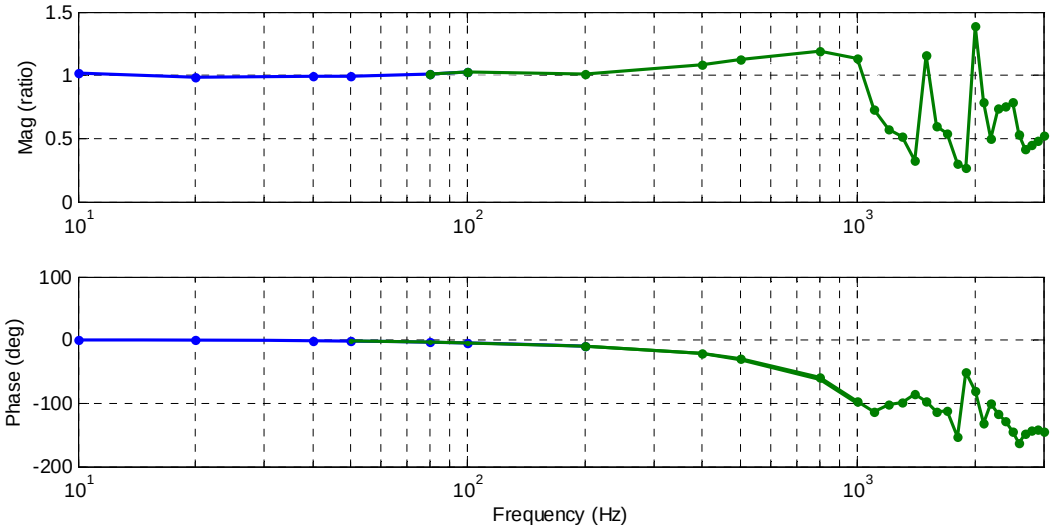

Figure 11. Open loop responses to sinusoidal excitation with increasing frequency and amplitude

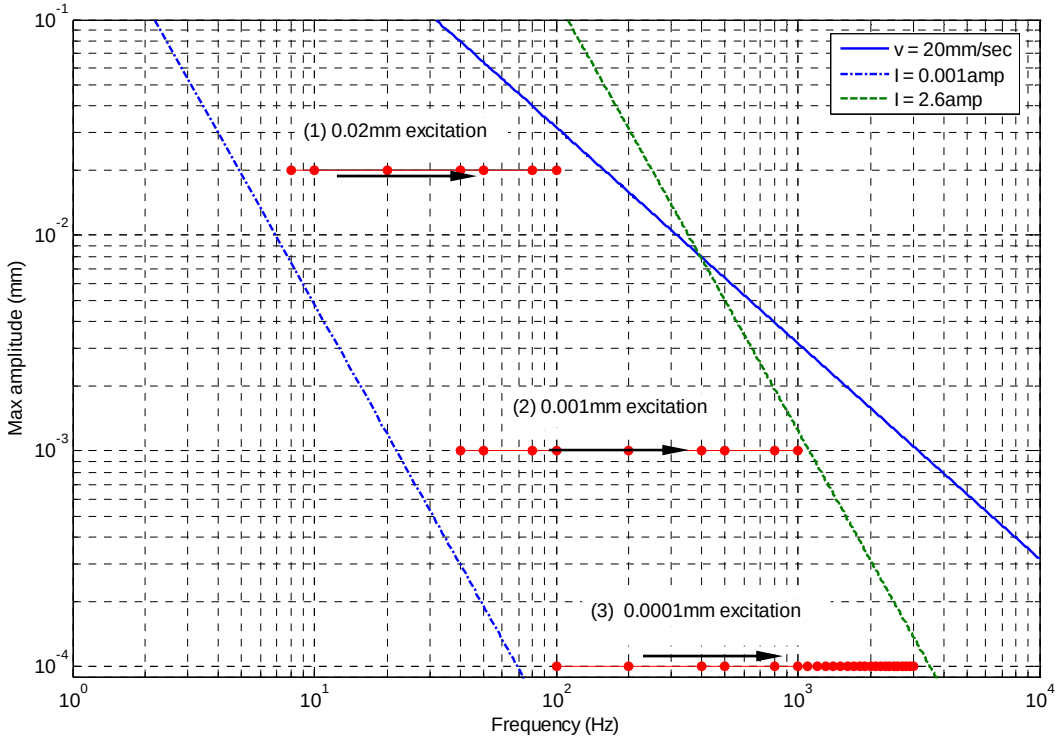

Figure 12. Commutated open loop system frequency responses

Discussion of Open Loop Results By combining the test results from three groups of tests, the commutated open loop frequency response is obtained in Figure 12. The magnitude response stays around 1 below 100 Hz and rises to a peak about 1.2 (ratio) at 800 Hz, and then has a sharp drop from 1000 Hz to 1400 Hz. After that, there are two more major peaks at 1500 Hz and 2000

Hz, and a minor peak from 2300~2500 Hz. The phase response stays around 0º below 50 Hz, and has a smooth curve down from 50 Hz to 1100 Hz. The phase response at higher frequencies rises and drops in an irregular shape. Based on the transfer function of the amplifier in Figure 4, the first peak around 800Hz can be traced back to the current loop dynamics. Appropriate current loop PI control may make the open loop system achieve unity gain over a large range of frequencies. The cause of additional peaks at higher frequency remains unknown.

4.6 MODEL FOR CONTROL SYSTEM

4.6.1 SYSTEM MODEL

The single DOF system shown in Figure 13 consists of an undamped mass m, a force disturbance $F_d(t)$ (representing cutting forces at the tool/workpiece interface), and displacement feedback $Z(t)$. The piston position is controlled by manipulating voltage $V(t)$ to a linear actuator, providing the actuation force $F_a(t)$, in response to a position error between the commanded position $Z_{ref}(t)$ and the feedback $Z(t)$.

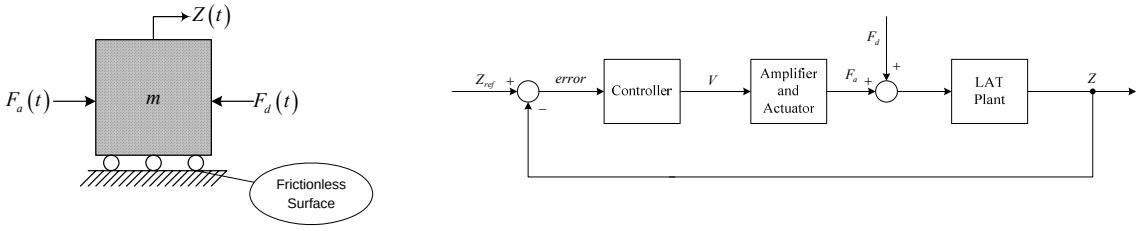

Figure 13. Model of LRS dynamics, with feedback control diagram

Baseline simulations of the LRS motion discussed earlier in this report described the impact of physical parameters (piston mass and motor force) and control system design (algorithm and update time), under the assumption that all hardware within LRS does not generate any internal noise, errors or disturbance. In addition, all high-frequency amplifier and motor dynamics are ignored, only motor force constant and current limit were considered in the simulations.

Simulations and Motion Control Strategy The *FLORA* hardware has deficiencies which introduce position errors in addition to those resulting from external cutting force disturbances. It is important to trace internal source of noise, errors and disturbance (other than vibrations) that can introduce nanometer level position errors. Figure 14 provides a more comprehensive representation of the system. The major components of physical dynamics are the linear motor (Airex P12-1), the power amplifier (Aerotech BL10-80A) and the encoder (Heidenhain LIP401R). Further simulations are conducted by incorporating various errors and noise

identified in previous sections; explicit three-phase sinusoidal commutation process is also modeled.

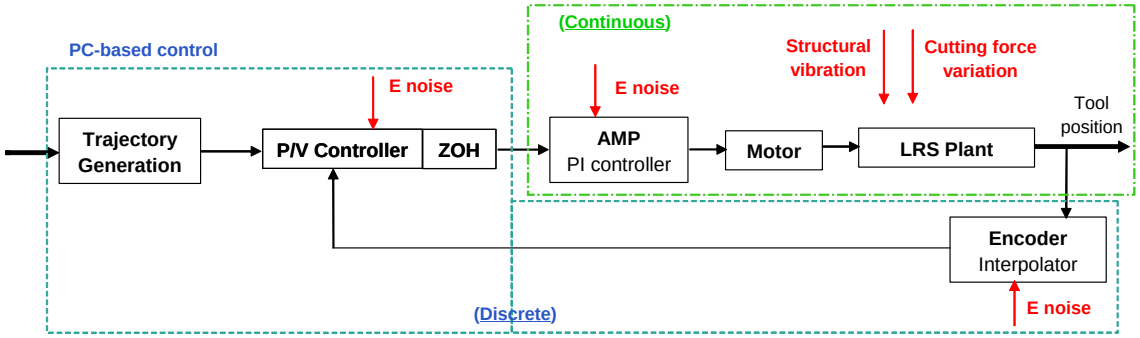

Figure 14. Representation of LRS motion axis

4.6.2 CONTROL SYSTEM PERFORMANCE CRITERIA

The functional requirement for the LRS is to track a commanded trajectory while confronted by disturbances, measurement noise, plant uncertainty, actuator saturation and bandwidth limitations. From the motion system response, the control performance can be assessed based on stiffness, sensitivity, responsiveness, overshoot, accuracy, stability and robustness. Among these performance criteria, commanded profile tracking error and disturbance rejection are most critical to the selection of physical parameters. The transfer function of position error *E(s)* in Equation (6) is defined as the difference between the tracking profile *R(s)* and the actual position *Y(s)* where $w(s)$ is the disturbance force, $N(s)$ is the encoder noise, G_I is the current transfer function and K_f is the motor torque constant for a WYE connection.

$$\begin{aligned} E(s) &= R(s) - Y(s) = E_R(s) + E_w(s) + E_N(s) \\ &= \frac{ms^2 + Bs}{ms^2 + Bs + PID \cdot K_f G_I} \cdot R(s) - \frac{1}{ms^2 + Bs + PID \cdot K_f G_I} w(s) + \frac{PID \cdot K_f G_I}{ms^2 + Bs + PID \cdot K_f G_I} \cdot N(s) \end{aligned} \quad (6)$$

Encoder Noise Induced Position Error, E_N The encoder measurement has been identified to have resolution quantization error, the scale grating error and periodic spatial error. The periodic spatial error is modulated by the velocity to generate a wide range of frequencies in position feedback error. Since the transfer functions for the tracking profile $R(s)$ and the encoder noise $N(s)$ are inversely related, the high PID controller gains that reduce the profile tracking error E_R, increase the encoder noise induced position error E_N. This is a classical challenge in the motion control system. The best solution is to select an encoder with as high a resolution as possible. A new encoder (Sony, 0.25 nm resolution and 750 mm/sec maximum velocity) will be installed on FLORA but requires the new PMDi control system. If needed, explicit compensation technique

can be used to remove encoder errors before they enter the control algorithm, so that effective the encoder noise induced position error E_N will be zero.

4.6.3 LRS MODEL PERFORMANCE

Time-domain simulations are performed to predict the performance of closed-loop *FLORA II* system for position holding, sine wave tracking and disturbance rejection. The controller gains were selected by optimizing the performance (both transient and steady response) using a cosine wave with -0.1mm offset, 0.1mm amplitude at a frequency of 20 Hz. The same gains (K_p = 120, K_i =42560, K_d=0.16) are also used to predict on position holding and disturbance rejection.

Position holding

Figure 15 shows the ±5 nm position holding error in 0.15sec. The simulated data is plus/minus one bit on the encoder feedback and positioning capability. This is clearly the best possible performance.

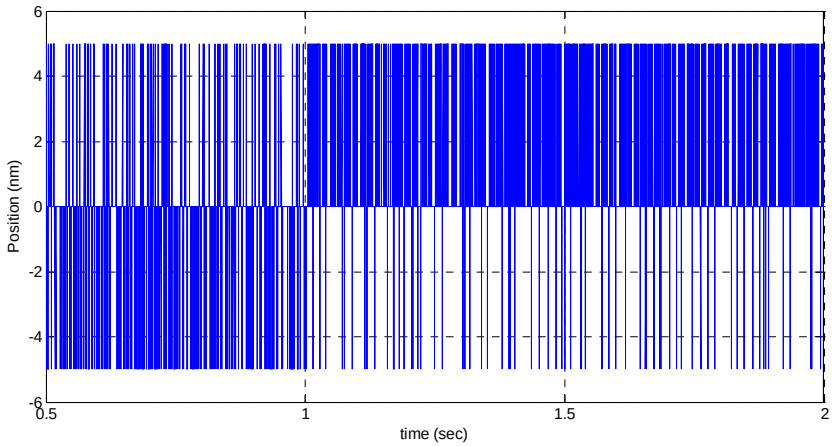

Figure 15. Simulation of position holding error

Sinusoidal profile tracking Figure 16 shows the simulated tracking error (difference between command and position) in first 0.15 sec. In the ±0.3026 μm (peak-to-peak) tracking error, the 20 Hz component could be removed by a adding a combination of feed-forward control gains and the command phase shift. The high frequencies errors may be caused by the Heidenhain pitch error which had a period of 1 μm and PP amplitude of 40 nm. Because this error is a position error, the frequency in Figure 16(A) should change from 0 to 12.5 KHz as the speed of the piston changes from 0 to 12.5 mm/sec. The frequency spectrum of this position error shows a broad band of frequencies from 1 to 10 KHz verifying this hypothesis. The new encoder should help to alleviate this problem.

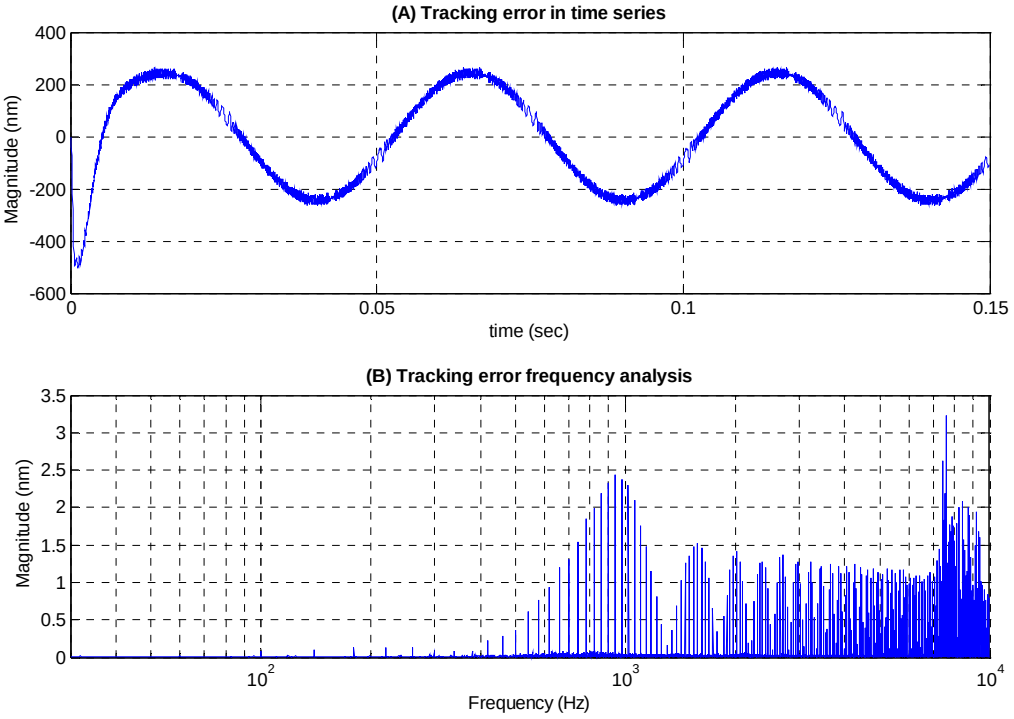

Figure 16. Simulation of 0.1mm 20Hz sinusoidal tracking error

Step command response The response to a step command input of 12.566 μm is shown in Figure 17. This magnitude is the maximum commanding position change in one servo cycle for 2mm 20Hz sinusoidal profile at 20 KHz sampling rate. The response has 27% overshoot, and settles to the desired value within 0.017 second

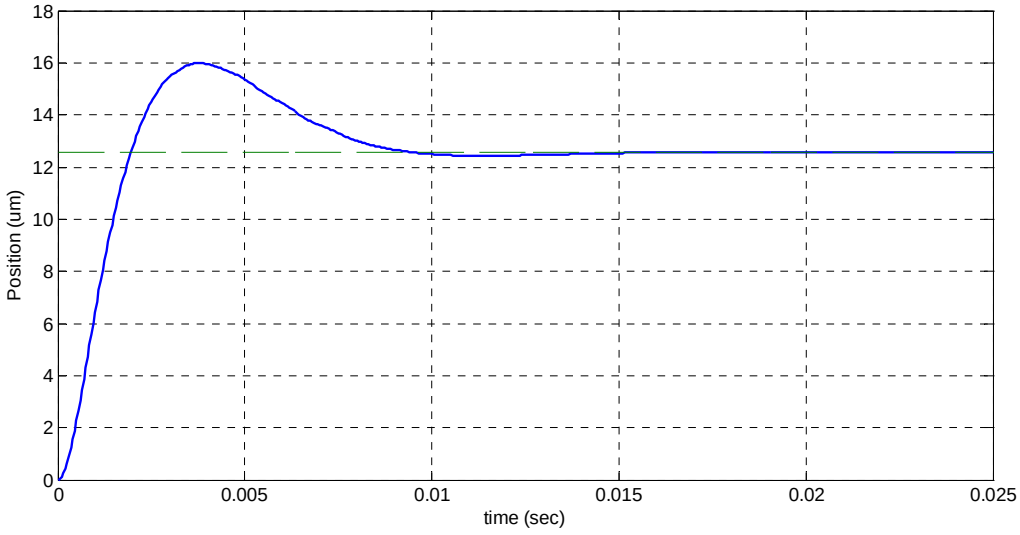

Figure 17. Simulation of system response to a step position command

Step disturbance response A 0.294 N step input disturbance force is introduced at 0.1 second at the mass. The response in Figure 18 shows the response has a peak error of 145nm, and it settles within 8 msec.

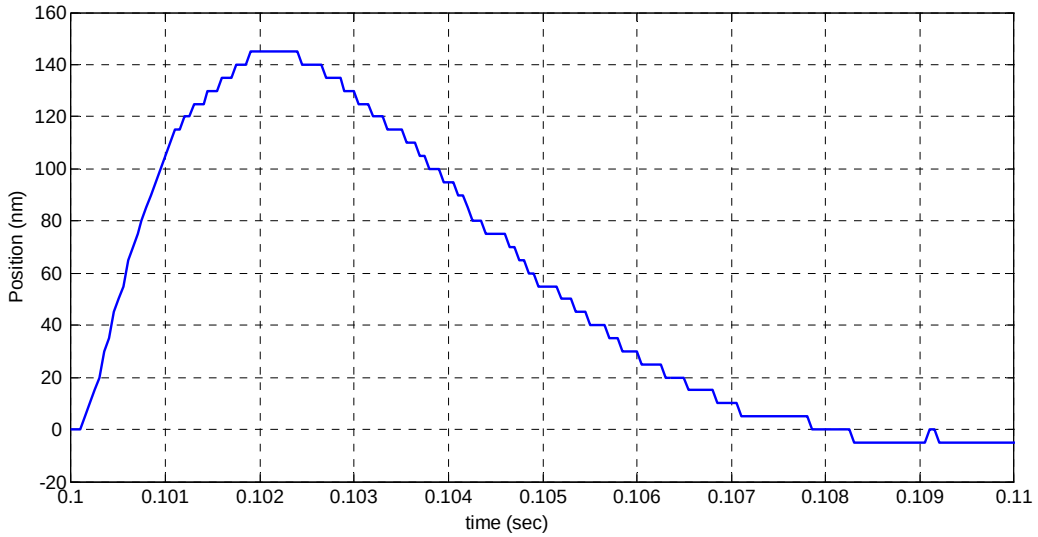

Figure 18. Simulation of system response to a 0.294 N step disturbance force input

4.7 CLOSED LOOP RESPONSE MEASUREMENTS

Experiments using the PID closed-loop control system were conducted to evaluate position holding, sinusoidal tracking and disturbance rejection. These experiments were done with the same position PID controller gains (K_p = 120, K_i =42560, K_d=0.16) as in the simulation.

4.7.1 POSITION HOLDING

Figure 19 shows there is ±40nm peak-to-peak position holding errors. This is a much higher value than the simulated position errors of ±5nm which is the encoder resolution. However, it is significantly lower than the *FLORA I* system where the error was on the order of ±200nm. Frequency analysis of the position error over 10 seconds is shown in Figure 19(B). The peak amplitude is at 60 Hz (probably line frequency seeping through the amplifier or other) and there is a cluster near 1000 Hz. This higher frequency shows up in the open loop response (Figure 12) so it may be a resonance in the mechanical system. Additional experiments will address this source of noise.

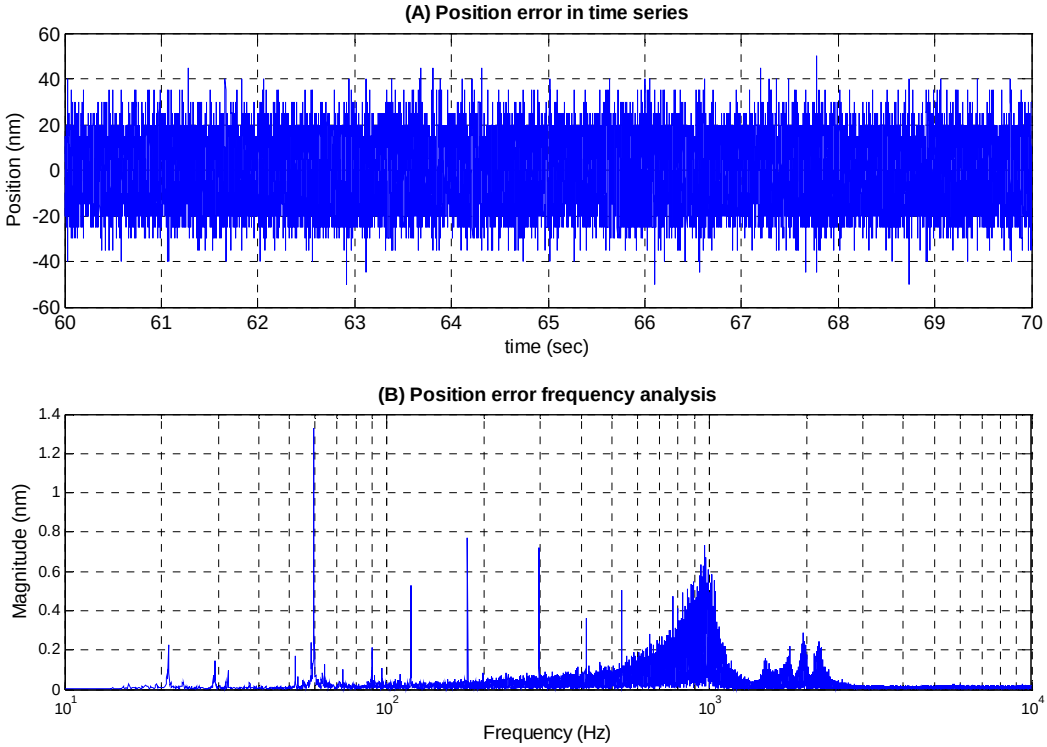

Figure 19. Position holding experiment

4.7.2 SINUSOIDAL PROFILE TRACKING

A cosine wave with -0.1 mm offset, 0.1mm amplitude at 20 Hz was used for the tracking profile. Figure 20(A) shows the tracking error in first 0.15sec. The motion profile is similar to the simulation in Figure 16(A). The tracking error component at 20 Hz frequency has magnitude of ±250 nm – Figure 12(B - but there are also components at 60 Hz and a cluster around 1000 Hz also observed in the position holding experiments. The high frequency on the top of the tracking error has a magnitude of 40 nm, which is the peak-to-peak value of periodic encoder spatial error.

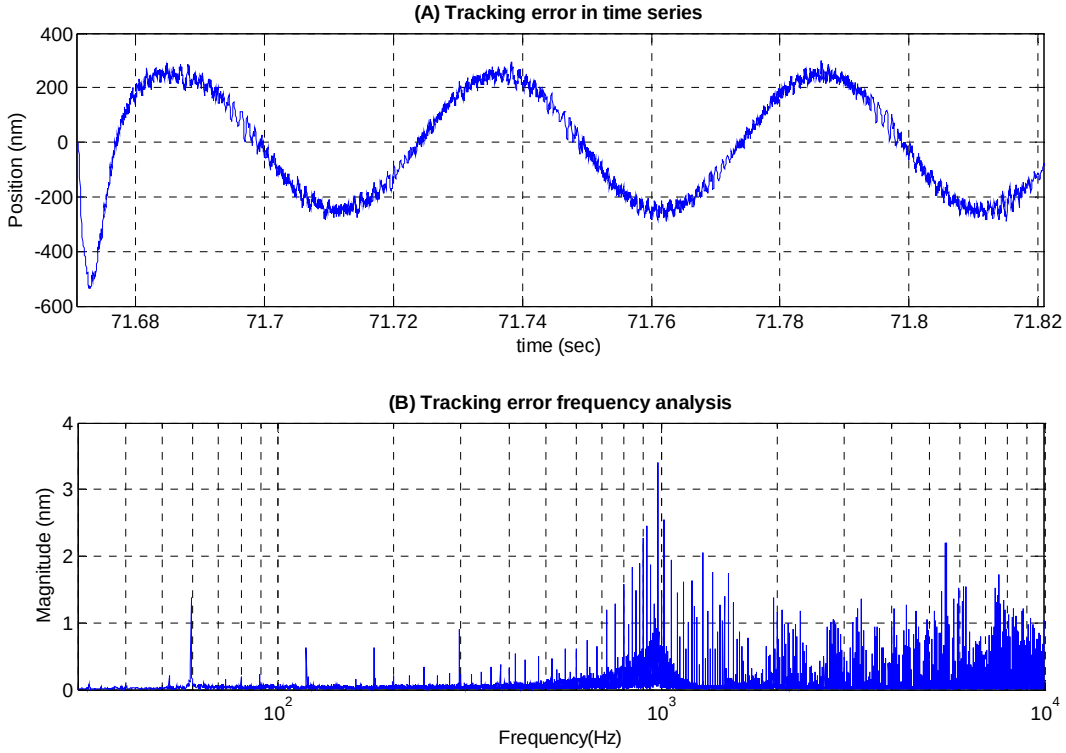

Figure 20. Experiment of 0.1mm 20Hz sinusoidal tracking

4.7.3 DISTURBANCE REJECTION

Step command response A 12.566 μm step command input is introduced at 50.66365 second into the experiment. A comparison of experimental and simulated results in Figure 21 shows good agreement between the model and experiment.

Step disturbance force response 0.294 N input disturbance force is introduced by attaching a 30 gram weight with a nylon string at the piston tool holder and hanging the string over a pulley. The weight is first added and then dropped. The response is only captured for the weight dropping process since it generates more consistent result, although it is not a perfect step input. Figure 21 shows the experimental response settles within 9 msec. The 900 Hz oscillation around zero position exists for position holding. These same features are on Figure 22 but the scale is 100 times less so they are not visible.

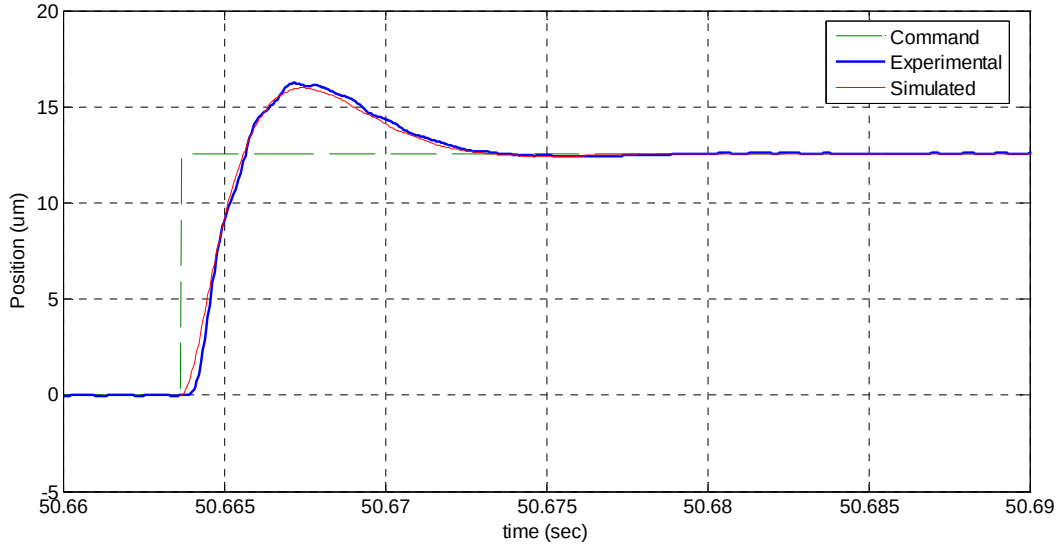

Figure 21. A comparison of experimental and simulated step command response

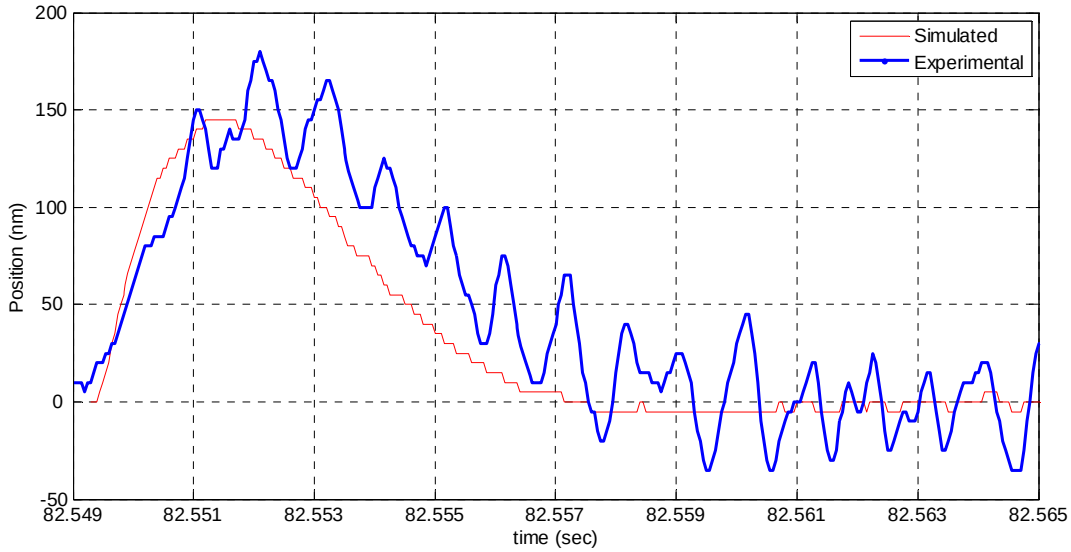

Figure 22. A comparison of experimental and simulated step disturbance force response

Discussion The results in Figures 19-22 emphasize the ± 40 nm noise at 1000 Hz that is present on the system under closed loop control. The origin of this disturbance has not been identified and may be external or feedback issues in the controller. Changes to the hardware and software are in progress as described in the next section and the performance will be determined when these changes are completed.

The development of the *FLORA* is an ongoing process among mechanical design, electronic components and the control system. The open loop measurements pointed to some anomalous behavior at 1000 Hz and this same frequency is showing up in the close loop measurements. Controller solutions are possible to deal with this undesirable feature but these will be put off until the planned changes described next are completed.

4.8 CONCLUSIONS AND FUTURE WORK

The goal of this project is to develop the design and control methodology to create a Fast Long Range Actuator that can machine non-rotationally symmetric (freeform) optical surfaces. The form error should be less than 150 nm ($\lambda/4$) and a surface finish on the order of 2 nm RMS. But speed is also an important issue and the design must have a bandwidth to produce these freeform surfaces with minimum deviation from current processing time for spherical or aspheric parts. The first prototype – *FLORA I* – was similar to commercial devices on the market with respect to performance and speed. However, the surface finish was much worse (16 nm vs. 2 nm) than currently possible with a symmetric surface.

The second prototype – *FLORA II* – improved the system by adding a linear amplifier, a higher resolution glass scale encoder (5 nm resolution) and increasing the sampling time by a factor of 8 (from 2.5 to 20 KHz). These factors improved the position holding capability from ±200 to ±40 nm and disturbance rejection from 1500 to 150 nm.

Over the next few months, several significant changes to the system will take place and a second prototype design will evolve.

Encoder To increase the speed and resolution of the feedback signal, a new Sony encoder has been purchased. This glass scale encoder has 0.2 μm grating and, combined with the new controller hardware, has a maximum speed of 750 mm/sec.

Controller Platform The xPC Target system will be replaced with a PMDi controller. The PMDi platform is more user friendly and faster than the xPC Target and has the necessary hardware (sine-cosine interpolation board) to read the new Sony encoder.

Motor The linear motor will be retained for the new controller/encoder experiments and then evaluated to see if a voice coil motor is preferable.

Damping A viscous damping apparatus has been fabricated and will be attached to the piston and experiments performed to see the impact of added damping. By changing the viscosity of the oil from 10 to 70 weight oil, damping factors from 1 to 20 N s/m can be achieved.

New Piston Design A new piston design is being developed by Dave Youden, supported by the PEC. The concepts developed using the *FLORA II* will guide the parameter values used in the next design.

ACKNOWLEDGEMENT

This work is supported by NSF grant DMI-0556209.

REFERENCES

1. Patterson, S.R. and Magrab, E.B., *Design and Testing of a Fast Tool Servo for Diamond Turning*. Precision Engineering, Vol 7, No 3, pg 123-128, (1985).
2. Patterson, S.R. and Saito, T.T., *Diamond Turning Wavefront Correctors: Opening New Optical Design Flexibilities*. Proc SPIE, Vol 676, pg 10-16, (1986).
3. United States patent 5,467,675. *Apparatus and Method for Forming a Workpiece Surface into a Non-rotationally Symmetric Shape*. Thomas A. Dow, Kenneth P. Garrard, George M. Moorefield, II and Lauren W. Taylor, (1995).
4. W.D. Allen, R.J. Fornaro, K.P. Garrard and L.W. Taylor, *A High Performance Embedded Machine Tool Controller*. Microprocessors and Microprogramming, 40, 179-191, (1994).
5. Thompson, D.C. *Theoretical Tool Movement Required to Diamond Turn an Off-axis Paraboloid on Axis*. Advances in the Precision Machining of Optics, Proceedings of the SPIE 93, (1976).
6. Gerchman, M.C. *A Description of Off-axis Conic Surfaces for Non-axisymmetric Surface Generation*. Proceedings of the SPIE 1266, (1990).
7. Douglas, S. *A Machining System for Turning Nonaxisymmetric Surfaces*. PhD Dissertation, U of Tenn, (1983).
8. Montesanti, R.C. and Trumper, D.L., *High Bandwidth Short Stroke Rotary Fast Tool Servo*. Proceedings of the ASPE, Vol. 30, pg 115-118, (2003).

5 DESIGN AND FABRICATION OF AN OPTICAL ASSEMBLY TEST

Alex Sohn
Precision Engineering Center Staff Member
Thomas Dow
Director, Precision Engineering Center
Professor, Department of Mechanical and Aerospace Engineering

In order to clearly identify the error sources in the machining and assembly of optical systems in a simple test system has been designed. This system could be used to test various aspects of the machining and assembly process, but through the use of simple geometries allow different error sources to be distinguished from each other. Ultimately, the test will be used to compare two different assembly techniques: The state of the art pin/slot assembly method and a quasi-kinematic assembly technique using features machined with a fast-tool servo.

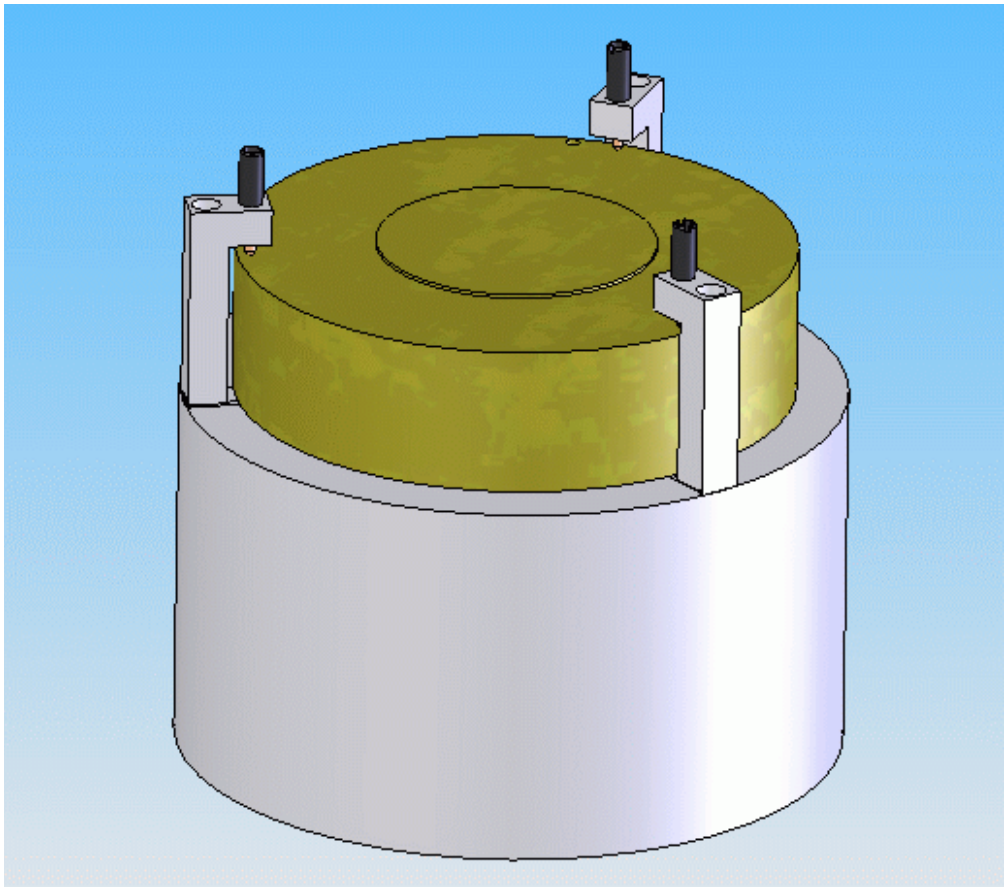

5.1 INTRODUCTION

With the evolution of ever better fabrication techniques for optical surfaces, assembly and accurate positioning of these surfaces is turning out to be the most challenging aspect of making advanced optical systems perform better and more cost effective. The use of compliant materials like aluminum is often dictated by other factors, making deformation and thermal expansion significant factors. To test the influence of these factors in addition to overall machining and assembly tolerances, a vastly simplified system that can be measured easily is needed.

Ultimately, two different assembly concepts will be tested: The currently used pin and slot method and a quasi kinematic mounting technique developed at the PEC. The pin/slot method has many drawbacks, such as a lack of available pins that are accurate to 1 μm, the possibility of interference and galling in aluminum. Some improvements, such as a toroidal diamond turned pin, have been made to the pin/slot method. These will be described and tested below. The quasi-kinematic mounting technique that represents a paradigm shift in optical assembly is also described.

5.2 SPHERICAL MIRROR EXPERIMENT

The simplest form of a lightweight alloy optical system would be one reflector attached to a support. The reflector could be a flat, sphere, off-axis sphere or conic with a matching optical surface machined into the end of the tube to test alignment. As shown in Figure 1, these varying configurations can be tested in an interferometer. Each component can be measured both independently and as part of the assembly so that the influence of the assembly can be tested. The plan is to start with a flat test because it is the simplest geometry to machine and measure. Tilt alignment of the flat mirror and the flat on the end of the tube can be measured as well as distortion in each surface due to mounting stresses. Once the flat has been machined and thoroughly measured, the next test is for a spherical mirror. A matching spherical surface in the end of the tube will allow the measurement of focus as determined by the length of the tube. This critical parameter is often difficult to measure in completed systems and, with multiple components placed in series, it is very difficult to distinguish error sources. The spherical mirror test will also identify translational errors in the system. Finally, upon completion of the spherical mirror test, an off-axis sphere will be machined on-axis using the Variform Fast Tool Servo. This will test the final degree of freedom necessary for accurate alignment of freeform systems: rotation about the optic axis.

5.3 COMPONENTS

For this demonstration purpose, four parts will be made: the spherical mirror, the mounting tube, two brass pins and an intermediate mounting chuck for the tube. The final assembly is shown in Figure 1.

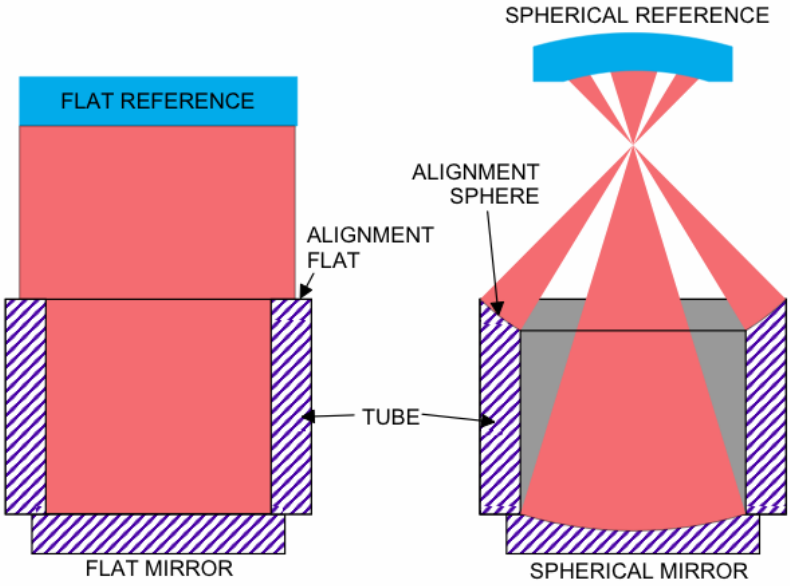

Figure 1. Two configurations of the test system. The flat mirror version is sensitive to tilt and distortion in the mirror while the spherical version tests focus and translation misalignment.

5.3.1 MIRROR

The mirror has a flat fiducial surface surrounding the optical surface. For the flat test configuration both surfaces will be the same. The spherical mirror, also shown in Figure 2, will have a separate annular region. Only the areas around the pin holes serve as the quasi-kinematic mounting regions that line up with the mounting pads on the tube. The two pinholes, bored with a diamond flycutter/boring tool provide translation alignment as well as clocking. Also, two threaded extraction holes aid in disassembly of the system. The pins may add a small interference component, so some force may be necessary to extract the pins from their mating holes. This will be performed by threading one setscrew into each hole until they lift the mirror from the tube.

Mirror material The material for the mirror was chosen based on the generally accepted mechanical properties and the high reflectance of 6061 Aluminum. Superior thermal stability

and absence of stress are achieved with a T 651 temper, so this was selected over the more common T6 temper. [1]

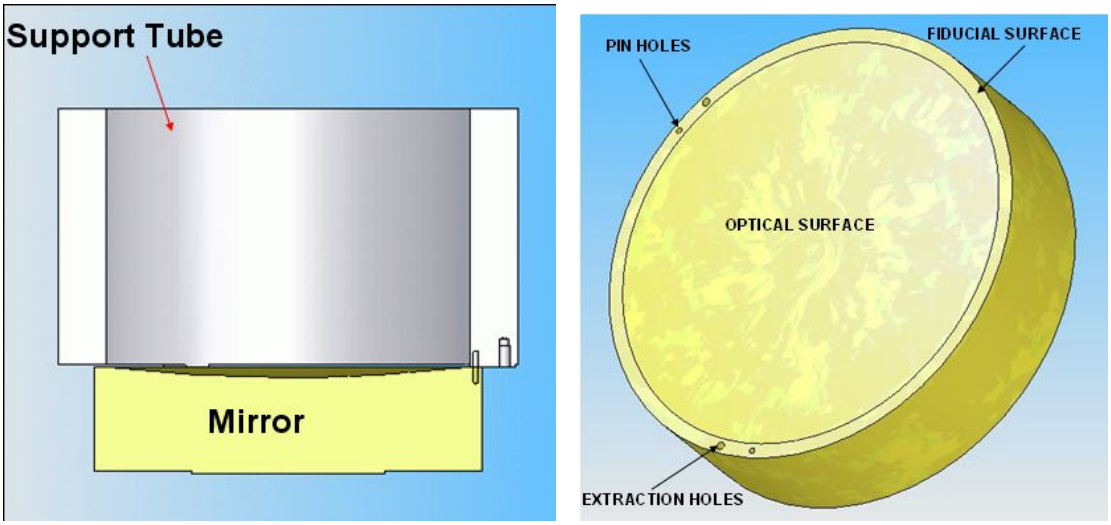

Figure 2. Assembly (left) showing mirror mounted to tube and mirror details (right)

Fabrication mounting Given that the total vacuum force on the mirror back from 10 psi vacuum is about 300 lbs, a significant amount of distortion can be expected if both mounting surfaces are not perfectly flat. One option would be to reduce the vacuum pressure, but a better method is to simply apply the same pressure over a smaller area. This has the added benefit that a smaller area is statistically less likely to contain distorting imperfections than the larger area. Thus, a 3" diameter raised region on the back of the part will minimize distortion when mounted on a vacuum chuck and the spherical optical surface. As Figure 3 shows, the reduced force of the smaller area significantly reduces overall distortion from 400 nm to 40 nm.

Clocking Fiducial A fiducial will be scribed into the mirror OD to test alignment of the optical system in the clocking direction. With pins inserted into the holes, the pins will be touched on the rake face of the diamond tool to establish clocking alignment (in the rotation direction) with the spindle encoder. A scribe mark as shown in Figure 4 will then be made on the OD that will match a similar scribe mark in the tube after assembly. While clocking alignment has no impact on the optical performance of the flat or spherical mirror system, when the off-axis system is machined, it will have a significant role.

[1] http://www.nasatech.com/Briefs/Sep05/GSC147361.html

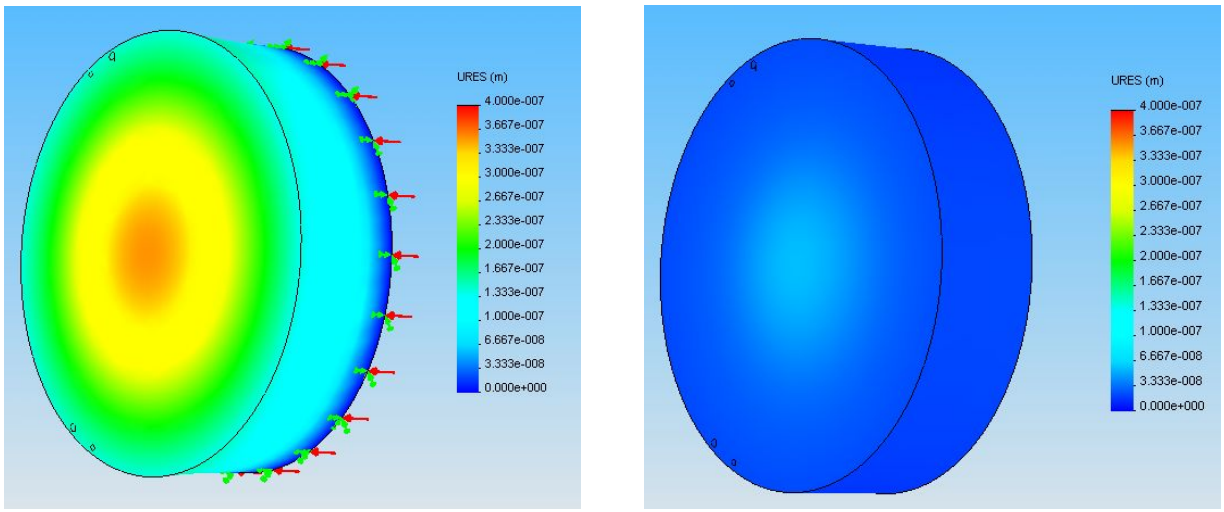

Figure 3. Distortion when the entire back surface of the mirror (150 mm) is used to vacuum the part to the chuck (left) and when only a 75 mm diameter region in is used (right).

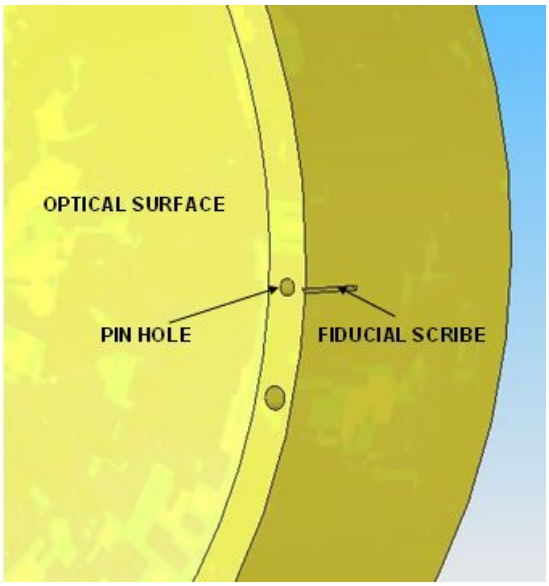

Figure 4. Clocking fiducial scribed in relation to pin hole.

5.3.2 PINS

The pins will be single-point diamond turned in 316 brass to reduce binding in the aluminum. The pins are toroidal, or barrel shaped as shown in exaggerated form in Figure 5. The overall diameter of approximately 2.3 mm is reduced by 20 µm at the ends of the pin. This will prevent binding due to misalignment, but still provide a positive fit when the pins are fully located in their holes. The two pins are turned with a diameter that is 3 µm smaller than the measured hole

diameter at the waist, allowing for manufacturing tolerances. This allows for a 1 μm tolerance on the hole measurement and a 1 μm tolerance on the pin fabrication while still permitting a slip fit.

5.3.3 TUBE

The tube in Figure 6 supports the mirror and is approximately 100 mm in length and has a 178 mm OD. One end, the alignment test surface, has an optical surface machined into it to match the mirror surface: flat, spherical, or off-axis spherical. The first test will be with a flat surface.

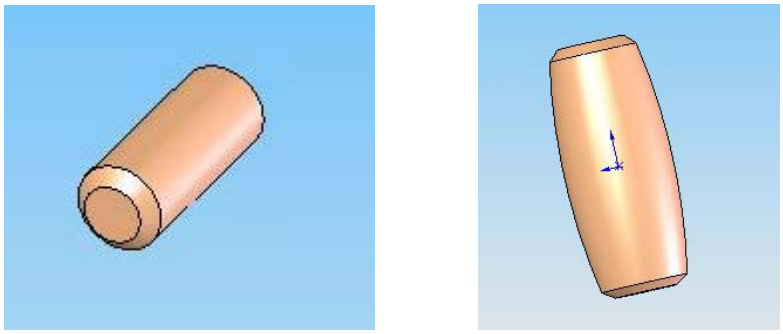

Figure 5. Locating pin for mirror-to-tube translation and clocking. Shown to scale at left and with exaggerated toroidal features at right (change in diameter is 20 μm).

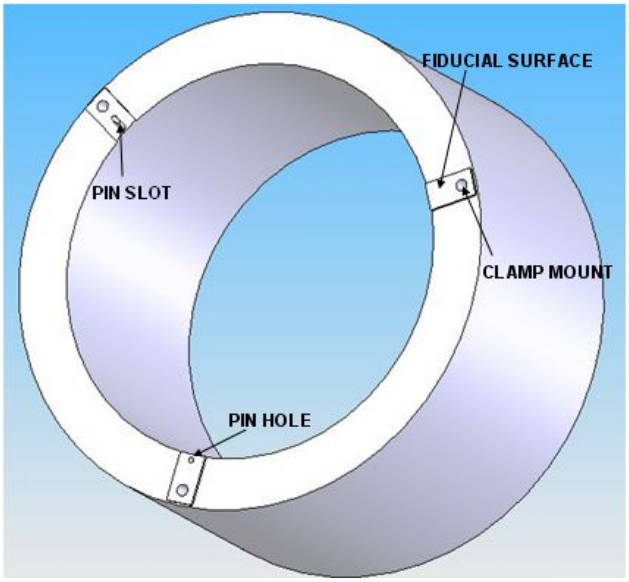

Figure 6. The mirror mounts on the end of the tube using the three fiducial surfaces. One surface has a hole and another has a slot to mate with the 2 pins in the mirror.

Figure 6 shows the mounting fiducial end of the tube. A pin hole and a slot mate with the pins inserted into the mirror without over-constraining the system. The pin hole and slot are bored and milled, respectively, with the same diamond boring tool used to put the two holes in the mirror. This ensures a uniform diameter using the same setup for both operations. Pilot holes were drilled because the boring tool will not cut to the center.

In the machining operation, one of the last steps will be to scribe a fiducial mark on the pad with the pin hole. The clocking location of the pin hole will be determined just as with the mirror; i.e., by touching the diamond tool to a pin inserted in the hole.

5.3.4 CLAMPS

A set of clamp mounting holes reside immediately outside the mirror contact area on the fiducial surfaces. Near the OD of the tube, the fiducial surfaces are squared off to mate with the clamps and prevent them from rotating. After examining a series of different clamp designs, it was decided that in the interest of flexibility, and adjustable spring plunger in an aluminum support would be appropriate for holding the mirror to the tube. Spring plungers are readily available in a variety of force ranges and are rugged as well as inexpensive. As shown in Figure 7, the spring plunger is held by an L-shaped support that will be screwed to the tube. Using this arrangement, a variety of retaining forces can be explored as well as their impact on distortion of the system and any alignment errors they may introduce. In a complete system, these spring plungers would be replaced by wirecut EDM machined flexures to save mass and eliminate the need for adjustment.

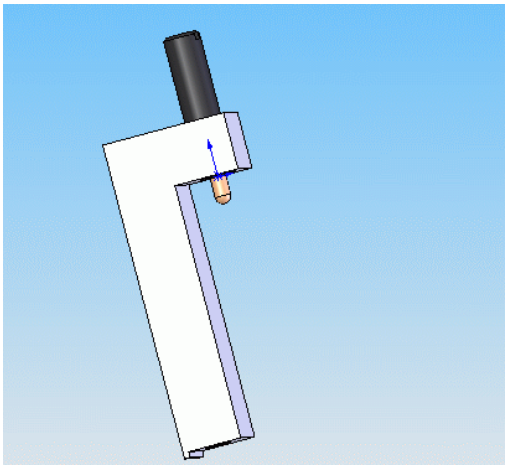

Figure 7. Spring plunger clamp used to retain mirror to tube.

5.4 ASSEMBLY PROCEDURE

The completed assembly is shown in Figure 8. The assembly procedure is as follows:

- Insert pins into mirror pin holes. Pins must slide completely into the holes.
- Place mirror on inverted tube and align pins in mirror with pin and slot in tube. Gentle pressure should drive the mirror home so that the fiducial surfaces on the mirror and tube mate.
- Bolt spring plunger clamps onto tube with spring plunger backed away from the mirror.
- Turn spring plungers until the make contact with the mirror, then turn to achieve the desired clamping force.

Stress Relieving was performed by Carolina Heat Treat according to the following procedure that was repeated twice.

- Cool the parts to -100°F and slowly warm to room temperature
- Heat the parts to 300°F and slowly cool to room temperature

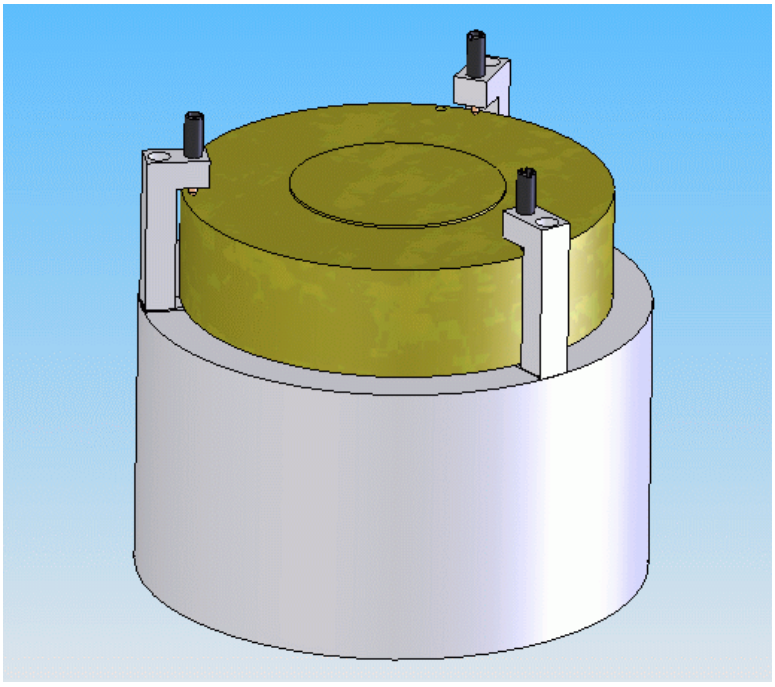

Figure 8. Completed test assembly shown from the rear. The spring clamps are bolted into their locations and the plungers can be adjusted to apply different loads to the rear of the mirror.

Flycutting tube fiducials The three fiducial pads on the tube are the first item that must be machined with a diamond tool. A .519 mm radius tool is mounted on the periphery of an aluminum plate and vacuumed onto the ASG 2500 DTM's main part spindle. The tube is held on a V-block by means of a bolt through the side of the tube. A 3/8" diameter hole was drilled

through the side of the tube for this purpose. The tube was then squared by its exterior to the axes of the machine as shown in Figure 9. Variation along the tube length was less than .010 mm in both the y- and x-directions. The flycutter was then rotated at 500 rpm to make 20 passes at .025 mm each to completely machine all three pads. A finish pass at 5 mm/min should produce a 24 nm PV theoretical surface finish.

Turning mounting plate Due to the raised areas of the fiducial pads, the mounting end of the tube cannot be vacuumed onto the part spindle to machine the other end. An intermediate mounting plate must be used. With three holes to bolt the pads on the tube, the plate is simply an 8" diameter, ¾" thick flat. The back of this plate has been lapped. Prior to machining the front, the vacuum chuck was faced. Figure 10 shows the plate being faced.

Facing off tube The error correction for yaw of the z-slide was set to parameters of yaw = 0.70 arcsec at z = 1.2 mm. With the tube bolted to the mounting plate, the opposite end of the tube can be machined to an optical finish using a 1 mm radius tool.

Figure 9. Tube mounted on a v-block is squared to the axes using an electronic indicator. The flycutter can be seen on the part spindle behind the tube.

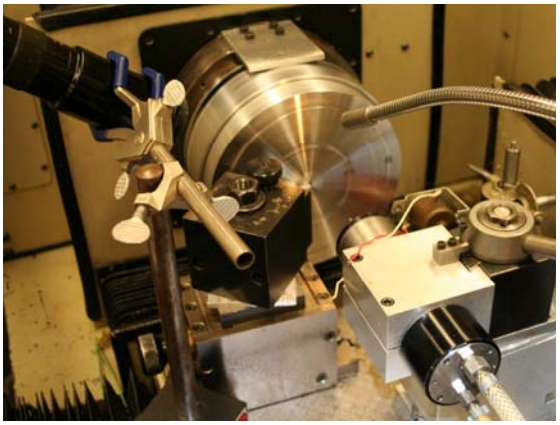

Figure 10. Tube mounting plate being faced. The plate is rotating on the spindle while material is being removed with the tool mounted on the micro-height adjuster The boring spindle is in position in the lower right.

Center boring spindle The pin holes are fabricated with a small-diameter diamond boring tool mounted in a Federal/Mogul Westwind high-speed grinding spindle. To find the location of the center of the boring tool with respect to the DTM coordinate system (and hence the mirror and tube) the boring spindle and the ASG 2500's part spindle must be aligned. The simplest way of achieving this goal is to bore a hole in a test part and then measure the runout of the hole with respect to the part spindle. When the two spindles are perfectly aligned, the runout is zero.

As shown in Figure 11, the boring spindle is driven by a small electric motor via an o-ring drive. This is necessary since the only tool available was made for clockwise rotation while the air turbine on the spindle rotates counterclockwise. The small DC electric motor reaches its maximum speed with 15 V. After locking the part spindle, the boring tool is plunged into a pre-drilled 1.8 mm diameter hole at 2 mm/min to a depth 3 mm. The setup is shown in Figure 11. Once the test hole is bored, an electronic indicator probe is placed inside the hole to measure the runout of the hole as a function of part spindle position. A sample plot of one of these measurements is shown in Figure 12.

From the displacement of the probe at 0 and 180, the horizontal (x) position is obtained while from the displacements at 90 and 270 degrees, the vertical (y) error is obtained. To correct for x-error, the x-axis offset is changed. To correct for y-error, the spindle must be physically moved by the inverse of the measured error using the tool height adjuster on the toolpost. The centering process may have to be repeated to obtain minimal runout. Final runout measurement should be less than 1 μm.

The test holes bored for the centering process are also used to determine the diameter of the bored hole. As measured on the NewView 5000 Scanning White Light Interferometer, the hole diameter is 2.3587 ± 0.001 mm. This value is then used to determine the diameter of the pins. The NewView was calibrated using a reticle scale and found to be within ±.0005 mm.

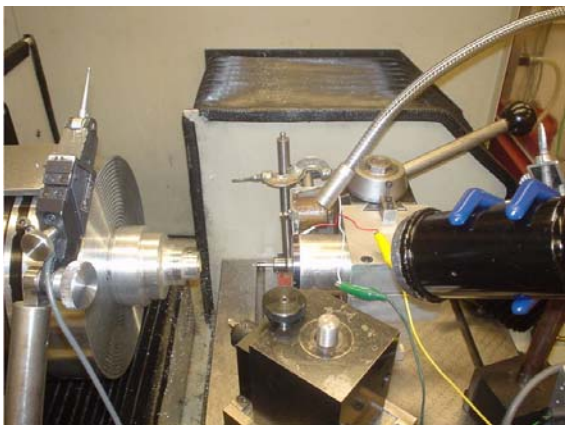

Figure 11. Boring tool mounted in high-speed spindle is used to bore a test hole in the part mounted on the spindle at left. The runout of the hole is measured with an electronic indicator.

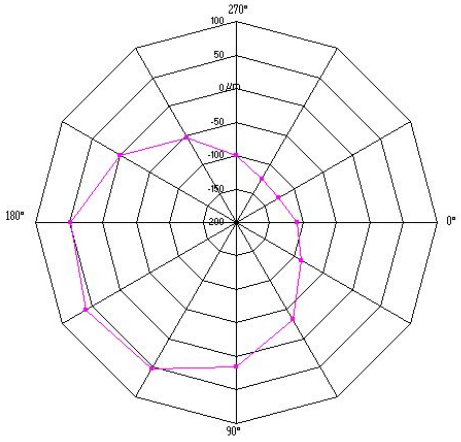

Figure 12. Boring tool centering. The measured runout from the procedure in Figure 5-41 shows that the boring tool center is 52 μm low and 80 μm left of center.

Machine Pins The pins are single-point diamond turned from alloy 360 brass to reduce galling in the aluminum. A small radius tool (0.519mm) is used to turn the pins. First, a cylindrical pin is turned to accurately center the tool. The end is faced and the center feature used to adjust vertical centering. The OD of the pin is then turned and measured in the NewView 5000 SWLI, so that even if systematic error exists in the instrument, the same method for measuring pin and hole diameter should ensure that the final clearance is correct. This allows for a 1 μm tolerance on the hole measurement and a 1 μm tolerance on the pin while still allowing a slip fit. Figure 13 shows one of the pins being machined and measured.

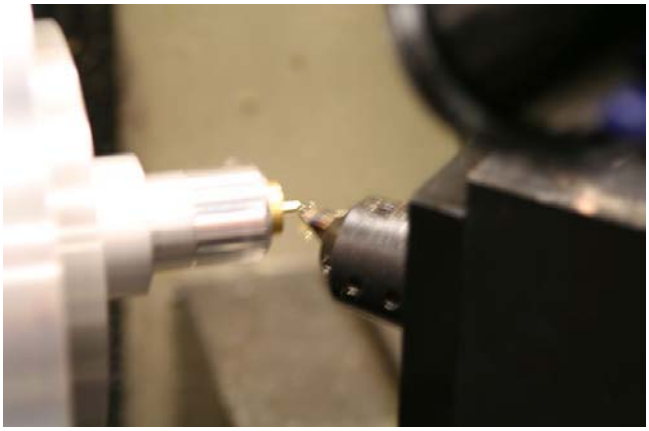

Figure 13. One of the brass pins being turned and the length measured.

Once the tool center was established, the toroidal pins could be fabricated. The diameter of the pins is reduced by 20 μm at the ends while the diameter at the center is 2.357 mm, approximately 2 μm smaller than the holes. The pins are turned while attached to a piece of brass rod about 20 mm in length. After the ends are faced, the toroidal profile is cut and a small chamfer turned at the end. The pin is then cut off in a conventional lathe using a modified box cutter blade as a cutoff tool. The pins are then approximately 0.2 mm long. After being cut off, the length is measured using a micrometer. The pins are then inserted into one of the test holes and faced to length and chamfered.

5.4.1 PIN HOLE AND SLOT

To bore the pin hole and slot, the existing rough machined hole and slot must be located. This turned out to be a particular challenge because the hole and slot did not appear to be registered to either the ID or the OD of the tube. So, to find the center of the coordinate system of the pin hole and slot, it was assumed that the spring clamp mounting holes were machined in the same setup. Hence, an 8-32 screw was threaded into each of the mounting holes and the tube, mounted on the vacuum chuck and centered on these three screws. The boring spindle was then

moved to the correct radius for the pins and a machine-mounted microscope was used to align the hole in the clocking (θ) direction. Alignment with the slot was then checked at 120º from the hole and was found to fall within the existing rough slot. With the part spindle locked at 120º, the slot was then cut by plunging into the part at 1 mm/min to a depth of 3 mm and then translating 1 mm at 1 mm/min. The tool was then retracted at the opposite end of the slot. The part spindle was rotated back to 0º, locked and the pin hole bored to a depth of 3 mm. Figures 14 and 15 show the holes being bored.

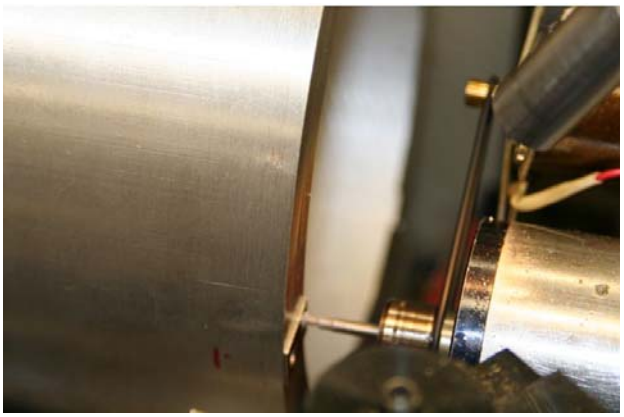

Figure 14. Pin hole being bored. Note belt drive on spindle to provide CW rotation

Figure 15. Closeup of pin hole being bored. View is through the on-machine microscope.

Center finishing tool The 1 mm finishing tool must be centered in both x and y to ensure that the contour of the spherical surface is correct and that the fiducial scribe marks are in the correct place. The tool was centered using a 12.7 mm diameter brass center plug. A centering error in the tool will produce both an ogive error (X-center) and a small feature at the center of the part (y-error). This centering technique is well established [*]

Machine mirror The mirror blank is placed on the vacuum chuck and centered as well as possible on the O.D. The mirror OD was turned with the pin tool to get a round part. Next the pin tool was used to rough cut the face of the mirror and remove most of the material. To get the best surface finish, a feedrate of 0.5 mm/min at 500 rpm and a DOC of 1 μm was used. This gives a theoretical PV surface finish of 0.1 nm. The finishing operation is shown in Figure 16.

Bore pin holes Chamfers were included at the edge of the mirror pin holes to keep burrs around the hole from preventing contact between the mirror and the tube. With the mirror chucked to

[*] M. Gerchman. Fundamental axial spindle motions and optical tolerancing. SPIE 1573, 49-52 (1992).

the spindle and the tool centered, the part is centered using an electronic indicator. The boring spindle is then placed at the correct radius (83.5 mm) and the spindle is positioned so that, using the on-machine microscope, the boring tool will coincide with the existing hole. Alignment is then checked with the other hole by repositioning the spindle 120º. Maximum clocking accuracy on this DTM is 20000 counts per rev or 22 µm at this radius. Each hole is then bored at a feedrate of 1 mm/min in z to a depth of 3 mm.

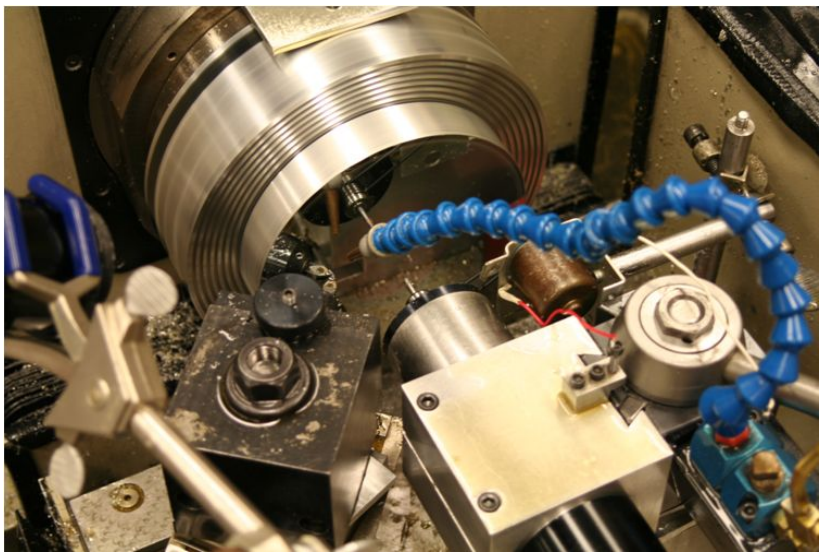

Figure 16. The finishing operation of the flat mirror.

Scribing fiducials With the part still mounted and the spindle in the +120º position, the optical figuring tool is moved to the OD of the part, brought into contact with it and dragged along the OD producing a mark. This will be the clocking fiducial that will test the clocking alignment. The tube is mounted on its face on the vacuum chuck with the straight pin that was used to center the pin tool inserted into the hole in the tube,. With the optical figuring tool positioned at 83.6 mm, the spindle is then rotated counterclockwise until the straight pin rests on the rake face of the tool. This position represents the OD of the pin. To center the tool on the pin in the θ-direction, the spindle is rotated another .808º. The face of the fiducial is then scribed with the optical figuring tool.

Assembly The toroidal pins are inserted into the mirror until they reach the bottom in their holes. Care must be taken to insert the pins straight into the holes. Thermal expansion is not a significant issue due to the small diameter of the pins. At this point, the mirror can be laid on top of the tube and, with the pins aligned with the hole and slot, gently pushed together. The spring clamps are then attached and tensioned to provide the appropriate retaining force.

5.5 METROLOGY

5.5.1 SURFACE FINISH

Preliminary measurement results for the fabricated flat show excellent surface finish results. The rms surface finish ended at 6 nm measured over a .11 X .14 mm area with the PEC's Zygo NewView 5000 white-light interferometer. Results are shown in Figure 17. Such a surface finish is quite good for 6061 aluminum as inclusions of iron and silicon preclude any improvement over this value for a diamond-turned surface.

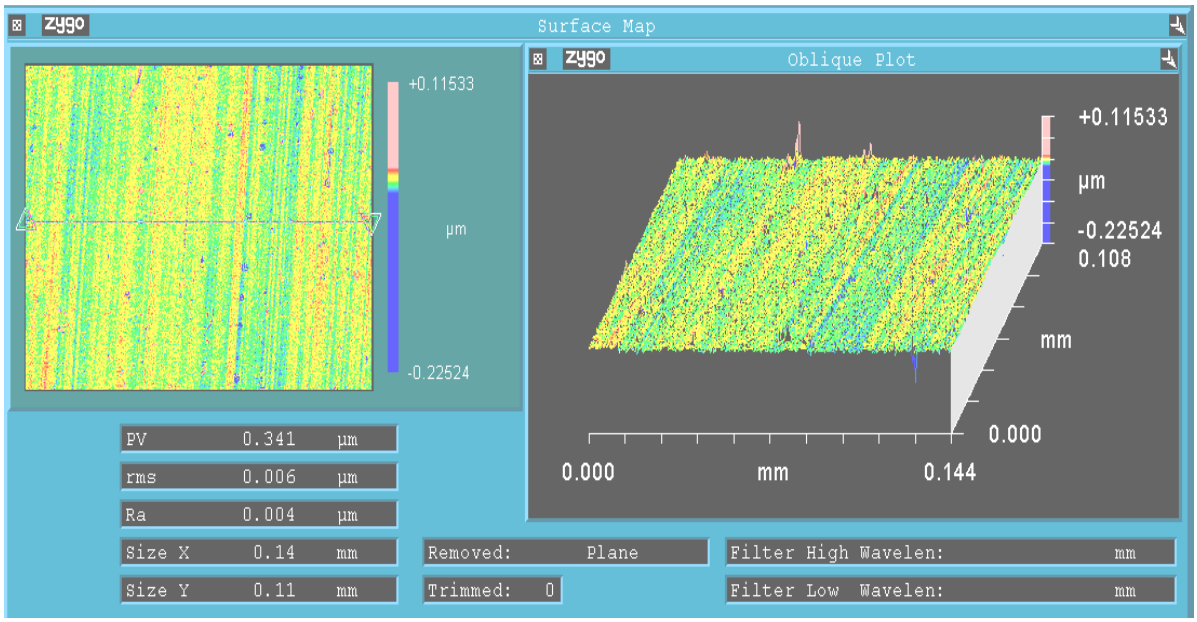

Figure 17. Surface finish measurement results from the Zygo NewView 5000 optical Profilometer. While the tool marks are still apparent on the surface, the overall rms finish 6 nm is excellent for 6061 Aluminum.

The calculated surface finish for this mirror was 0.1 nm P-V, though the material effects and machine vibrations make this finish impossible to achieve under the conditions. Figure 18 shows a cross-sectional plot perpendicular to the lay of the surface. No regular tool marks can be discerned at the 1 µm theoretical crossfeed. This confirms that the range where tool geometry and machining parameters no longer determine the finish, but material effects and vibration do.

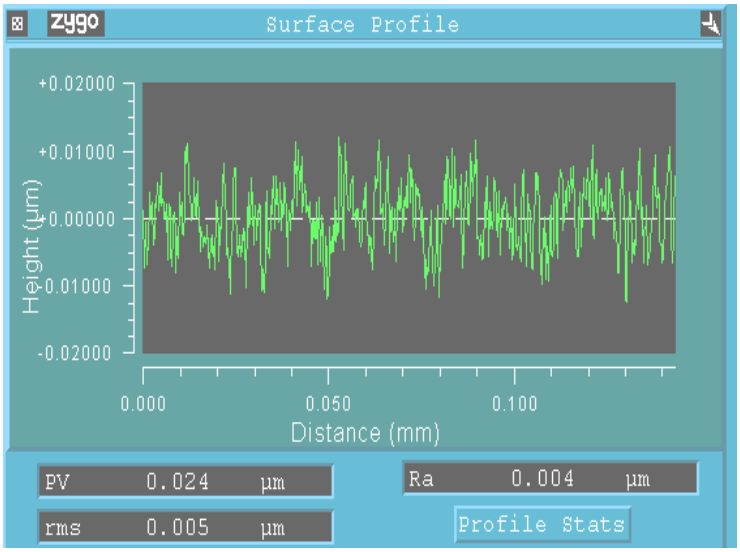

Figure 18. Cross-sectional trace of 3-D plot shown in Figure 17 shows no regular tooling marks, showing that the surface finish is dominated by material effects and machine vibrations.

5.5.2 SURFACE FIGURE

Surface figure measurements for the first cut of the flat are shown in Figure 19. The cut was made with the ASG 2500's geometric error compensation activated. This error compensation scheme compensates for errors due to X-axis straightness, Z-axis yaw and squareness between

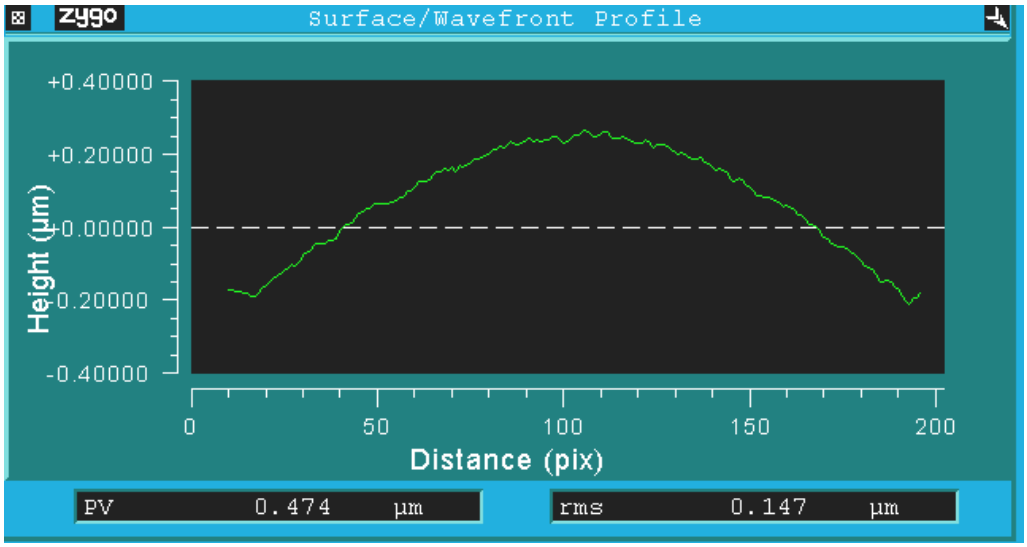

Figure 19. Surface figure measurement of 150 mm diameter aluminum flat before correcting 1.0 arcsec squareness error.

the two axes. The squareness compensation is part of the Z-axis yaw compensation and represents the intercept of the yaw curve. This value must be periodically updated if the spindle or axes have been moved on their mountings. Some residual squareness error is shown in the measurement as a conical component of the cross section. Independent measurements of the cone angle of a freshly faced vacuum chuck verified the squareness error. The cone angle was measured and found to be 2.0 arcsec. This cone angle is double the squareness error, so the current value of 0.7 arcsec squareness compensation was increased to 1.7 arcsec. A final cut of the flat surface is shown in Figure 20, showing 32 nm of RMS figure error. The residual error is possibly due to uncompensated roll or yaw errors in the x-axis.

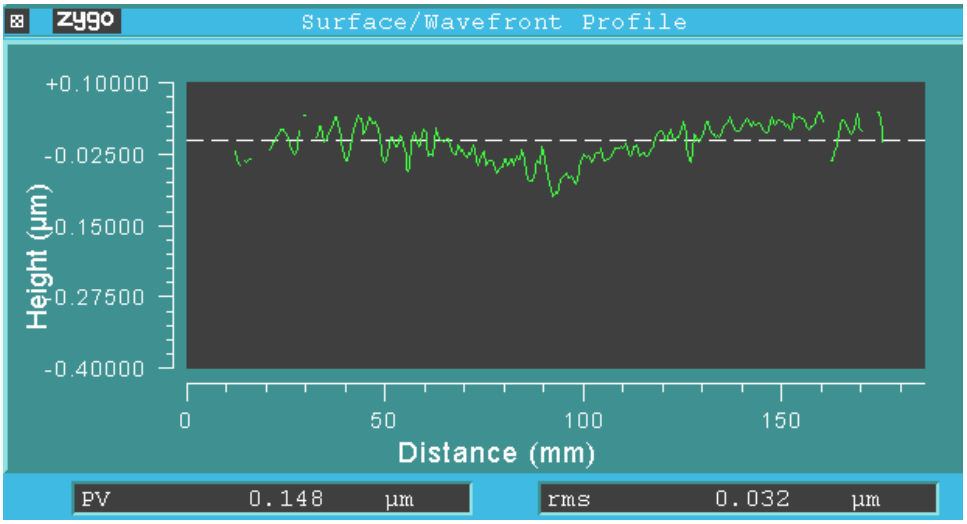

Figure 20. Surface figure of flat cut after removing for 1.0 arcsec squareness error

5.6 QUASI-KINEMATIC MOUNTING TECHNIQUE

5.6.1 FIDUCIAL DESIGN

Kinematic (and Kelvin) couplings provide deterministic location in all six degrees of freedom of two components in relation to each other without overconstraint. Overconstraint is to be avoided since it causes stress in the structures of components that results in distortion and non-repeatable location. Ideally, three points on a structure that are rigidly coupled to each other will mate with six planes rigidly connected on another component. Ignoring contact stresses for a moment, this mating will provide a unique and critically constrained relative location of the two components with respect to each other regardless of small location errors in the points or planes. Considering an actual physical system, however, there are other considerations: first and foremost are contact stresses and their effect on the components.

A Kinematic coupling is shown in Figure 21. The hemispheres are attached to the top and the bottom has a physical system consisting of points on spheres mating with planar grooves that must be kept in contact by an external force. That force may be gravity, as illustrated, or it may be a system of flexures. Regardless, the localized stresses inherent in kinematic design must not reach the point where they significantly alter the placement or shape of the mating components or plastically deform the mating surfaces.

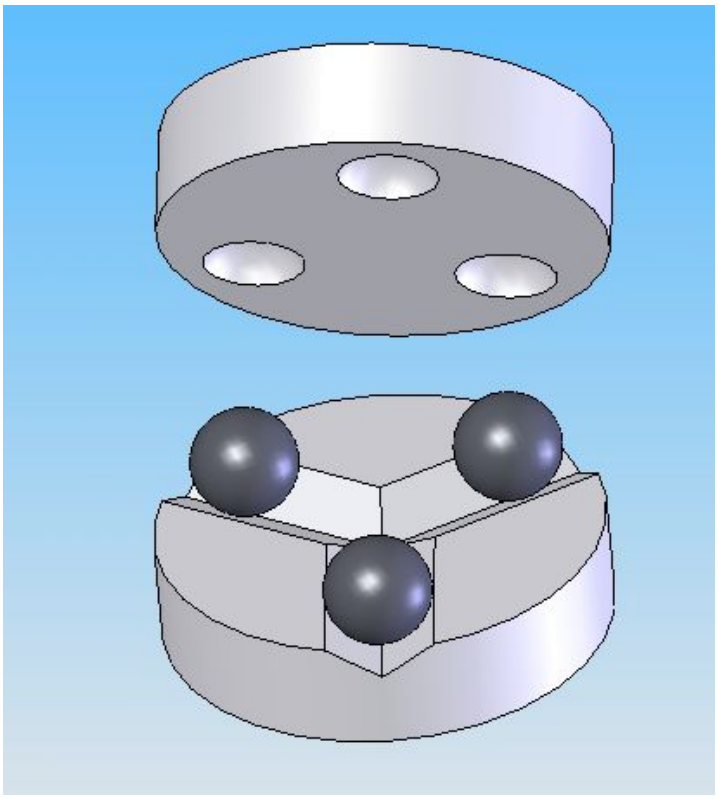

Figure 21. Kinematic coupling for constraining a rigid body in six degrees of freedom.

Taking in consideration the challenges associated with kinematic mounting techniques, they represent an ideal way to locate optical components in diamond-turned optical systems. Particularly when the capability to diamond machine non-rotationally symmetric optical systems presents itself, the advantages become clear. This is because optical features as well as locating features can be machined in the same setup, preserving the relative placement of these features to within the tolerances of the diamond turning machine. These tolerances are typically around 0.5 μm over the machining envelope of the machine. Additionally, intermediate components that contribute to inaccuracy and lack of repeatability, such as balls, pins, and alignment marks are eliminated.

A kinematic coupling generated by diamond turning would look something like that shown in Figure 22. The figure shows the features greatly exaggerated for clarity. The ball features on one component, the mirror, mate with the grooves on the other component, which is part of the support frame. The ball features on the mirror are produced in the same setup as the mirror surface, possibly even using the same tool, thus preserving alignment between the optical surface and the fiducial surfaces. Similarly, multiple grooves generated with a flycutter on a 4-axis diamond turning machine can be related to each other via the metrology system of the machine.

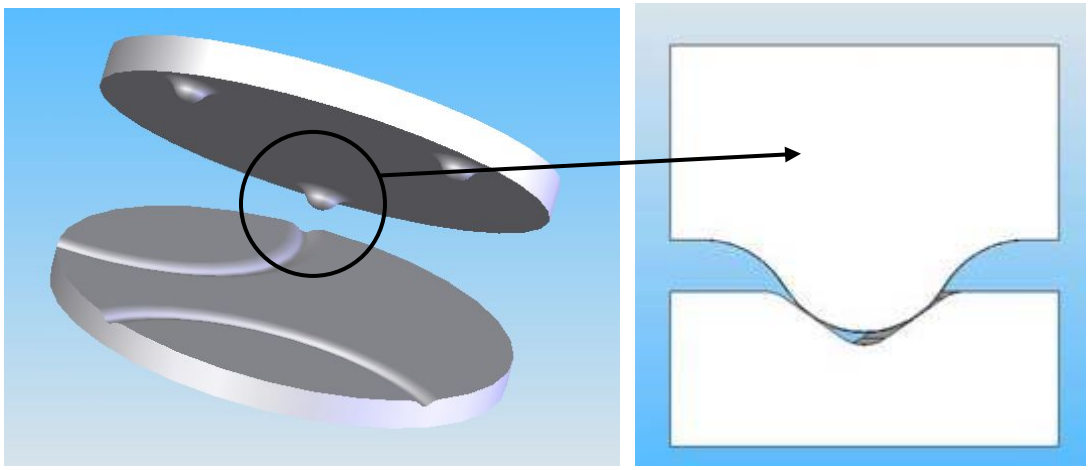

Figure 22. Schematic illustration of kinematic coupling on mirror blank top and telescope housing

5.6.2 CONTACT STRESSES ON FIDUCIAL FEATURES

Two main concerns must be addressed to design a kinematic coupling; elastic contact stresses and friction. The elastic contacts can produce yield of the surface and friction can prevent the surfaces from aligning properly if the if the loads and geometry are not selected correctly.

Contact stresses The elastic contact stresses between the ball features on the mirror fiducial surface and the grooves cut into the housing must be less than the bearing yield stress, 379 MPa, of the 6061-T651 aluminum material selected for the system. The stress will depend on the load and the geometry of the mating surfaces.

The equations to calculate the Hertz contact stress for the generalized case of two mating surfaces each defined by a radius of curvature in two orthogonal planes is discussed below. A sketch of the mating surfaces defining the two planes and radii is shown in Figure 23. At the contact point, the relative sizes of the radii control the contact stress. The smaller the surface radius, the larger the contact stress for a given load. The dimensions of the contact surface will

be an ellipse with a major radius of "*a*" and a minor radius of "*b*". An expression of contact dimensions are given in Equation 1.

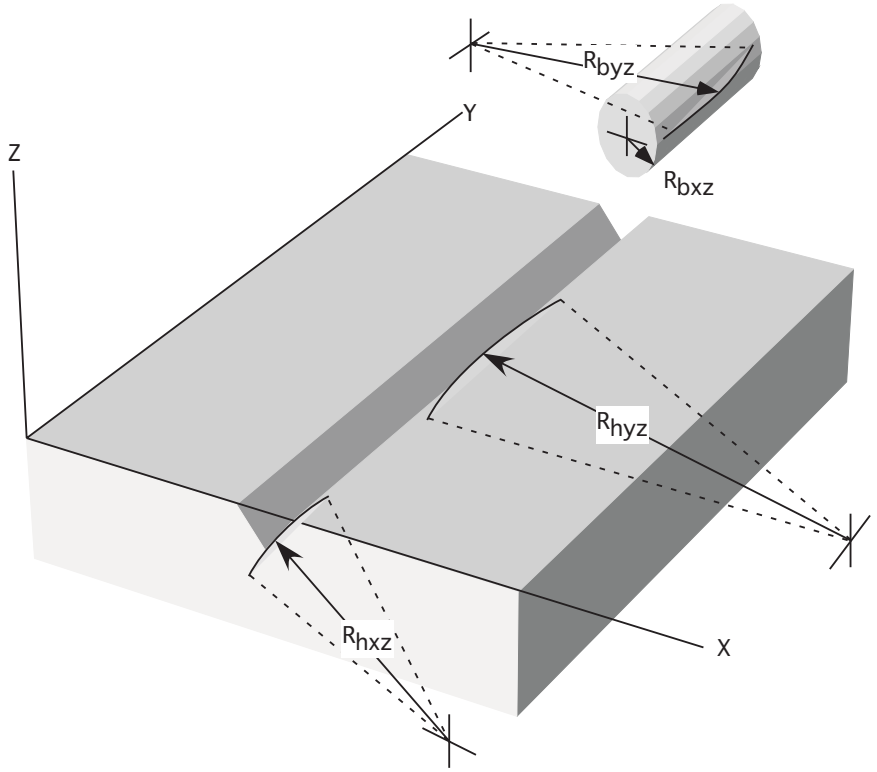

Figure 23. Definition of the contact radii on the housing (h) and the ball features (b)

$$a = m\sqrt[3]{1.5\frac{P\left(1-\nu^2\right)}{E(A+B)}}$$
$$b = n\sqrt[3]{1.5\frac{P\left(1-\nu^2\right)}{E(A+B)}} \qquad 1$$

where *m* and *n* are parameters dependent on the radii of Figure 23, *P* is the load applied to a single contact, *E* is the elastic modulus of the material and *A* and *B* are geometry factors dependent on the two radii of each contact component.

The size of the features on the ball and the housing must be carefully selected to keep the maximum stress less than the bearing stress of the 6061 aluminum and to keep the slope of the surfaces such that the friction does not prevent seating of the balls on the slots.

5.6.3 MIRROR FIDUCIAL FEATURES

Based on the calculated stresses for different ball and groove shape, an acceptable feature size has been determined that can be fabricated with the existing equipment in the PEC. Figure 24 shows a schematic of how the ball features are machined in the same process as the optical surface using the Fast Tool Servo (FTS).

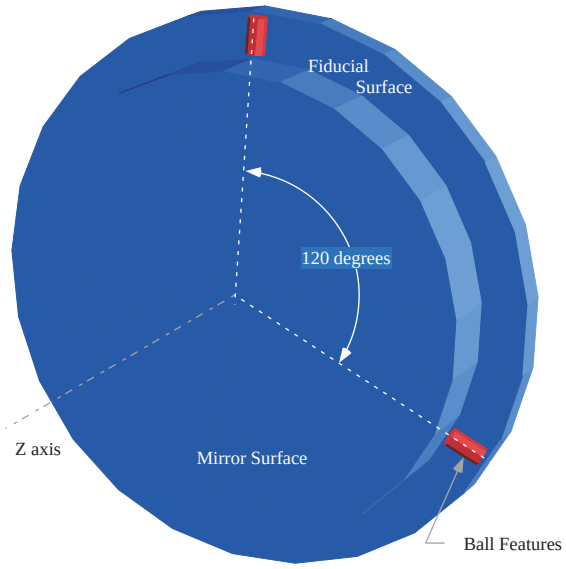

Figure 24. Sketch of the mirror surface showing the ball features on the outside fiducial surface

Figure 25 shows the details of an example of alignment features machined on the face of the mirror. Just as the FTS moves rapidly in the z-direction as the part is being rotated by the spindle to generate the NRS optical surface, it also moves to generate the alignment ball features. The features are shown greatly exaggerated for clarity. In the actual part, the ball features would have a height of only a few hundred μm. The features will be created with a FTS that has a 400 μm range of motion at a maximum speed of 140 mm/sec. By creating a modified cosine wave on the mirror, feature sizes appropriate for the material can be selected. Table 1 shows the spindle speed, slope, radius and contact stress on each ball/slot contact.

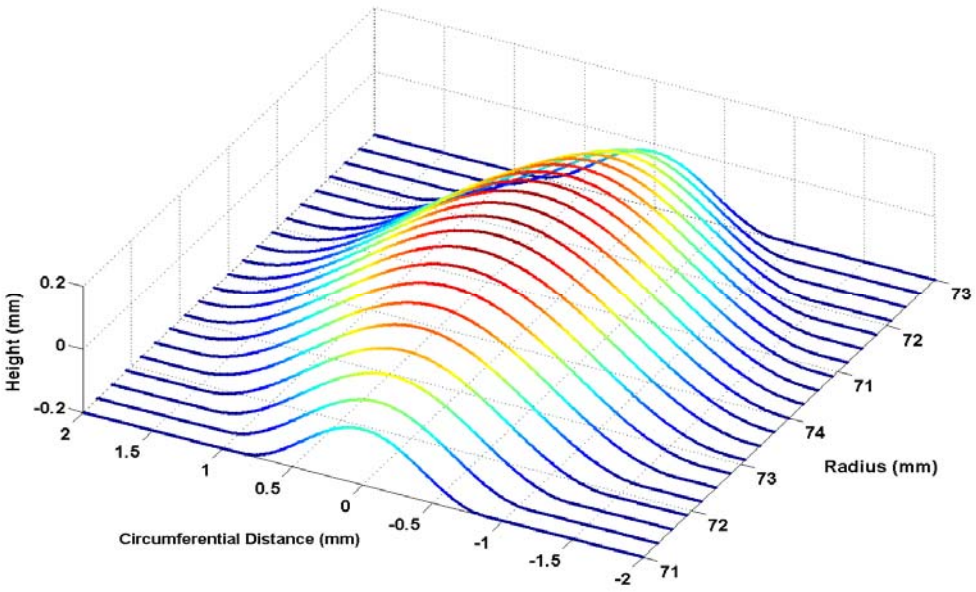

Figure 25. Details of the three ball features on the mirror fiducial surface

Table 1. Operating conditions to fabricate ball feature on the fiducial surface

Mirror		
R_{bxz}	40	mm
R_{byz}	6	mm
Housing		
R_{hxz}	1000000	mm
R_{hyz}	1000000	mm
Load	25	N
Ball Fabrication conditions		
spindle speed	50	rpm
Average radius	72.5	mm
surface speed	379.60	mm/sec
Amplitude of cosine	0.2	mm
Wavelength of cosine	4	mm
max slope	18.00	deg
variform speed	123.34	mm/sec
minimum radius of cosine	2.02	mm
slope at housing contact	16.9	mm/mm
radius at housing contact	5.9	mm
Min slope for engagement	14	deg
Engagement range	4	mm

Ideally, the same tool will be used for the optical figuring as for the fiducials to guarantee relative placement, though the rotational nature of the turning operation allows very precise positioning of several different tools through Ogive error measurement. Additionally, the deconvolution algorithm described in the fabrication section will allow the relatively high-frequency content signals involved in fabricating the fiducials to be corrected for phase and attenuation.

5.6.4 TEST ASSEMBLY FIDUCIAL FEATURES

To test the principle and implementation of the quasi-kinematic assembly technique, the test tube and mirrors will be machined with kinematic features. The tube will be machined with a flycutter to produce arcuate grooves similar to the ones shown in Figure 22. Bumps will also be machined around the perimeter of the mirror. The final assembly will appear as shown in the schematic in Figure 26. The features in the Figure are exaggerated for clarity. The actual features will be on the order of 200 μm tall. The tube will be mounted on the x-table of the ASG 2500 DTM and a flycutter will machine the grooves. The profile of the grooves will be determined by the toolpath of the axes while the radius will be fixed. The "bumps" on the mirror will be machined using the Variform fast-tool servo in the same operation as the mirror surface to maintain alignment.

5.6.5 DEMONSTRATION SAMPLES

Since the actual features on the tube/mirror assembly will be quite small and delicate, and a means of providing a clearly visible demonstration of the principle, a set of demonstration samples was machined. Shown in Figure 27, the samples are a miniature (75 mm diameter) version of the tube and mirror described previously. They were machined using a standard CNC machine with toroidal section bumps and linear profile grooves. The samples clearly show how the assembly works and gives a good feel for the mounting technique.

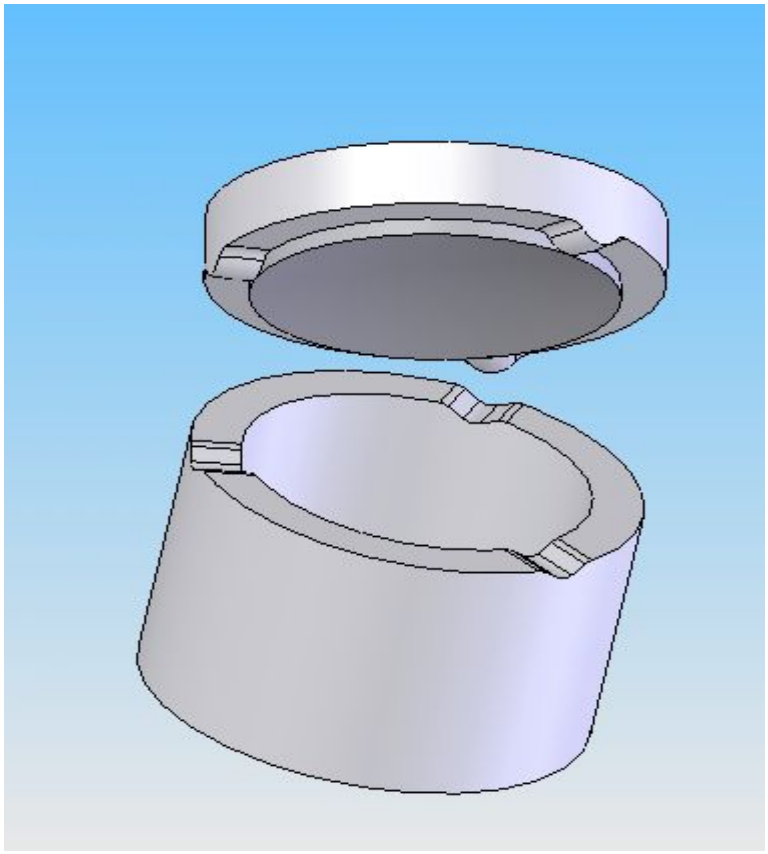

Figure 26. Schematic view of tube/mirror assembly with quasi-kinematic mounting features exaggerated for clarity.

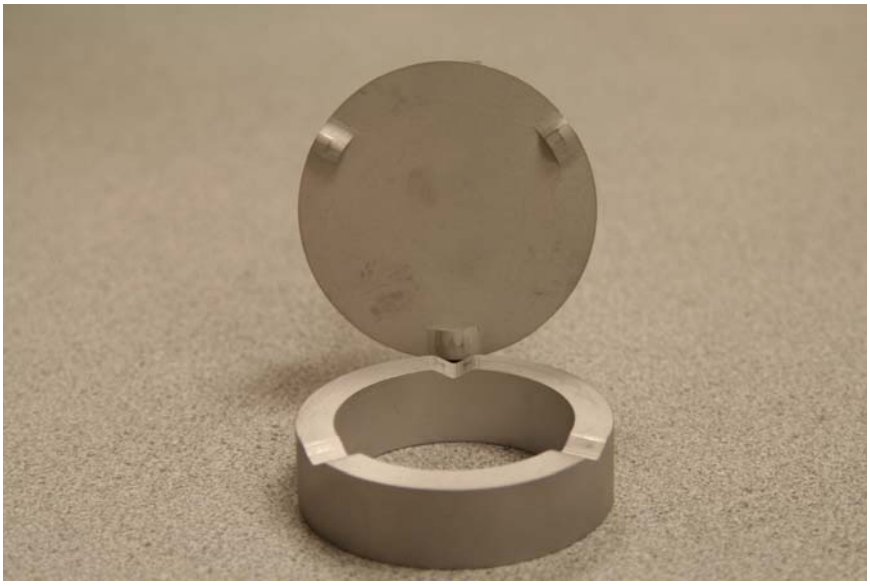

Figure 27. Demonstration assembly of the quasi-kinematic mounting features.

5.7 CONCLUSION

The optical assembly test described here has revealed a number of challenges in fabricating a complete optical system. Fiducial design and location to reduce overconstraint but still provide a rigid mounting can be achieved through optimization of mechanical structures using finite element modeling. Fabrication considerations such as mounting components during machining are pivotal to achieving a high degree of accuracy in fabrication. Often, in complex, multicomponent systems, these considerations are obscured because of the large number of variables. As work progresses on this simplified test system, further nuances in the assembly process will be revealed.

With the development of the test system, a new concept in optical assembly will be tested. The quasi-kinematic features that will be machined on the diamond turning machine to a much greater degree of precision and less overconstraint than in pin/slot mounting system will allow greater ease of assembly and better precision. Finally, a demonstration piece was machined to show the advantages of the new mounting technique.

6 ELLIPTICAL VIBRATION-ASSISTED MACHINING

David Brehl
Graduate Student
Thomas Dow
Professor
Department of Mechanical and Aerospace Engineering

The Ultramill EVAM tool is used to machine MEMS scale features with complex 3-D geometry. A procedure is developed to establish the toolpath needed to produce a desired surface, using the morphological operation "dilation" to determine the required tool center offset given the tool cutting edge profile and the dimensions of the elliptical vibratory motion. Test parts are machined using tools with both round-nose and sharp-nose geometry. The parts made with round-nosed tools have sculpted 3-D and non-orthogonal planar features. These features are up to 20 μm tall, whereas parts previously made by EVAM had heights of less than 1 μm. Because round-nosed tools can only make low aspect-ratio structures with shallow curved sidewalls, sharp-nosed tools are tested as a way to overcome these limitations. Relative motion between a sharp-nose tool's cutting edge and the workpiece is found to result in non-orthogonal cutting, whereas round nosed tools can be modeled by orthogonal cutting. Sharp-nose tools are used to make two types of part: 80 μm tall trihedrons and small (< 15 μm wide) groove structures featuring sculpted 3-D geometry with an aspect ratio of 0.3. Suggestions for improving sharp-nose tool geometry are developed based on examination of these test parts. Tool wear results are presented for sharp nose tools used to machine stainless steel. Thermal expansion of the Ultramill, which can cause form error in parts, is measured and found to be partially caused by expansion of the base block upon which the piezoelectric actuators rest.

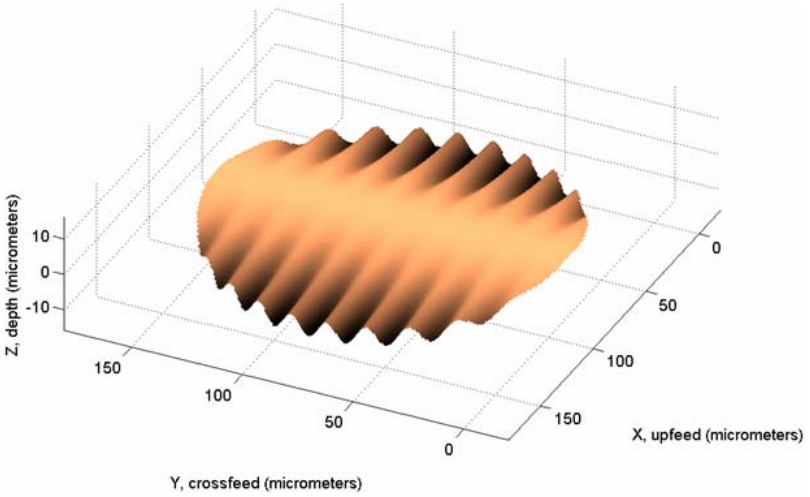

6.1 INTRODUCTION

Microstructures can be defined as fabricated features with critical dimensions in the range 1 to 100 μm. They can be functional small-scale devices in themselves, or features of a large structure. Microstructures can also take the form of ultraprecision molds and dies used in mass replication methods like injection molding and hot embossing. Effective microstructure creation is essential to the success of miniature integrated systems such as micro-electromechanical systems (MEMS), micro-optoelectronics systems (MOEMS), and biomicrofluidic "lab-on-a-chip" packages.

The Ultramill is a precision cutting tool using "elliptical vibration-assisted machining" (EVAM). It avoids many of the issues associated with other methods for micro-device fabrication. In EVAM, a piezoelectrically-driven toolholder moves the tip of a diamond cutting tool in a tiny elliptical path at frequencies of 1 to 4 kHz. This elliptical tool motion is superimposed on the feed motion of the workpiece. Advantages of the Ultramill EVAM process are:

- Optical quality surface finish
- 3-D features at micrometer scale, with sub-micrometer tolerance
- Near-zero burr at the edges of cuts
- Large range of materials that can be machined
- Extended diamond tool life when used to machine ferrous materials

Previously the Ultramill was used to create binary micro-structures in materials such as copper and stainless steel [1, 2]. These included the Angstrom symbol logo at sizes of 1mm square and 200 μm square (hard-plated copper) and the Sandia thunderbird logo (17-4 PH stainless steel). This demonstrated the potential for the Ultramill to create microstructures of arbitrary geometry and smaller than 200 μm overall size, with individual feature resolution as small as 15 μm and surface finishes of 15-25 nm RMS.

Practical microdevices require an ability to create features with complex geometry and minimum sizes < 10 μm. For example a micro-optical component could require a precisely curved surface while a biomicrofluidic device might need steep-sidewall channels of the same dimensional range as a single cell. Many functional microdevices require structures 10's of μm tall with aspect ratios of 1:1 or better. In comparison the binary features in Figure 1 are < 1 μm tall relative to the background. The goal of the present research is to demonstrate the ability of the Ultramill to make microstructures with characteristics such as a horizontal resolution of ~10 μm, vertical aspect ratio approaching 1:1, steep and/or straight sidewalls, and complex sculpted 3-D or non-orthogonal planar geometry.

6.2 EVAM PROCESS AND EQUIPMENT

Figure 1 depicts the Ultramill's elliptical tool-tip motion generated by a pair of piezoelectric actuators. Sinusoidal voltage signals, 90 degrees out of phase, are supplied to the two parallel actuators. The linear motion of the actuators is converted to an elliptical tool motion by means of a mechanical linkage that is part of the toolholder design. The ellipse dimensions can be varied by changing the amplitude and relative phase of the voltage signals applied to the actuators.

The elliptical tool motion is superimposed on the upfeed motion of the workpiece. Thus the toolpath takes the form of overlapping ellipses. The geometry of successive overlapping ellipses results in chips with a maximum thickness that is less than the chip thickness (depth of cut). This causes tool forces to be significantly smaller than in conventional diamond machining. The reduced tool forces mean that in EVAM vibration and chatter are suppressed, resulting in improved surface finish and permitting smaller features to be made at tighter tolerances. The periodic entry and exit of the tool from the work creates cusp-like features regularly spaced in the upfeed direction. Short, discontinuous chips are created when the depth of cut (DOC) is smaller than the semi-minor axis of the toolpath ellipse. This is because the tool tip exits the workpiece before its motion reverses relative to the work feed, and so the chip edge is cut from the work material.

The Nanoform diamond turning machine (DTM) provides 3-axis X-Y-Z motion for raster machining (the spindle is currently locked when using the Ultramill). All three axes possess hydrostatic oil bearings and nanometer-accuracy positioning ability. Laser interferometers give position feedback information for the X and Z axes, while a linear encoder is used by the Y-axis. A UMAC controller provides motion and control commands to the Nanoform axes, with the capability to execute motion programs written using standard CNC ‘G’and ‘M’ codes. A vacuum chuck on the spindle face holds the workpiece during machining. A side-mounted video microscope camera affords a view of the tool rake face and the work surface, to facilitate touchoff. A second video microscope camera is mounted on the Y-axis adjacent to the Ultramill, as shown in Figure 2(a). This gives a magnified aerial view of the workpiece surface. Figure 2(b) depicts how the Y-axis camera is used to position the tool tip at a specified X-Y location. The desired location is lined up with the camera crosshairs on the video display. The workpiece is then translated through pre-determined X and Y offsets to position the tool tip at the correct location.

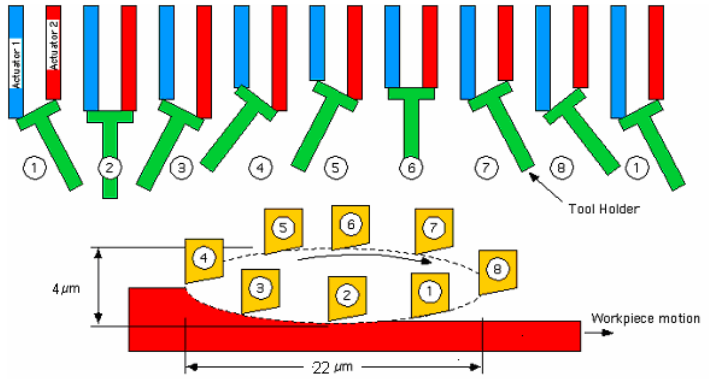

Figure 1. Ultramill Vibration-Assisted Machining Concept

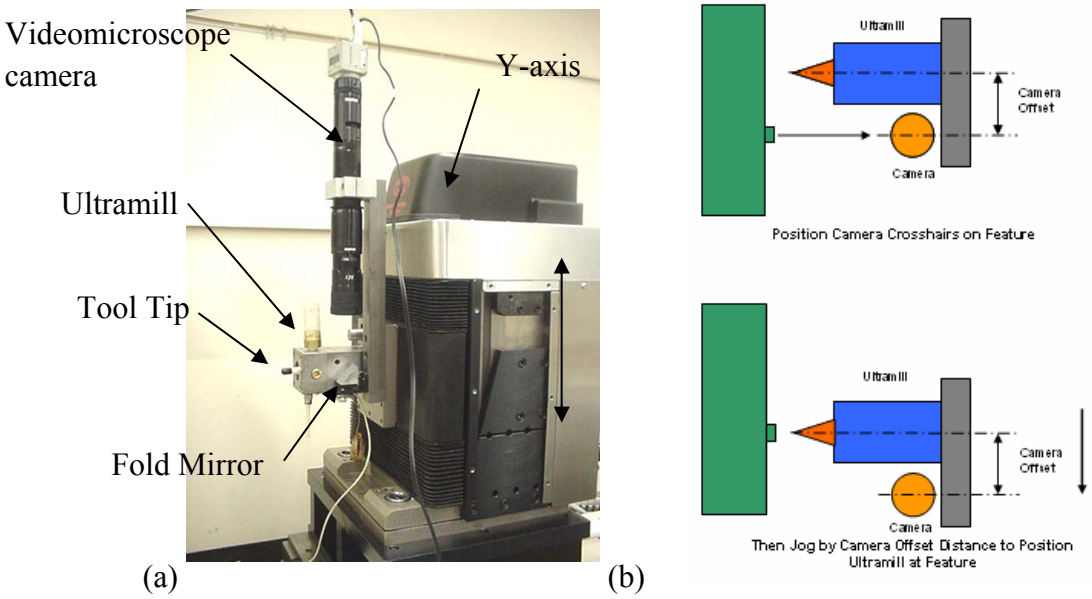

Figure 2. (a) Nanoform Y-axis with video microscope camera for plan view of workpiece. (b) Top view of Ultramill showing microscope alignment of tool to part.

6.3 DETERMINING TOOL PATH FOR 3-D MICROSTRUCTURE FABRICATION

Features with arbitrary non-rotational geometry can be made by raster machining. Figure 3 shows the required sequence of axis moves for several adjacent crossfeed passes. Prior to cutting at the start of a pass, the tool is at crossfeed position *Y* and is raised from the workpiece surface. The tool moves downward to contact the workpiece (motion 1) and then in the upfeed (X) direction to execute a cutting pass (motion 2). During the cutting pass the depth of cut is varied to create the contours of the desired surface. At the end of the cutting pass, the tool moves vertically upward to disengage from the workpiece (motion 3). It then retracts back along the upfeed pass to the original position (motion 4), and steps incrementally in the crossfeed (Y)

direction to a new starting position (motion 5). The sequence is repeated, with the depth of cut varied along the new upfeed pass as required make the specified surface.

For EVAM, the toolpath commanded by the motion program represents the motion of the centroid of the vibration ellipse. At each point in an upfeed pass, the toolpath must be offset from the desired machined surface in both the Y-Z and X-Z planes. The offset in the Y-Z plane is determined by the profile of the tool's cutting edge, and is the difference between the centroid and the point(s) of contact of the edge profile with the surface. This Y-Z offset is not different from the situation in conventional diamond turning. However, in EVAM the centroid must also be offset in the *X-Z* plane by the difference between it and the tangent point between the machining ellipse and the surface. The combined X-Z and Y-Z offsets form the bottom portion of an ellipsoidal surface with a cross section the same as the tool's. When its centroid is placed at any location on the correct toolpath, this ellipsoid is always tangent to the desired part surface at one or more points, but never intersects it.

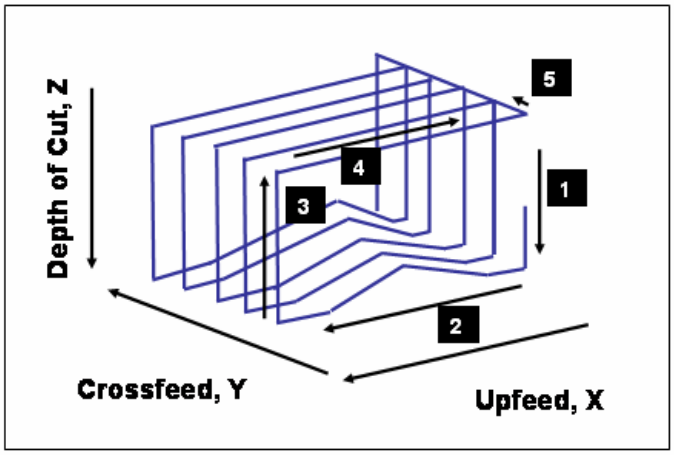

Figure 3. Raster machining of a part with 3-D geometry. (1) Move to contact workpiece (2) Upfeed cutting pass with variable depth of cut to machine contoured surface (3) Withdraw from workpiece (4) Backfeed (5) Incremental crossfeed move to position for next pass.

Given the machining ellipse geometry, tool cutting edge profile and toolpath, determining the resulting surface is relatively straightforward. The inverse problem—finding the correct toolpath to generate a specified surface—is usually more difficult. The toolpath required to produce a specified surface can efficiently be determined using the morphological operation of "dilation". This operation is well-developed for image construction by contact microscopes such as the Atomic Force Microscope (AFM) [4]. It is also used in image processing, and supporting software is readily available (e.g., the MATLAB Image Processing Toolbox). For a probe tip of known geometry, dilation is used to construct an "image" of a surface. This is illustrated conceptually in Figure 4 (for clarity only a profile is shown in the figure, but the results are applicable to 3-dimensional surfaces). A probe is positioned above the target surface. The probe

then approaches the surface until it makes contact at one or more points. Dilation makes use of set theory operations such as union, intersection, and translation to determine when the probe is in contact with the surface, avoiding complicated analytic geometry calculations to determine the contact points. The location of the probe apex at contact defines the image height or Z coordinate for the X-Y coordinates of the apex. By probing the surface at multiple points an image can be constructed for the entire surface.

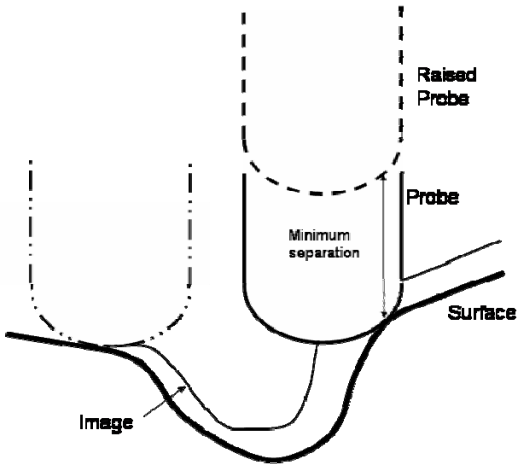

Figure 4. Concept of dilation

An inverse operation, "erosion," can be used with a probe of known geometry to reconstruct the surface resulting from a specified image. Erosion is therefore equivalent to predicting the error-free machined surface resulting from a motion program. It is evident from Figure 4 that there is a resolution limit resulting from the probe geometry. Surface features smaller than this limit are not captured in the image. Nor will they appear in a surface reconstructed by eroding the image produced from the probe's dilation of the surface.

A MATLAB program was written to generate toolpaths using the dilation operation. The desired surface *S* is defined within the program as $S= Z(X,Y)$, where $Z(X,Y)$ is the depth of cut relative to a datum plane at each upfeed point *X* and crossfeed point *Y*. The program creates a MATLAB representation of *S* at an *X-Y* resolution of 1 μm, using either an analytical expression or an operator-defined input data set. A morphological probe is created using the tool nose radius and the dimensions of the machining ellipse. This probe also has an X-Y resolution of 1 μm. The image *I* is then obtained by dilating *S* with the probe using the appropriate MATLAB image processing functions.

The program next determines the actual toolpath for each raster machining pass and generates G-code commands used by the diamond turning machine's controller. The toolpath in each raster pass is the set of X and Z points in *I* at the crossfeed coordinate of the pass; if the spacing

between crossfeed passes ΔY is a constant, then the crossfeed coordinate of the Nth pass is $N*\Delta Y$. The toolpath extracted from image I at crossfeed coordinate Y is a set of points spaced at 1 μm intervals in the upfeed (X) direction, which very closely approximates the required curvilinear toolpath. For each raster pass the toolpath's critical points (minima, maxima, or inflection points) are found, and the intervening curve is approximated by 2 to 8 linear moves, depending on the curvature of the toolpath segment. The end points of these linear moves are used as X and Z coordinates in the G-code commands.

Figure 5 shows toolpath planning for a simple microstructure which has a constant section in the crossfeed direction. In this case the toolpath for all raster passes are identical. The morphological probe is defined by the elliptical vibration path, and the image produced by dilation is seen to be the path followed by the ellipse's center when it is tangent to all points on the surface. If the feature was non-uniform in the crossfeed direction, then each raster pass passes would be different, and would need to include the effect of offsetting the toolpath from the contact point of the tool cutting edge with the surface.

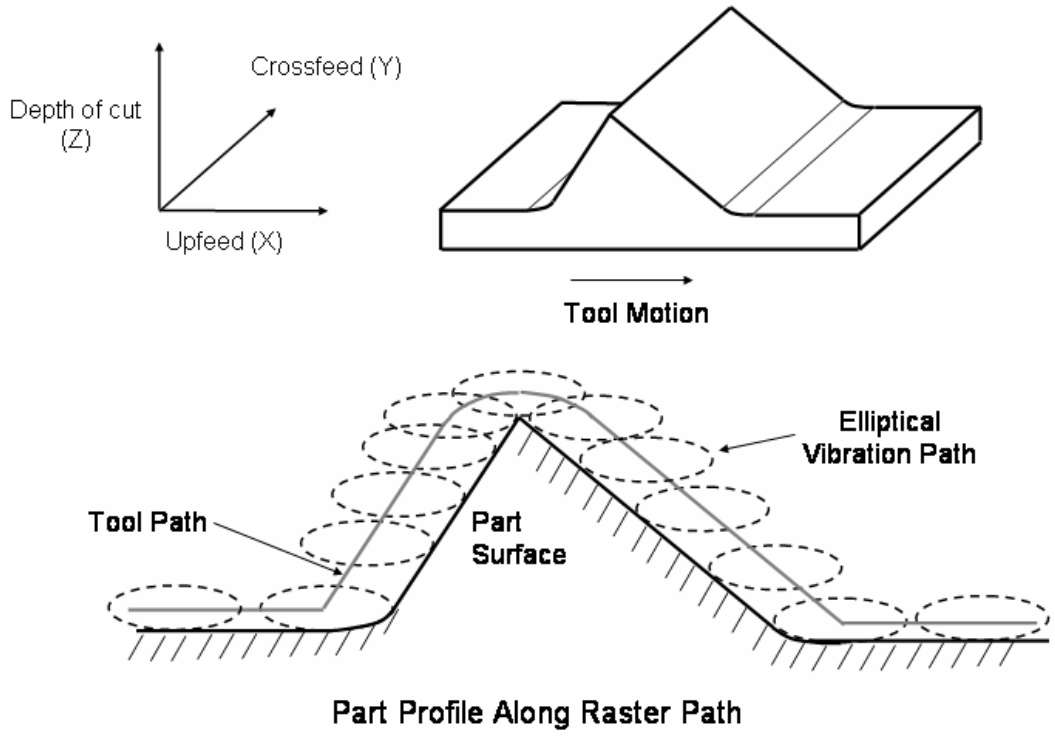

Figure 5. Toolpath planning for a simple 3-D feature. The part *(oblique view)* is created by raster machining in the upfeed direction. The toolpath required to create the part surface *(cross section along raster path)* is obtained from the center points of the elliptical vibration path when it is tangent to all points on the surface.

6.4 3-D MICROSTRUCTURE FABRICATION—ROUND-NOSED TOOLS

Microstructures with 3-D geometry were machined in hard-plated copper using a single-crystal diamond tool with 1 mm nose radius, 0° rake angle, and 10° clearance angle. The toolpath planning method described in Section 6.3 was used to create the motion programs. Two of the part designs—a convex section of a cylinder, and a groove with sinusoidal profiles in upfeed and crossfeed directions—required making curved or sculpted 3-D geometry. A third part was designed to have planar surfaces not orthogonal to the machining axes. These features had a vertical relief of 7 to 20 μm. In comparison, the binary features previously made with the Ultramill have a vertical relief of < 1 μm.

6.4.1 SCULPTED 3-D FEATURES

Figure 6(a) shows an SEM image of a part with a convex cylindrical surface, oriented with its longitudinal axis parallel to the upfeed direction. The design cylinder radius is 1000 μm, with a chordal width of approximately 400 μm and a length of 1 mm. From the flat background to the top of the part is 20 μm. The part was machined with a single series of crossfeed passes at a spacing ΔY=5 μm, and took 58 minutes to complete. Figure 6(b) is an interferogram of the part obtained using the Zygo New View white-light interferometer. Figure 7 shows a cross section of the top of the cylindrical part extracted from the interferometry data. A least-squares best-fit circle was applied to this cross section to estimate the radius of the machined feature. The feature radius is estimated at 1133 μm, indicating the part has a dimensional error of about 11% compared to the design radius of 1000 μm. The residuals between the measured surface and the best fit radius are approximately the outward normal surface profile of the part. For the cross-section in Figure 7 this corresponds to a crossfeed surface roughness of approximately 100 nm PV. This compares with a crossfeed surface roughness of 30 nm PV in the flat portion of the part background. The theoretical crossfeed roughness derived from the tool radius and crossfeed spacing is 3.1 nm.

Figure 8 shows a part consisting of parallel grooves with sculpted 3-D geometry. The grooves have a sinusoidal section in the crossfeed direction, which is superimposed on a cosine profile in the upfeed direction. The width (or wavelength) of each groove is 320 μm and their maximum depth is 5 μm, giving an aspect ratio of 0.016. The length (or upfeed wavelength) of the part is 1.28 mm with the amplitude of the sinusoidal section 4.5 μm. The part was machined with a crossfeed spacing between raster passes of ΔY = 5 μm. This part took 51 minutes to cut.

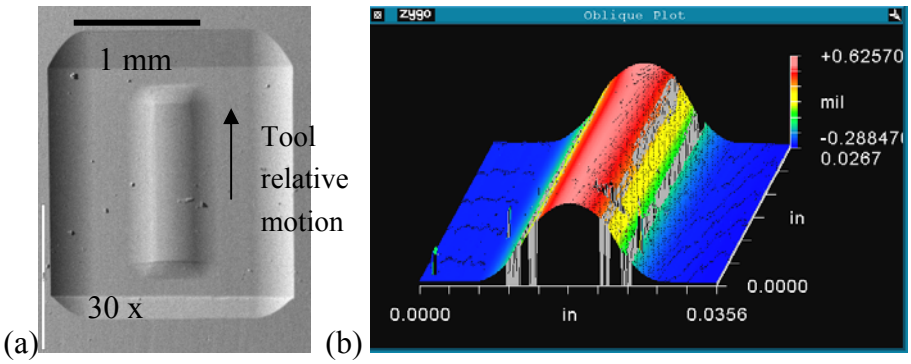

Figure 6. Convex cylinder feature machined in hard-plated copper with 1 mm nose-radius tool. Feature radius 1 mm , height 20 µm. (a) SEM image. (b) White-light interferometer image.

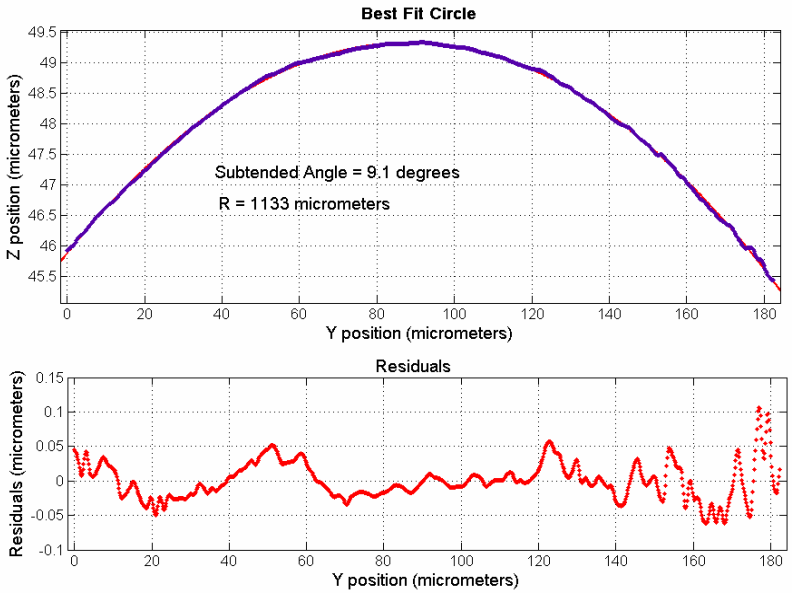

Figure 7. Cross section of cylinder feature in Figure 10, made using white-light interferometer data. Residuals from best-fit circle approximates the outward normal surface profile.

White-light interferometery was used to measure the sinusoidal groove part. The tilt of the surfaces was sufficiently shallow so that data could be obtained over almost the entire part. Figure 9 shows upfeed and crossfeed profiles made from the interferometry data. In the upfeed direction the machined profile closely matched the intended profile. In the crossfeed direction, there is form error with one groove bottom and one ridge top being displaced vertically by as much as 500 nm. It is believed this form error resulted from thermal expansion and contraction of the Ultramill, in the depth of cut direction, during the machining run.

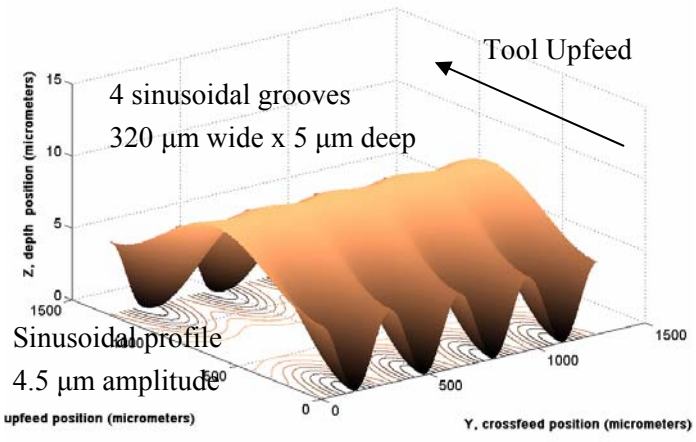

Figure 8. 3-D groove feature with sinusoidal profiles in upfeed and crossfeed direction.

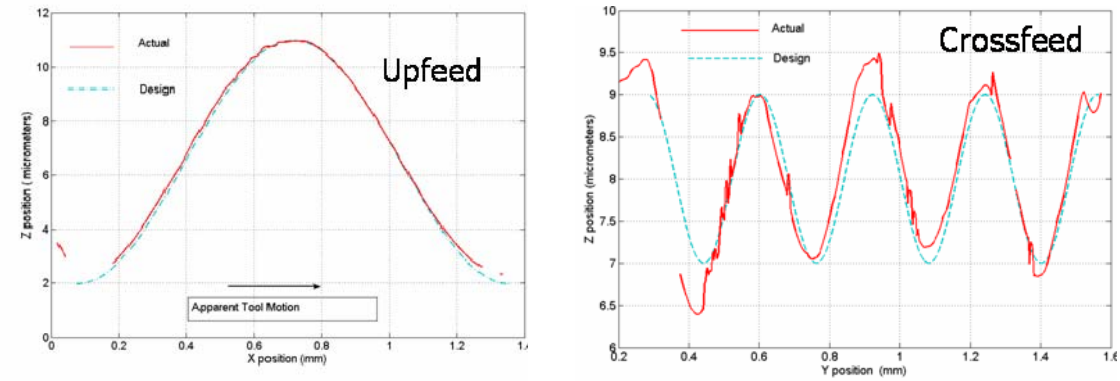

(a) (b)

Figure 9. Profiles of part in Figure 12 from white-light interferometry data. (a) Upfeed profile (b) Crossfeed profile showing form error believed to be caused by thermal instability.

6.4.2 NON-ORTHOGONAL PLANAR FEATURE

The "flying wing" part shown in Figure 10 was made to test EVAM's ability to make planar features that have arbitrary tilt and are not orthogonal to any of the machining axes. The part is 20 µm tall from the background to the vertex. It was machined in 49 minutes with a single series of crossfeed passes at a spacing ΔY=5 µm. Figure 11 shows upfeed profiles at two cross section locations. It is evident that this part has both geometrical and form error as well as unexpected surface features. The tilted "leading edge" surfaces have concave curvature rather than the intended flat surface. This curvature can also be glimpsed in the interferometer intensity map shown in Figure 10(b). Also present in the leading edges are parallel linear features roughly perpendicular to the upfeed motion of the tool. Under the highest possible interferometer zoom these are found to be regularly spaced at an interval of approximately 15 µm and are 20-60 nm

high. The cause of these errors has not yet been determined. Of concern is whether they are the result of an operating or motion programming error—something which can be corrected—or represent a fundamental limitation in the types of structures which can be machined using EVAM.

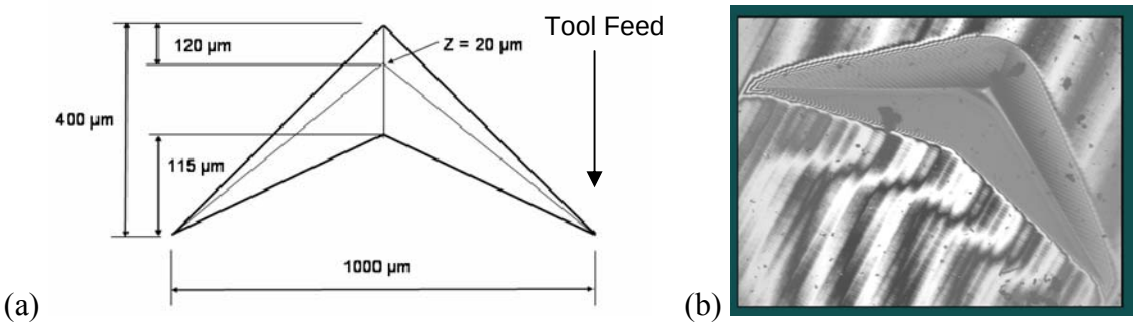

Figure 10. (a) Dimensional sketch of "flying wing" feature with non-orthoganal planar faces. (b) Intensity map image from white-light interferometer. Part is 20 µm tall relative to background.

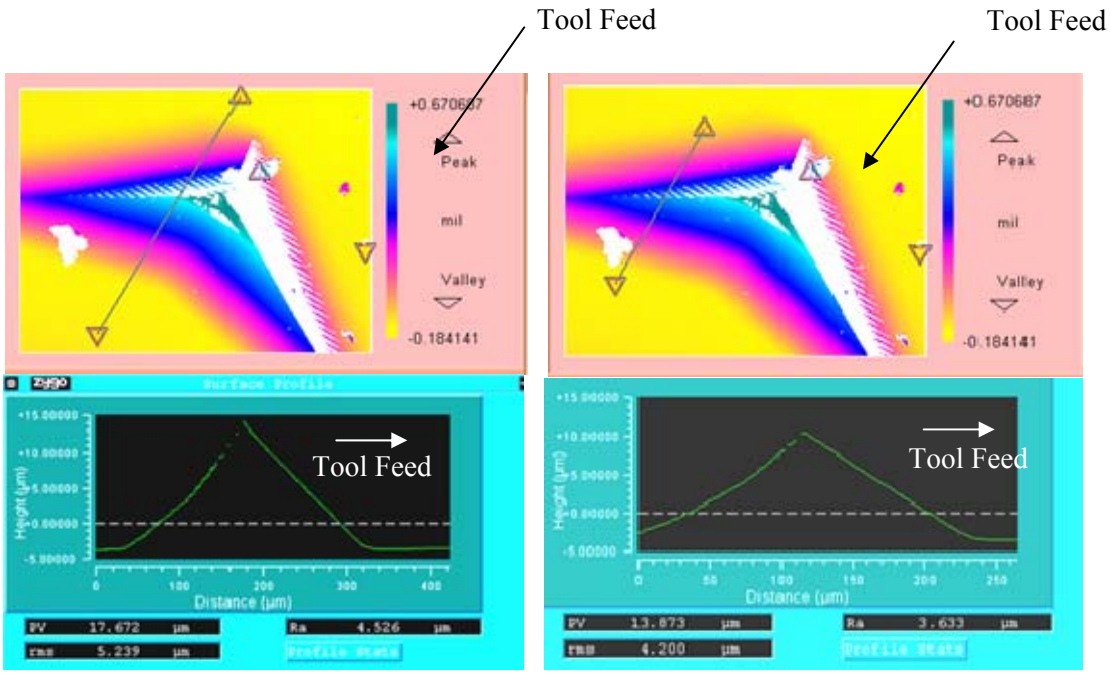

Figure 11. White-light interferometry images of the "flying wing" shape shown in Figure 15. Cross sections show that leading edge has a concave curved cross section instead of being flat.

6.5 3-D MICROSTRUCTURE FABRICATION--SHARP-NOSED TOOLS

6.5.1 TOOL GEOMETRY CONSIDERATIONS

Round-nosed tools are limited in the features they can machine. This is illustrated by Figure 12, which shows the types of grooves and ridges (positive features) that can be cut using a round-nosed tool with a relatively small nose radius of 50 μm. The round profile of the tool results in very shallow curved sidewalls. Increasing the depth of cut simultaneously increases the minimum spacing between adjacent positive features, in proportion to the square root of the ratio of the depth increase. Therefore, only low-aspect ratio features can be created.

A tool with sharp-nosed geometry is suggested as a means of overcoming the restrictions of round-nosed tools. Figure 13(a) shows an SEM image of a sharp-nose tool with a 40° nose-angle. Such a tool was evaluated for cutting features with high aspect ratios, close feature spacing, and straight / near vertical sidewalls. Figure 13(b) shows the size and shape of ridge and groove features that the 40° tool might be used to make. Because of their small cross section area, sharp-edged tools have small material removal rates per raster pass compared to round-nosed tools.

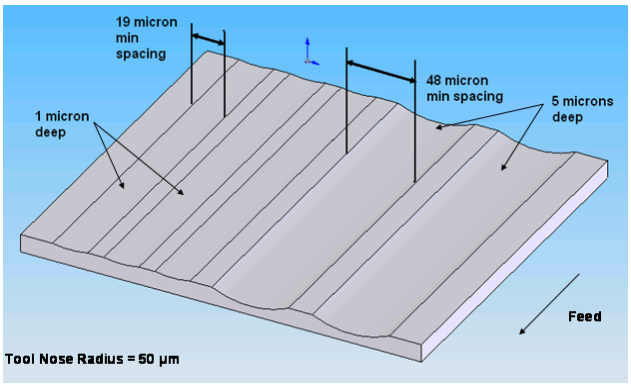

Figure 12. Groove and positive features (ridges) made with 50 μm nose radius tool, illustrating limitations features geometrically possible with round-nosed tools

Figure 14 shows an important difference between round-nosed and sharp-nose tools. The angle ζ between the engaged portion of the cutting edge and the tool vertical centerline is almost perpendicular for a round-nosed tool (even at the sides of the cut where it is maximum, ζ will be only a few degrees for normal conditions when the tool nose radius is much larger than the depth of cut). For a sharp-nose tool ζ is acute and is equal to half the tool nose angle. This leads to different relative velocities between the cutting edge and the work material for the two tools.

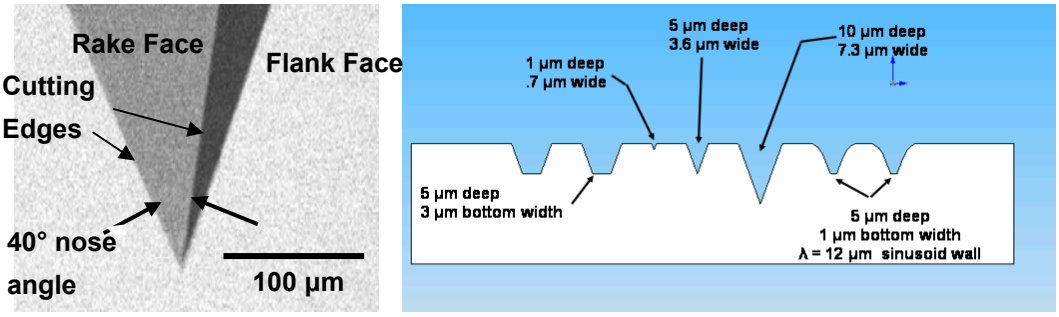

Figure 13. (a) Sharp-nose tool with 40° nose angle (b) Grooves and positive features (ridges) geometrically possible with 40° nose angle tool.

In raster machining the upfeed velocity of the tool, $\dot{X}(t)$ is orthogonal to the cutting edge and is equal to upfeed velocity of the workpiece plus the instantaneous horizontal component of the tool's elliptical motion. The crossfeed velocity $\dot{Y}(t)$ is zero. The vertical velocity $\dot{Z}(t)$ at time t is the instantaneous vertical component of the elliptical motion and is given by

$$\dot{Z}(t) = 2\pi f * B * \cos(2\pi f) \qquad (1)$$

where f is the vibration frequency in Hz and B is the vertical amplitude of the elliptical tool path (equivalent to the semi-minor axis of the ellipse).

As shown in Figure 14 the rake face lies in the yz plane. An alternate coordinate system $y'z'$ can be defined with the y' axis aligned with the tool edge. This done by rotating the yz axes around the x axis through an angle 90°-ζ. The components of the vertical axis motion $\dot{Z}(t)$ in the rotated coordinate system are given by

$$\dot{Y}'(t) = \dot{Z}(t) * \cos(\zeta) \qquad (2)$$

$$\dot{Z}'(t) = \dot{Z}(t) * \sin(\zeta) \qquad (3)$$

$\dot{Y}'(t)$ is the instantaneous relative tool-work velocity directed along the cutting edge and $\dot{Z}'(t)$ is the instantaneous relative tool-work velocity at right angles to the cutting edge.

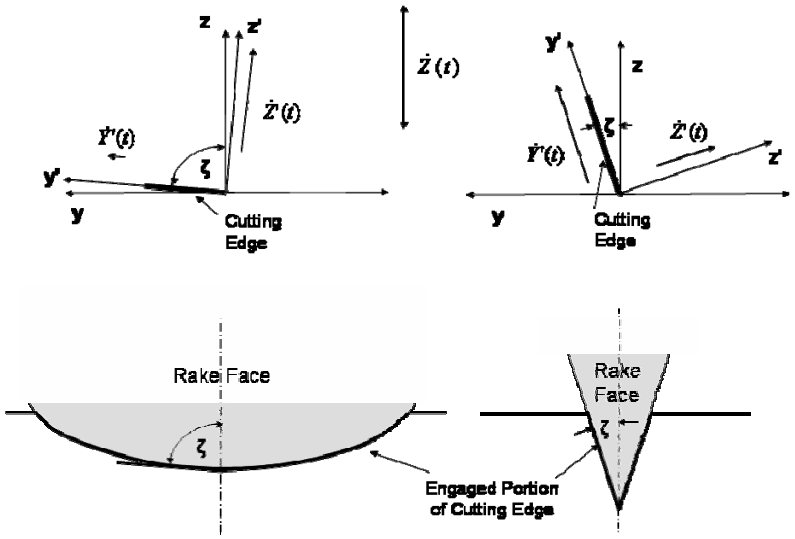

Figure 14. Cutting Edge Relative Velocities for Round-Nose and Sharp-Nosed Tools.

For a round-nosed tool with depth of cut small compared to the nose radius, $\dot{Y}'(t) \approx \dot{Y}(t) \approx 0$ and $\dot{Z}'(t) = \dot{Z}(t)$. There is no relative velocity along the tool cutting edge between the tool and the workpiece, and the motion normal to the cutting edge is the vertical component of the elliptical vibration. In other words, the motion relative to the cutting edge for a round-nosed tool in EVAM is 2-dimensional and orthogonal cutting can be used to model the tool-workpiece interaction. For a sharp-nose tool, ζ is significantly smaller than 90 degrees. $\dot{Y}'(t)$ is non-zero except at the instants when the tool is reversing direction in its vertical motion. This means there is a sideways relative motion along the cutting edge between the tool and workpiece. $\dot{Z}'(t)$ is also non-zero and is at an angle to the tool's vertical centerline. From the perspective of the cutting edge, the tool-workpiece motion is 3-dimensional and cutting is non-orthogonal. Furthermore, the direction and magnitudes of the cutting edge relative velocity components change continuously as the tool moves through the machining ellipse. This 3-dimensional cutting edge motion when using sharp-nosed tools likely has ramifications for cutting dynamics, chip formation and flow direction, kinematics, theoretical surface features, and tool wear. However, they have not yet been explored in any depth. Based on a literature review, this appears to be the first use of sharp-nose tools in combination with EVAM [11].

6.5.2 TRIHEDRON STRUCTURES MADE WITH SHARP-NOSED TOOL

Regular trihedrons 80 μm tall on 112 μm horizontal pitch were machined using a sharp-nose tool with a nose angle of 75.3°. The rake angle was 0°. This tool was "dead sharp"; that is, the nose radius was only about 50 nm or effectively a point. The trihedron array was to serve as a metal master for making polymer corner cubes used in an experiment at Oak Ridge National Laboratory (Oak Ridge, TN). These trihedrons are the tallest features ever made with the

Ultramill. In order to achieve the 80 μm height it was necessary to make repeated cutting passes at progressively increasing depths in the same crossfeed location.

Figure 15 shows how regular trihedron arrays were made by rotating the DTM's spindle after cutting each set of grooves. A first set of parallel grooves was cut, using a local coordinate system based on a datum point located a distance R from the center of rotation (Cut I in Figure 15). The spindle was then rotated through a nominal 60° angle. The part was next translated along the X and Y axes through a distance $\Delta X = R \cos \theta$ and $\Delta Y = R \sin \theta$ to bring the tool back to the datum point for the groove coordinate system where, where θ=60°. A second set of grooves was then machined (Cut II). The part was again rotated through another 60° and the tool translated through ΔX and ΔY, before machining the final set of grooves (Cut III). The spindle motor had insufficient torque to hold a fixed position so the spindle was rotated by hand and locked into place. The spindle axis encoder was used to measure the actual angle of rotation which was found to have a worst case of 0.043° for the intended value. This resulted in a positioning error of 7 μm for the largest value of R used in the cutting experiments, but corrections were made in the ΔX and ΔY translation before machining the next set of grooves. The center of rotation of the part was found using the plan view camera to measure the shift in test grooves when the spindle is rotated. The accuracy of this method is limited to the camera resolution of 5 μm / pixel. When making parts in the future requiring 4-axis machining, a more accurate means of center-finding will be required, such as the center-post method described in [8].

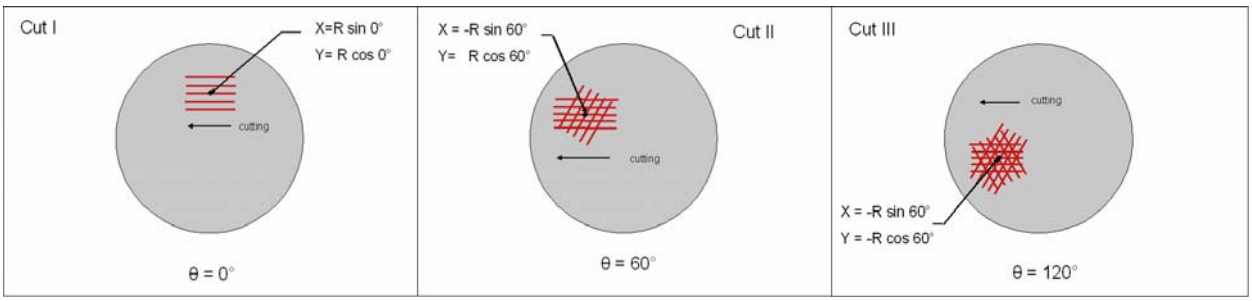

Figure 15. Making trihedrons by rotating spindle 60° between each set of cuts.

Figure 16 is an SEM image showing trihedron features made in hard-plated copper. The edges of the 80 μm tall trihedrons are effectively burr-free. The small interstitial trihedrons resulted from centering error. They are less than 8 μm tall and are the smallest features made to date with the Ultramill. Even at 4000 x (lower right detail in Figure 16) no burr is visible on these features. The sequence used to make these features was 7 cuts each at 10 μm depth of cut, followed by finishing cuts of 4, 3, 2, and finally 1 μm.

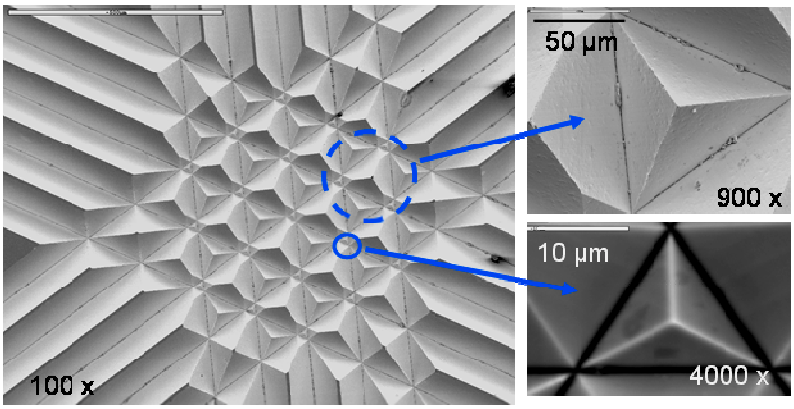

Figure 16. *Left* Array of regular trihedrons machined in hard-plated copper with dead-sharp tool of 75.3° nose angle. *Upper right* 80 µm tall main trihedron feature. *Lower right* Interstital feature approximately 10 µm wide.

Figure 17 shows the results of machining trihedrons in OFHC copper (UNS C1100). This material is softer and more ductile than the hard plated copper. Noticeable edge burr is visible on the trihedrons in Figure 17(a) which used 8 cuts each of 10 µm depth. Figure 17(b) shows the improvement in burr suppression gained by using the same cutting sequence as for the parts made in hard-plated copper (7 cuts of 10 µm followed by finishing cuts of 4, 3, 2, and 1 µm). Burring is reduced, but not eliminated, by the combination of deep material removal followed by progressively shallower finishing cuts.

(a) 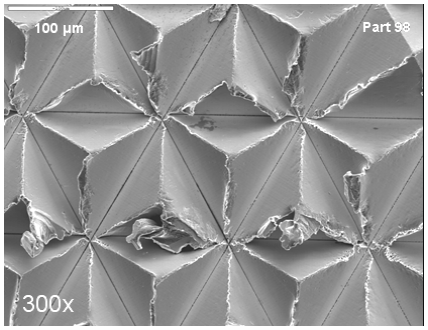

(b) 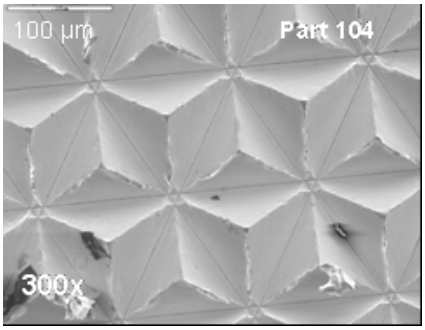

Figure 17. Trihedron features made in OFHC copper. (a) Significant burrs are produced with eight 10 µm deep cuts. (b) Burring is reduced by using 10 µm deep cuts for material removal, followed by a series of finishing passes at small depth of cut.

(a) 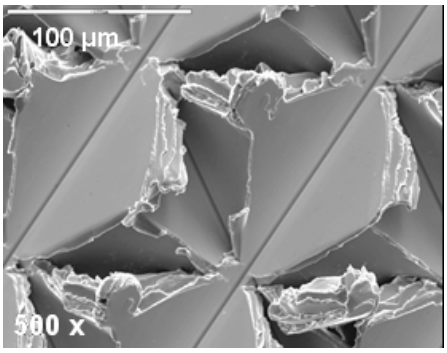

(b) 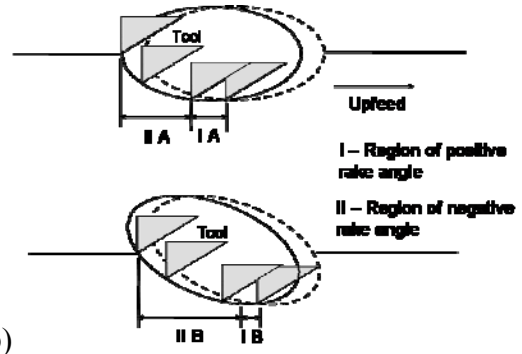

Figure 18. (a) Burr formation when attempting to machine trihedrons in 17-4 PH stainless steel. (b) Tilting toolpath achieves longer distance of cutting with positive rake angle (length of I-B > length of I-A) and smaller value of negative rake during rest of cutting pass. It is suggested that this will help suppress burr formation.

An attempt was also made to machine trihedrons in 17-4 PH stainless steel. Figure 18(a) is an SEM image showing that severe burr formation resulted when cutting this material. Table 1 lists the hardness and ductility (expressed as percent elongation at failure sample failure) for each of the above three materials along with the degree of burring. A qualitative correlation appears to exist between degree of burring and increasing material ductility.

Burring does not occur when the Ultramill is used to machine ductile metals and stainless steel with round-nosed tools [1,2,3,5]. The cutting dynamics of sharp-nose tools are believed to be a principal cause for its appearance here. Cutting with positive effective rake angle for a greater part of the machining ellipse has been suggested as a means to limit burrs [7]. In each vibration cycle, contact with the uncut workpiece material takes place mostly during the upward portion of the elliptical toolpath, so that cutting occurs at an increasingly negative rake angle. A longer length of positive rake angle could be achieved by using a tool with positive rake, or by tilting the machining ellipse relative to the upfeed velocity as shown in Figure 18(b).

Table 1. Properties of Materials Used for Trihedron Fabrication Experiments

Material	**Hard Plated Copper**	**OFHC Copper**	**17-4 Stainless Steel**
Temper	--	H4	Annealed
Hardness (Vickers) [1]	320	110	280
Ductility Index (% elongation)	< 4 [2]	11 [3]	15 [4]
Burr	Negligible	Slight to moderate	Severe

[1] Hardness test by author [2] from R.O. Scattergood [3] Ref [9] [4] Ref [10]

The tool was imaged using the SEM to assess wear following completion of the trihedron machining tests. At this point the accumulated machining distance was a total of 1.6 m in copper and 2.0 m in stainless steel. The actual contact distance (due to the repeated passes in EVAM) was approximately 28 m for copper and 36 m in stainless steel. Figure 19 shows the tool condition before and upon completion of the trihedron machining. Cutting edge radius shows noticeable increase due to wear. The tip of the tool is also worn back from the rake face, consistent with the tip region having the most cumulative contact distance with the material, due to the repeated cuts made at increasing depth in each raster pass. Although wear occurred, it was smooth rather than being irregular with chipping and cracking, similar to that previously noted for round-nosed tools [5].

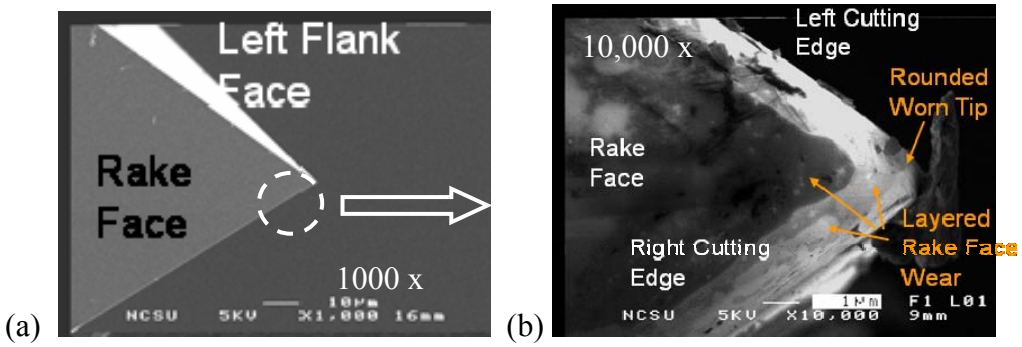

Figure 19. Wear on dead-sharp diamond tool after machining copper and stainless steel trihedrons. (a) Tool before machining (b) Worn tool showing rounding wear on cutting edges and tool tip, and wear back of the rake face from the tip. FESEM images by R. Garcia.

6.5.3 COMPLEX SINUSOIDAL GROOVES

Figure 20(a) shows the design of a part with sinusoidal profiles in the upfeed and crossfeed directions. It is the same part as in Figure 8 (see Section 6.4.1) but on a smaller scale. Ultimately, this groove pattern will be machined onto the contactor pins of the micro-relay shown in Figure 20(b), to demonstrate the Ultramill's ability to add features to a preexisting MEMS component. The groove width or wavelength in the crossfeed direction is 16 μm with a maximum depth of 5 μm for a vertical aspect ratio of 0.31. The wavelength in the upfeed direction is 160 μm with amplitude of 4.5 μm. Since a sharp-nose tool is used, the height-to-width aspect ratio of the groove can be larger than with a round-nosed tool. For example, the part shown Figure 8 was made using a 1 mm nose radius tool and has an aspect ratio of only 0.016. Initially a tool with 40° nose angle was to have been used, permitting a groove width of only 8 μm and an aspect ratio of 0.6. Unfortunately, this tool was damaged before a machining test could be executed, so the part was cut using the tool previously used to make trihedrons (Section 6.5.2). This tool has a 75.3° nose angle, which limited the minimum groove width.

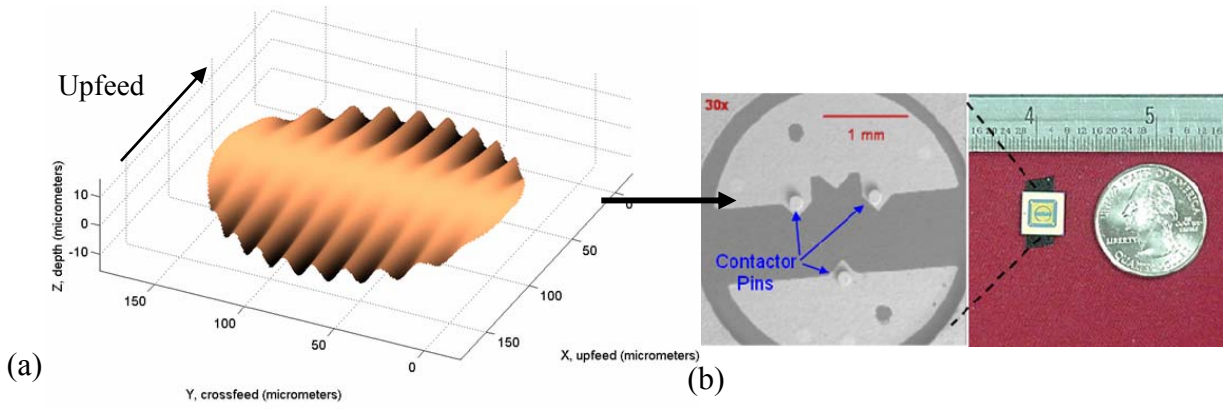

Figure 20. (a) 3-D groove feature with sinusoidal profiles in upfeed and crossfeed direction. Upfeed amplitude 4.5 μm. Crossfeed grooves are 16 μm wide x 5 μm maximum depth. (b) Ultimately, the feature will be machined onto contactor pins of the microrelay.

The part was machined in hard-plated copper. The crossfeed increment ΔY was 500 nm and the part took 81 minutes to make. Useable interferometry data could not be obtained owing to the steep slope of most surfaces on the finished part. Figure 21 is an SEM image of the central region of the part. The bi-directional sinusoidal groove contour is evident but there are at least two issues visible in this image. The first is that the surface is seen to consist of parallel grooves or striations. This is believed to be caused by using a "dead sharp" tool with a nose radius of <100 nm. Figure 22(a) is a sketch showing the theoretical crossfeed surface formed by a dead-sharp tool. The resulting theoretical peak-to-valley height of surface features for a 75.3° tool with 500 nm crossfeed spacing is 650 nm. This result suggests that in the future, a "hybrid" tool should be considered, such as that sketched in Figure 22(b). It retains the straight cutting edges and the acute nose angle of the dead-sharp tool, but its nose radius of 1 to 2 μm allows formation of smoother surfaces. For example, a tool with 1 μm nose radius used at 500 nm crossfeed spacing will produce a theoretical P-V surface roughness of 62.5 nm.

Burrs are also visible in Figure 21. Wide "ribbon" burrs occurred in the portion of the part where the tool was entering or exiting the workpiece. The ends of several of these burrs can be seen at the margins of the figure. Smaller local burrs also are visible on the contoured surface. The tool was used after attempting to machine trihderons in stainless steel, and as shown in Figure 19 the cutting edges were worn. It is believed that the worn tool caused these burrs.

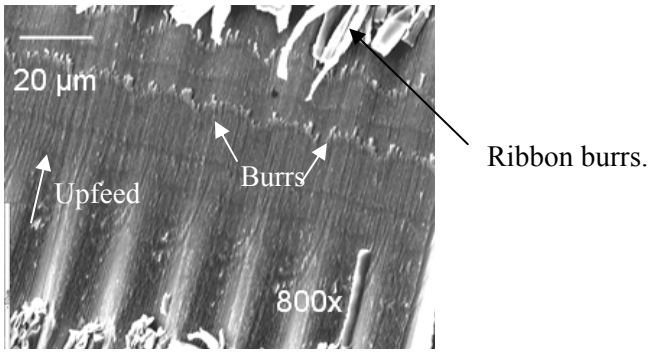

Figure 21. SEM image of central section of sinusoidal groove part shown in Figure 23.

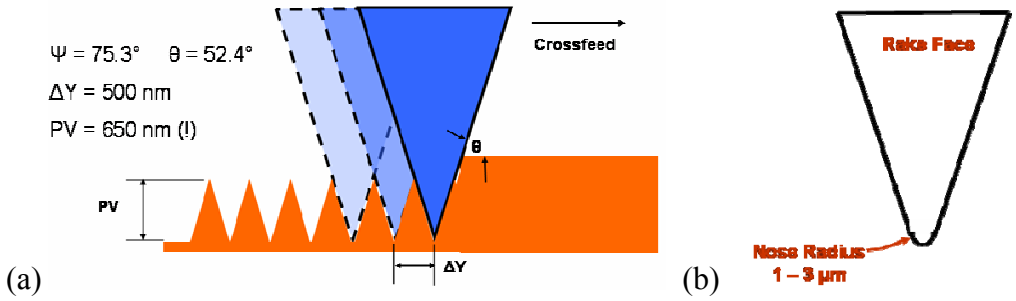

Figure 22. (a) Surface features created by a dead-sharp tool.
(b) "Hybrid" sharp-nose tool with small-radius tip.

6.6 ULTRAMILL THERMAL STABILITY

6.6.1 BACKGROUND

Thermal stability of the Ultramill has long been a concern, since temperature variations of its structural elements will cause thermal expansion or contraction in the depth of cut direction. This will result in form error in the machined surface, potentially of extreme degree. An RTD (resistance temperature device) is installed on the face of one piezo actuator stack to provide a general indication of the stack temperature during operation. While machining parts the indicated stack temperature has been observed to fluctuate, sometimes very rapidly, and over a range of more than 1 °C. Temperature transients with a duration of up to a few tens of seconds can cause form error between adjacent or across several raster passes, while longer excursions can cause error over the entire part. For example, the cross-section view of the sinusoidal groove feature shown in Figure 9(b) displays elevation errors of up to 500 nm, which are believed caused by thermal variations in the Ultramill.

Figure 23 shows the assumed thermal expansion for the Ultramill in the depth of cut direction. Assuming no expansion caused by the diamond turning machine, the thermal expansion at the tool tip is the combination of the individual expansions of two elements, the piezoelectric actuator stacks and the base block which supports them and anchors them to the Y-axis. The cooling chamber housing is coupled to the stacks by the titanium preload diaphragm acting through the toolholder, and any expansion by it is absorbed by the diaphragm's flexibility. Thermal expansion in the ceramic toolholder is assumed to small. The Ultramill's thermal expansion at the tooltip, ΔZ, is therefore given by

$$\Delta Z = \sum_{i=1,2} \alpha_i * \int_0^L \Delta T_i(z) dz \qquad (4)$$

where i=1,2 are the base block and piezo stacks respectively. L is the overall length of each component (22 mm for the stacks and 76 mm for the base block), α_i is the component coefficient of linear expansion (11 x 10^{-6} / ˚C for the steel base block, 3 x 10^{-6} / ˚C for the stacks) and $\Delta T_i(z)$ is the local temperature difference from the reference temperature at location z, with z=0 the end of the component closest to the DTM Y-axis. Unfortunately, the Z-axis temperature distribution in the stacks and base block is believed to be complex. Negishi [3] modeled the stacks and found that their temperature distribution was non-linear and three-dimensional and, in any case, is usually not known in any detail. Therefore, at best, Equation 4 can be used only to make order-of-magnitude estimates of ΔZ.

Thermal energy is released during operation by hysteresis in the piezoelectric stacks when they are driven cyclically. The heat generated by both stacks is $k*C*f*V_{pp}^2$ where C is the capacitance of a single stack, f is the vibration frequency, V_{pp} is the peak-to-peak value of the sinusoidal voltage signal applied to the actuators, and k is a constant representing the portion of the total electrical energy supplied to the stacks which is lost as heat. For the semi-circular stacks currently installed, Q_{STACK} is estimated to be 13.1 W with f=1000 Hz and V_{pp}=400 V.

Heat transfer within the Ultramill is complex. Most, but not all, of the thermal energy generated in the stacks is transferred by convection to the coolant. The remainder of the thermal power input is transferred from the stacks by conduction to the base block. Heat can be transferred from the base block to the coolant by convection, to the environment by convection, and to the cooling chamber housing by conduction. A plastic thermal barrier insulates the base block from the Y-axis. The cooling chamber housing can transfer heat to the environment and to the coolant by convection. Only when all components are in thermal equilibrium with one another will temperatures remain constant. Otherwise, heat flows between components, which changes their temperature and consequently their dimensions as a result of thermal expansion or contraction.

Thermal capacitance is the product of an element's mass and the specific heat of its constituent material, and is a measure of how much energy is required to cause a unit temperature change.

The total thermal capacitance for both piezo stacks in the Ultramill is 32 J/˚C while for the base block it is 966 J/˚C. This means that the stacks can be expected to show large, relatively rapid responses to change in net thermal input. The base block will change temperature more slowly and can be expected to dominate the long term thermal behavior of the Ultramill.

6.6.2 EXPERIMENTAL SETUP

Type "K" thermocouples were installed on the Ultramill at seven locations to obtain temperature data. An eighth thermocouple was used to monitor ambient temperature in the vicinity of the toolholder. Figure 23 shows the location of these temperature sensors. The thermocouple for monitoring stack indicated skin temperature, TC6, was taped to the stack on the face closest to the Ultramill centerline (inboard face), approximately on the longitudinal centerline. The piezo stacks were previously determined to have a significant 3-D temperature distribution [3] so this measurement at a single point is only representative of the direction and magnitude of stack temperature changes. Temperature measurements were taken at 1 Hz and logged using a LabVIEW program running on a dedicated PC. Due to I/O limitations only six thermocouples could be monitored on a given test.

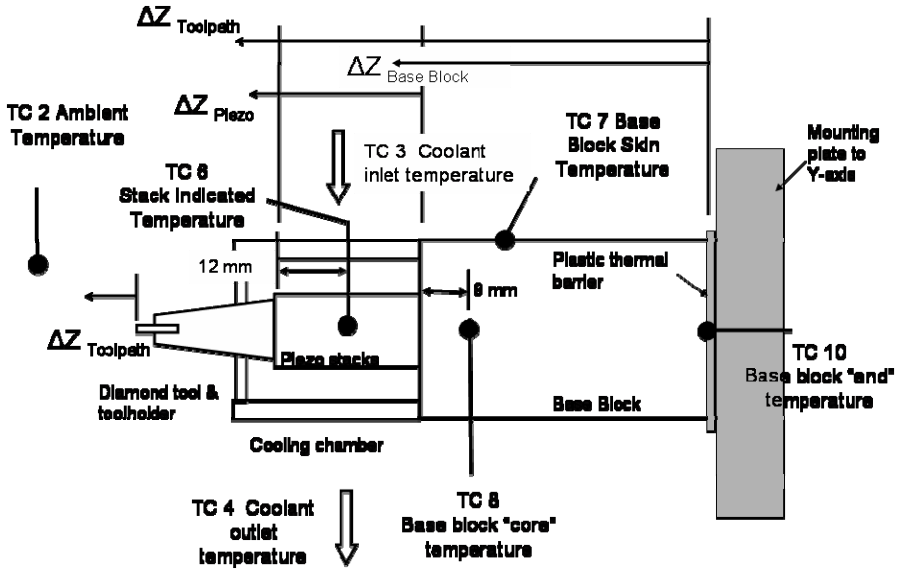

Figure 23. Thermocouple locations for measuring Ultramill thermal behavior. Only six TC's can be logged at any time due to data acquisition limitations.

To measure thermal expansion when the Ultramill is running, a small aluminum capacitance gauge target was glued to the ceramic toolholder to replace the diamond tool. The target is of approximately the same mass as the tool and is driven in an elliptical path similar to that experienced by the tool. The cap gauge measures the Z-direction position of the target at a sampling rate of 4000 Hz. Every 100 data points are averaged. This average position can be

considered to be the Z-direction location of the machining ellipse centroid. This point is fixed relative to the Ultramill, therefore any motion by it in the Z-direction must be caused by the net thermal expansion or contraction of the base block and stacks.

6.6.3 THERMAL EXPANSION MEASUREMENTS

To understand the role of stack temperature on the length of the Ultramill, the stacks were operated at three different frequencies (1000, 1500, and 2000 Hz) and with constant V_{pp} of 400 V. This corresponds to thermal inputs of 13.1, 19.6, and 26.2 W. The power was held at each value for 1000 seconds and changes between levels were executed stepwise. The power sequence was applied going up and coming down. Figure 24 shows the indicated piezo stack skin temperature during the test and the corresponding change in length of the Ultramill. The stack temperature increases significantly in response to step changes in the power input, reaching a new average temperature after 100 seconds. The indicated stack temperature fluctuates when the power input is held steady. These fluctuations have a peak magnitude of about 0.6 °C for stack frequencies of 1000 and 1500 Hz, but increase to 3-4 °C at 2000 Hz. These large variations appear to have a cyclic characteristic with a period of about 150 seconds. Bubble agglomeration and dispersal in the coolant chamber is one hypothesis for this behavior. The bubbles reduce the convection heat transfer from the stack to the coolant, causing the stack temperature to rise. When the bubbles break the stack heat transfer increases and the temperature drops quickly. Figure 24 also shows the change in position of the capacitance gauge target during the same test. The large step changes occur when the power supply is turned on and off to change operating conditions. The position response to the change in thermal power input appears to be logarithmic. The change in position of the tool tip, as measured by capacitance gauge, approximately 2 µm over a period of approximately 300 seconds, followed by a slower continued change that does not reach a steady state over the time period presented.

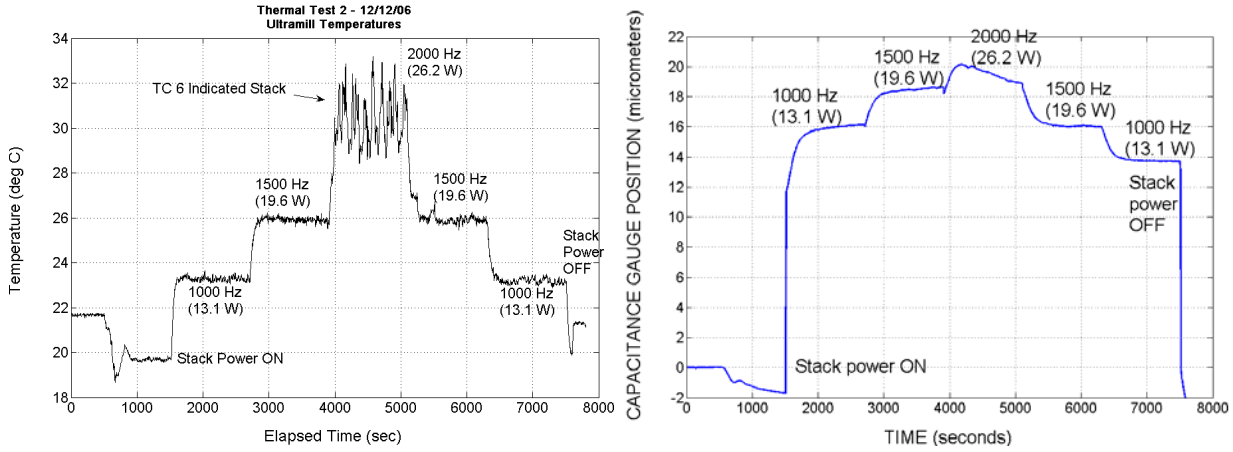

Figure 24. Stack temperature during operation (left) and position of capacitance gauge (right).

Figure 25 shows the block core and skin temperatures during the test. The base block core temperature, only 9 mm from the base of the Ultramill and the cooling chamber, shows a noticeable response corresponding to changes in the stack thermal power input. However there do not appear to be short-term fluctuations corresponding to the quasi-periodic stack temperature fluctuations. The base block end temperature shows a smooth long term trend of increasing temperature. This is consistent with the thermocouple being at the opposite end of the block from the thermal inputs (stack conduction and convection to the coolant). The slow response means that the base block will take a long time to come to equilibrium, and that it will therefore affect the thermal expansion of the Ultramill over a long period. The large and slow thermal response of the base block is undesirable from the standpoint of machining accuracy. Reducing the length of the base block will result in a smaller magnitude expansion for a unit temperature change. The smaller mass of a shortened block should also reduce the time for the block to reach equilibrium following a change in conditions at its end nearest the piezo stacks.

The position response is dominated by the large, slow changes caused by the step changes in thermal power input. During normal machining operations, the thermal power input to the stacks is kept constant. This means that thermal expansion will have two components: a slow response of the base block as it comes to equilibrium following the initial application of power to the Ultramill and expansion associated with the quasi-periodic stack fluctuations at steady power input identified.

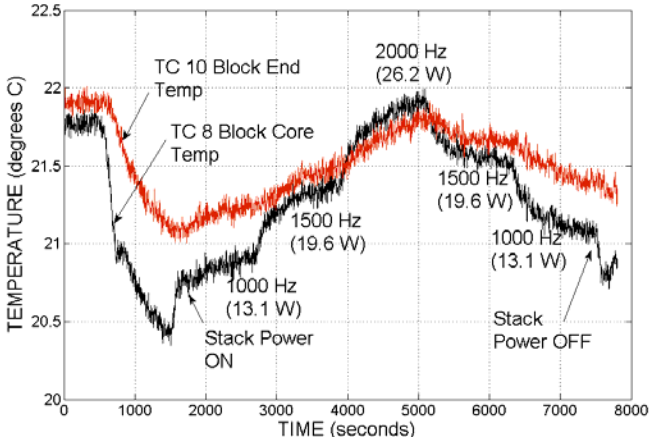

Figure 25. Base block temperature response during Ultramill operation.

6.7 CONCLUSIONS

1. A procedure was developed that determines the toolpath required to produce a specified surface, using the morphological operation of dilation. A MATLAB program was written to generate motion controller G-code commands with tool cutting edge profile, machining ellipse dimensions, and desired surface geometry as inputs.

2. Three microstructures with 3-D geometry were machined in hard-plated copper using a round-nosed tool of 1 mm radius:
   - A convex cylindrical segment, representing the top portion of a 1000 μm radius circular cross section, with a height above background of 20 μm and a surface roughness < 90 μm
   - A set of parallel grooves with a sinusoidal cross-section (320 μm wavelength) superimposed on a cosine section in the upfeed direction (1.28 mm wavelength).
   - A "flying wing" shape 20 μm tall above the background. The faces of the microstructure were planes not orthogonal to any of the machining axes. Good dimensional accuracy was obtained but the planar features were discovered to have a concave section along the upfeed profile.
3. Round-nosed tools can only make low aspect ratio structures with shallow, curved sidewalls. Sharp-nose tools were investigated to make steep-walled high-aspect ratio structures with horizontal feature resolution of less than 15 μm.
   - When used in EVAM, narrow, sharp-nose tools have relative tool-workpiece motion sideways along the cutting edge. This 3-D tool-material motion contrasts to round-nosed tools, where the material motion relative to the cutting edge is orthogonal.
   - Trihedron parts (80 μm tall and < 10 μm tall) were made in several materials using a dead-sharp tool. Parts made in hard-plated copper showed virtually no burr. Parts machined in stainless steel had serious burr.
   - A part was machined in hard plated copper with sculpted 3-D features consisting of grooves with sinusoidal profile in both upfeed and crossfeed directions. The groove depth was 5 μm with an aspect ratio of 0.31.
   - The optimum tool for making small, high-aspect ratio features with steep sidewall and 3-D geometry is a sharp-nose tool with a very small radius at the nose.
4. Thermal expansion behavior of the Ultramill was measured at different power levels. Initial findings include:
   - Quasi-periodic fluctuations in piezoelectric actuator stack skin temperature with a period of about 150 sec. Above a stack thermal power level of ~ 20 W, the magnitude of these fluctuations jumps from less than 1 ˚C to 3-4 ˚C
   - The thermal expansions related to the above stack temperature changes have not yet been extracted from long-term thermal expansion behavior associated with the base block, and so have not been assessed.
   - The base block has a very slow thermal response time -- on the order of 3 hrs to come to equilibrium--but is capable of expansion / contraction by several micrometers in that time period.
   - Changing the base block to one of smaller length will reduce the magnitude of its expansion.

ACKNOWLEDGEMENTS

This work is supported by NSF grant DMI-042335, monitored by G. Hazelrigg with additional support from Sandia National Laboratories, Oak Ridge National Laboratory, and Chardon Tool.

REFERENCES

1. Brocato, B., *Micromachining Using Elliptical Vibration Assisted Machining.* MS thesis, North Carolina State University, (2005).
2. Brehl, D., Dow, T., Sohn, A., *Micromachining Using Elliptical Vibration-Assisted Machining (EVAM)*. Precision Engineering Center Annual Report, 23, (2006).
3. Negishi, N., *Elliptical Vibration Assisted Machining with Single Crystal Diamond Tools*. MS thesis, North Carolina State University, (2003).
4. Villarubia, J.S., *Algorithms for Scanned Probe Microscope Image Simulation, Surface Reconstruction, and Tip Estimation*. Journal of Research of NIST, 102, 425-454, (1997).
5. Cerniway, M.A., *Elliptical Diamond Milling: Kinematics, Force, and Tool Wear.* MS thesis, North Carolina State University, (2001).
6. Ma, C., Shamato, E., Moriwaki, T., Zhang Y., Wang, L., *Suppression of Burrs in Turning with Ultrasonic Elliptical Vibration Cutting*. Int. Journal of Machine Tools and Manufacture, 45, 1225-1230, (2005).
7. Author's conversation with O.B. Ozdoganlar of Carnegie-Mellon University, (2006).
8. Miller, A.C., Cunningham, J.P., *Nanometer Tool Centering for Diamond Turning Applications*. ASPE Proceedings, 7th Annual Meeting, 216-219, (1992).
9. Copper Development Association, New York, New York, http://www.copper.org
10. Ferguson Metals, Hamilton, Ohio, http://www.fergusonmetals.com
11. Brehl, D., Dow, T.A., *Vibration-Assisted Machining for Precision Fabrication*. Unpublished, submitted to Precision Engineering, (2007).

7 METROLOGY ARTIFACT FOR DYNAMIC PERFORMANCE EVALUATION

Karalyn Folkert
Consolidated Diesel Company, Whitakers, NC
Kenneth Garrard
Precision Engineering Center Staff
Thomas Dow
Professor
Department of Mechanical and Aerospace Engineering

Part acceptance based on dimensional inspection by comparison to tolerance specifications is influenced by the static and dynamic errors in the inspection instrumentation, typically a Coordinate Measuring Machine (CMM). Traditional calibration artifacts are used to determine static influences due to machine geometry. The goal of this project was to design and fabricate a calibration artifact that will test a CMM both statically and dynamically. The artifact developed is a diamond turned, electroless nickel plated, 17-4PH stainless steel ring gauge (150 mm ID, 200 mm OD, 25 mm thickness). Sinusoidal features (5µm amplitude) were machined on the inside and outside diameter of the ring using a fast tool servo. The feature wavelength varies linearly along each surface between the longest wavelength (6.4 mm) and shortest wavelength (0.4 mm) without discontinuities. A reference flat was also machined on the ID and OD. The dynamics of a CMM under a specific set of measurement conditions can be found by computing a transfer function between a measurand of the ring gauge and the accepted "true" shape of the gauge. This allows an operator to devise a measurement strategy for a part that does not exceed the dynamic capabilities of the CMM and to predict the error in a measurement.

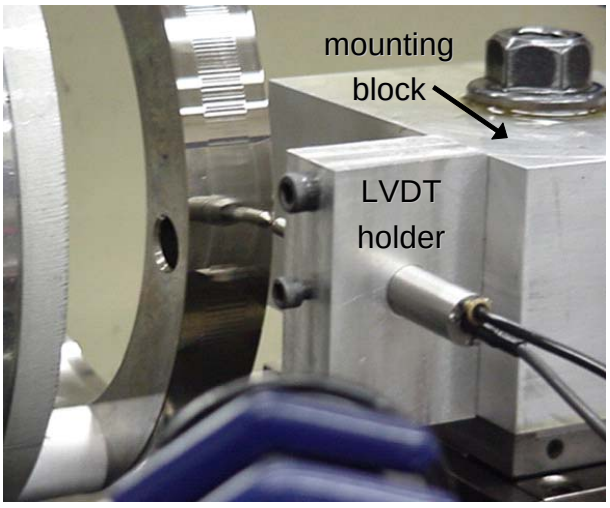

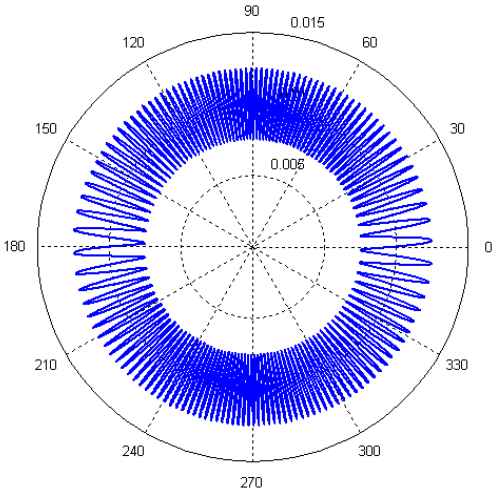

7.1 BACKGROUND

An artifact has been designed and built to assess the static and dynamic performance of a Coordinate Measuring Machine (CMM). CMMs can measure a wide variety of component shapes and have accuracy and repeatability comparable with most manufacturing operations. The Y-12 National Security Complex manufactures precision parts for the government and private companies. Part acceptance is generally based on dimensional inspection and comparison with tolerance specifications. The goal of this project was to design and fabricate an artifact that can be used to expose the measurement errors in a CMM due to static (error motion of slides, control system) and dynamic sources (following error, probe dynamics). With this information, a measurement strategy for a part shape can be developed that will limit the errors to an acceptable value. If the artifact includes a broad band of excitation sources, the measurement will show how the actual gauge motion is transformed by the dynamic environment to produce a new motion with amplitude and phase errors. A ring gage was found to be the best artifact geometry for Y-12 and the addition of small sine wave features allow both static and dynamic calibration.

7.2 RING GAUGE GEOMETRY

The ring gauge has a 200 mm OD, a 150 mm ID and a thickness of 25 mm. The material was 17-4 PH stainless steel, heat treated for maximum dimensional stability and electroless nickel plated. Diamond turned flat surfaces on the top and bottom as well as circular sections on the ID and OD can be used as a standard ring gauge to measure machine geometry and the effectiveness of control systems and error correction schemes. The OD and ID have raised sections on which a sine wave features were machined to measure the dynamic response of the machine and probe [1].

7.2.1 SWEPT SINE WAVE

The small features on the surface of the ring are designed to create a range of excitation frequencies to evaluate the response of a CMM (or other measurement instrument) to a dynamic environment. A number of different geometries were investigated and the best candidate was a swept sine wave with constant amplitude. A swept sine wave is a sine wave with a continuously varying wavelength; that is, each point on the swept sine wave has a different spatial frequency. For the ring gauge, the wave begins at a long wavelength and progresses to a short wavelength in the first 90 degrees. To produce a continuous wave, the wave is “flipped” to line up with the last wave and then the wavelength increases to the starting wavelength as it reaches 180 degrees. From 180 to 360 degrees, the wave is a mirror image of the first 180 degrees. Four quadrants

with the same wavelengths and smooth transitions between quadrants allow any smaller section of the ring to be measured. Figure 1 illustrates these features.

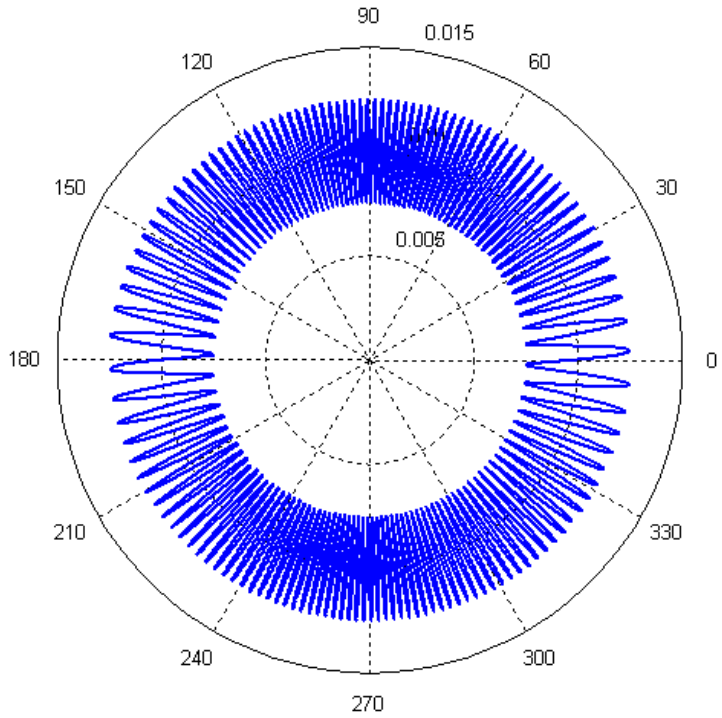

Figure 1. A continuous swept sine wave in polar coordinates.

The allure of the swept sine wave is that it contains a wide range of wavelengths and thus many excitation frequencies. Different measurement speeds change the temporal frequency range for computing a transfer function while the spatial wavelengths remain constant. The linear swept sine wave from 0º to 90º is given by Equation 1 where A is amplitude, t is circumferential distance, d is the modulation parameter and f is the base wavenumber. The total number of waves over length L is $d+f$.

$$y = A \cdot \sin\left(\frac{2\pi t}{L}\left(\frac{d}{L}t + f\right)\right) \tag{1}$$

7.2.2 Swept Sine Wave Excitation

The swept sine wave creates a frequency rich environment that reveals the dynamics of the CMM, its ability to respond to small surface anomalies and the performance of the CMM as it traverses the varying wavelength features. The wept sine wave parameters for the ring gauge were selected based on desired minimum and maximum spatial wavelength. Because the

wavelengths can be considered as individual frequencies, a Fourier transform can be performed on the data set. With sampled data from a continuous scan, the units on a frequency spectrum plot are usually Hertz.

However, with the generated spatial data, it is more useful to plot the results in terms of wave number[1]. The wave number is the reciprocal of the normalized spatial wavelength. Figure 2 shows the FFT of the first quadrant of the ideal wave for the ID. The magnitude is largest near the shortest wavelength at wave number 223/λ which translates to a wavelength of 0.537 μm (λ is 119.69 mm which is one quarter of the circumference of the ring ID). The phase values accumulate for half of the wavelengths and then return to zero, since phase indicates when each frequency occurs relative to the beginning (or end) of the data window.

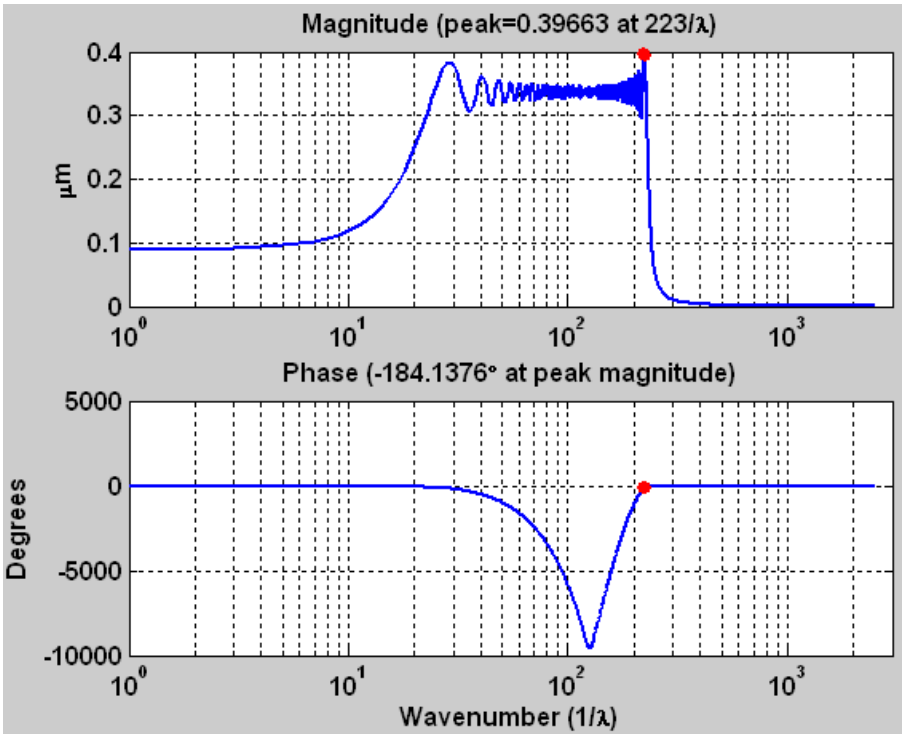

Figure 2. Spatial frequency spectrum of the first quadrant of the swept sine wave in Figure 1.

The FFT of the swept sine wave is more difficult to interpret than a single frequency sine wave due to the constantly varying nature of the wavelength. Rather than strictly interpreting the ideal FFT and directly comparing it to an FFT of an actual measurement, the data analysis may be simplified. A CMM has dynamic characteristics that will influence the overall measurement of the artifact and the ability of the probe to detect small perturbations changes with the radius of

[1] The number of waves per unit distance (one quarter of the ring circumference).

the probe, measurement speed, radius of the part and size of the feature. Since the swept sine wave on the surface of the ring has an "accepted" value[2] and the CMM measurement will generate another data set, the CMM's dynamics, or transfer function, may be found by comparing these measurements using a form of deconvolution. Convolution in the time domain describes how a dynamic system (the CMM) modifies or filters a signal (the swept sine wave) to create an output waveform (the measurement data). Since the dynamics of the CMM are not known, the inverse of convolution, or deconvolution, is used; the CMM dynamics are calculated given the accepted shape of the ring surface and the measurement data. To expedite calculations, deconvolution may be performed in the frequency domain [2]. The magnitude and phase components in the frequency domain are separated to create a Bode plot of the CMM's dynamics. Multiple measurements with different speeds can be used to create the desired frequency range of the Bode plot to determine the dynamics of the system. The transfer function of the CMM provides a significant amount of information about the machine. It specifies the natural frequency as well as the machine's performance within a frequency range. If a measurement speed is specified, the speed may be converted to frequencies present in the swept sine wave data and an appropriate CMM operating speed determined based on the transfer function and an acceptable amount of error.

7.3 ARTIFACT FABRICATION

A Fast Tool Servo (FTS) was used to machine the swept sine wave on the ring [1,3]. The piezoelectric stacks of the FTS are excited by the signal from a high voltage amplifier. The frequency and voltage signal affect the movement of the tool on the FTS. Feedback control from the built in cap gauge can correct for position error at low frequency. The closed loop controller uses position feedback with a proportional-integral control algorithm to correct position error. Gains are selected to shape the response of the system, to prevent overshoot and to correct for the following error. Although the system dynamics of the FTS are improved with closed loop control, there is still significant phase error in the system at higher frequencies. Since the FTS will operate at close to 600 Hz when machining at 20 rpm, deconvolution is applied to the swept sine wave before it is input into the controller. Deconvolution uses the magnitude and phase characteristics of the FTS with the information of the desired wave output to adjust the amplitude, phase and shape of the command signal; that is, it alters the input to produce the expected output [4]. This technique significantly decreases fabrication error to about 300 nm for the swept sine wave.

[2] The actual swept sine wave may not be exactly equal to the designed shape.

7.4 CONTACTING PROBE MEASUREMENTS

7.4.1 DETERMINING PROBE DYNAMICS

The dynamic transfer function of the air-bearing probe depends on the dynamics of the probe/gauge interface contact and any filtering built into the cap gauge electronics. Typical air-bearing probes capture some of the exhaust air and use it to preload the probe against the surface. This preload is a constant force independent of the deflection of the probe.

When confronted with the dynamic forces from the ring gauge motion, the probe will follow the surface until the dynamic forces exceed the preload and then it will leave the surface. The initial conditions, mass and damping will determine its motion and it will bounce when it returns to the surface depending on the relative speed and slopes at the contact interface.

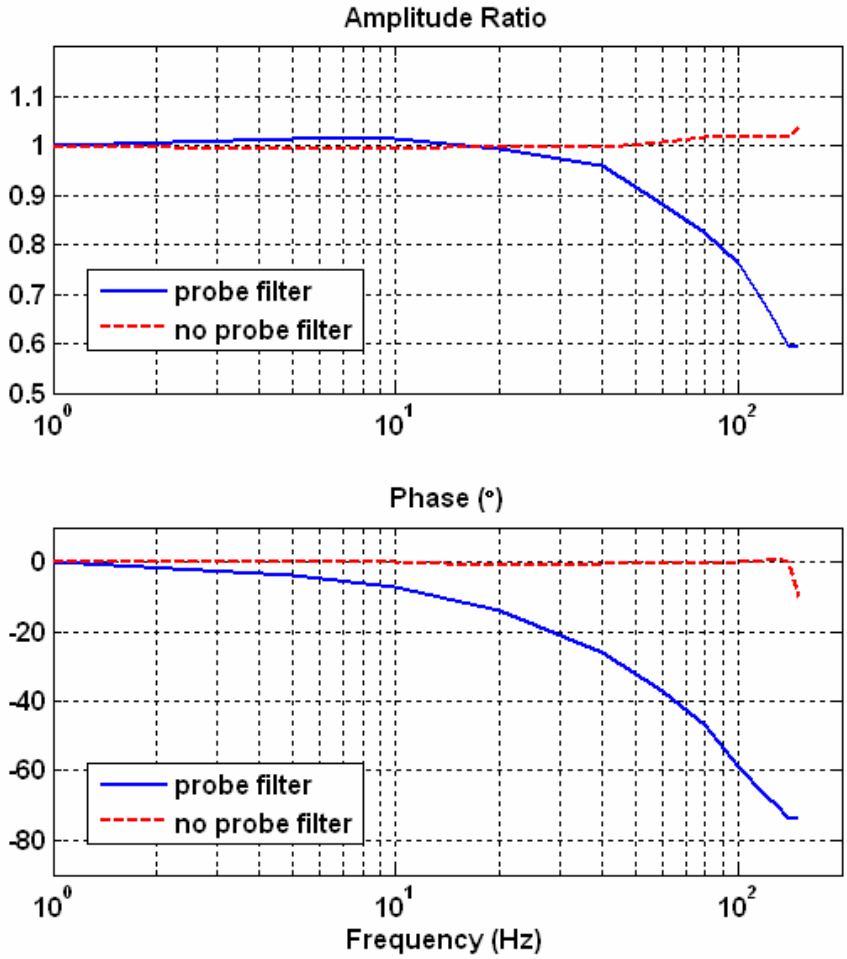

Figure 3. Transfer function of the air-bearing capacitance gauge with and without filtering.

Electronic filtering will change the apparent position of the probe by reducing the amplitude and introducing phase lag. An example of the probe response when excited with a sine wave motion with and without the electronic filtering is shown in Figure 3. A preload of 3.4 grams keeps the 7.4 gram mass of the probe in contact until about 150 Hz. The filtered amplitude ratio (air-bearing probe motion divided by excitation) drops as expected and is down about 3 dB (0.707) and lags the input by 64° at 113 Hz due to the filter. If the filter is removed the bandwidth is 20,000 Hz and the probe measures the motion up to the acceleration limit of 150 Hz after which it 'bounces' and contacts the surface sporadically.

The motion of the probe when it exceeds its acceleration limit will become a part of the dynamic measurement. This motion will depend on the dynamics of the probe (the friction, damping and spring constant) but not the shape of the part. A model of the motion of an air-bearing cap gauge was developed and corroborated by experimental measurements.

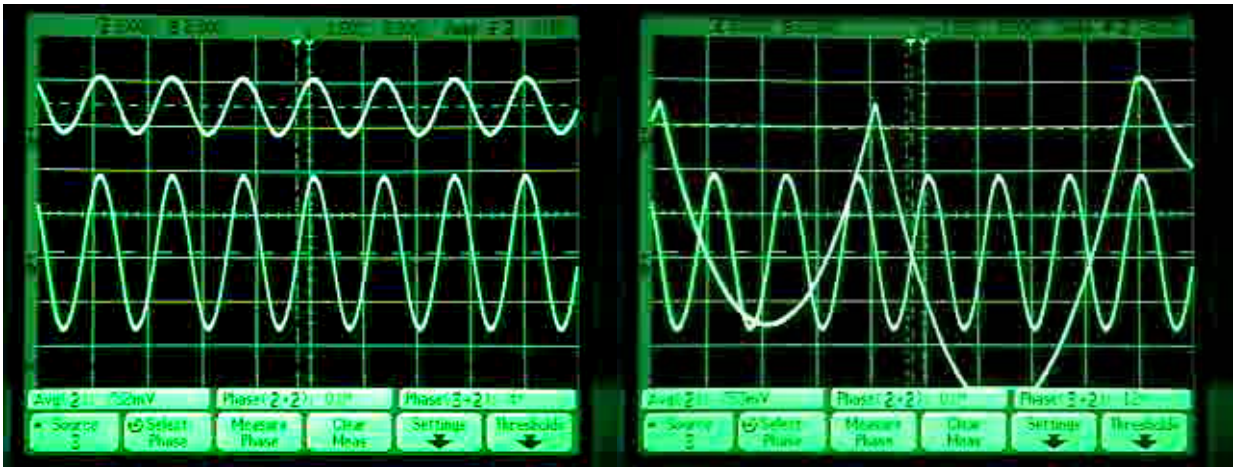

Figure 4. Motion of the probe (top) and gauge (bottom) in contact (left) and bouncing (right).

An example of the probe motion is shown in Figure 4 from an oscilloscope measuring probe and excitation motion at 50 Hz. The preload was reduced in the right to allow bouncing. Because of the range of the cap gauge, there is a 2.5x gain difference in the two signals. Notice that the amplitude of the probe motion grows significantly when bouncing occurs but the frequency is much lower than the excitation. The response changes depending on the gauge velocity and direction when the probe contacts it.

7.5 RING GAUGE MEASUREMENT

Measurement of the swept sine wave on the ring gauge (Figure 5) provides a rich dynamic input to assess the response of the structure, controller and probe of the CMM. The advantage of the

ring gauge is that the entire CMM structural loop is included. This is also a problem if any bouncing behavior of the probe is measured.

As the probe moves from the low frequency region to higher frequencies, the magnitude and phase of the measured shape will be modified by the dynamics of the CMM. This change can be quantified by comparing the measured shape to the 'accepted' shape of the surface. However, the data must be modified before analysis to eliminate the non-contact regions. If the probe leaves the surface the observed system behavior will not be LTI (linear time invariant).

Figure 5. Setup of a CMM probe measurement of the swept sine waves.

An algorithm has been developed to compute the CMM/probe transfer function given the gauge shape, a measurement data set and the circumferential speed of the measurement. The algorithm detects probe bounce in the measurement signal and windows the data appropriately before performing a transfer function calculation in the frequency domain.

To demonstrate the capability of this measurement technique, the air bearing probe with and without the electronic filter was used to measure the ring gauge shape. The air bearing preload was set for contact up to about 80 Hz and a linear sine sweep was sent through a FTS to the probe. The data was collected using XPC Target and a National Instruments 6052E multifunction board at a 20 kHz sample rate. The results are shown in Figure 6 and can be compared to the probe transfer function in Figure 3. Without the filter the probe behaves as expected with unity gain and flat phase response until it loses contact. Attenuation and phase lag with the probe filter are in good agreement up to about 50 Hz.

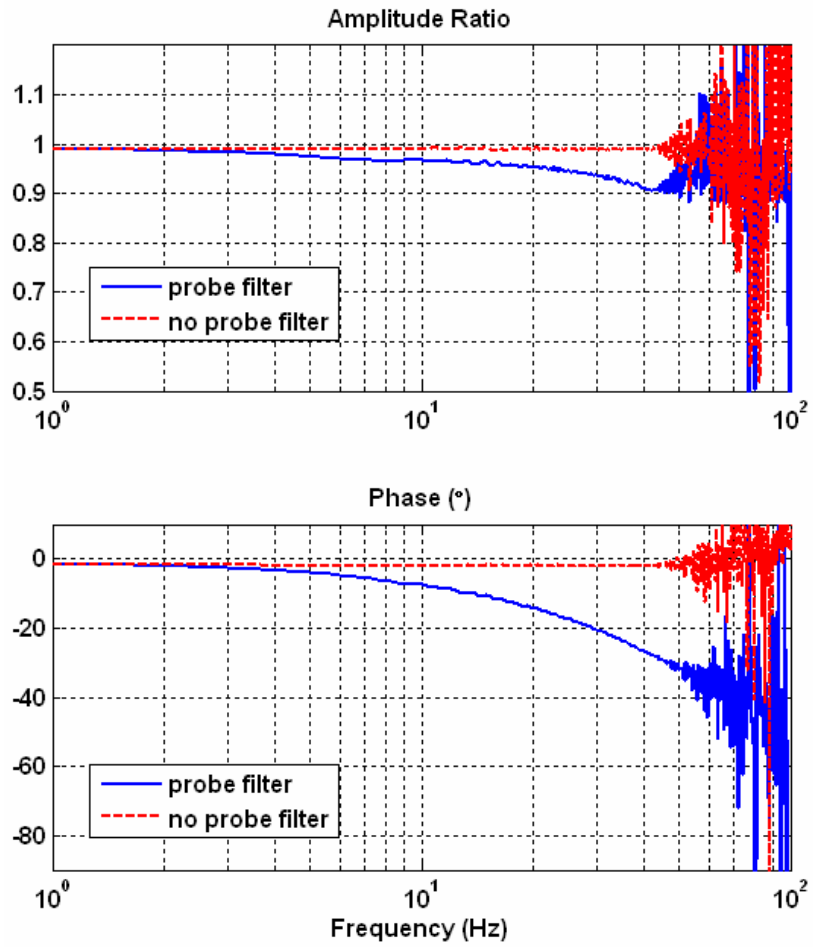

Figure 6. Probe transfer function derived from measurement data with and without probe filter.

7.6 CONCLUSIONS

A ring gauge artifact with cylindrical and cylindrical with swept sine wave features has been designed and fabricated. The form error associated with its ± 5 µm amplitude features is 300 nm PV and the ring is round to 120 nm PV with a surface roughness of 37 nm RMS. The swept sine wave contains spatial frequencies on the OD from 6.384 mm to 0.383 mm which correspond to 1.6 to 27 Hz at 1 rpm.

The effectiveness of the swept sine wave to measure dynamics performance was demonstrated by changing the transfer function of an air bearing capacitance probe by modifying the preload. An algorithm was developed to extract the dynamics of the probe from the swept wave measurement by only using data collected when the probe is not bouncing. Dynamic errors change the shape of the measurement and add error to the result. Probe dynamic response from

the ring gauge measurement will allow a CMM operator to devise a measurement strategy to limit dynamic errors to a specified range.

ACKNOWLEDGEMENT

This work was supported in part by the BWXT Y-12 National Security Complex.

REFERENCES

1. K. Folkert, *Metrology Artifact Design*. MS Thesis, North Carolina State University, (2005).
2. Smith, S.W., *The Scientist and Engineer's Guide to Digital Signal Processing*. 2nd Edition, California Technical Publishing, (1999).
3. Folkert, K., Dow, T. and Garrard, K., *Metrology Artifact Design*. ASPE Proceedings, 34, 462-465, (2004).
4. Panusittikorn, W., *Error Compensation Using Inverse Actuator Dynamics*. PhD Dissertation, North Carolina State University, (2004).

8 METROLOGY OF REFLECTIVE OPTICAL SYSTEMS

Robert Woodside
Graduate Student
Thomas Dow
Department of Mechanical and Aerospace Engineering

Once the surfaces of a telescope are fabricated, an accurate metrology process must be available to ensure the optical and fiducial surfaces conform to the design specifications. This section describes metrology techniques for reflective optical systems, specifically a two mirror Ritchey-Chretién diamond-turned aluminum telescope. This system has two rotationally symmetric hyperbolic mirrors, a complication because of the added variable of a second focusing location. The goal is to provide a knowledge base to build metrology techniques for more complicated systems such as a three mirror anastigmatic optical system. The techniques applied include interferometers, profilometers, coordinate measuring machines and image evaluation. A laser interferometer was used in a dual-pass setup to measure optical surface form error and the assembled optical system performance and a white light interferometer was used to measure the surface finish. Linear and rotary profilometry were used to measure the form error of the optical surface and the fiducial surface errors. The secondary mirror showed form error as expected near λ/4 while the primary mirror had a large form error of over 3λ. The optical component measurement showed a surface finish (4 nm RMS) that is expected for the 6061-T6 material. The system has 1.5 μm of wavefront error at its best focus point. The wavefront aberrations caused spot sizes that were 2x the magnitude predicted by Code V model and the MTF values were approximately 10-20% of the theoretical values.

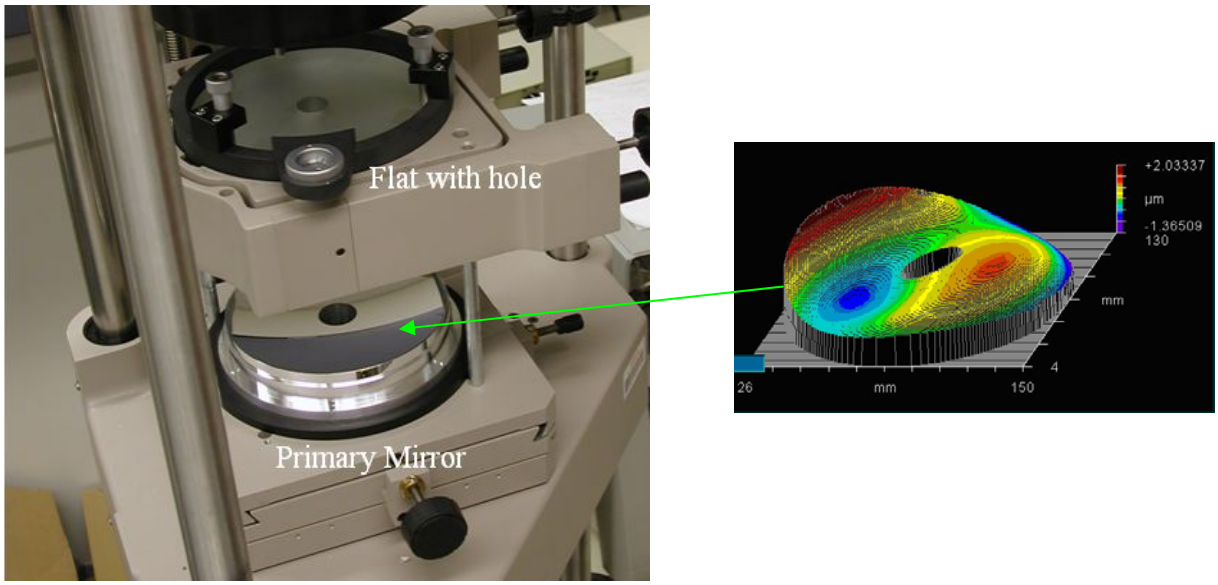

8.1 BACKGROUND

Reflective optical systems have been important since Isaac Newton made a reflecting telescope that could compete with the dominant refracting telescopes of the time [1]. Modern reflective optical systems surpass refractive systems because of the ability of a large reflector to gather light [7]. The primary obstacle to making reflective systems competitive with refractive systems is eliminating the spherical aberrations characteristic of many reflective systems [1]. Corrector plates or aspheric mirrors are used to correct these aberrations. Cassegrain and Gregorian systems can eliminate spherical aberrations but are still plagued by off-axis coma. The Ritchey-Chretién design is a modification of the Cassegrain system that uses two hyperbolic mirrors to eliminate off-axis coma [2]. However, this design is also limited by astigmatism at high field angles [3]. Three mirror optical systems can further reduce aberrations because there is a third surface. Each added component offers a chance to reduce aberrations present in the optical system but, at the same time, adds complexity and size to the system [4]. For reflective systems to be successful, techniques must exist to measure the features of the individual optical components, fiducial surfaces and the assembled system.

Metrology techniques have been developed to measure individual components as well as optical systems. For individual lenses or mirrors, surface measuring techniques such as interferometry and surface profilometry have been used. For the entire system, other techniques such as modulation transfer function and point spread function are used. The individual components can be measured with contacting or non-contacting techniques. Interferometry is a non-contact technique that uses interference between light reflected from a reference surface and the test surface to find the 3D shape of the test surface. Profilometers use a contacting probe that traces along the surface of the optic to measure its shape. This is typically a 2D technique and causes some damage to the surface. Therefore, the profilometer is not as attractive as the interferometer for optical systems. However, interferometers are limited to measuring surfaces that are close to the reference surface shape and only flats and spheres are normally available and are limited by the slope of the measured part. For different surface shapes (such as parabolas and ellipses), auxiliary reflectors are needed in the optical path to perform the measurement. For surfaces that are neither conic, spherical nor planer, a Computer Generated Hologram (CGH) is needed to create a reference wavefront but technique as with all interferometric techniques are limited to small surface slopes.

8.1.1 DESCRIPTION OF OPTICAL SYSTEM

A two mirror Ritchey-Chretién telescope was used to evaluate metrology techniques for measuring the performance of reflective optical systems. The Ritchey-Chretién telescope consists of a concave hyperbolic primary mirror and a convex hyperbolic secondary mirror. The

radius of primary is 300 mm with a conic constant of the primary is -1.0195 (close to a parabola). The secondary has an 89.56 mm radius and the conic constant is -2.166 [12]. The two mirrors are connected mechanically by a tube that connects to the outside of each mirror, as shown in Figure 1. To evaluate the system, the form and surface finish of each optical surface was measured. The fiducial surfaces of each mirror and the tube were also measured to evaluate the relative placement of the optical components. Finally, the assembled system was measured to determine its overall performance.

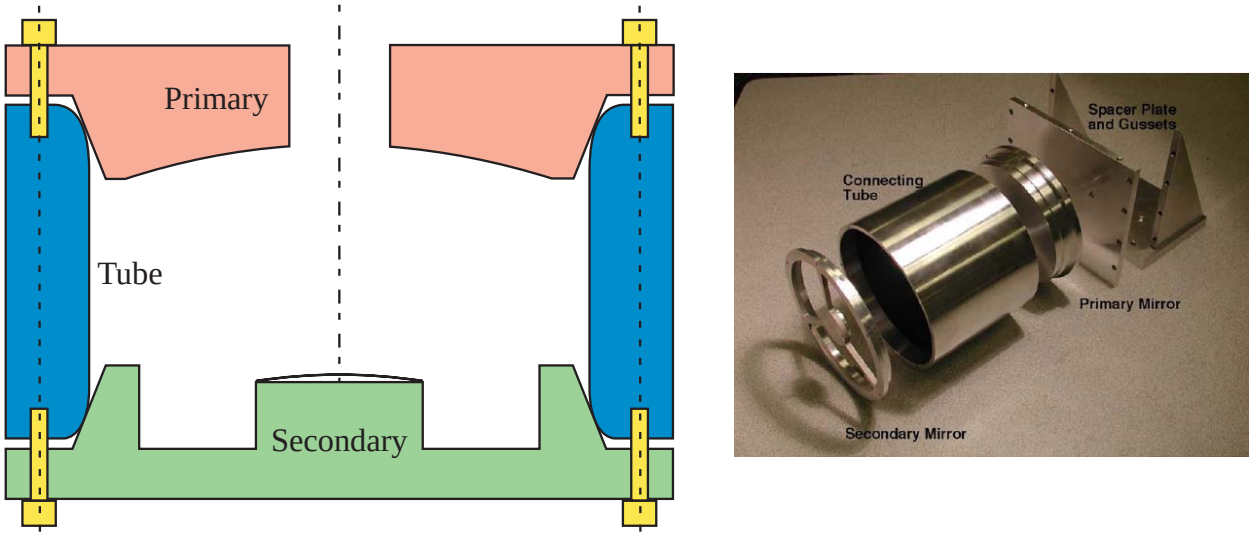

Figure 1. Ritchey-Chretién Telescope Assembly

8.1.2 METROLOGY TECHNIQUES

Interferometer Phase-shifting interferometry compares the laser light from a planar or spherical reference lens to that reflected from the test surface. The form error is measured by calculating the difference in phase between these two wavefronts. Differences produce fringes; for example, a tilted flat would produce parallel fringes with one full fringe for every half-wavelength of tilt. At high slopes the fringe spacing becomes too small and one cannot be discerned from the other. For this reason, interferometers are slope limited.

There are two common methods of phase-shifting interferometry: single frequency or multiple frequencies. Single frequency interferometry is generally used for large surface area measurements where form error is the important component. The single frequency interferometer used for this project is the Zygo GPI. The GPI is a Fizeau interferometer [5] with a HeNe laser source. Single wavelength interferometry cannot measure steps because they represent steep slopes. Multiple frequency, or white light, interferometry is used for small surface area measurements where highly sloped surface features are is the important goal. White light interferometers eliminate the step ambiguity by using a full spectrum of wavelengths.

Profilometer Profilometry can be used to determine both form error and surface finish of an optical surface. This project utilized profilometry solely for form error measurements. Both linear and rotational techniques were used to determine the shape of an optical surface. A linear profilometer involves a probe contacting the measured part while the probe is translated along a straight line and records surface height data. A rotary profilometer uses a spindle in place of a translator to turn the part and collect height data in a circle of constant radius around the part.

Coordinate Measuring Machine Coordinate measuring machines (CMM) are used to determine the shape of a part by measuring the coordinates (x,y,z) of points on the surface. CMMs, like profilometers, involve a contacting probe but it typically collects individual points rather than a continuous scan of the surface. The probe on a CMM is supported in a three dimensional translation apparatus that is able to record the location of the probe when it contacts the measured part to determine height, length and diameter.

Optical Performance Optical functions such as the Point Spread Function (PSF) and the Modulation Transfer Function (MTF) can supply additional information on the performance of a lens or optical system. The PSF measures the ability of the system to resolve a point. If an infinite conjugate optical system is focused at infinity, a spot will be produced at the best focus location. The PSF determines the theoretical size of this spot and allows the measured spot to be analyzed to determine path errors. Astigmatism or coma in the system will show up as flares or asymmetric errors in the spot shape [6]. The MTF defines the ability of an optical system to resolve fine features. MTF plots for a designed optical system can be calculated in optical design codes such as Code V and then compared to MTF values from the measured system.

8.1.3 RESEARCH GOALS

The goal of this research is to apply metrology techniques to measure a Ritchey-Chretién optical system with rotationally symmetric optical components. The application of metrology techniques should measure the aberration present in the optical system and the errors present in the optical and fiducial surfaces. The results of the different metrology techniques were compared to verify the shape of the surfaces.

8.2 COMPONENT MEASUREMENTS

8.2.1 PRIMARY

The primary mirror, shown in Figure 1, was designed with a hyperbolic surface (conic constant = -1.0195) and a radius of 300 mm. The optical surface has a diameter of 152 mm and a sag of 9 mm. It has a 26 mm diameter hole in the middle of its optical surface. The conic shape of the

surface, relatively large aperture and sag as well as the hole through the center all make measuring the form error a unique challenge.

Phase-Shifting Interferometry

Method The hyperbolic primary mirror was measured using the Zygo GPI phase-shifting interferometer. The hyperbolic shape requires a non-standard, dual-pass arrangement. The typical arrangement is single-pass with a flat or spherical reference lens. This arrangement covers a wide range of surfaces because every flat surface has the same conic constant and radius while every spherical surface has the same conic constant but a can have different radii. The radius can be compensated by moving the test part closer to or farther from the reference element. However, other conic surfaces can have different conic constants as well as different radii of curvature. No single conic reference element could be used for a variety of conic shapes as there would be no way to adjust the conic constant.

Measuring a conic on the GPI requires a specific secondary reference element between the test surface and the primary element. The secondary element must have a central hole to allow light to pass through to hit the test surface. This is called a double-pass setup because the light hits the measured element twice before returning to the instrument. A hyperbolic measurement setup utilizes a spherical primary reference element and a spherical secondary reference element. A hyperboloid has two foci: a focus in front of the mirror, shown as F_1 in Figure 2, and a focus behind the mirror, shown as F_2. The primary reference element shares a focus with the front focus of the hyperboloid while the secondary reference element shares a focus with the rear focus of the hyperboloid. The spherical secondary element must be fabricated and aligned correctly to measure the hyperbolic shape. The element must also have a machined flat rear surface for alignment purposes. In the case of the telescope primary, the conic constant is -1.0195, or very close to a parabola, (-1). As a result, it is possible to use the simpler setup required to measure a parabaloid surface and that is to use a flat as the secondary reference.

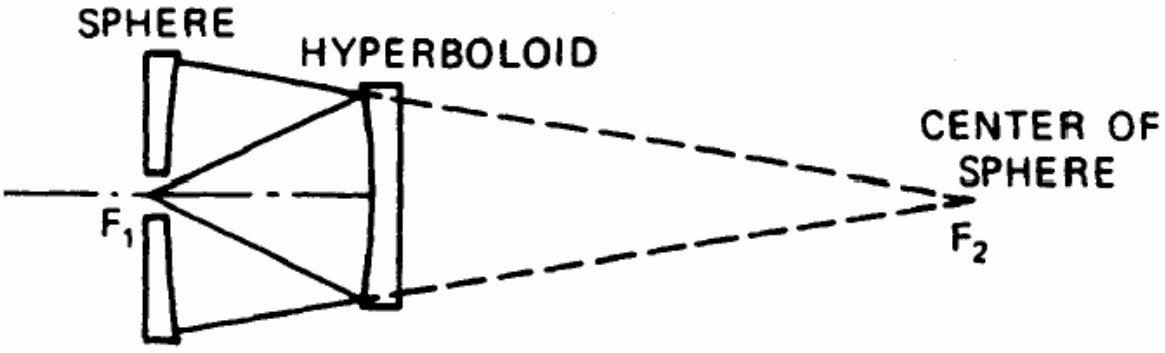

Figure 2. Silvertooth Test for Measuring Concave Hyperboloid Mirrors

Measurement Setup and Alignment An *f/1.1* spherical reference element was used in the interferometer for the dual-pass interferometry primary mirror measurement. The *f/1.1* element is selected because its *f/#* is the closer to the *f/#* of the primary mirror, *f/2* (300 mm radius of curvature, 152 mm aperture diameter). A λ/9 perforated glass reference flat was placed in a tip/tilt stage supported by 3 posts about 150 mm above the primary mirror as shown in Figure 3. This places the center of the mirror at the focal point of primary mirror and allows all of the light to pass through the hole. At this point, the focal point of the primary mirror and the focal point of the reference sphere are close to being coincident. Small adjustments are made until fringes again appear. At this point, the spherical wavefront is transformed to nearly collimated light by the hyperbolic mirror (a parabola would make collimated beam) which bounces off the reference flat and returns to the mirror. The wavefront emitting from the primary mirror at this point is a spherical wavefront with the aberration of the primary optical surface. Because the primary is not a parabola, aberrations inherent in measuring a hyperbola as a parabola will also show up in the measurement and were compensated using a Code V model of the measurement.

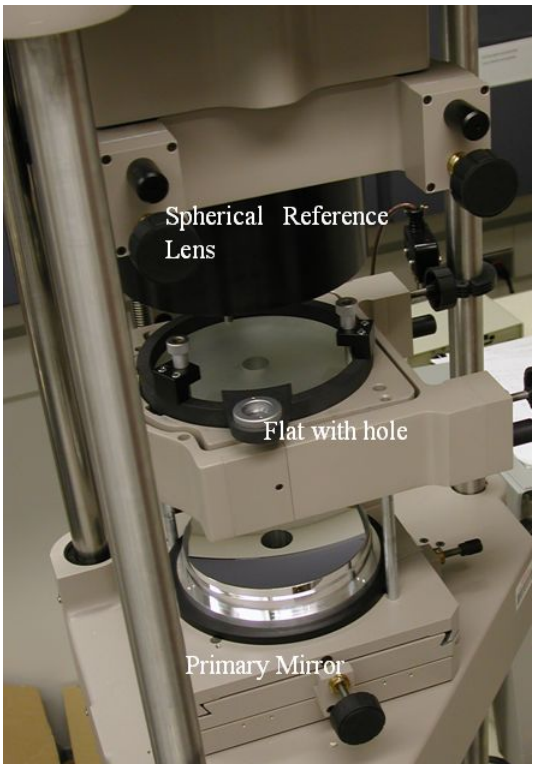

Figure 3. Measurement of primary mirror

Primary Surface Waveform Error To see the error between the machined primary and the theoretical hyperbola, the wavefront error in the primary must be corrected for the dual-pass geometry using the Zernike coefficients from the Code V model. The error surface can be generated in MetroPro software by entering the Zernike values of the surface. The Zernike coefficients of interest were #8 (spherical and focus) and #15 (5th order focus) and each was divided by two (because of the dual-pass model). Then, this Zernike surface[1] is subtracted from the primary measurements to give the true primary error.

The primary surface shown in Figure 4 has a surprising Non-Rotationally Symmetric (NRS) component, on the order of 4 μm. This value is much higher than the λ/4 (~ 160 nm) form error anticipated from past fabrication efforts using the DTM. Careful evaluation of the components

[1] Care must be taken to mask the annular area during measurement to generate Zernike coefficients that are consistent with the Code V model.

in the measured shape (astigmatism, coma and tilt) pointed to the possibility that Figure 4 might not be a measure of the mirror shape but rather the result of an alignment error in the dual-pass setup. The astigmatism and coma could result from an angular misalignment of the flat mirror with respect to the optical axis of the primary and a decenter of the primary mirror in the interferometer. Additional measurements using a contacting profilometer were used to confirm the NRS shape.

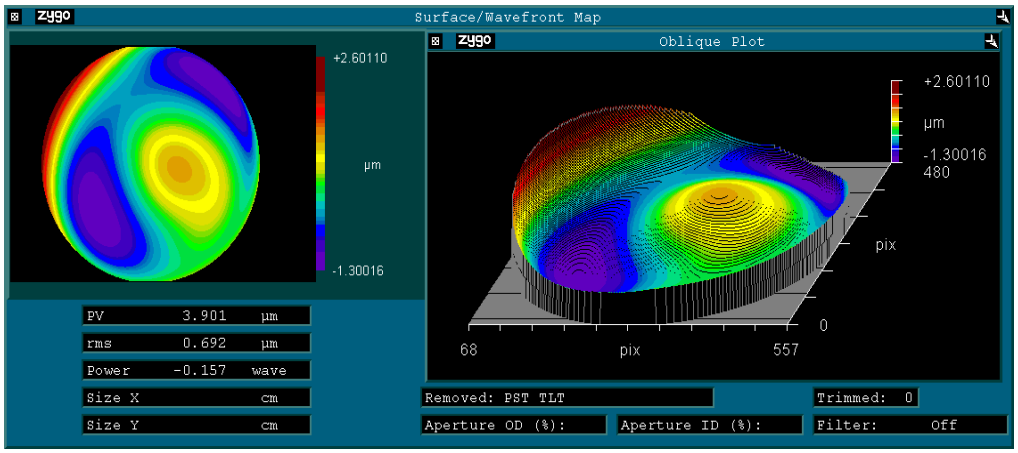

Figure 4. Measurement of hyperbolic primary with software correction for the dual-pass geometry using a flat mirror secondary rather than a spherical shape.

Profilometer

To evaluate any measurement error in alignment of the interferometer, the optical surface of the primary mirror was measured on a Talysurf linear profilometer. The Talysurf features a contacting probe with 6 mm of vertical motion and 120 mm of horizontal travel. Unfortunately, the horizontal travel is 30 mm shorter than the aperture of the primary and the central hole prohibits a full radial profilometer trace. Taking either a radial trace of the surface or a trace along a non-radial chord created problems in post processing the Talysurf data and fitting it to a conic. The radial traces do not contain the apex of the hyperboloid surface and, as such, are more difficult to align because they have more degrees of freedom. Chord traces contain an apex, but not the apex of the surface. Therefore, each these measurements must also be translated, rotated, or both before being fit to a hyperboloid surface.

Measurement The Talysurf was used to measure a series of seven radial scans from the edge of the center hole to the OD of the mirror. The seven scans were made at 60° angular increments with the 7th being a duplicate measurement at the zero degree orientation. The sag of the mirror (9 mm) is larger than the range of the Talysurf stylus (6 mm) so the mirror had to be tilted to

measure each segment. Positioning the mirror for each trace required lifting the stylus from the surface and moving the mirror so the seven scans do not have a common reference system.

The desired hyperbolic shape (R = 300, K = -1.0195) was fit to each trace by the "large-scale trust-region reflective Newton method" of nonlinear least squares using the Matlab optimization toolbox. The parameters for the least squares minimization were the center location in x and z of the desired hyperbola in Cartesian coordinates. The measurement data was rotated (i.e., tilted in the XZ plane) and the fit repeated until a minimum residual RMS value was obtained for each trace.

The data for each partial scan of the primary trace is shown in Figure 5. The bold lines are the result of smoothing the residual data with a linear least squares robust polynomial algorithm using a 1 mm spatial scale centered at each successive data point. The scans are similar and show 300 nm of error from the hyperbola. Also note that the positive error at the ends and negative error in the middle of the plot indicates that the concave mirror surface is "low" in the center and at the outer edge with respect to the desired hyperbola. For the combined residual primary mirror data with the smoothing filter applied, the peak-to-valley is 289 nm (λ/2.5) and the RMS form deviation is 54 nm. This data seems to support a conclusion that the unassembled primary mirror is rotationally symmetric. However, because there is a hole in the center of the primary, the mirror could be asymmetric and still have matching radial traces. The inability to trace through the center removes the possibility of connecting the traces together at a shared center point. This leaves open the possibility of an asymmetric part that would have, for a full surface, an impossible discontinuity at the center.

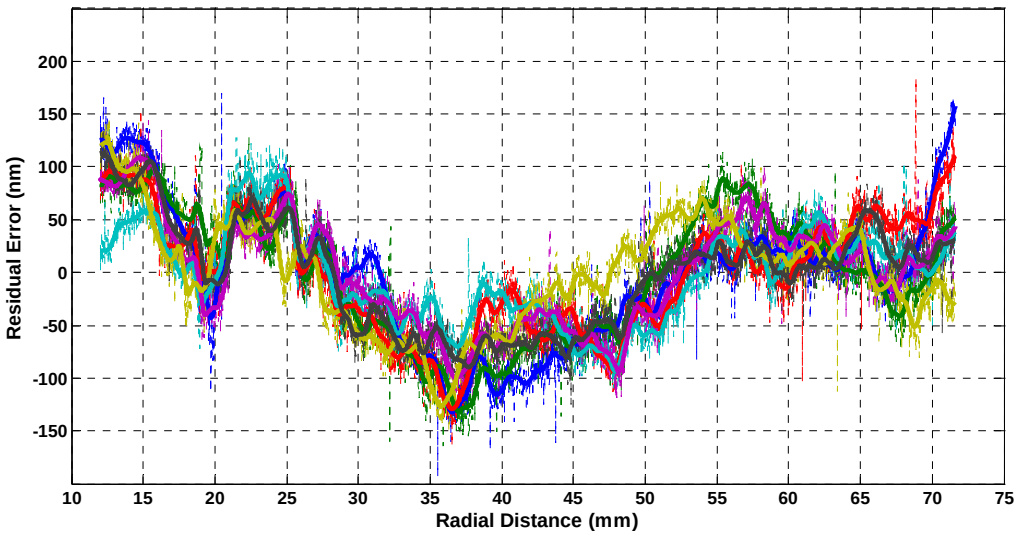

Figure 5. Primary Mirror Form Error - Talysurf Profilometer. Error is with respect to hyperbola with R = 300 mm and k= -1.01948378

Because the true form error of the primary remained unclear after the analysis of the radial traces, traces were also taken in a hexagonal shape around the outside of the optical surface as shown in Figure 6(b). These traces were then fit to the designed hyperbola. The residuals of the fits, shown in Figure 6 (a) and (c), showed that the traces did not fit the designed hyperbola and showed errors of over 2 μm in some cases. Figure 6(a) also shows that the traces have clear NRS components as the peaks of some traces are higher than others. This supports the conclusion that the error seen in Figure 4 is form error in the primary and not a result of measurement error. Because the two Talysurf measurements appear to disagree, another measurement is necessary to determine the error present in the primary mirror.

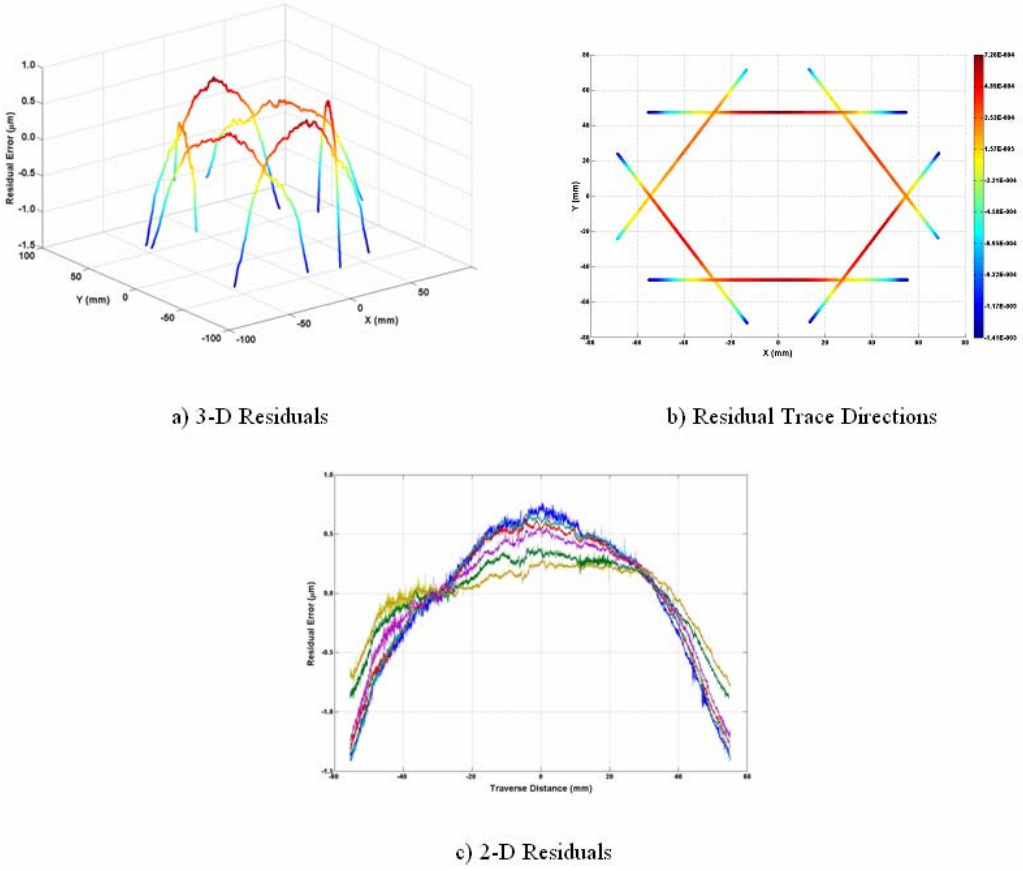

a) 3-D Residuals

b) Residual Trace Directions

c) 2-D Residuals

Figure 6. Hexagonal primary mirror Talysurf traces fit to the designed hyperbola

Rotary Profilometry To provide additional data on the shape of the primary, the surface was measured on a rotary measuring machine; that is, a vertical axis air bearing spindle with a contacting gage head that measured the shape of the primary in annular rings. A photograph of the measurement setup is shown in Figure 7. Before the mirror was placed on the spindle, the stage was leveled to a P-V value of 400 nm by adjusting tip-tilt screws in the stage.

Figure 7. Rotary Measurement Setup

The primary mirror was placed on the spindle and centered. Data was recorded for three rotations and separated into single resolutions using the fiducial mark. The curve fitting tool in Matlab was used to remove any tilt or other once per rotation error. Once the tilt was removed, only the non-rotationally symmetric error remained. Figure 8 shows a trace of the primary optical surface along with the residuals from the sin wave curve fit. The residuals show 2 μm of non-rotationally symmetric error with a twice per revolution cycle. This data agrees with a circular trace taken of the primary mirror interferogram, as seen in Figure 9, which shows a twice per revolution error of 1.5 μm.

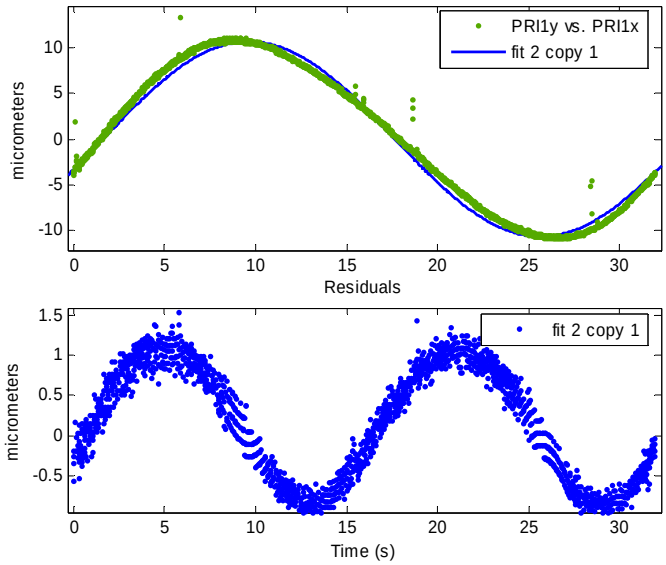

Figure 8. Primary mirror rotary data and curve fit (top) and curve fit residuals (bottom)

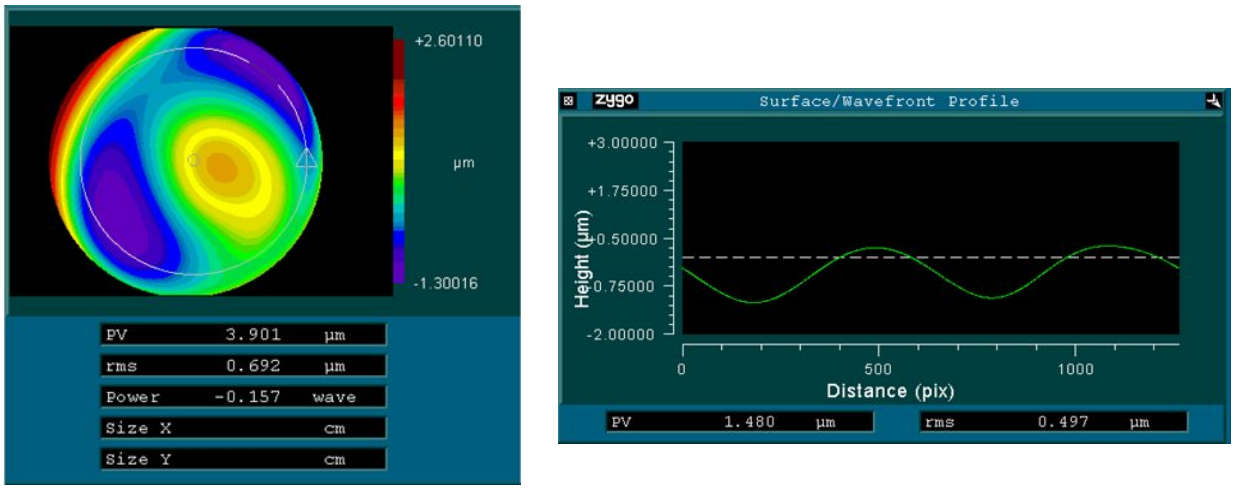

Figure 9. Corrected Zygo Primary Measurement with Circular Trace

Summary The magnitude and shape of rotary form error corresponds with the interferometry measurement. Therefore, there is a combination of coma and astigmatism present from the fabrication process. The error seen by the interferometer is form error in the primary and not produced by alignment or measurement error.

Surface Finish

The surface finish of the optical surfaces was measured with the Zygo NewView white light interferometer. The primary mirror was machined at 530 rpm with a feed rate of 2 mm/min and a 3 mm tool nose radius. This produced a feed of 3.77 µm/rev and a theoretical PV surface finish of 0.57 nm and an RMS of 0.19 nm. At this feed rate, one pass of the primary took 77 minutes indicating the need for excellent temperature control.

Figure 10 shows the surface finish of the primary measured over an area of 50x70 µm. The measured PV and RMS (23 nm and 5 nm respectively) are 40 times higher than the theoretical values. The profile plot in the lower left of Figure 10 shows a trace perpendicular to the feed direction covering 17 µm over which 4+ tool passes should be visible. While not obvious to the naked eye, the autocovariance function at the right shows a peak around 3.7 µm indicating a repetitive feature at that spacing. Autocovariance correlates the properties of the surface roughness and a peak indicates a feature that repeats with spacing equal to the peak location [7]. Other features such as the second phase particles in the 6061 structure and scratches from chip management failures disguise the feed rate and increase the surface finish.

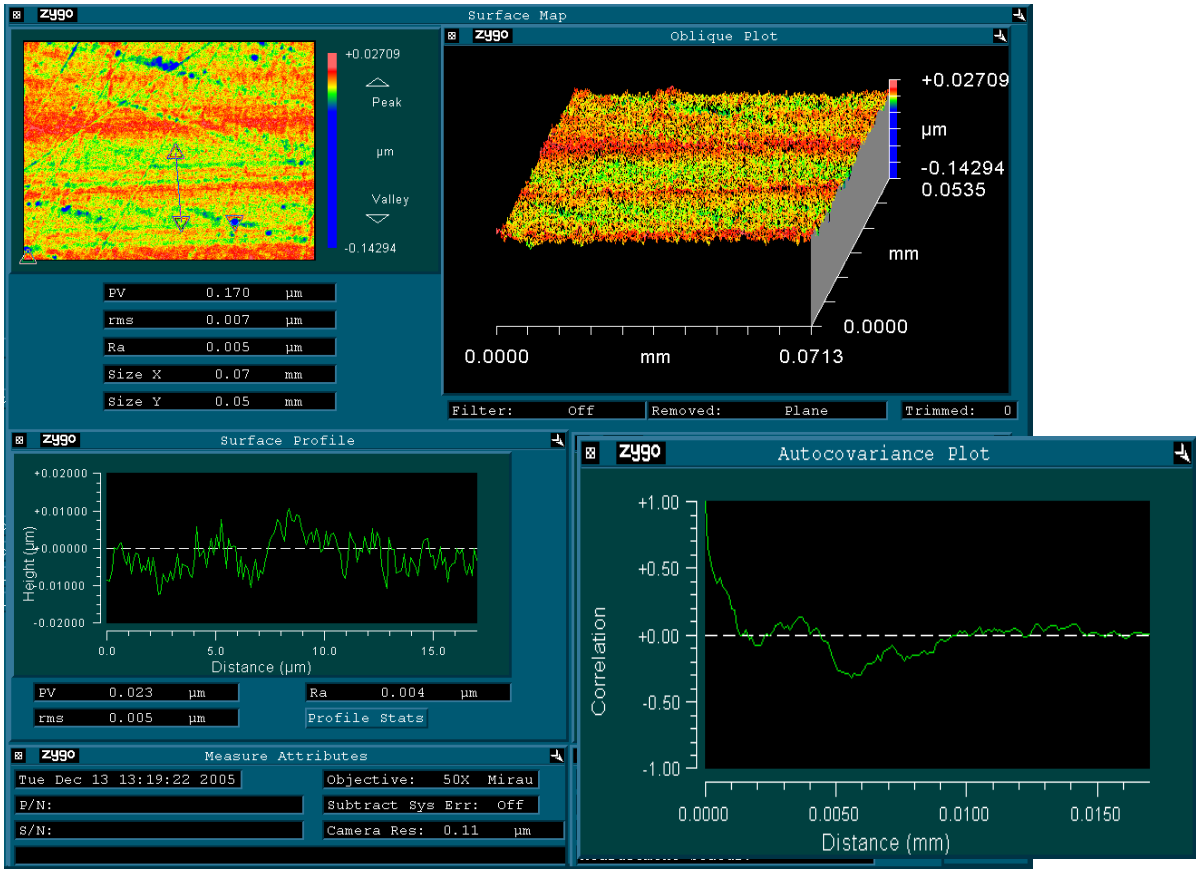

Figure 10. Surface finish of the Primary Mirror Optical Surface from Zygo NewView

8.2.2 SECONDARY

Interferometer

The measurement of the secondary hyperbolic surface could not be performed using the same method as the primary because the secondary is much farther from a parabola with a conic constant of -2.1666. A specialized spherical element could have been machined but it was deemed an unacceptable expense and the profilometer techniques discussed above were used.

Profilometer

Linear Profilometry The Talysurf profilometer has enough range and resolution to measure the entire width of the mirror rather than only half for the primary. However, because this instrument produces a linear scan, a series of scans must be pieced together to provide a view of the entire surface. The six holes in the secondary mount were used to index the mirror in 30º

increments and 12 measurements were made across the width of the mirror. The second 6 measurements cover the same region of the mirror but are taken in the opposite direction as the first 6 to address the repeatability of the measurements.

For each scan, a crowning procedure was used to ensure that the scans crossed the apex of the mirror. The same fitting and smoothing procedure was followed for the twelve scans as that described for the primary mirror and only the center location and in-plane tilt were varied. The residual errors from the least squares fit to the desired secondary hyperbola (R = 88.1225, K = -2.1666) are shown in Figure 11. The unassembled secondary mirror appears to be rotationally symmetric with positive error at the edges and negative error in the middle indicating that the convex mirror is "high" in the middle with respect to the reference hyperbola or has a larger radius of curvature than desired. The form error is the desired hyperbola minus the measured sag at each radial location. For the combined residual secondary mirror data with the smoothing filter applied, the peak-to-valley is 198 nm and the RMS form deviation is 31 nm.

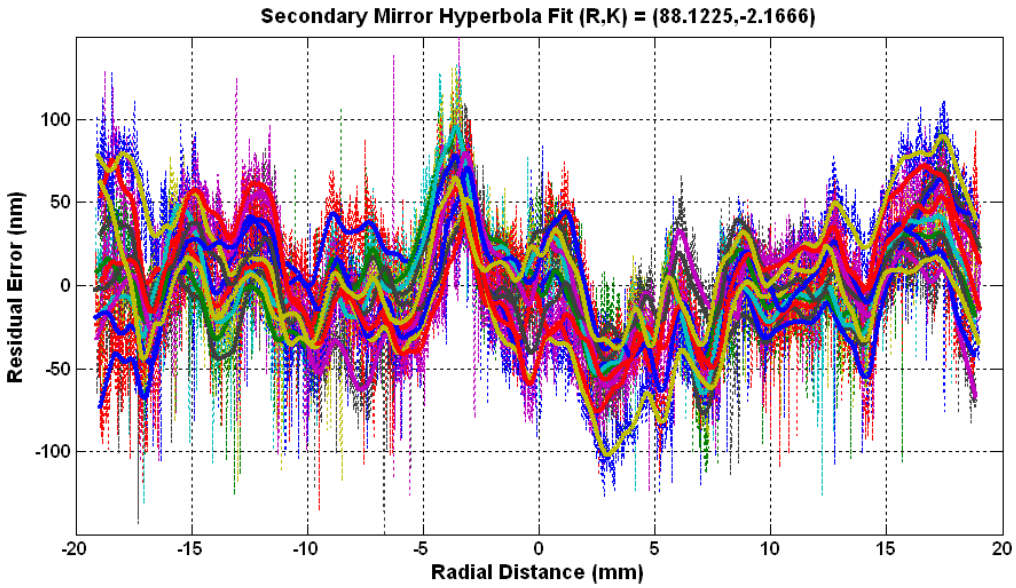

Figure 11. Secondary mirror form error from Talysurf profilometer. Error is with respect to desired hyperbola R = 88.1225 mm and k=-2.1666

Rotational Profilometry The surfaces were also measured using the rotary table and air-bearing capacitance gage. The cap gage was set at different radii and circular traces were made of the surface of the mirror. These traces were put together to provide a similar but different representation of the mirror compared to the Talysurf measurement. The secondary mirror trace and best fit residuals are shown in Figure 12. The once per revolution error, seen in the top plot

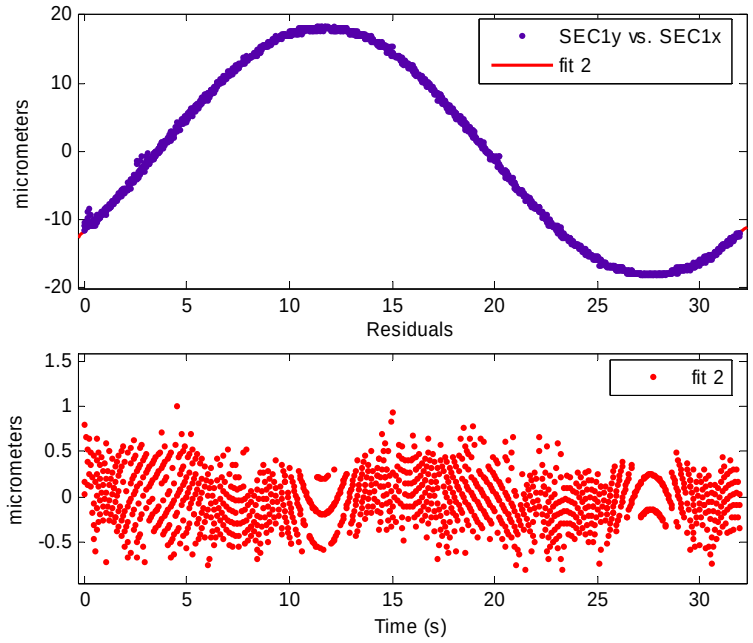

Figure 12. Secondary mirror rotary measurement data and best fit line (top) and best fit residuals (bottom)

is removed to show the form error of the secondary mirror. The residual form error data is rotationally symmetric and confirms the Talysurf measurements. The 1 μm P-V of the residual data comes from a combination of the capacitance gage sensitivity, rotary spindle noise and the measurement repeatability; but all errors are at high frequency.

Summary The linear and rotary measurements indicate that the secondary mirror optical surface was fabricated to specifications. The linear traces fit the theoretical hyperbola to λ/3 or 200 nm.

Surface Finish

The secondary mirror optical surface was machined at a lower feed rate because it is smaller. The smaller size allows the machine time to remain the same with a lower feed rate that should improve surface finish. The feed rate was 1 mm/min which will produce a feed/rev of 1.89 μm and a theoretical PV of 0.14 nm and an RMS of .05 nm. Figure 13 shows the measured surface finish over the same field of view as the primary in Figure 10. The profile plot in the lower left shows a trace perpendicular to the feed covering a width of 10 μm or about 5 tool passes. The surface has a PV of 18 nm and an RMS of 4 nm, which are 100 times greater than the theoretical value. The material properties, spindle dynamics and tool management limit the possible surface finish. The vertical lines on the profile plot represent the theoretical wavelength and the arc represents on the nose radius of the tool. The autocovariance function in lower right shows a

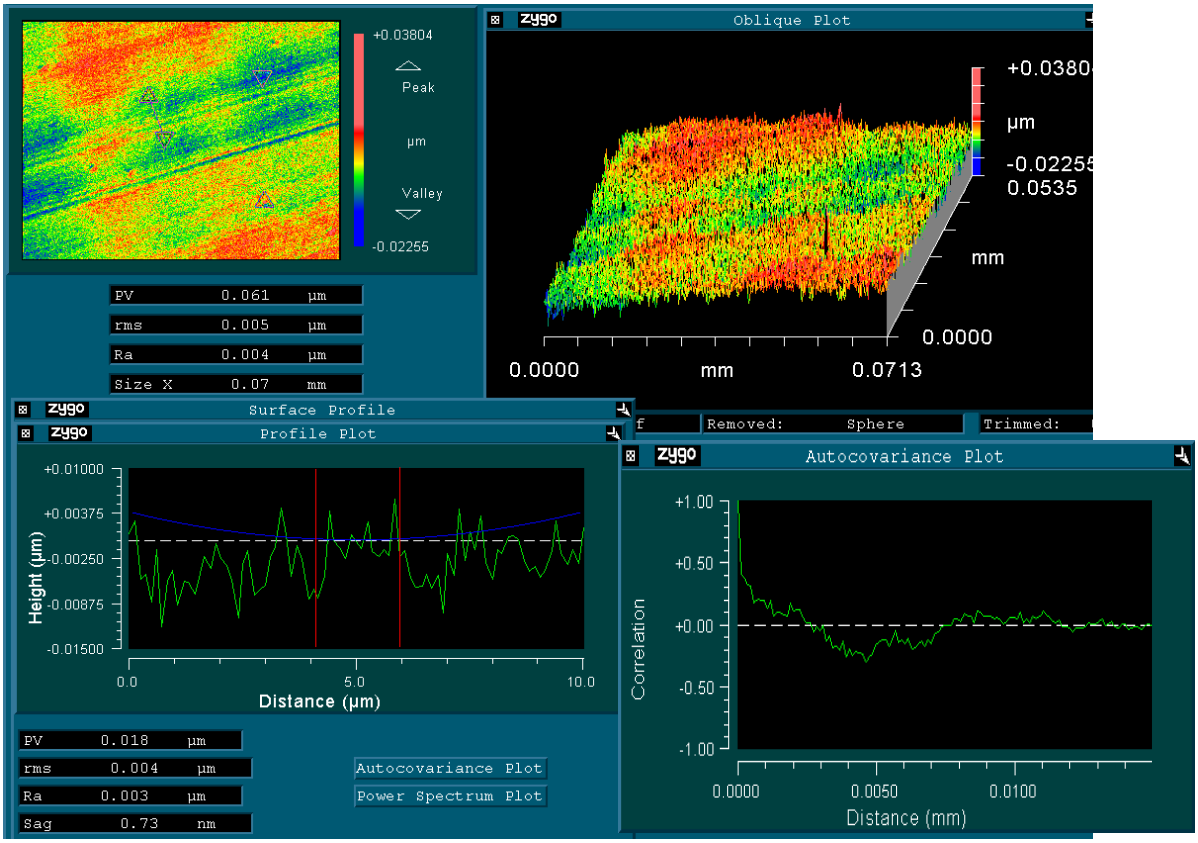

Figure 13. Secondary mirror surface finish with tool profile

slight peak at the feed rate 2 µm. Again, as in the case of the primary surface, the particles and contamination in the 6061 limits the surface finish possible to about 20 nm. The smaller feed rate does improve the surface finish (18 nm vs. 23 nm), but the effect is small.

8.2.3 TUBE

The primary and secondary mirrors are connected by a 150 mm tube. Each mirror has a fiducial interference surface to radially locate the mirrors and the tube. Each mirror also has a planar fiducial surface to axially locate the mirrors and the tube. Each mirror is held in place by three screws 120º from each other that connect through the back of the mirror to threaded holes on the tube. Each mirror also has three threaded holes (60º from the assembly holes) so that the mirrors pushed away from the tube for disassembly.

Rotary Profilometer Based on the measurements of the fiducial surface of the primary and the fiducial surface of the tube, each have different form errors, both in magnitude and shape. The tube is much longer than the thin primary mirror fiducial surface and is more than two times

stiffer. This means that when the two are pulled together, the primary will distort more to allow the two surfaces to mate. Each surface has two highs and two lows but the primary surface has a much larger peak-to-valley value and the highs and lows of the two are out of phase. Therefore, the highs of the primary would rest on the highs of the tube as shown in Figure 14 and, when bolted together, the primary would be distorted more than the tube. The difference between the two surfaces is on the order of 4 μm which is similar to errors discussed later for the system.

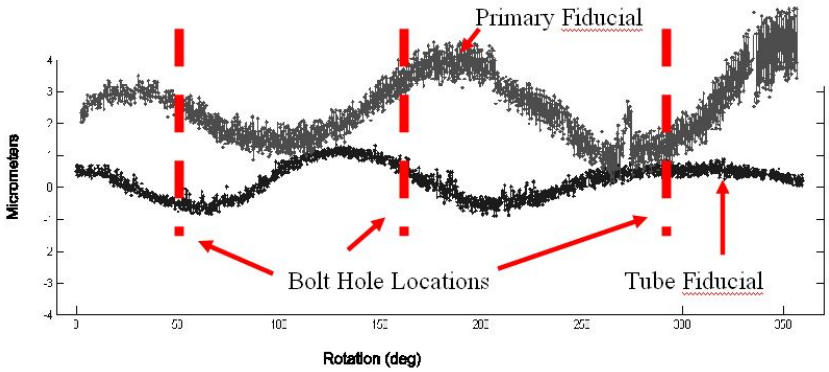

Figure 14. Primary Fiducial and Tube Fiducial Form Error Relationship

CMM The surfaces of the mirrors and tube were also measured using the CMM. Figure 15 shows the key dimensions on the primary, secondary and tube. Each optical component was measured alone and assembled onto the tube. For example, the primary axial fiducial was measured as it rested on the granite flat of the CMM. The granite flat is set as a plane datum and the height measurements are taken using this flat as a zero location. 18 points were measured and the average is the distance A shown in Table 1 was 7.563 mm.

The apex of the hyperbolic surface of the primary was found by taking three points near the edge of the center hole on the optical surface. The radial distance from the center was calculated by using the X, Y coordinate of each point and a reference coordinate system set by measuring the fiducial surface and the outer interference surface. Measuring these outer surfaces gives the x and y center of the mirror. Given this radius, the theoretical sag was calculated for each measured point and subtracted from the Z dimension of each point. For the secondary mirror, the three points taken to find its apex were within a 5 mm of center so that there is less deviation from a sphere. These measurements provide values for B and D in Table 1.

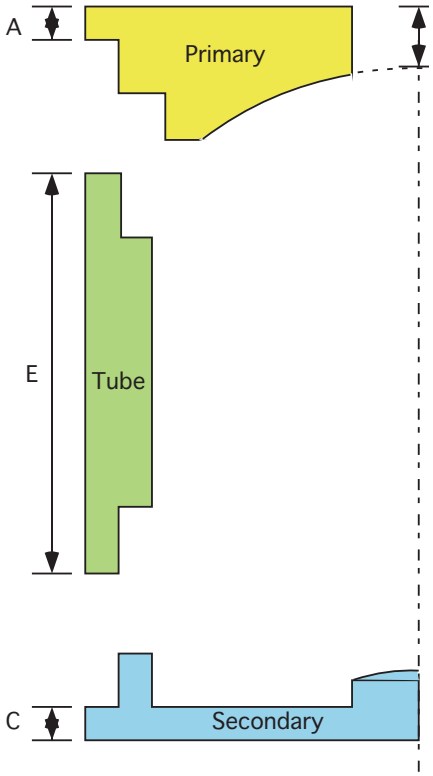

Figure 15. Definitions of measurements in Table 1

The difference in height between the fiducial surface and the apex is B-A for the primary and D-C for the secondary. The values show errors of 3 and 9 μm, respectively. The 3 μm of error in the primary fiducial surface is expected based on the errors in the primary optical surface. The 9 μm of height error in the secondary is a result of not diamond turning the rear surface and the thin aspect ratio of the fiducial surfaces of the secondary mirror. Each these errors change the spacing between the primary and secondary mirrors. The distance between the end of the tube and the mirror apex are determined by E+C-D for the secondary and E+A-B for the primary design and fabrication. The distance between the unassembled tube fiducial and the secondary apex is 128.638 mm which is 13 μm farther than expected upon design and fabrication. The distance between the unassembled tube fiducial and the primary apex is 119.401 mm which is 1 μm farther than expected. These spacing measurements combine to give a theoretical apex-to-apex assembly spacing distance of 113.635 mm which is 10 μm farther than designed. This separation should result in a 150 μm change in the focal length of the system.

Table 1. Dimensions of the mirrors and tube using the CMM

Dimension	Measured (mm)	Variation (mm)	Designed (mm)	Error (μm)
A	7.563	±.0025	7.571	-8
B	22.566	±.0035	22.571	-5
B-A	15.003	-	15.000	3
C	5.022	±.0125	5.000	22
D	10.788	±.0005	10.775	13
D-C	5.766	-	5.775	-9
E	134.404	±.0005	134.400	4
E+C-D	128.638	-	128.625	13
E+A-B	119.401	-	119.400	1
F	113.635	-	113.625	10

To determine the assembled dimensions and the change in dimensions upon assembly, each mirror is assembled to the tube. The exposed tube interference surface and fiducial surface are used as datum surfaces to find the center and z locations, respectively. The optical surface apex points were found using the same process discussed above. First, the primary is assembled to the

tube and the distance from the exposed end of the tube to the mirror apex is measured. This measurement result of 119.442 mm compared with the value of 119.401 mm for E+A-B. This indicates the primary optical surface moves away from the secondary by 41 μm upon assembly. The secondary is then assembled and the distance from the exposed tube end to the apex is measured. The result of 128.653 mm compares with the value for E+C-D of 128.638 to indicate a 15 μm movement of the secondary away from the primary upon assembly. This shows a total increase in apex-to-apex distance of 56 μm. This separation would result in a 2 mm change in the focal length of the system. These measurements also indicate that the primary mirror changes upon assembly and the secondary mirror shifts with its support arms.

The apex-to-apex distance is the crucial element of these measurements as it directly affects the system optical qualities. The designed apex-to-apex distance is optimized for the best system image. Changes to this value move the focal point and increase the wavefront error of the system. The unassembled apex-to-apex value is in error by 10 μm. However, when the system is assembled the primary and secondary apexes move away from each other resulting in an assembled error of 66 μm. The spacing error has an effect on the focal point and optical performance of the system. The effect is large because the focal lengths of the two mirrors are the same magnitude as the system spacing. The effect would be minimized if the focal distance of the elements were longer than the spacing between them. Code V has a best focus function where it determines the smallest wavefront error for each field selected by moving the focal plane closer along the optical axis. When adjusting the spacing by 0.066 mm the best focus becomes -2.348 mm, or a change of 2.003 mm.
The calibration of the CMM gave an anticipated accuracy of ± 3 μm. The primary fiducial surface thickness and the tube height each have errors approaching this value with errors of 3 and 4 μm, respectively. This shows that these parts were, at worst, out of form by the measured value but leaves the possibility that the form error is actually better than the measurement accuracy.

8.3 SYSTEM MEASUREMENTS

WAVEFRONT ERROR

The performance of the optical system can be found by setting up the complete telescope as shown in Figure 16. A plane mirror returns the light to the telescope and back into the interferometer. Since this is a dual-pass arrangement, the errors are doubled.

System wavefront error interferograms can be compared to those produced in Code V. Code V produced wavefront error plots on-axis focus and the best system for on- and off-axis rays. To compare these results, the system must be measured at each of these field locations and at the

measured best system focus. The results of the wavefront error measurement for best system focus are shown for on-axis rays, Figure 17(a), off-axis rays at 0.35º, Figure 17(b) and off-axis rays at 0.5º Figure 17(c).

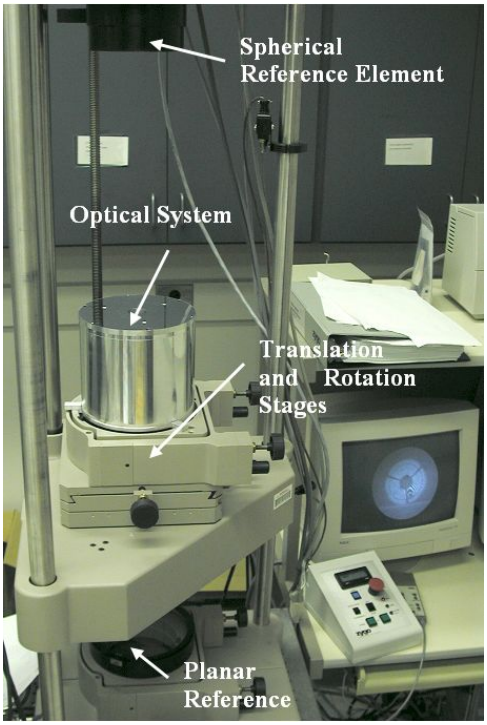

Figure 16. Zygo GPI setup to measure system performance.

To measure the off-axis components, the reference flat must be tilted to change the ray angle. Once the flat mirror is tilted, the system must be translated using the x-y stage to find the new focal point of the system. The four lobed shape produced by Code V at 0.35 degrees is not perceptible because the system is dominated by trefoil errors. Also, the wavefront error of 3λ is six times the theoretical wavefront error of 0.5λ at this location. However, the 0.35 degree field should be at the best focus and, therefore, have minimum power. The power value in Figure 16(b) confirms this with a value of 0.002 waves. Also, the 0.35 degree field should have a reduced error compared to the on-axis at this focus location but the P-V errors are almost identical. However, if the trefoil error from assembly is removed from each measurement the wavefront error at 0.35 degrees is minimized while significant power based wavefront error remains in the on-axis measurement. The 0.5 degree field wavefront error, shown in Figure 16(c), does have the slight oval shape as predicted by Code V, but is still dominated by trefoil errors. Also, the 4.5λ magnitude of the wavefront error is twice the wavefront error of 2.25λ seen in the theoretical model at this location.

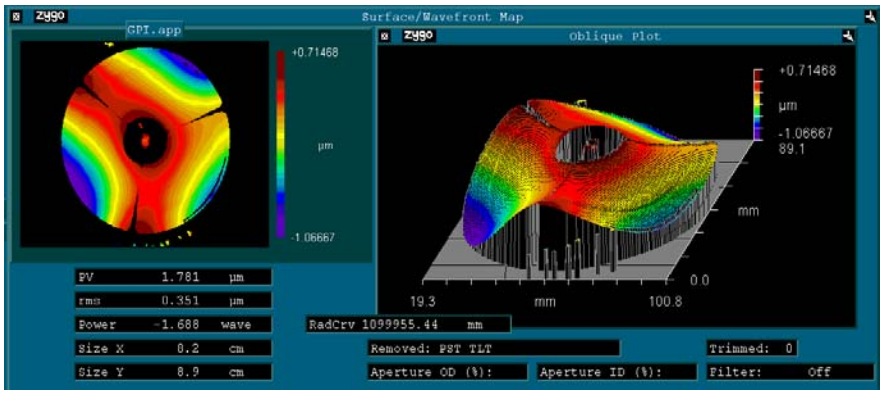

(a) On-Axis plot at system best focus

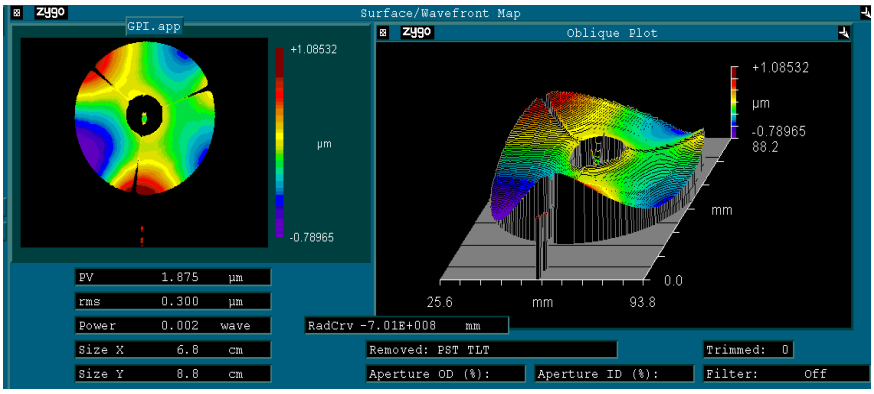

(b) Off-Axis plot (0.35º) at system best focus

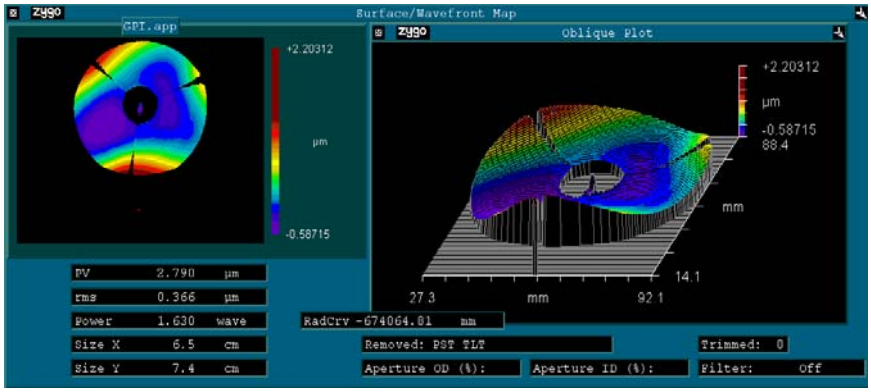

(c) Off-Axis plot (0.5º) at system best focus

Figure 17. Wavefront error measurements for complete telescope system

Modulation Transfer Function (MTF)

The MTF is a measure of the ability of an optical system to transmit contrast from an object to an image plane. MTF testing is frequently done by viewing an optical target and analyzing the quality of the image. The MTF target shown in Figure 18 uses square and sin wave patterns of black and white with a progressively higher frequency. As the lines in get closer together, the difference in density of the black and white is reduced and eventually they blend together in a uniform gray. MTF is measured by determining the maximum wave frequency at which the individual lines are still visible and have not become a uniform gray. This frequency is returned as cycles/mm.

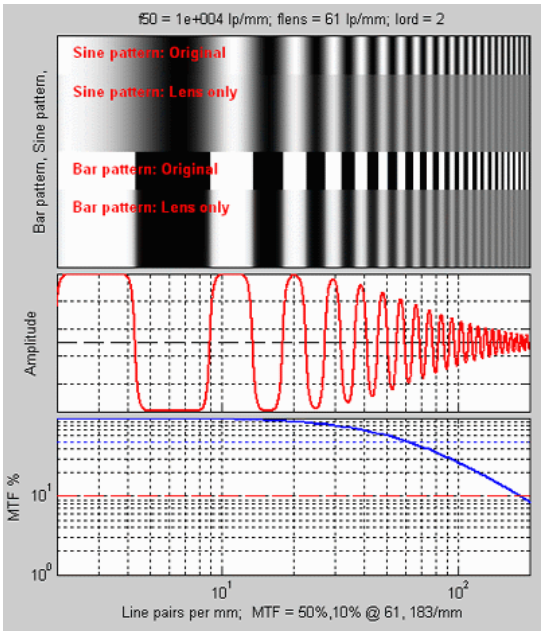

Figure 18 shows the loss of amplitude from photographing a bar pattern. The MTF% represents the percentage of black or white amplitude left in the image at progressively higher line spacing frequencies. A common watermark for MTF measurements is the frequency at which 50% of the original contrast remains, known as the MTF50 point. An MTF value of 100% indicates full resolution whereas a 0 indicated no resolution. MTF values of 0.5 are frequently used as a comparison point. The MTF50 point in Figure 18 is 61 lines/mm and the MTF10 is 183 lines/mm. The MTF10 is the point below which resolution is unknown. The frequency at this value is known as the cutoff frequency.

Figure 18. MTF Measurement Chart

Interferometer Measurements MTF measurements in Figure 19 using the Zygo GPI in the dual-pass arrangement (see Figure 16) present the MTF for on- and off-axis rays. The best performance is at the 0.35º field angle because that point was chosen for best focus to optimize the performance over the entire field of view. The GPI produces a three dimensional MTF plot that analyzes the system MTF in all directions of the aperture. The right hand side of Figure 19 is a plot of four slices from the GPI measurement taken from the center to the outside edge. The GPI produces an MTF plot produced by the GPI is normalized based on the *f*/# and the wavelength of light used. The normalization factor for this measurement is 276 cycles/mm. The Code V model in Figure 19 produced MTF50 value of approximately 60 cycles/mm whereas the measured value is about 10% of the norm or 25 lines/mm. This shows that the actual telescope has a MTF50 value which is about half the theoretical performance predicted by Code V. The surface roughness of the optical surfaces plays a role by scattering light and any focus error would cause edges to lose their sharpness and reduce the MTF.

Image Evaluation The telescope was designed to image objects that are infinitely far away, like the moon. Because the uncertainty of the atmospheric conditions on the sharpness of such an image, closer objects—finite conjugates—were measured. When the model in Code V system is changed from infinite conjugates to finite conjugates, the aberrations added to the system degrade the MTF. With infinite conjugates at the on-axis best focal point, the on-axis MTF of the optical system is diffraction limited and the MFT50 is approximately 120 lines/mm. When

the system is changed to finite conjugates, the theoretical MTF drops significantly. For an object distance of 21.5 m, the on-axis MTF50 value is approximately 16 lines/mm.

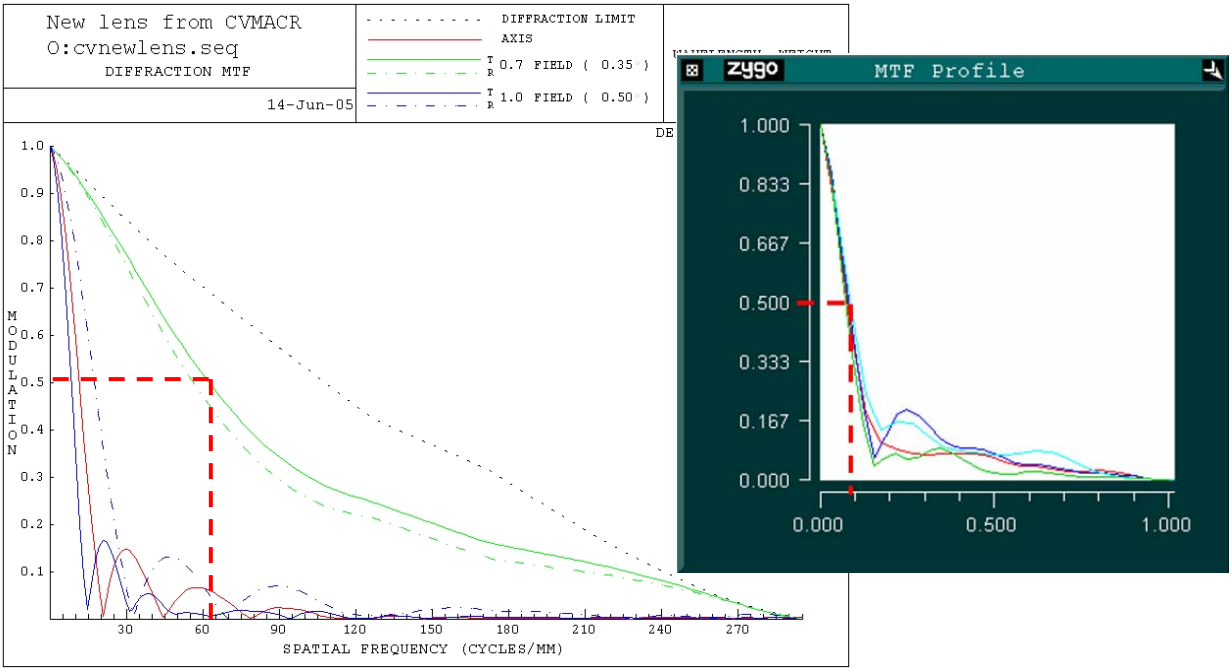

Figure 19. MTF for optimized 2-mirror system presented on-axis and at two locations off-axis (0.35º and 0.5º). Measurements at right is from the GPI at best focus for on-axis rays.

Figure 20 shows the results of two experiments where a optical test target was photographed using a Canon digital camera attached to the telescope. The difference in the images is the size of the aperture used. In Figure 20(b), the entire 150 mm aperture was used and the light collected from the target was imaged on the CMOS array. The image looks out of focus (these images are at best focus) and the MTF50 is about 6 lines/mm; a significant drop from the Code V predictions. If the aperture is reduced and only a part of the primary and secondary are used to image the target, the MTF50 is doubled and the image looks much better – but still not good.

Limiting the aperture reduces the errors on the mirrors (think about taking only a small segment of the surface in Figure 17) and improves the MTF.

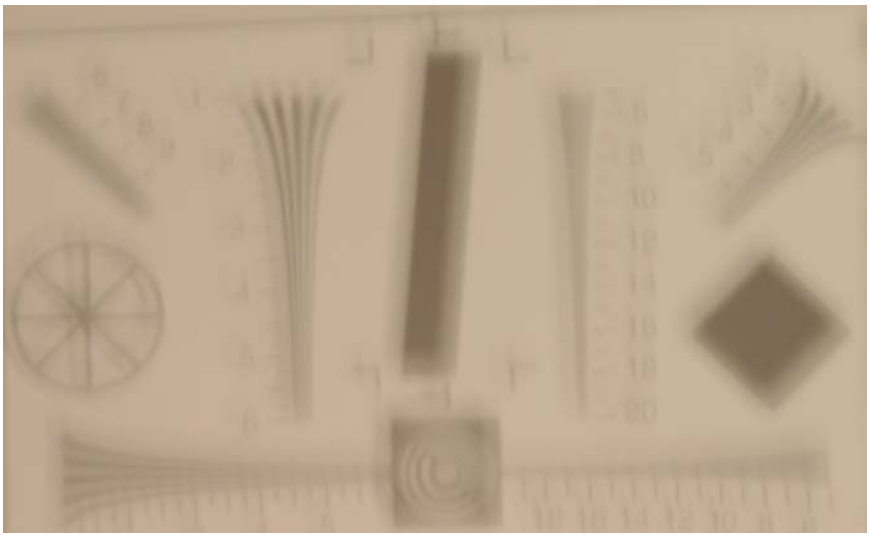

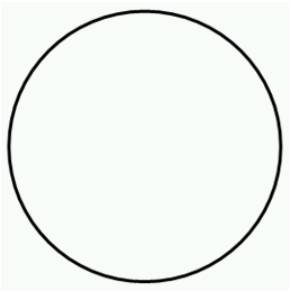

a) Full Aperture Telescope Image at 21.5 m Object Distance. MTF50 = 5 lines/mm

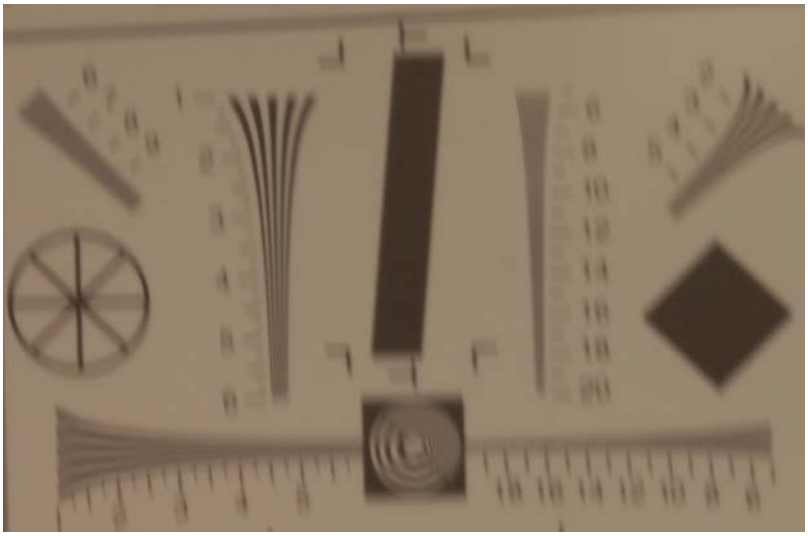

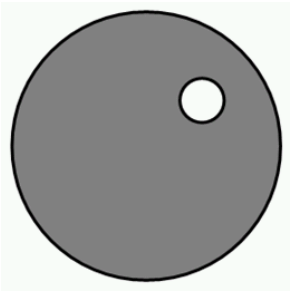

b) Reduced Aperture Telescope Image at 21.5 m Object Distance. MTF50 = 11 lines/mm

Figure 20. Telescope image of the test target with full aperture (a) and reduced aperture (b). The reduced aperature was a 38 mm circle or about 6% of the full aperture.

Spot Size

The ability of the telescope to image a spot can be found by setting up the system as in Figure 16. A flat reference element was used to send collimated light into the telescope and it should focus a collimated light beam into a spot on the CMOS array of the camera. To compare measured spot sizes to the predicted values, the width of the spot at half the maximum intensity was used. MATLAB was used to determine the intensity across different cross sectional traces of the spot. The traces were taken both vertically and horizontally over only the central spot as

shown in Figure 21. The x-unit of these plots is the pixel length of the trace. The pixel size of the camera array (6.1 μm/pixel) was used to convert the x-axis of these plots to μm.

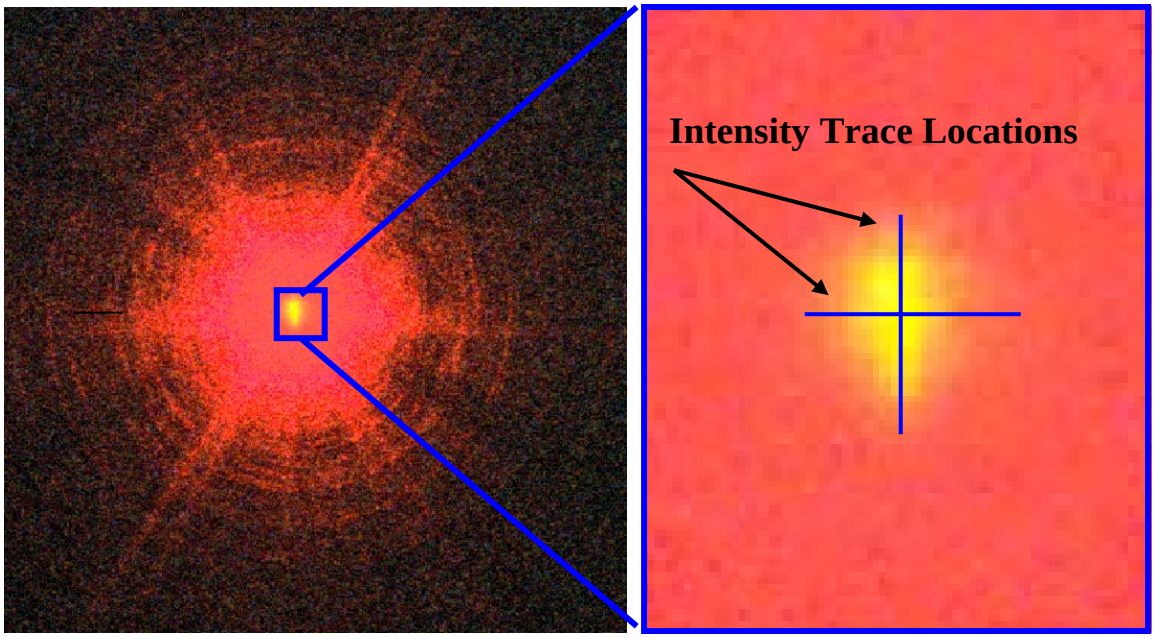

Figure 21. On-Axis Spot Size Intensity Trace Example

The plots of these traces showed that the measured spots differed in shape and size from the Code V predictions. For the on-axis element, Figure 22 shows that the Code V produced spot size is approximately 10 μm and symmetric whereas the measured spot sizes, also in Figure 22, are 133 and 82 μm respectively.

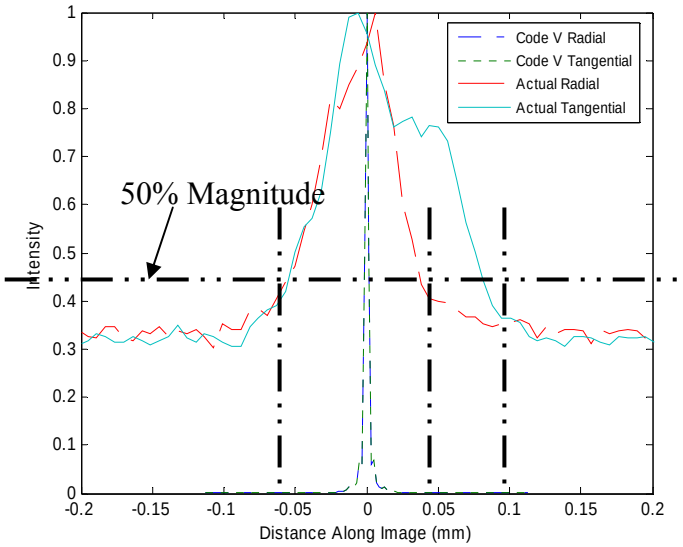

Figure 22. On-Axis Spot Sizes: Code V Produced vs. Measured

Comparing spots on- and off-axis to the Code V predictions showed that the spots were both larger than expected and of a different shape. The spots predicted are symmetric on-axis and at 0.35º off-axis whereas the measured spots have a triangular shape. The triangular shape shortens and fattens from on-axis to 0.35 degrees off-axis and even more so to the 0.5 degree off-axis spot in which the triangle appears equilateral. The triangular shape is caused by the trefoil error seen in the wavefront error of the system.

8.4 CONCLUSIONS

The goal of this research was to measure the optical performance of the Ritchey-Chretién telescope and evaluate the source of the errors. The metrology techniques used included interferometers, profilometers, coordinate measuring machines and photographic analysis. The optical surface results are as follows:

Primary Mirror

- 4 μm of form error in the optical surface
- 1 μm of form error in the back surface
- 5 nm measured RMS surface finish vs. 0.19 nm theoretical surface finish

Secondary Mirror

- 300 nm of form error
- 4 nm measured RMS surface finish versus 0.05 nm theoretical surface finish

The distortion of the optical components as a result of the fabrication and assembly processes are responsible for degraded performance.

The assembly fiducial surfaces and the assembled optical surfaces were measured with profilometer, interferometer and a coordinate measuring machine. The assembly errors include:

- 6 μm of axial fiducial surface flatness errors
- 66 μm of spacing error between the two mirrors
- Trefoil error in the primary surface
- Reduction of overall primary form error from 4 μm to 1.7 μm

The assembly process changed the shape of the optical surfaces due to the machining process, errors in the shape fiducial surface, over constraint and distortion from the bolting forces.

The assembled system was measured with interferometry and photographic analysis. The measured system compared with the Code V produced system as follows:

- 3 λ measured wavefront error versus λ/2 Code V produced wavefront error
- Primary measured aberration is trefoil, not seen in Code V model
- Measured MTF 30% of Code V produced MTF
- Measured spot sizes increased by 30% for best case, 1000% for worst case

These measurements show the primary system error is the assembly error. The trefoil caused by bolting forces is the primary aberration in the wavefront measurements and without these errors the system wavefront would be similar to the Code V model predictions of λ/2 RMS.

REFERENCES

1. Wilson, R.N., *Reflecting Telescope Optics I*. Springer, 2nd Edition, Berlin, (2004).
2. Schroeder, Daniel J., *Astronomical Optics*. Academic Press, 2nd Edition, San Diego, (2000).
3. Ritchey, G.W., *On the Modern Reflecting Telescope, and the Making and Testing of Optical Mirrors*. Smithsonian Contributions to Knowledge, 34:1-51, (1904).
4. Korsch, Dietrich, *Reflective Optics*. Academic Press, Boston, (1991).
5. Malacara, Daniel, *Optical Shop Testing*. John Wiley & Sons, 2nd Edition, New York, (1992).
6. Horne, Douglas F., *Optical Production Technology*. Adam Hilger Ltd, 2nd Edition, Bristol, (1972).
7. Bennett, Jean M., and Mattsson, L., *Introduction to Surface Roughness and Scattering*. Optical Society of America, Washington, DC, (1989).

9 TEM AND RAMAN SPECTROSCOPIC ANALYSIS OF HIGH PRESSURE PHASE TRANSFORMATIONS IN DIAMOND TURNED SINGLE CRYSTAL SILICON

Timothy Kennedy
Graduate Student
Ronald Scattergood
Professor
Department of Materials Science and Engineering

Single point diamond turning was performed on (100) Si along the <011> type direction using both -30° and -45° diamond tools with feedrates of 1 and 5 μm/rev> Machining was performed using a t-lathe and a parallel fly cutting setup. All samples were analyzed with Raman spectroscopy, and cross sectional Transmission Electron Microscopy (TEM). Dislocation loops and slip planes were found at depths up to 250 nm below the surface of both feedrates of the t-lathe machined samples. In the fly cut samples, Raman spectroscopy showed that depending on tool edge design an amorphous layer was not always created. This was contradicting by the TEM images showing a thin a-Si layer. A correlation between the Raman spectra and cross sectional TEM images of the diamond turned silicon was not possible. TEM analysis is needed to analyze subsurface damage, and to determine the deformation mode (i.e., high pressure phase transformation (HPPT) or dislocation movement). Recent results have provided more insight into the lack of dependence between feed rate and the depth of the amorphous layer.

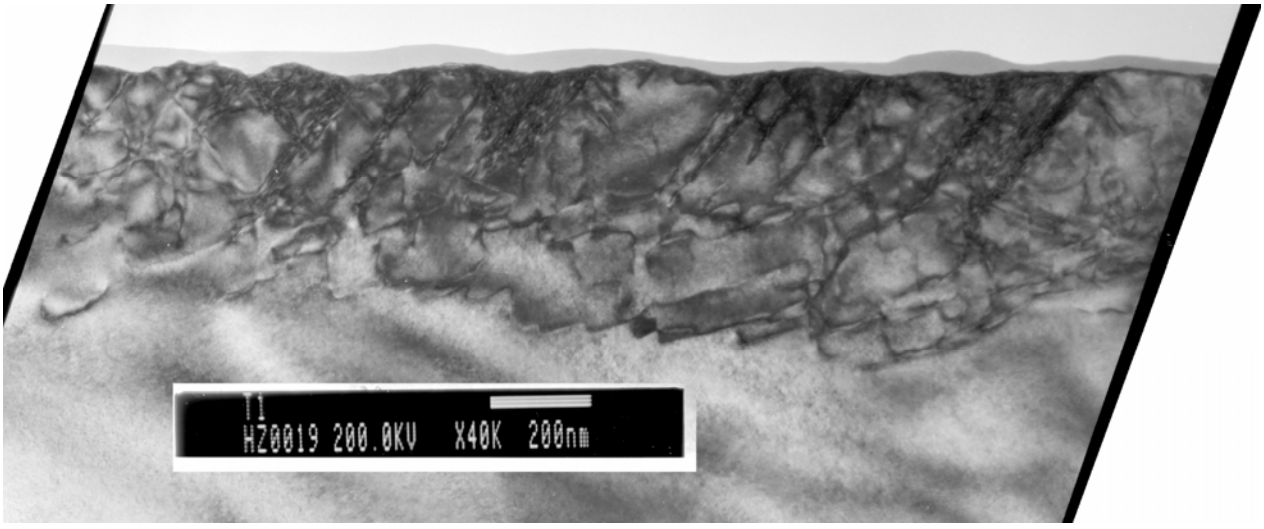

9.1 INTRODUCTION

Diamond cubic silicon (Si-I) is a brittle material under standard temperature and pressure, but when exposed to a high pressure environment the crystal structure transforms into a ductile β-tin metallic phase (Si-II). Once the Si-II is unconstrained it back transforms into multiple forms of Si, mainly amorphous Si (a-Si) and Si-I. The total transformation of silicon depends on loading, unloading, and temperature. This is shown in the transformation schedule in Figure 1. This transformation allows silicon to be machined without brittle fracture occurring, but the back transformation alters the subsurface (~500 nm in depth). This alteration can be divided into two layers: an amorphous layer and a damage layer. The amorphous layer can extend from the surface down as far as 200 nm; this is the byproduct of the back transformation process which creates amorphous silicon (a-Si). Below the amorphous layer a damage layer extends another 300 nm; this layer is comprised of dislocation structures. In situ analysis of this transformation during the manufacturing process is impractical. Using transmission electron microscopy (TEM) and Raman spectroscopy a portrait can be formed of the deformation mechanism in diamond turned silicon.

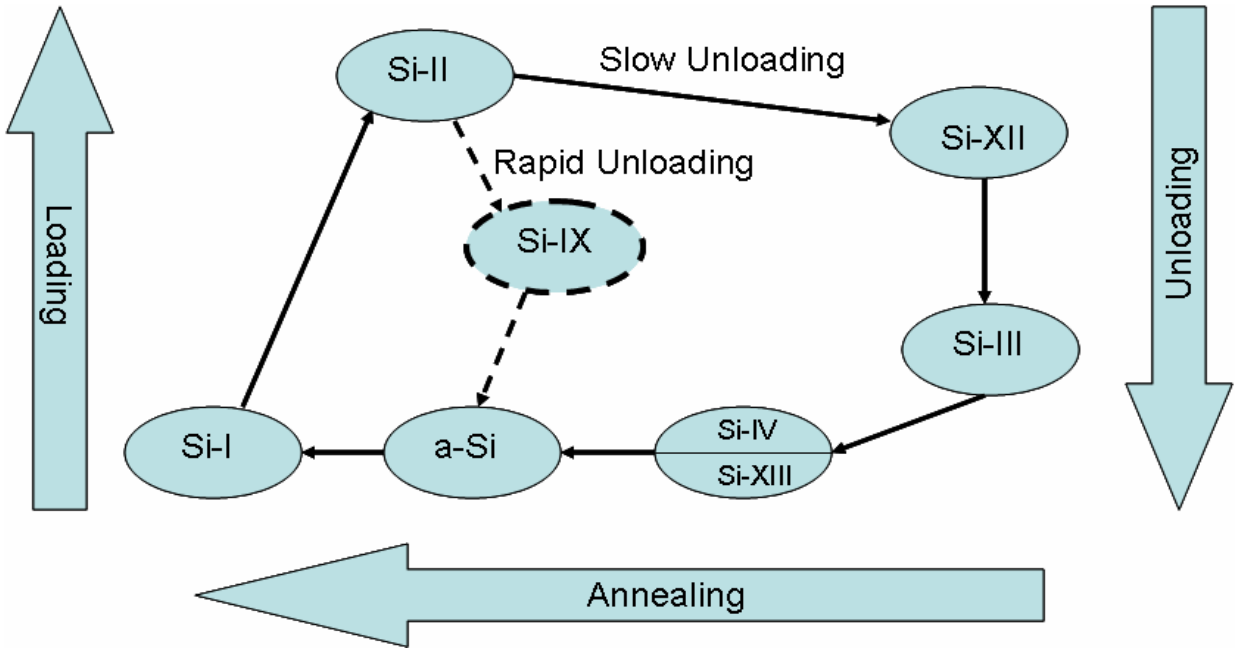

Figure 1. Silicon transformation schedule. [1]

9.2 PROJECT DETAILS

TEM and Raman data was collected from (100) oriented silicon that was diamond point turned along the <110> type direction. Different crystal orientations are available but it has been shown that (100) oriented silicon provides the best ductility.[2] Samples were machined at 1 and 5

μm/rev using a t-lathe diamond turning setup and a parallel fly cutting technique, the latter using two sets of tools consisting of a -30° and -45° rake angle round nose diamond tool.

9.2.1 EXPERIMENTAL SETUP

A Rank Pneumo ASG 2500 Diamond Turning Machine was used to create the samples for this study. Two diamond turning setups were used; the first a traditional T-lathe setup and the next a parallel fly cutting setup. The fly cutting samples were 10 mm wide by 20 mm long, and are oriented so that the cutting direction follows the <110> type direction across the 10 mm width; as compared to an entire wafer for the lathe operation. Two sets of tools were used; one set sharpened by IMT and the other manufactured by Edge Technologies. The tools used were 3 mm radius round nosed diamond with rake angles of -30° and -45°. Unlike the traditional T-lathe setup where the tool is on the x-axis and the sample in on the spindle; parallel fly cutting places the tool on the spindle while the sample is on the x axis parallel to the tool so that a flat cut can be produced. Since carbon reacts with silicon, the latter technique reduces the diamond tool wear since the diamond is not always in contact with the silicon. Spindle speed and feed rate need to be optimized so that the layered structure can be controlled and possibly eliminated through machining, instead of other processes such as thermal annealing. Samples have been prepared with feed rates between 1 and 5 μm/rev, since previous research has suggested a possible transition in the subsurface through Raman spectroscopy.[2]

9.2.1 MATERIAL CHARACTERIZATION

To characterize the machined silicon two techniques will be used; Raman spectroscopy and transmission electron microscopy (TEM). Raman spectroscopy measures the intensity and wavelength of inelastically scattered light from molecules. The scattered light is shifted by the molecular vibrational energy, which is directly controlled by the interatomic bond length of the atoms in the sample. In the case of silicon each crystalline phase has its own interatomic bond length, thus each phase would have a unique and sharp Raman spectrum. In the case of a-Si, the interatomic bond lengths vary so the Raman spectrum from a-Si is broadened. For this study it is important to know crystalline silicon (Si-I) has a peak at around 520 cm^{-1} while amorphous silicon (a-Si) centers around 470 cm^{-1}.

A different Raman technique known as polarized Raman (non-polarized Raman was described previously) was also used to analyze the machined silicon. In polarized Raman different structures have different Raman active modes, which will scatter photons with energy (cm^{-1}) different from the incident wave. The scattering intensity *I* is given by

$$I = C\sum_j \left| e_i \cdot R_j \cdot e_s \right|^2$$

Where C is a constant, e_i and e_s are the incident and scattered polarization vectors, respectively, and R_j is the Raman tensor, determined from group theory for the different crystal structures. Linear polarizers were used to fix the directions of e_i and e_s, and the Si wafer was on a rotating sample stage. Rotating the stage by an angle θ changes R_j such that

$$I \propto \sin^2 2\theta$$

for single crystal Si cut along the (100) plane. Amorphous Si has no directional dependence, so the intensity for its peak should remain constant as θ varies. Scans were done on wafers machined at different rates and with different tool tip rake angles. The incident polarization was set vertical, and the scattered was set horizontal. The [110] direction of the sample initially pointed vertically. The angle θ with the vertical was increased in increments of 10° for each scan. Data was taken for the first quadrant, and the values of the others were extrapolated by symmetry. Intensities of the peaks at 470 cm^{-1} (a-Si) and 520 cm^{-1} (Si-I) were plotted on polar graphs as a function of θ[1]. Even though Raman spectroscopy is a useful tool for its qualitative information it does not provide quantitative data on subsurface structures like TEM.

TEM can provide high resolution micrographs through the use of a high energy electron beam (200 kV) that is transmitted and diffracted through the electron transparent sample. Cross-sectional TEM (XTEM), selected area diffraction (SAD), and bright field-dark field (BFDF) imaging were utilized for this study. XTEM provides the proper view of the subsurface layers compared to the more traditional planar view. To help corroborate the Raman spectroscopic data SAD was used to determine the phases present in the subsurface. SAD involves the use of an aperture to reduce the intensity and the area of the incoming beam, and then viewing the ensuing diffraction pattern. A diffuse halo pattern indicates an amorphous material, while evenly spaced spots would indicate a crystalline phase. Bright field images result from the selection and viewing of the transmitted spot, while dark field images are created by selecting the diffracted spot that appears to the left of right of the transmitted spot. BFDF can show differences in phases in the sample, the presence of dislocations, and strain fields.

[1] All Raman spectroscopy data and information provided by Benjamin Gilbert, Masters Student, Department of Physics, NCSU

9.3 RESULTS

9.3.1 T-LATHE MACHINING RAMAN RESULTS

Previous research at the NCSU Precision Engineering Center used samples that were lathe machined using the IMT tools with -30° and -45° rake angle tools at feed rates of 15, 7, 3, 2, and 1 µm/rev, and then analyzed through non-polarized Raman spectroscopy.[2] A possible dependence between feed rate and the thickness of the a-Si layer can be seen in Figure 2 when machined with a -30° rake angle tool. This dependence is based on the decreasing Si-I peak at 520 cm^{-1} as feed rate lowers until it is consumed by the shoulder of the a-Si peak at 1 µm/rev.

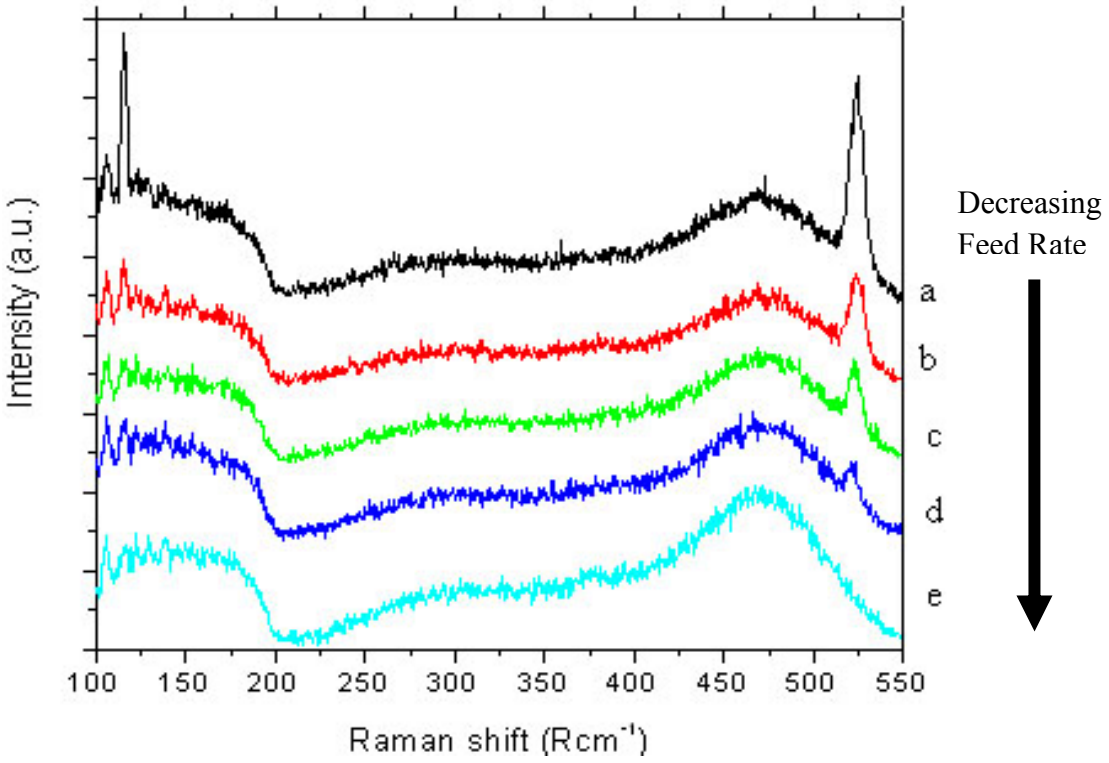

Figure 2. Raman spectra at feed rates a) 15, b) 7, c) 3, d) 2, and e) 1 µm/rev IMT -30° tool, showing a possible dependence on feed rate and a-Si thickness. [2]

Samples that were machined with a -45° rake angle tool did not show the same feedrate dependence as seen in the spectra in the Figure 3. The Si-I peak does not disappear into the a-Si shoulder as in Figure 2. A comparison between the results of the two tools is impractical due to the various factors. Tool forces, tool wear, and stress states at the tip are all dependent on the rake angle and initial tool condition.

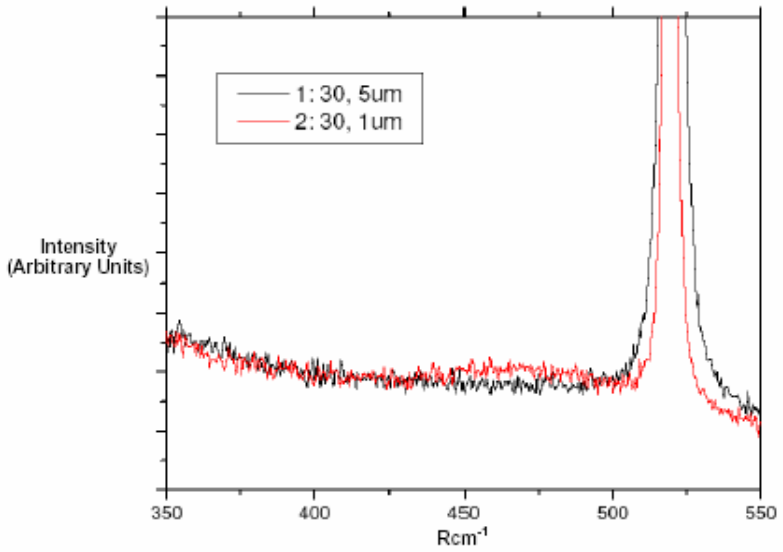

Figure 3. Raman spectra showing no dependence between feed rate and a-Si layer thickness with a -45° rake angle tool. [2]

9.3.2 T-LATHE MACHINING TEM RESULTS

Once the Raman spectra were recorded the silicon samples were made into TEM samples. It was determined that only the samples machined with the -30° IMT tool at 5 and 1 µm/rev would be viewed since the Raman spectra showed that these parameters would provide the best view of the differing thickness of the a-Si layer. The micrograph in Figure 4 provides the best view of the subsurface layers for silicon machined at 5 µm/rev. Starting from the bottom up the following layers are present; undisturbed silicon, then a layer of dislocations 400 nm thick, above the dislocations is the a-Si layer which is on average 44 nm thick. Inside the dislocation layer slip planes and dislocation loops exist. The slip planes lie at a 54° from the (100) surface, signifying a (111) slip system. The (111) slip system is the most common in plastic deformation in diamond cubic materials. Figure 5 shows that the a-Si and the beginning of the dislocation layer do not have the same topography which is somewhat unexpected. SAD indicated a diffuse halo, showing that he top layer was indeed amorphous silicon.

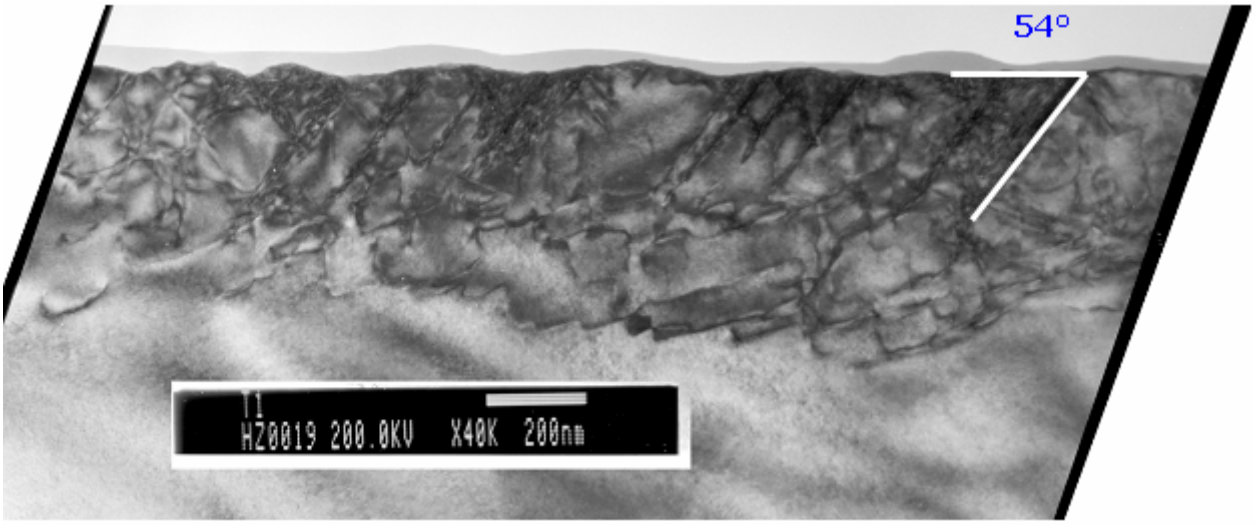

Figure 4. TEM micrograph machined 5 µm/rev with a IMT -30° tool at 40,000x. The (111) slip system angle is shown along with the a-Si layer and the dislocation microstructure.

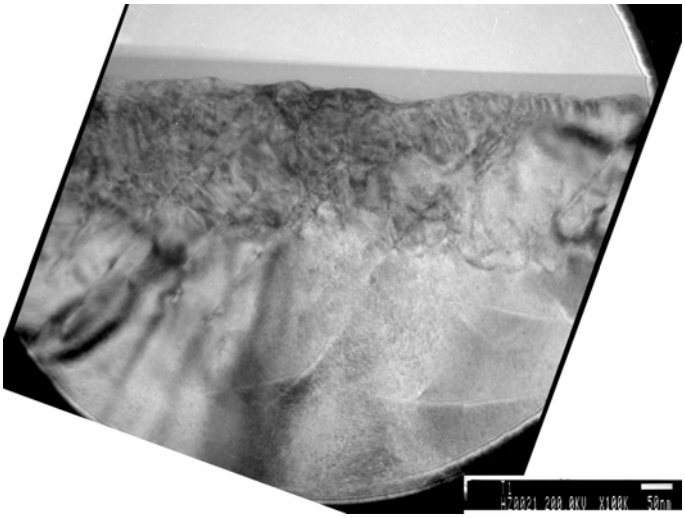

Figure 5. TEM micrograph machined 5 µm/rev with a IMT -30° tool at 100,000x.

The use of bright field/dark field (BFDF) pairs helps to view the dislocation structures, any phase contrast, and the strain fields that are present in the silicon. Strain fields and dislocation loops are present in the BFDF pair in Figure 6, 7, and 8. When the lattice of a crystalline material is strain, it changes the way electrons are transmitted through the structure. This change is usually seen by contrast change. It is another way to help indicated a strained lattice, view dislocations, and view alloying elements or precipitates.

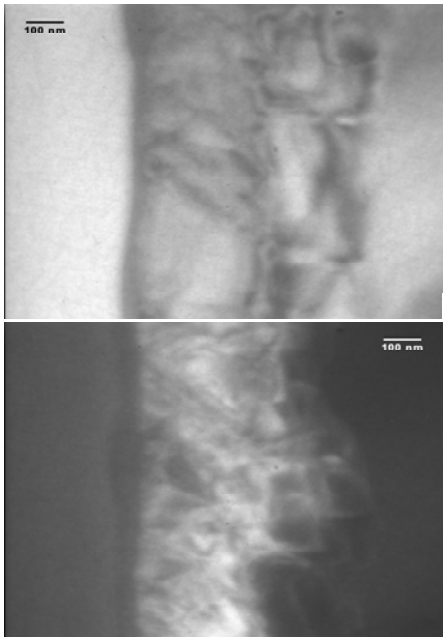

Figure 6. BFDF pair, machined at 5 μm/rev with a IMT -30° tool, 196,764x. Notice the strain induced contrast change in the dislocation layer.

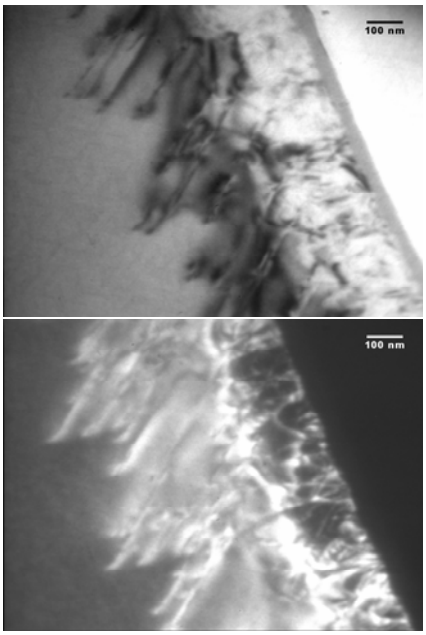

Figure 7. BFDF pair, machined at 1 μm/rev IMT -30° tool, 196,764x. Notice the slip planes going deep into the undisturbed silicon.

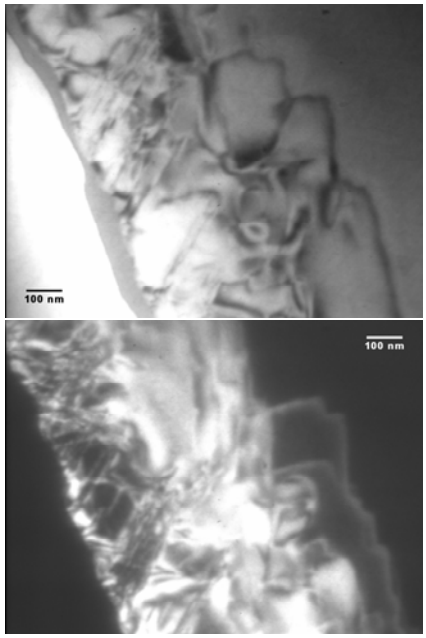

Figure 8. BFDF pair, machined at 1 μm/rev with a IMT -30° tool, 196,764x. Notice the dislocation loops going in and out of the undisturbed silicon.

The machining parameters in Figure 7 and 8 are the same, 1 μm/rev with a IMT -30° tool. Even though one does not see the same structure in the subsurface, it all depends on the angle of the sample and the angle of the diffracted electron beam. So in Figure 7 slip planes penetrate deeply (400nm) into the undisturbed silicon. While Figure 8 shows dislocation loops and a highly strain dislocation layer.

9.3.3 LATHE RAMAN SPECTRA AND TEM COMPARISON

It is important to try to compare the TEM and Raman spectroscopy results. The Raman results indicate that the a-Si layer at a feed rate of 1 μm/rev should be thicker than the a-Si at a feed rate of 5 μm/rev. To compare the TEM results, the a-Si layer is measured and then plotted versus feed rate, Figure 9. The result from this comparison is surprising. There is no statistical difference between the thicknesses of the a-Si layer at the two feed rates. Only 4 nm separate the layers, and this is contradictory to the Raman spectroscopy results. Due to time constraints no fly cutting samples were imaged in the TEM. The reason for this discrepancy will be discussed in a later section.

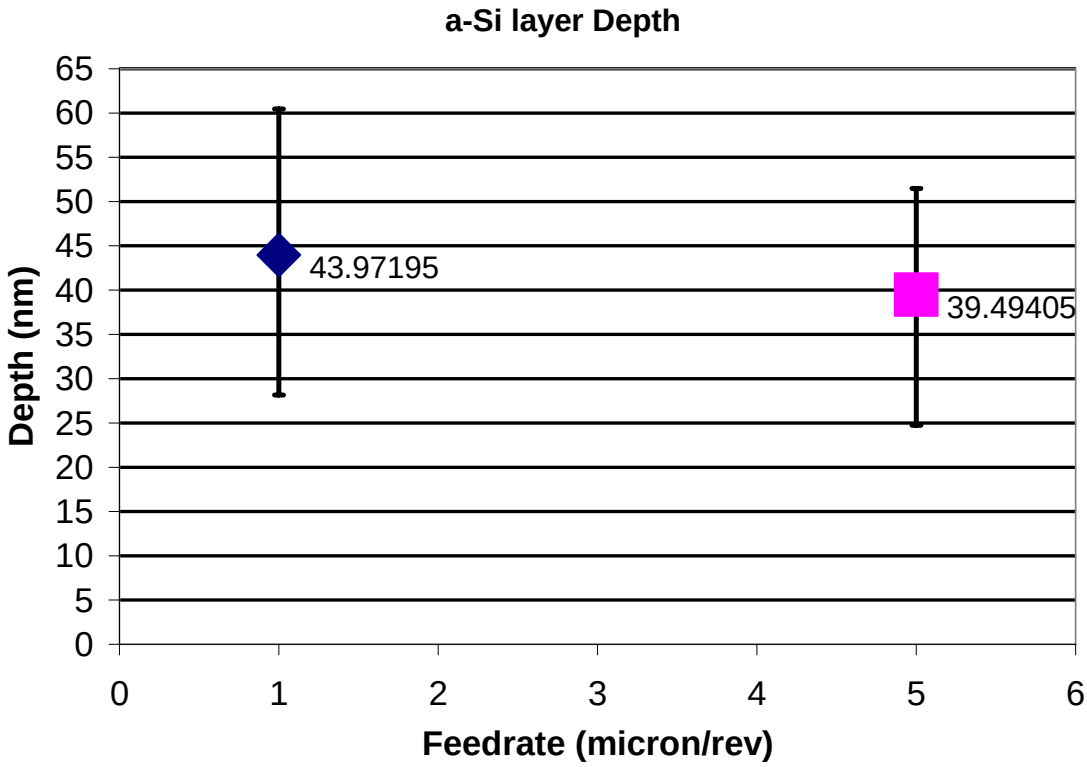

Figure 9. Depth of the a-Si layer versus feed rate. There is no statistical difference between the to feedrates, which counters the Raman spectra for those feed rates.

9.3.4 FLY CUTTING RAMAN RESULTS

It was important to make sure that the t-lathe machining and fly cutting created the same Raman spectra. None of the fly cutting Raman spectra matched the lathe machining spectra. Figure 10 is a representative spectra for the fly cut silicon. It is apparent that the a-Si peak is missing from the spectra as compared to the Raman spectra from the t-lathe set up. Both sets of tool were used in fly cutting and neither set showed any amorphous material, only a sharp Si-I peak at 520 cm^{-1}. This is troublesome since the surface showed no signs of brittle fracture. For machining silicon it is usually assumed that when brittle fracture occurs on the surface no amorphous material is created. One of the ideas behind ductile machining of brittle materials is that a second phase is formed through a high pressure phase transformation to facilitate the plastic deformation of the machining process. The Raman spectra of both the -30° and -45° rake angle tools, regardless of feed rate, showed the same lack of an a-Si peak at 470 cm^{-1} . All of the tool parameters are the same between the two machining parameters, so it is unclear to why there should be a difference between the two sets of Raman spectra. So to ensure that the Raman spectra were accurate from both tool sets, polarized Raman was utilized. The results that come from the polarized Raman help to clear the picture of the characterization of the subsurface.

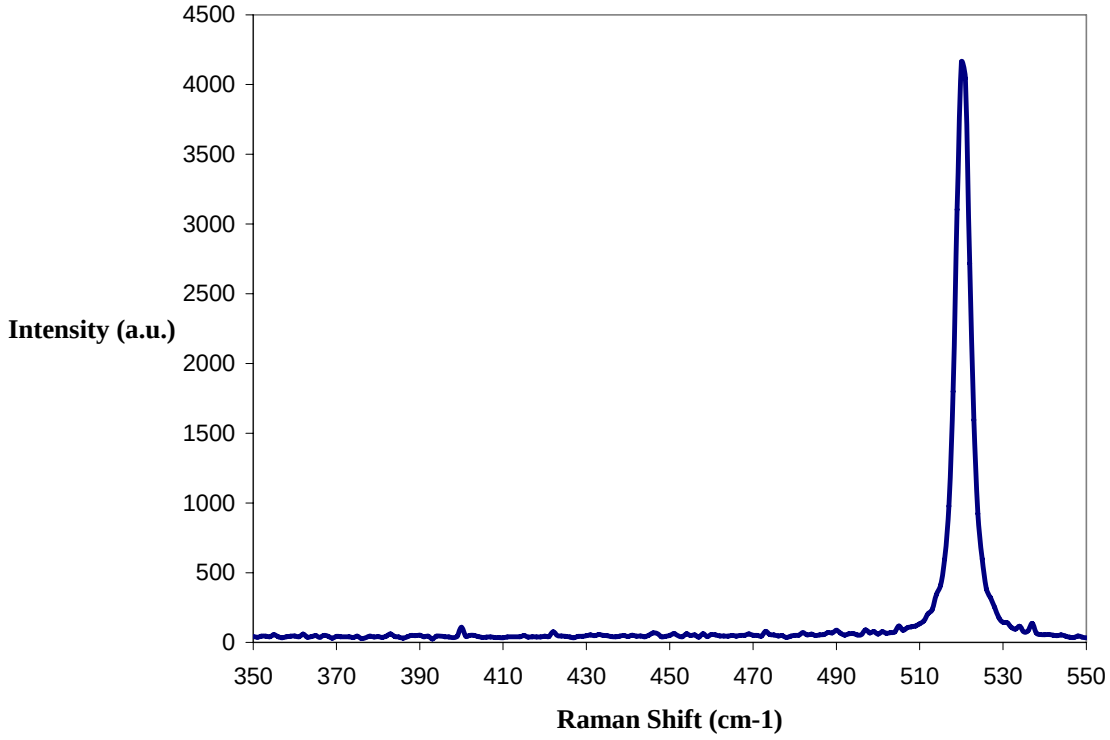

Figure 10. Raman spectrum of silicon machined at 1 µm/rev using a -30° Edge tool showing lack of a-Si at 470 cm^{-1}

As mentioned in a previous section to create a polar Raman spectra the intensities of the a-Si and Si-I were plotted as a function of polarization angle. The a-Si peak has no dependence on angle since it has no crystal structure. Si-I follows a clover leaf pattern that is expected from the physics of Raman and the direction <110> as can be seen in Figures 11 and 12. Once again there appears to be no correlation between feedrate and the a-Si layer. The layer thicknesses shown in Figure 9 can now be considered valid knowing that there could be no dependence.

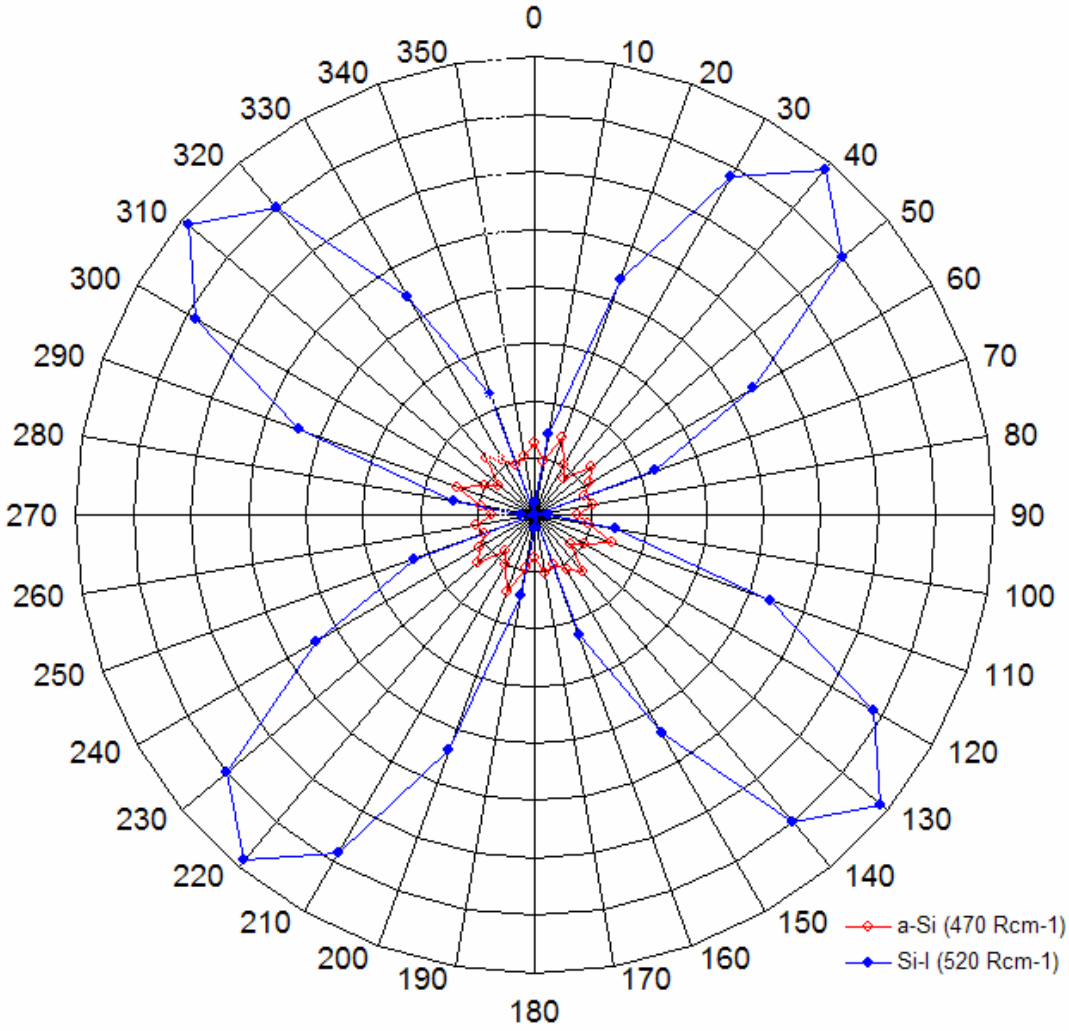

Figure 11. Polar Raman plot of silicon machined at 1 μm/rev with a IMT -30° tool.

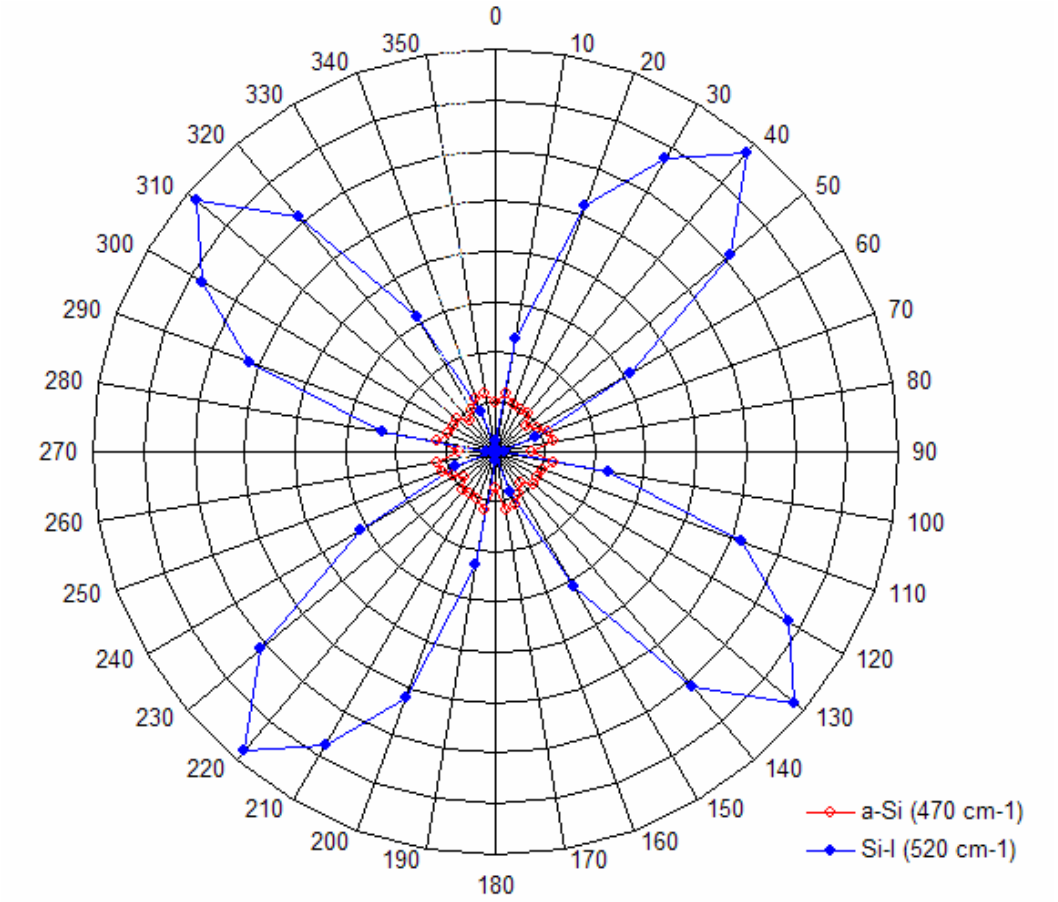

Figure 12. Polar Raman plot of silicon machined at 5 µm/rev with a IMT -30° tool.

9.3.5 FLY CUTTING TEM RESULTS

When the machining technique is switched to parallel fly cutting a change in the subsurface is evident. Figures 13 and 14 were fly cut at 5 µm/rev with an IMT -30° tool, and there is no damage layer beneath the a-Si layer when compared to Figure 2. Even the a-Si layer is dramatically thinner than previously measured. When the tool vendor is changed to Edge Technologies the same microstructure is seen. Figures 15 and 16 were fly cut at 5 µm/rev with an Edge Tech -30° tool, and the same lack of dislocations and a thin a-Si layer is apparent.

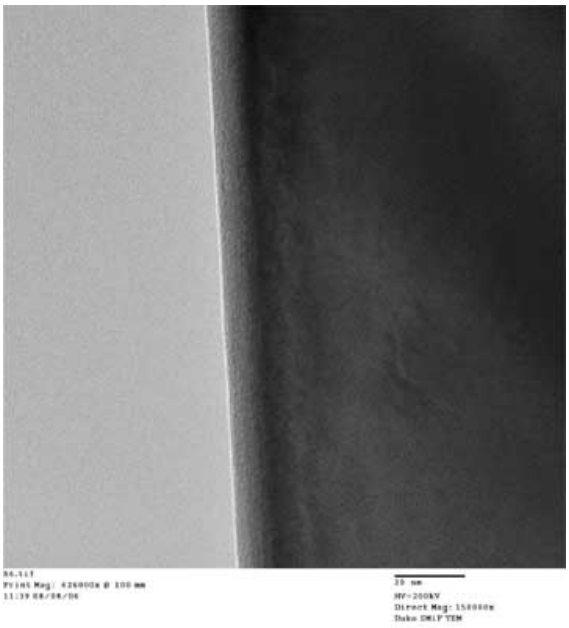

Figure 13. TEM micrograph fly cut at 5 μm/rev with an IMT -30° tool. Notice the lack of a damage layer.

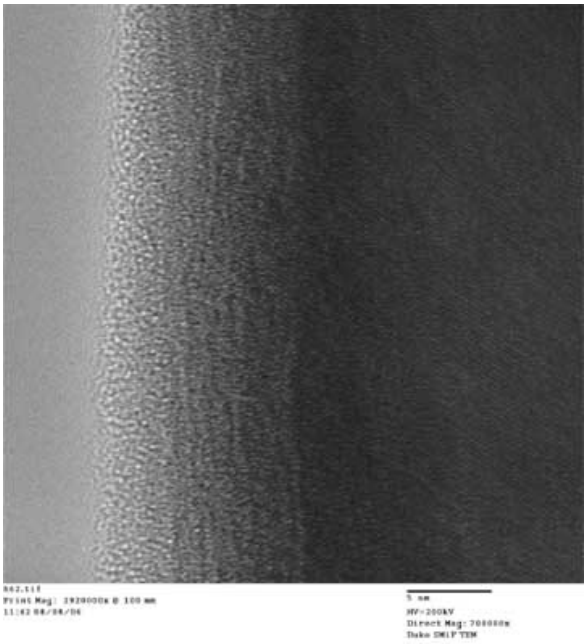

Figure 14. TEM micrograph fly cut at 5 μm/rev with an IMT -30° tool showing a higher magnification of the a-Si layer at the surface.

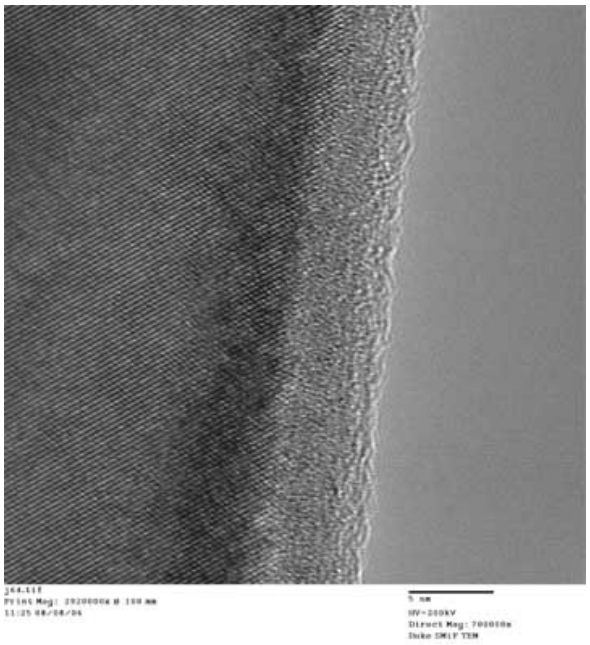

Figure 15. TEM micrograph fly cut at 5 μm/rev with an Edge Tech -30° tool showing a higher magnification of the a-Si layer at the surface.

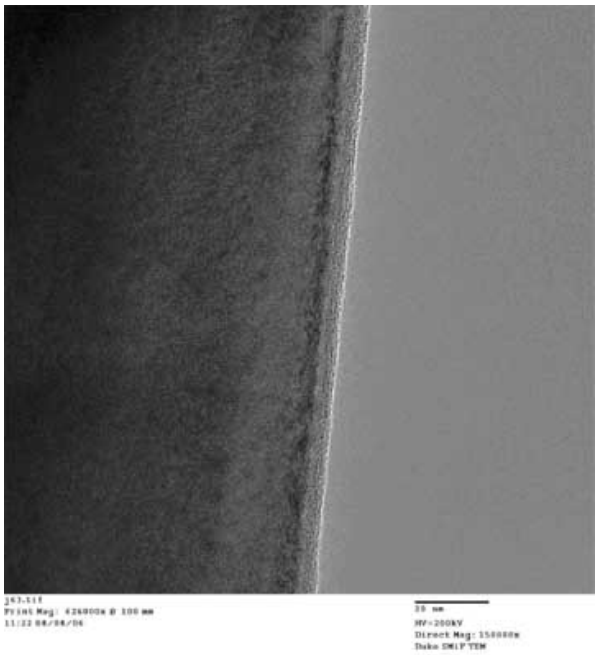

Figure 16. TEM micrograph fly cut at 5 μm/rev with an Edge Tech -30° tool. Notice the lack of a damage layer.

When the feed rate is lowered to 1 μm/rev with an Edge Technologies -30° tool nanocrystals appear below the a-Si layer, Figure 17. It is unclear how these nanocrystals were formed in the

sample, since the same piece of silicon was used for the 5 μm/rev samples shown in Figures 15 and 16. As of now it is believed to be an anomaly. Unfortunately the IMT -30° 1 μm/rev sample was destroyed while placing it in the TEM sample holder.

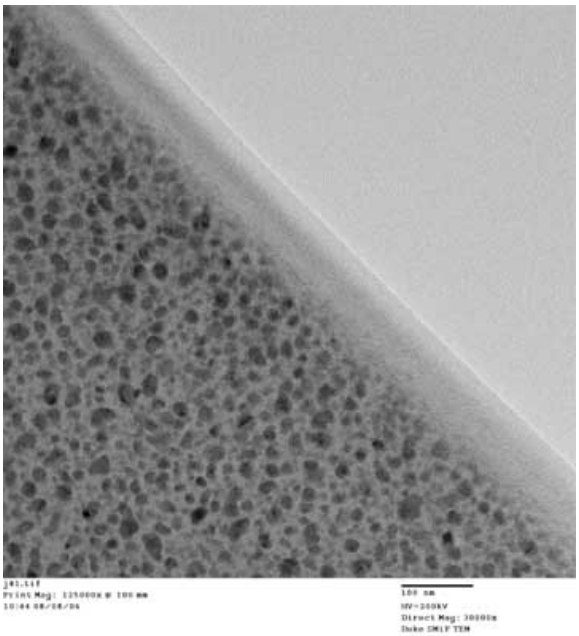

Figure 17. TEM micrograph fly cut at 1 μm/rev with an Edge Tech -30° tool. Notice the existence of nanocrystals.

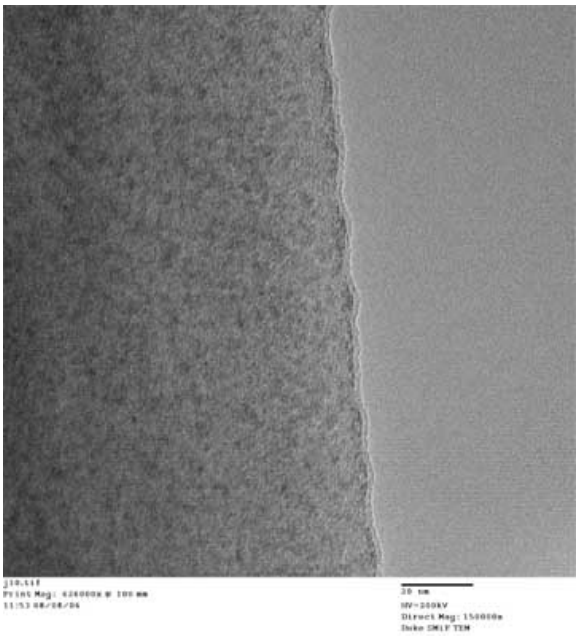

Figure 18. TEM micrograph of as received CMP polished silicon wafer.

9.4 MACHINING TECHNIQUE COMPARISON

Beyond comparing t-lathe machining and fly cutting it is important to compare these results with the results found from CMP processing. It is interesting to compare these new TEM results to the as received CMP silicon wafer in Figure 18, which shows a nominal a-Si layer thickness of around 2 nm. It was previously thought that CMP was the only way to achieve optical surface finish with very little subsurface damage, but that has been proven not to be the case.

Figure 19 shows the comparison of a-Si layer depth versus the machining feed rate and technique. Due to the fact that lathe machining and fly cutting are equivalent machining techniques, the various tool parameters seem to have an affect on the a-Si layer depth.

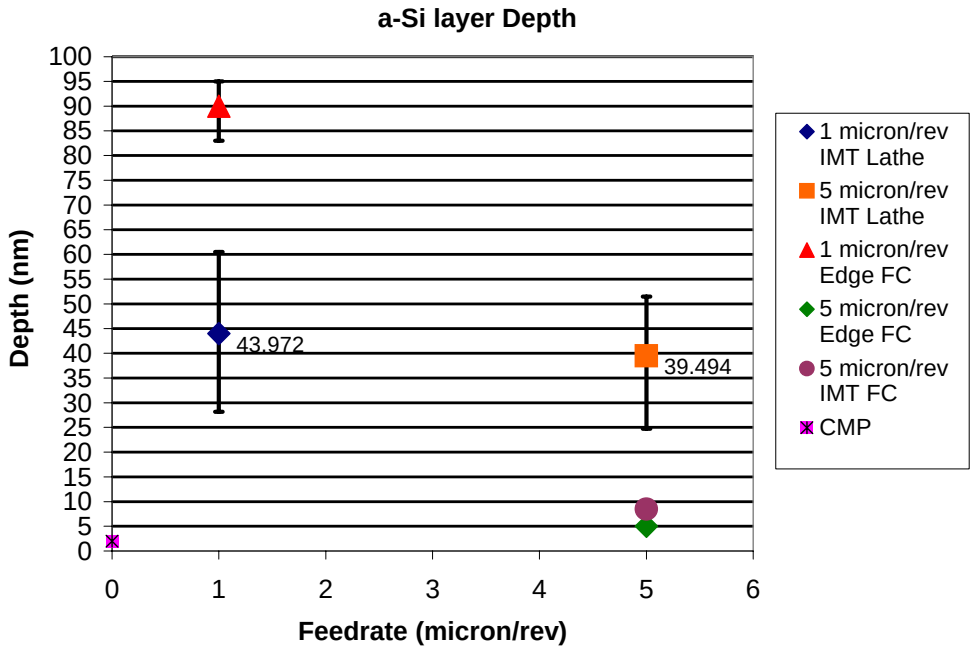

Figure 19. TEM micrograph fly cut at 5 μm/rev with an Edge Tech -30° tool. Notice the lack of a damage layer.

9.5 COMPARISONS AND CONCLUSIONS

To make sure that the TEM results are on par with what other research groups have seen a comparison is need. Other groups [3, 4] have reported dislocations, dislocation loops, and slip planes. If an HPPT is occurring then the loops and slips planes indicate a normal metallic deformation mode when the silicon transforms into ductile Si-II. Another point is the existence of the amorphous layer. Once again there is evidence for either an HPPT or other deformation mode. The theory in silicon HPPT is that upon unloading the Si-II will back transform through various phases until it reaches the amorphous stage, at which time it does not have enough energy to recrystallize into Si-I leaving a metastable a-Si, as illustrated in Figure 2. If viewed through a traditional deformation mode, the amorphous layer exists due solely to the extreme high pressure at the surface under the diamond tool, and the dislocations underneath follow traditional silicon slip mechanisms. More in depth studies will need to be performed to pin point the true deformation mechanism.

From the TEM data it is clear that the back transformed material contains an amorphous layer and a deeper damage layer. Multiple research groups have also seen this structure, but it is important to note that there has been no in-depth evaluation of the damage layer before. Before the polar plots were recorded the Raman spectra and TEM images were contradictory to each other, due to

the lack of a statistical difference in a-Si layer thicknesses. Now taking into account the polar plots the TEM data and Raman data can now be seen in good comparison to each other. As shown the samples machined with fly cutting showed no a-Si peak in the Raman spectra. This is due to the fact that the resolution limit of Raman spectroscopy is around 10 nm. The resolution limit is larger than the a-Si layers seen in the TEM images. At this point, the existence of an HPPT in silicon during diamond turning is looking more probably, and any mode or mechanisms set forth in future research are only theoretical.

9.6 FUTURE WORK

Upcoming research will not use Raman spectroscopy due to the resolution limit, but will rely heavily on TEM imaging. Other factors that will be looked at included how feedrate, rake angle, cutting speed, tool force, sample orientation, and tool wear have on the subsurface of the machined silicon. Beyond silicon, lithium niobate will be examined due to the lack of research on the subsurface created during single point diamond turning of this important optical material.

REFERENCES

1. Domnich, V. and Gogotsi, Y., *Phase Transformations in Silicon Under Contact Loading*. Rev. Adv. Mater. Sci. 3 1-36, (2002).
2. Randall, T., *Characterizing the Ductile Response of Brittle Semiconductors to Dynamic Contact Processes*. M.S. Thesis, North Carolina State University, (2004). http://www.lib.ncsu.edu/theses/available/etd-06182004-104005/
3. Shibata, T., *Cross-section transmission electron microscope observations of diamond-turned single-crystal Si surfaces*. Appl. Phys. Lett. 65 (20), 2553, 14 November (1994).
4. Kunz, R., *High Resolution studies of crystalline damage induced by lapping and single-point diamond machining of Si(100)*. J. Mater. Res., Vol. 11, No. 5, 1228, May (1996).

10 FRESNEL LENSES FOR SCANNING SYSTEMS

Alex Sohn
Kenneth Garrard
Precision Engineering Center Staff
Thomas Dow
Professor
Department of Mechanical and Aerospace Engineering

Using Fresnel lenses in scanning systems can have several benefits for the manufacturing process and certain performance advantages. Among the advantages are that the thinner Fresnel lenses are more economical to injection mold while reducing dispersion in the material. Designing and fabricating Fresnel lenses for these systems does, however, present some unique challenges. First, the issue of designing these systems is addressed by evaluating possible geometries and simple designs. Second, some design concepts are evaluated. Manufacturability is the next challenge due to the unique requirements for these scanning systems and finally, the fabricated surfaces must be evaluated. Concepts and strategies for addressing all these issues are explored.

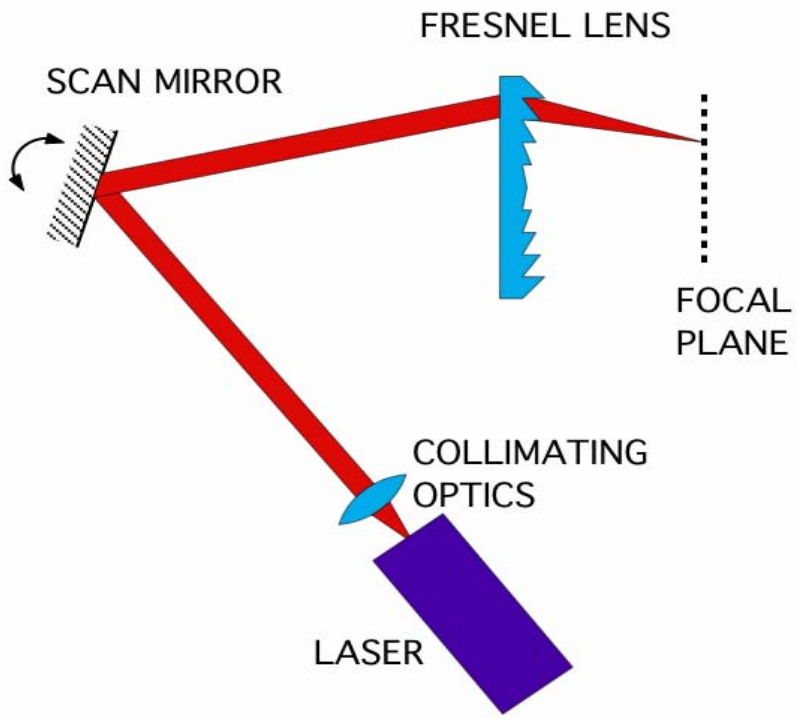

10.1 INTRODUCTION

10.1.1 DESCRIPTION

Fresnel lenses are a type of lens that eliminates the bulk of a conventional lens by collapsing the lens thickness while retaining surface slopes necessary for focusing. Figure 1 [1] shows the Fresnel lens equivalent of a conventional lens. For a rotationally symmetric lens, the discontinuites or grooves formed when collapsing the lens are annular. This produces a much thinner lens, particularly for large apertures.

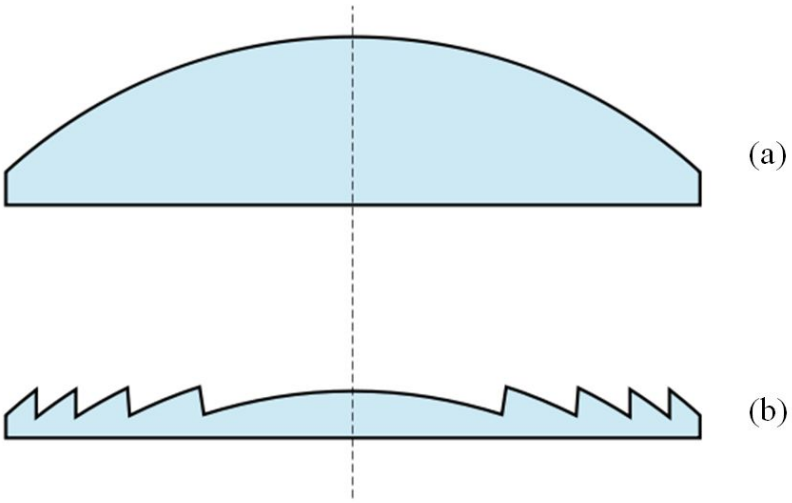

Figure 1. A Fresnel lens (b) is basically a collapsed version of a conventional lens (a).

The advantages of a Fresnel lens are that more light is transmitted due to less absorption and dispersion in the material and with more uniform thickness, a Fresnel lens is typically easier to replicate by molding. The latter of these two reasons is why Fresnel lenses are being considered for improving scanning systems in this project. Cost is a driving factor in scanning systems for laser printers, so a switch to a easily moldable Fresnel lens could provide a significant advantage.

Fresnel lenses are intended as purely refractive lenses. A common misnomer is to refer to a diffractive lens as a Fresnel lens. Properly, this is called a Fresnel zone plate [2]. Separate and distinct from a Fresnel lens, a zone plate focuses light using diffraction from a series of annular rings. A Kinoform lens combines refractive and diffractive properties of Fresnel lenses and zone plates to produce a more efficient diffractive lens that can also cancel chromatic aberration.

Fresnel lenses have found their way into a number of applications including infrared motion detectors, overhead projectors, solar collectors, theatrical lighting and many more. Typically, Fresnel lenses are used for non-imaging applications where the effects of scatter and multiple

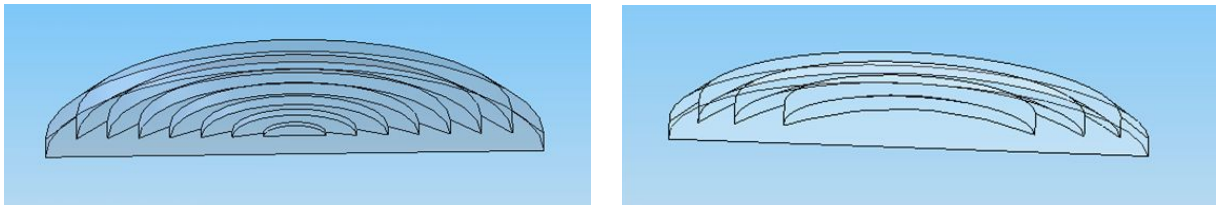

(a) (b)

Figure 2. Conical groove Fresnel lenses (a) and aspheric profile (b) Fresnel lenses

internal reflections are not critical problems. While it also qualifies as non-imaging, the application of focusing a rapidly scanning beam to a small spot size is, however, challenging.

10.1.2 TYPES OF FRESNEL LENSES

There are a number of different types and configurations of Fresnel lenses each with its own set of advantages and disadvantages. A number of options in the design affect performance and cost of the final product, the most significant of which are outlined below.

Aspheric vs. conical grooves

Shown in Figure 2a, conical grooves are the case for the simplest form of Fresnel lens. With diamond turning, conical grooves can be produced with a sharp tool that can be rotated, thus producing a range of groove angles. Fabrication is typically much faster for conical grooves. Aspheric grooves as in Figure 2b must be contoured with a small-radius tool, making fabrication more time consuming, particularly when a good surface finish is desired. Aspheric grooves do, however produce a more optically "correct" profile and do not require a rotary positioner for the diamond tool.

Constant depth vs. constant spacing

Constant depth grooves minimize the number of grooves and, hence, losses caused by grooves. Interference in the output caused by coherent groove spacing is also eliminated, though as groove spacing becomes large at the center of a constant depth lens modulation of a scanned beam as it crosses a single groove may have undesirable effects.

Grooves in vs. grooves out

Groove orientation with respect to the image/object direction has a significant impact on lens performance. If the grooves of the lens are facing the shorter conjugate as shown in Figure 3a, the lens is said to be "grooves in" while grooves facing away from the shorter conjugate as

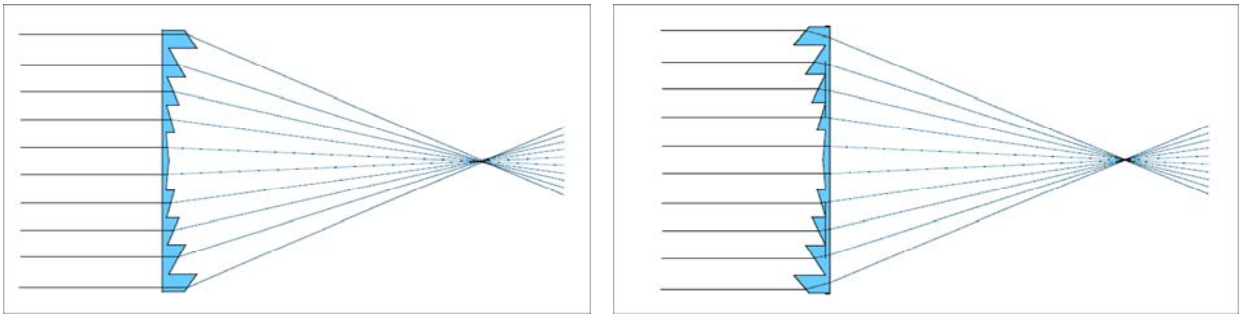

(a) (b)

Figure 3. Grooves in (a) orientation has the grooves facing the shorter conjugate while grooves out has the grooves facing away from the shorter conjugate

shown in Figure 3b are referred to as "grooves out". Certain advantages and disadvantages exist for each configuration, mostly having to do with groove shadowing discussed below and Fresnel reflection losses. The Fresnel reflection laws apply to any interface where a change in refractive index occurs. Basically, the larger the angle of incidence, the larger the amount of light that is reflected and the smaller the amount of light that is refracted. This means that the steeper angle of incidence for the "grooves in" case at the grooves causes more reflection losses than the two smaller angles of incidence at each interface of the "grooves out" lens. This must, however, be balanced against groove shadowing effects to select the proper configuration.

10.1.3 OTHER DESIGN CONSIDERATIONS

Various aspects of groove geometry each have their role to play in the performance of a Fresnel lens. The following characteristics and their effects are illustrated in Figure 4.

Groove density

Increased number of grooves will reduce the structure produced in the image by the groove transitions while increasing diffraction and edge losses. The number of grooves should thus be made appropriate to the application. Reducing the number of grooves decreases scattering losses, but may introduce structure.

Groove shadowing

Groove shadowing is unavoidable when the grooves face away from the shorter conjugate (grooves out), but can be eliminated when the grooves face away from the source (grooves in). The grooves in configuration does, however lead to higher Fresnel reflection losses, thus approaching parity between the two configurations.

Tip radius

Tip radius should be made as small as possible, though molding may cause these features to not be filled completely. "Sharp" tips are possible in both conical and aspheric groove lenses.

Trough radius

The trough radius is limited by the tool radius in aspheric profile lenses, while conical groove lenses can be produced with no trough radius. Making the tool radius smaller will make the trough radius smaller, but increases machining time for the aspheric profile

Relief angle

A relief angle is necessary for molded Fresnel lenses. Typically, this angle is between 3 and 5 degrees. Optical losses due to this angle are normally small, since it lies in the area that is usually shadowed anyway.

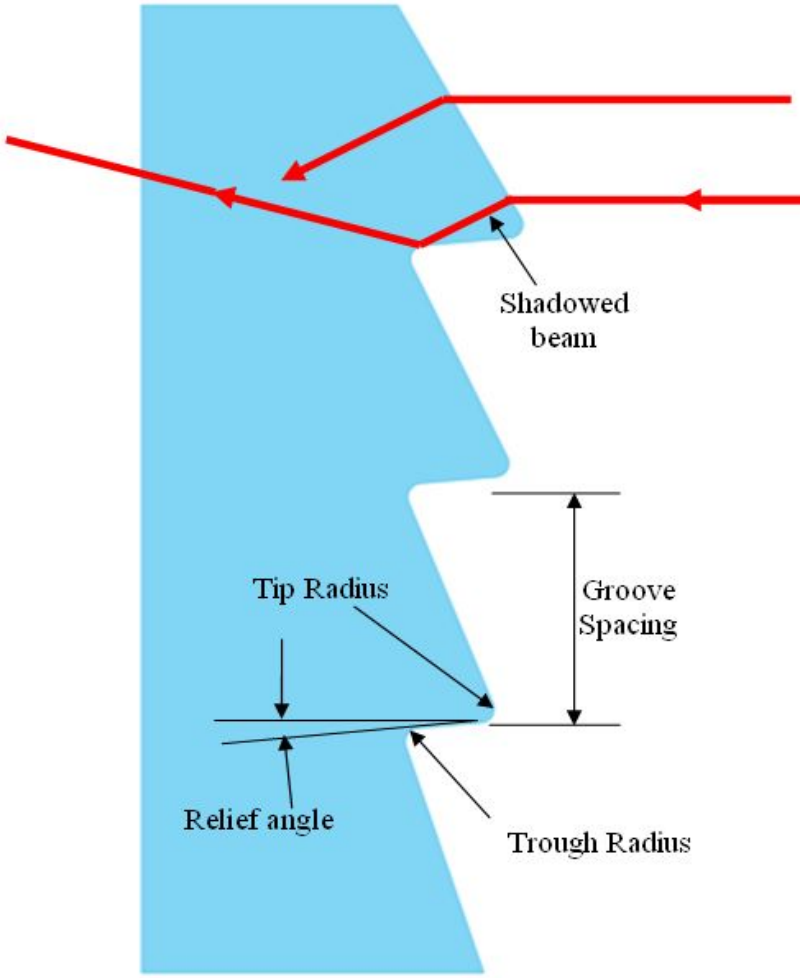

Figure 4. The critical factors of Fresnel lens groove structures

10.2 FABRICATION

The fabrication of Fresnel lenses requires some unique considerations. Basic parameters such as material selection and fabrication techniques are outlined below.

10.2.1 MATERIALS

Acrylic (PMMA)

Low birefringence, high clarity, index of refraction: n=1.49, moderate cost, easy to mold, medium melt temperature, low stress, high molding fidelity.

Polycarbonate (CR-39)

Low birefringence, extremely high clarity, n=1.58, high cost, difficult to mold (thermoset), high melt temperature, high stress, extremely tough.

Polystyrene

High birefringence, medium clarity, n=1.55, low melt, molds moderately well, high stress, poor mechanical properties., very low cost.

Glass

Very difficult to mold. Requires tungsten carbide molds, n=1.55, low cost.

10.2.2 MOLDING

Injection

Hot fluid polymer is shot into a closed cavity. Short cycle times, high tooling prices, high stress. 5-10 second cycle times, more for thick parts.

Compression

Sheet or powder material is melted in hot mold under pressure with open cavity. Can be made economical by making large molds. Molds with 100's of cavities are possible. Cycle times 10-20 mins.

10.2.3 FRESNEL LENSES FOR SCANNING SYSTEMS

Laser scanning systems

A simplified schematic of a laser scanning system using a Fresnel lens is shown in Figure 5. The laser, collimating optics and scan mirror are as in a conventional system. The scan lenses, however would be replaced by one or two Fresnel lenses. Since the beam must be scanned over a large distance (usually around 200 mm), the scanning lens is usually long in the scan direction. The orthogonal or "process" direction (out of the plane of the page in Figure 5) usually has different focusing requirements so that the lens is typically anamorphic or non-rotationally symmetric.

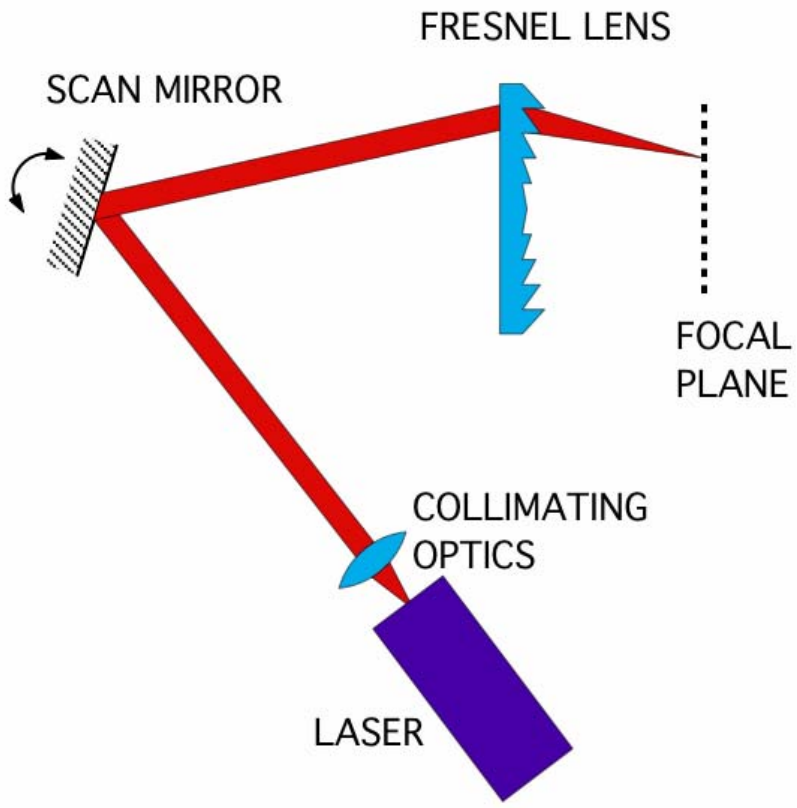

Figure 5. A simplified laser scanning system using one Fresnel lens for the scanning optics

Possible Scanning lens configurations

Fresnel zones in the process direction This would have the advantage of being able to place a very fast lens close to the print surface, therefore reducing sensitivity, though also reducing depth of field. These types of lenses would be difficult to fabricate, most likely by flycutting or turning

a curved substrate at a large radius of up to 300 mm. The beam would likely be quite uniform, however, since grooves would not vary much as a function of scan angle. Lenses could have either a planar configuration or be curved as shown in Figures 6 and 7. A curved lens could have certain optical benefits while being just as easy to mold as a flat one since it still maintains a relatively uniform thickness. Since this type of lens will have no power in the scan direction, it will have to be used in conjunction with a relatively thick lens.

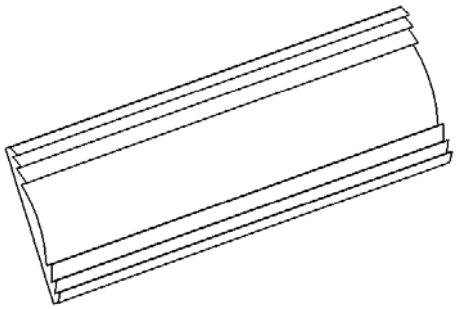

Figure 6. Grooves in the process direction in a planar configuration

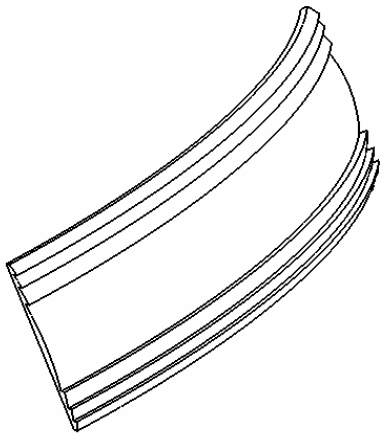

Figure 7. Grooves in the process direction in a curved configuration

Fresnel zones in the scan direction This would reduce the overall thickness of the lens since the scan direction makes up the thickest segment of the lens as shown in Figure 8. It could be fabricated via cylindrical turning and grooves could be made aspheric by use of a fast tool servo. Reduction in overall thickness is important to improving molding times.

Fresnel zones in both directions The greatest freedom and maximum thickness reduction is afforded by this configuration as shown in Figure 9, though machining would be most difficult. Machining could only be performed via either 5-axis diamond milling or slow-slide servo turning.

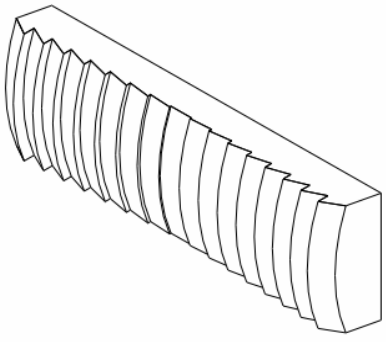

Figure 8. Grooves in the scan direction reduce the most thickness.

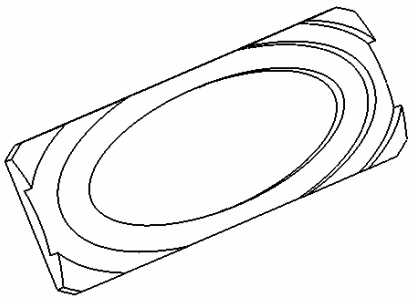

Figure 9. Grooves in both directions will result in an even thinner lens

10.2.4 FABRICATION

A number of techniques are possible for fabrication of Fresnel scan lenses. This depends greatly on the final configuration of the lens as described previously. Purely cylindrical Fresnel lenses could be machined either by turning or flycutting. Flycutting is particularly slow, though it reduces potential chatter.

Fabrication of lenses with grooves in the scan direction could be diamond turned in a cylindrical turning configuration as shown in Figure 10. Since the grooves are generally in the direction of the rotation of the cylinder, the grooves would be formed by the slow (X and Z) axes of the machine. Curvature in the process direction would produce most of the power for that direction with a fast tool servo providing any aspheric shape or change in power in the scan direction.

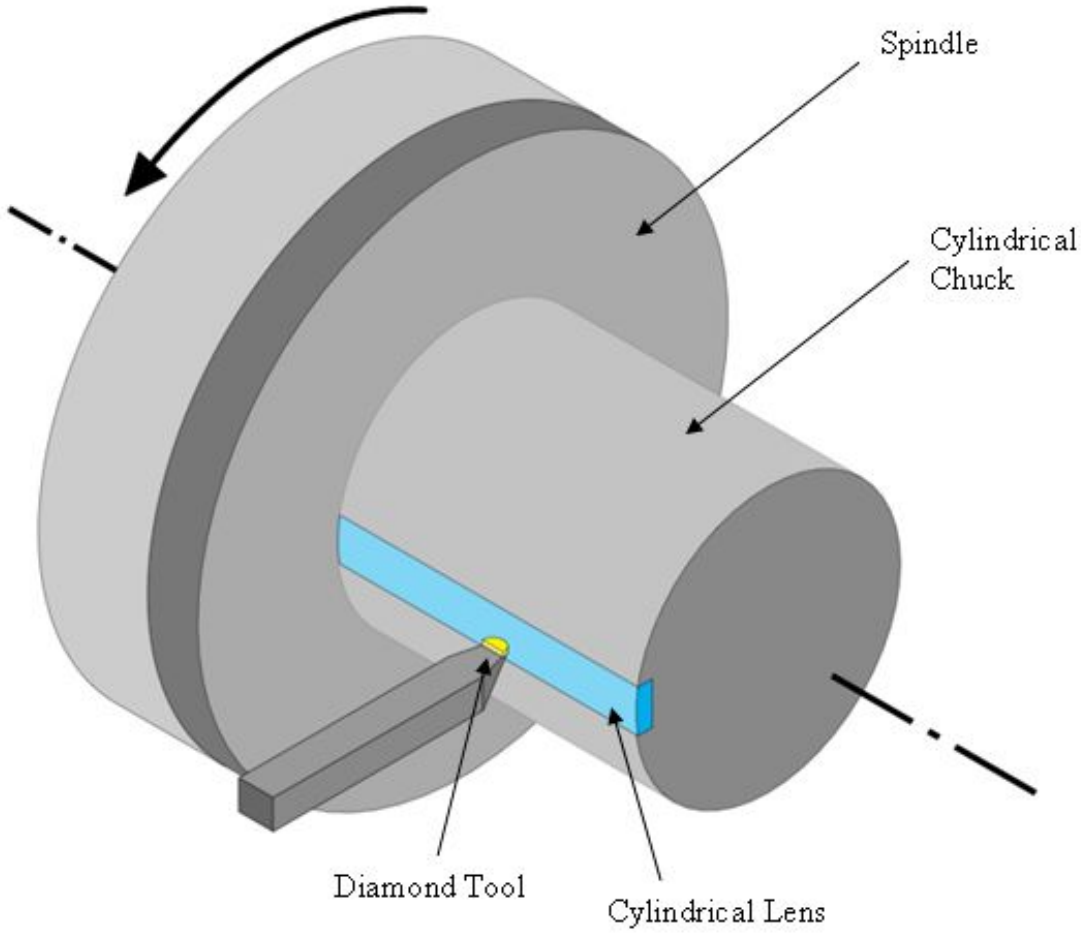

Figure 10. Diamond turning process for a cylindrical lens or a Fresnel scan lens with grooves in the scan direction.

10.3 ANALYSIS OF SCANNER LENS FOR DIAMOND TURNING

A quasi-toric laser printer scan lens was assessed for feasibility of direct machining on a diamond turning lathe with a fast tool servo. Figure 11 shows the basic shape of a prototype scan lens. The front and back are mirror images. Curvature is not constant in any direction along the surface of the lens.

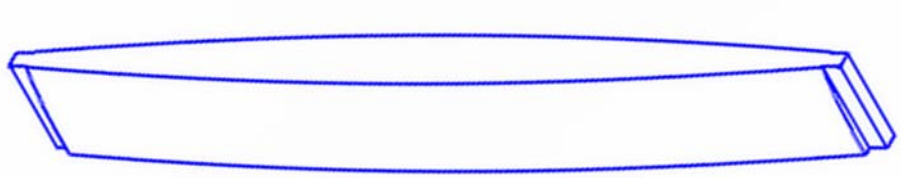

Figure 11. Quasi-toric scan lens.
The lens is about 142 mm long, 16 mm high and 12 mm thick.

Figure 12 shows the surface of the lens plotted using radial contours, equal sag contours and a non-uniform xy-grid. The left plot shows sag variation along the radial contours, especially at the ends of the lens, the center plot shows equal regions following apparently ellipsoidal contours and the right plot is similar to the radial plot with contours parallel to the y axis. The similarity is because the ratio of nominal lens curvatures is about the same as the aspect ratio of the lens (10:1).

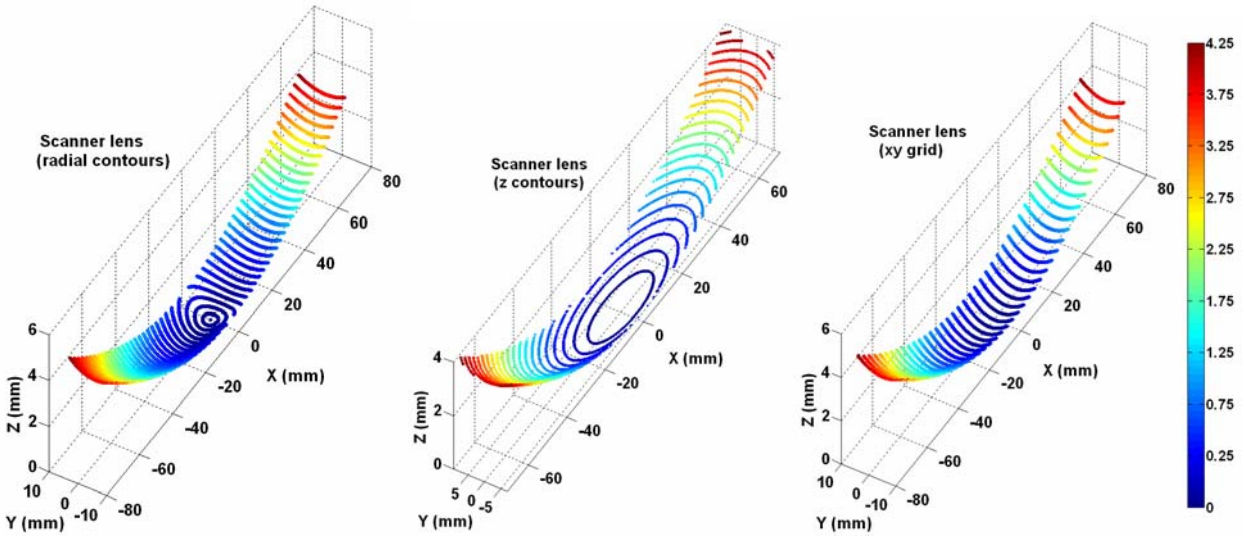

(a) radial contours (b) equal sag contours (c) xy-grid

Figure 12. Non-rotationally symmetric scanner lens surface.

If the lens was turned on-axis, that is with the spindle centerline coincident with the z axis in the plots in Figure 12, then a fast tool servo (or slow slide servo) would have to machine the residual after removing some rotationally symmetric shape. Minimizing the non-rotationally symmetric (NRS) residual is desirable for producing good surface finish and reducing process time.

Figure 13 shows the effect on NRS sag of removing three different rotationally symmetric profiles from the lens surface. The short vertical lines represent the z sag along each radial contour in Figure 12a and the three labeled lines show three different rotationally symmetric surfaces fit to the data. The optimal fit with respect to minimizing NRS sag is shown by the dotted red line which is obtained by building an asphere through the midpoint of the z sag at each radius. The maximum NRS residual (617 μm) occurs at a radius of 9.9 mm. The green and blue lines are circles obtained by a least squares fit considering all of the data (green or lower curve) and only the extreme values at each radius (blue or upper curve). The latter fit gives a slightly smaller NRS residual. In both cases the sphere was constrained to be aligned with the spindle centerline (i.e., z axis). Relaxing this constraint to allow ogive spheres does not reduce the NRS residuals.

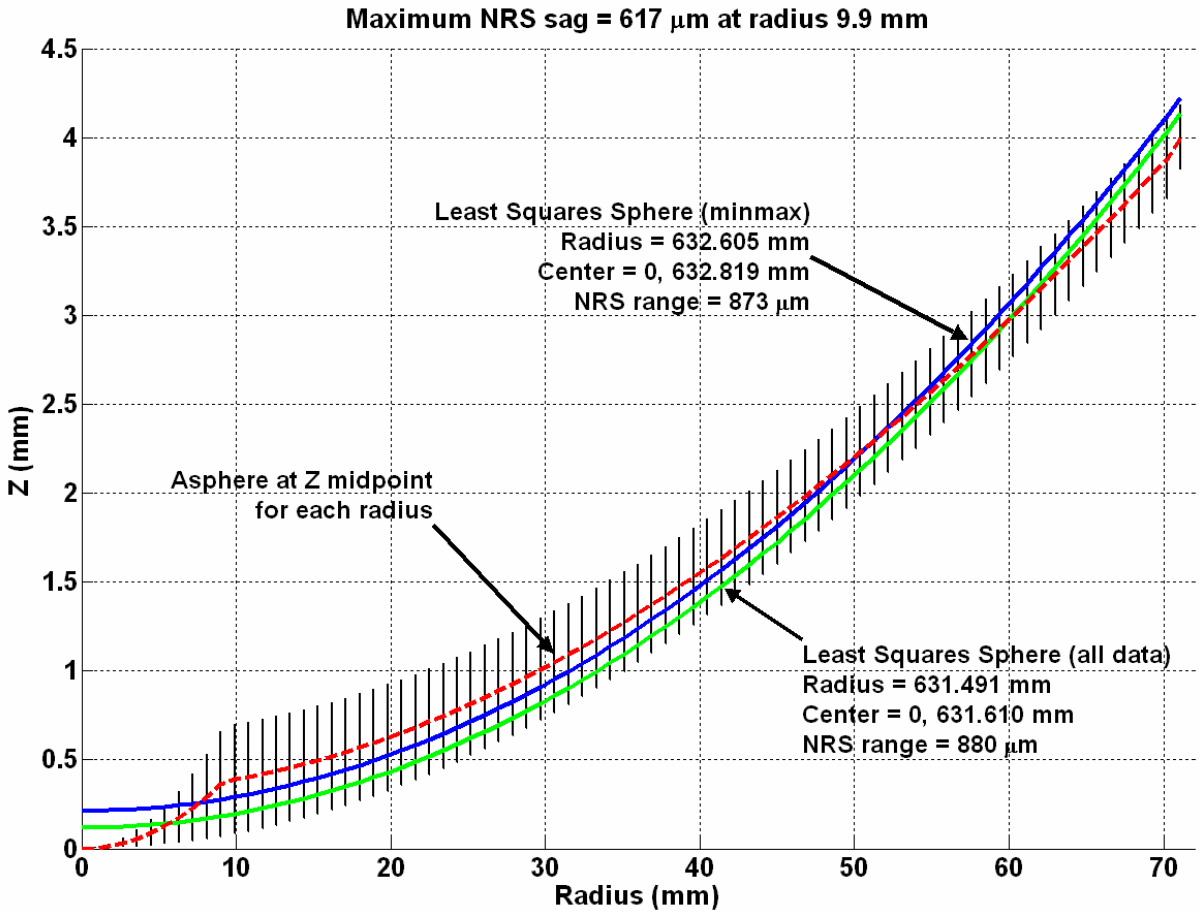

Figure 13. NRS sag, a best fit asphere and two least squares spheres.

The left plot in Figure 14 shows the NRS residual after removing the best fit radial asphere shown in Figure 13 as the dotted line. Note that the radial contour lines are all high (red) at +y and low (blue) at -y. By tilting the surface about 1° before subtracting the asphere the NRS sag can be reduced by about 25%. This tilt would have to be accounted for in either the machining or mounting fixture for the lens.

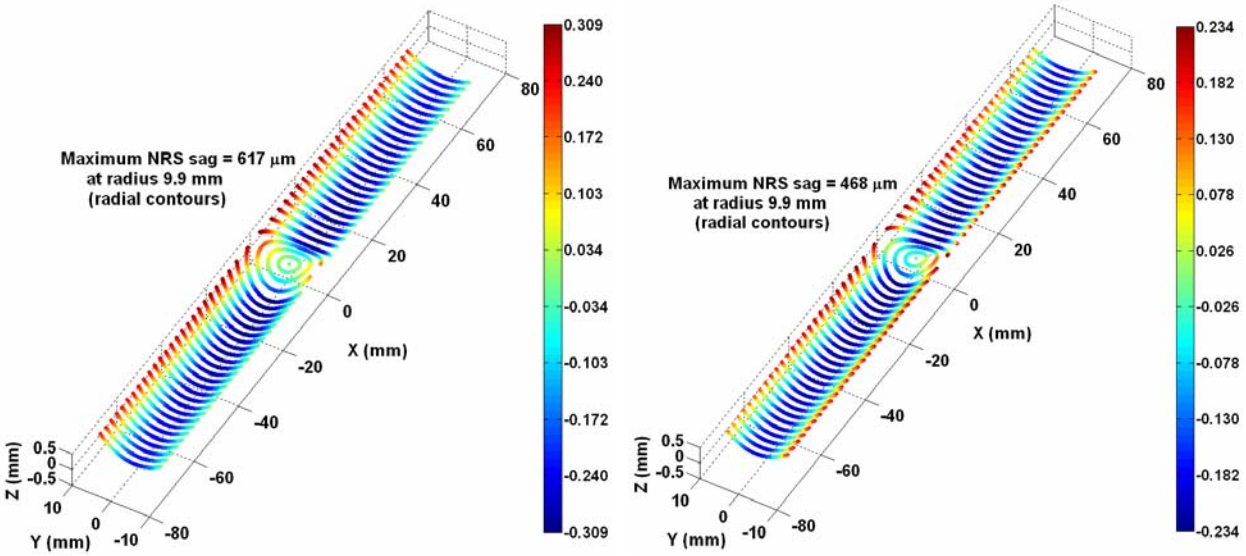

Figure 14. Radial NRS sag contours after removal of best fit radial asphere (left) and after rotating 0.996° about the x axis before removing asphere (right).

Close examination of the data from the xy-grid plot in Figure 12c shows that the variation along the y direction contours is nearly circular. That is, the lens can be closely approximated by a cylinder. Performing a least squares fit of a cylinder to the lens data reduces the residual NRS sag to 119 µm. The aspheric cylinder shape shown in Figure 15 has a nominal radius of 68.21 mm but is deformed along its length with a similar shape to the best fit asphere in Figure 12. The two black lines parallel to the "length" axis represent the position of the lens relative to the spindle centerline (along the zero radius line). An appropriate fixture and alignment mechanism would have to be constructed for cylindrical turning of the lens on both sides. Throughput would also be impacted since the cutting duty cycle is less than 4%. Figure 16 shows the NRS shape that would have to be machined by a tool servo synchronously with the cylinder in Figure 15. The maximum excursion occurs at either end of the lens.

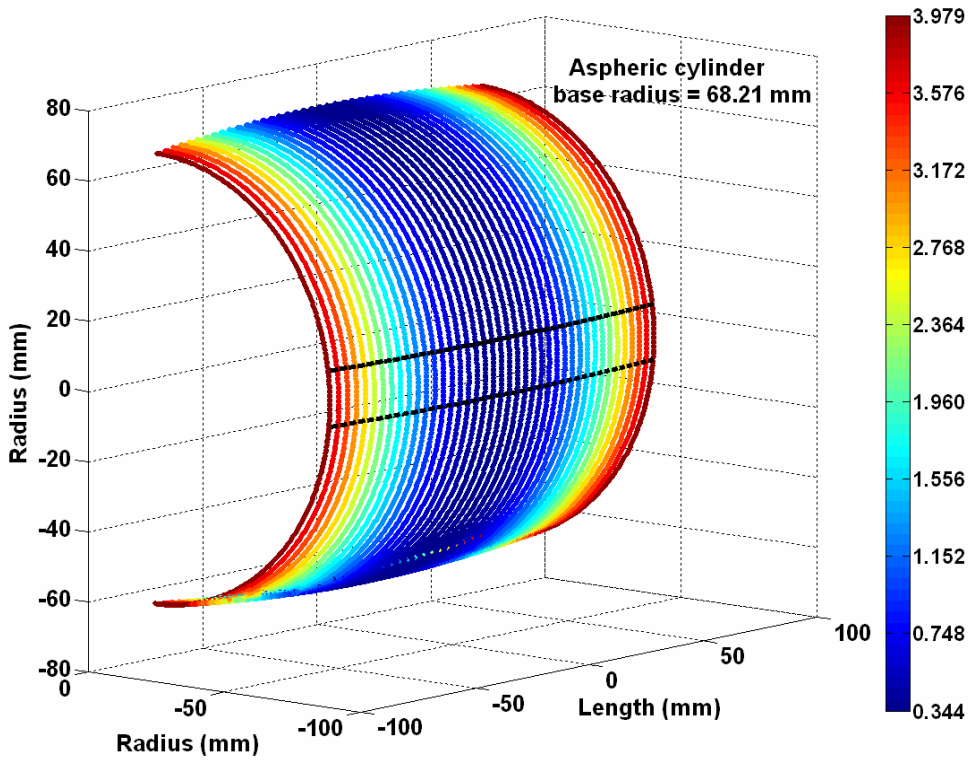

Figure 15. Aspheric cylinder fit to scan lens data.

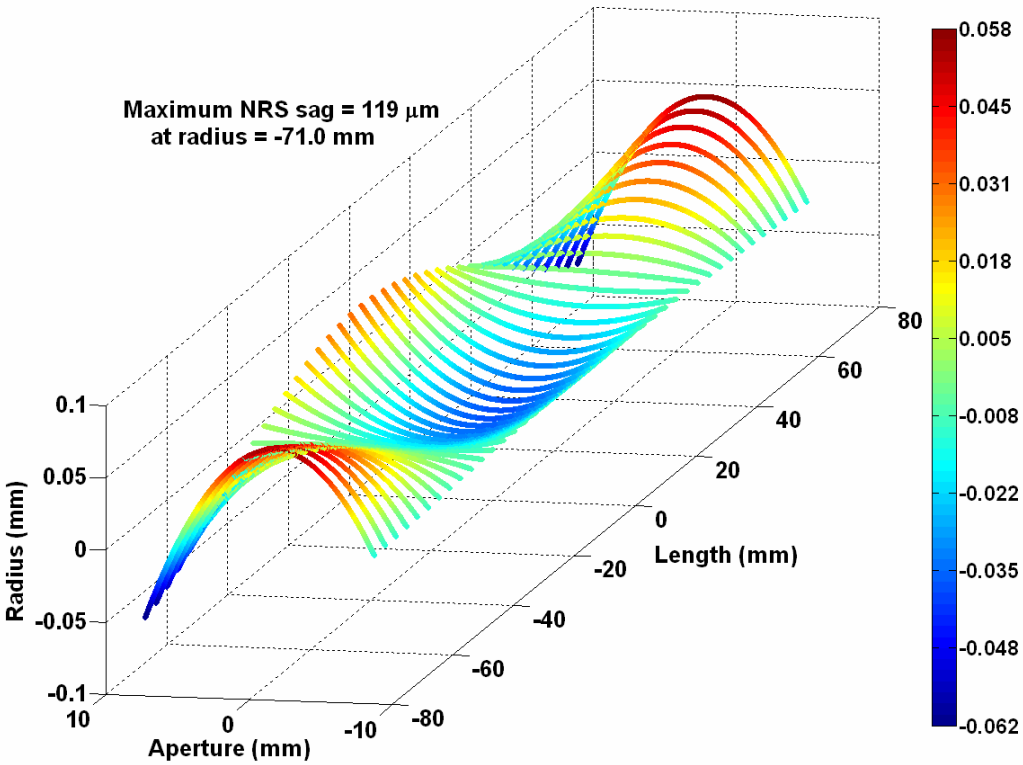

Figure 16. NRS residual for scan lens in cylindrical orientation.

10.4 IMAGING DESIGN

Fresnel lenses have normally been relegated to non-imaging applications, usually due to undesirable effects on image quality. For this reason, optical design software that has been focused on imaging applications generally only addresses Fresnel lenses in a very simplified manner. Optical design software such as Zemax, Code V and Oslo all treat Fresnel lens surfaces as ideal thin lenses. They have no thickness yet a surface function provides local curvature to give the lens power. Groove structures are not considered in this handling of the lenses. While this approach is adequate for many applications, it appears to lack attention to the item of most concern in the design of Fresnel lenses for scanning systems: The influence of the groove structures. It is for this reason that a more direct design and modeling approach will be taken and tailor-made optical design software used.

10.5 CONICAL FRESNEL LENS DESIGN SOFTWARE

Consider the single zone of a conical Fresnel lens shown in Figure 17 where a single ray is shown (in red) propagating from an object to an image plane. For a scanning system the object is a rotating polygon mirror and the rays are a laser beam. In Figure 17, if the distance between surfaces (J, M and S), the lens thickness (T), the indices of refraction (N1, N2 and N3), the pointing angle β and the surface normal angle, α, are known, then Snell's law and the definition of the tangent function can be used to find ray heights, intersection angles and angles of refraction at each ray – surface intersection. The process of tracing rays through a simple conical system is deterministic and easily automated. However to design the Fresnel lens, a surface normal for each zone must be found that satisfies some constraint on the relationship between object pointing angle, β, and image intersection height for each ray. For a scanning system one possible design constraint is the F-theta condition, that is, a linear relationship between β and y_4.

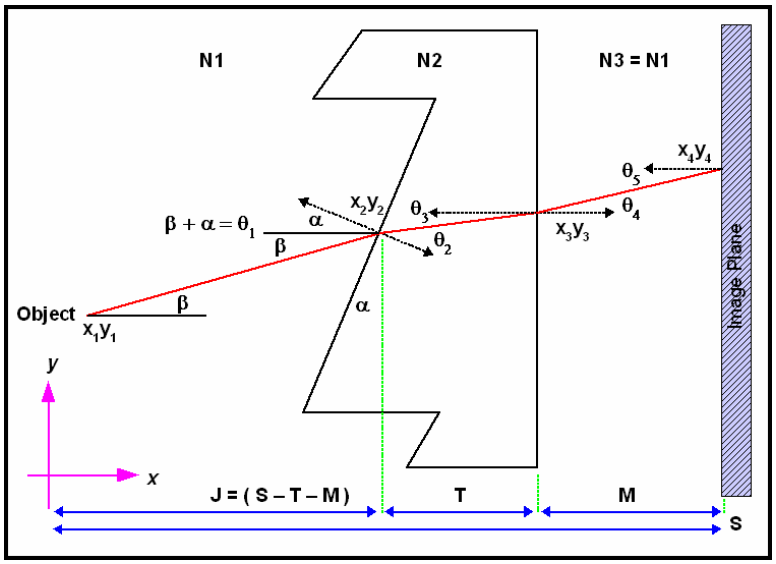

Figure 17. Ray propagation through a Fresnel lens zone.

The simple one lens system show in Figure 17 is described by Equations (1) through (8). The *x's* are fixed by the system layout as $x_1 = x_1$, $x_2 = J$, $x_3 = x_2+T$ and $x_4=x_3+M$. The object is at (x_1,y_1) which is not necessarily the origin. Note that Equations (2) and (4) are Snell's Law.

$$\theta_1 = \beta + \alpha \tag{1}$$

$$\theta_2 = \sin^{-1}\left(\frac{N1}{N2}\sin\theta_1\right) \tag{2}$$

$$\theta_3 = \theta_2 - \alpha \tag{3}$$

$$\theta_5 = \theta_4 = \sin^{-1}\left(\frac{N2}{N3}\sin\theta_3\right) \tag{4}$$

$$y_1 = y_1 \tag{5}$$

$$y_2 = y_1 + (x_2 - x_1)\tan\beta \tag{6}$$

$$y_3 = y_2 + (x_3 - x_2)\tan\theta_3 \tag{7}$$

$$y_4 = y_3 + (x_4 - x_3)\tan\theta_4 \tag{8}$$

When the pointing angle, β, and the Fresnel normal, α, are known, Equations (1) through (8) can be used to find the intersection angles and ray heights. However if the Fresnel normal angle is unknown then Equation (8) must be expanded by substitution of Equations (1) through (7), set equal to a desired image height, h, and solved for α. This is expressed as Equation (9),

$$h = y_1 + (x_2 - x_1)\tan(\beta) - (x_3 - x_2)\tan(w) - (x_4 - x_3)\frac{N2}{N3}\frac{\sin(w)}{\sqrt{1-\frac{N2^2}{N3^2}\sin^2(w)}} \tag{9}$$

where ω is given by Equation (10).

$$\omega = -\sin^{-1}\left(\frac{N1}{N2}\sin(\beta+\alpha)\right) + \alpha \tag{10}$$

A value for α can be found by finding a real root of Equation (9) between $-\pi$ and $+\pi$. Only complex roots will exist for degenerate cases such as total internal reflection inside the Fresnel lens (i.e., θ_3 exceeds the critical angle for the lens material).

An iterative approach to designing a Fresnel scanning system is proposed. For a single lens system as shown in Figure 17, a Maple™ worksheet was developed to repetitively solve Equation (9) followed by Equations (1) through (8) to iteratively build up a Fresnel lens surface. The iteration starts with two parallel rays equally spaced on opposite sides of the optical axis. The initial beam pointing angle, β, is zero. Equation (9) is used to find the Fresnel normal angle

required to focus these two rays to a point at height zero on the image plane. Then Equations (1) through (8) are used to find the remaining ray heights and intersection angles. Next the beam is rotated so that the lower ray at the new beam position intersects the Fresnel lens at the point where the upper ray intersected on the previous iteration. This new lower ray is traced through the system to the image plane. Finally, Equation (9) is solved to find the surface normal that focuses the new upper ray to the same point on the image plane. The process is repeated until either the desired ray height on the image plane is reached or the pointing angle limit is exceeded. At each iteration, the beam straddles two adjacent Fresnel zones.

In Figure 18, the current beam position is represented by three rays BE (lower), AD (center) and CF (upper). The pointing angle is β_1 and for the next iteration the new pointing angle is $\beta_2 = 2\tau$ which is easily calculated from the values of w and p as show in Equation (11).

$$\beta_2 = \beta_1 + 2\tan^{-1}\left(\frac{w}{\sqrt{p^2 - w^2}}\right) \tag{11}$$

A single lens scan system was designed using this iterative procedure. The overall system length was set to 247 mm, the lens thickness at 1 mm, the lens to image distance was 200 mm and the object to lens distance was 46 mm. For an acrylic lens material N2 = 1.49 and the critical angle is 42.16°. The program stepped a 1 mm wide beam from 0° to 35° in 31 iterations reaching a ray height on the image plane of 122 mm. The Fresnel surface normal angles ranged from 0° along the optical axis to 15° for the upper ray at zone 31. At each iteration an upper, lower and center ray was traced for the beam. Figure 19 shows that the Fresnel angle increase is nearly linear with beam pointing angle.

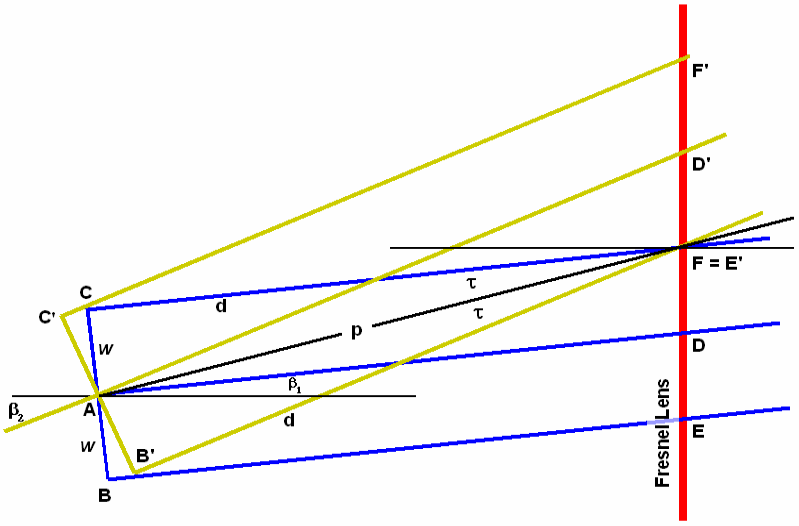

Figure 18. Iterative beam position.

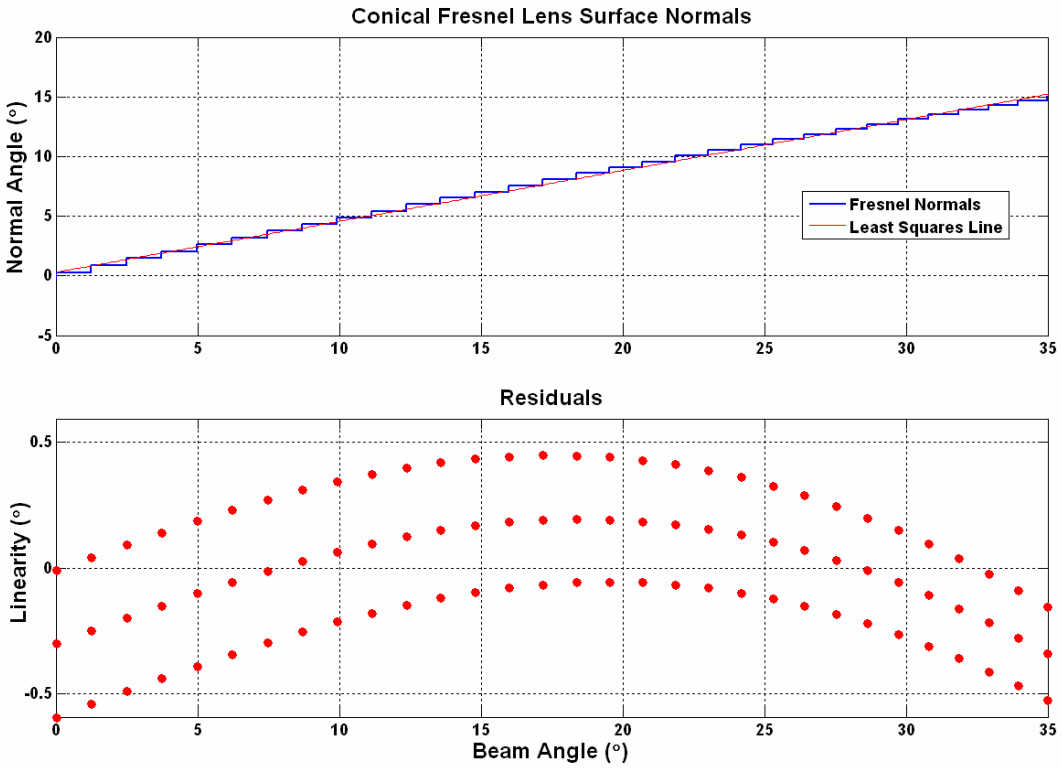

Figure 19. Fresnel lens normal angles.

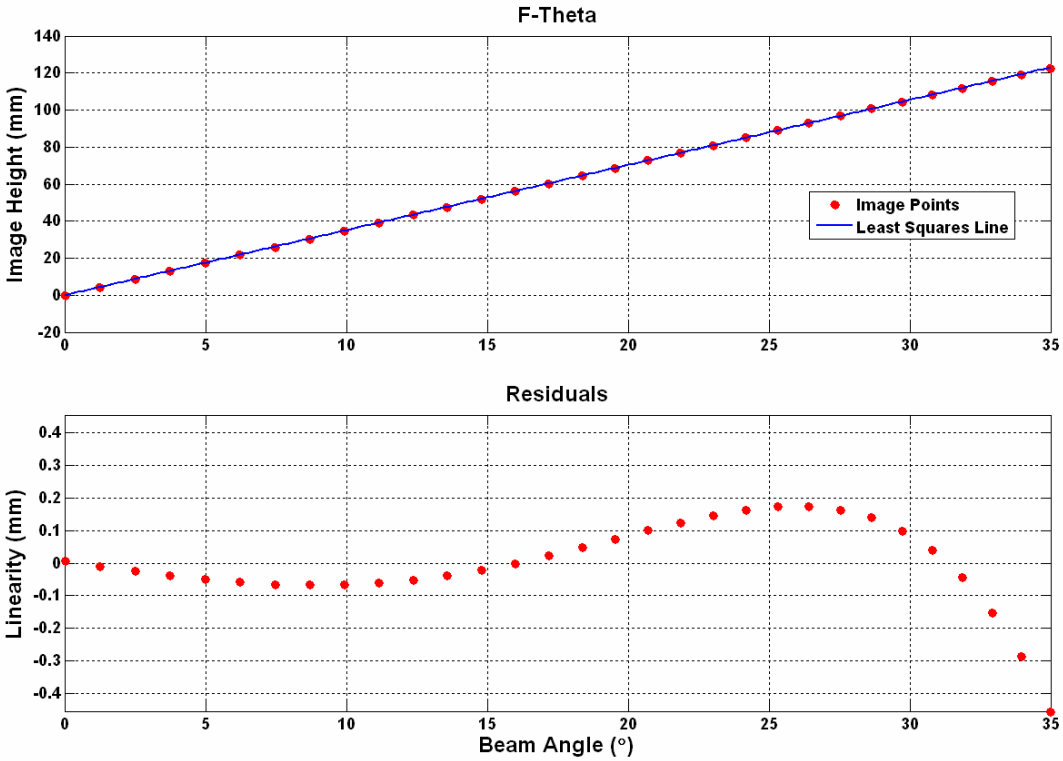

Figure 20. F-theta requirement of Fresnel scan lens.

In Figure 20 the F-theta condition is demonstrated by plotting image height versus beam pointing angle. Linearity is better than 0.5%. This simple conical zone Fresnel lens demonstrates the feasibility of designing an F-theta scanner system. Current work will extend the iterative ray tracing algorithm to include more surfaces, aspheric zone shapes, and the 3D geometry of the beam and lens system.

10.6 DESIGN EVALUATION

Fresnel scan lens designs are evaluated in two different ways: Non-sequential ray tracing and optical testing. The optical testing will be used to verify simple designs that will be modeled in Lambda Research's TracePro non-sequential ray-tracing software. This program can evaluate scatter, refraction and secondary internal reflections, all of which are of concern in this endeavor. As with all modeling, however, model parameters and assumptions greatly influence the result of the modeling. It is thus good practice to test the model with a simplified test.

The test will to examine the influence of Fresnel lens grooves on the spot size of a focused laser beam. As shown in Figure 21, a collimated laser beam is focused by a lens and then passes through a Fresnel prism. The Fresnel prism has no power, hence only the impact of the Fresnel grooves is seen in much the way it would on a laser scanner lens. This eliminates the impact of the focusing ability of the Fresnel lens and isolates the groove structure. A digital array at the focal plane will collect image data.

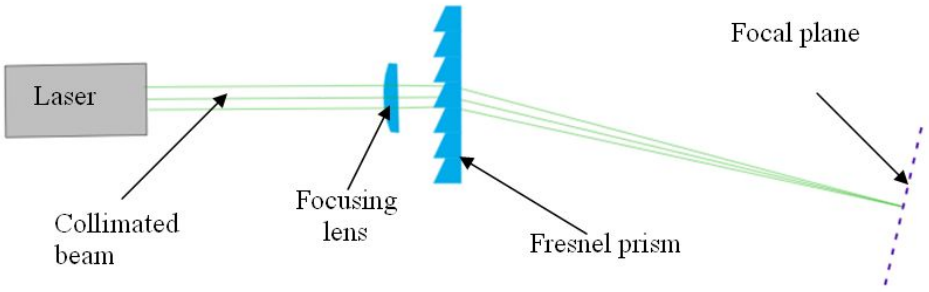

Figure 21. Test setup for measuring impact of Fresnel lens grooves

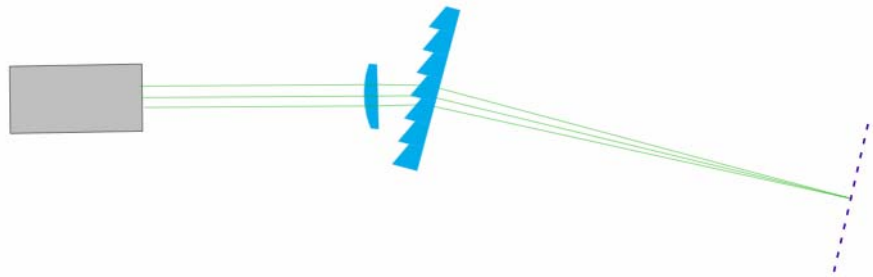

Figure 22. Test setup with Fresnel prism rotated to change groove exposure

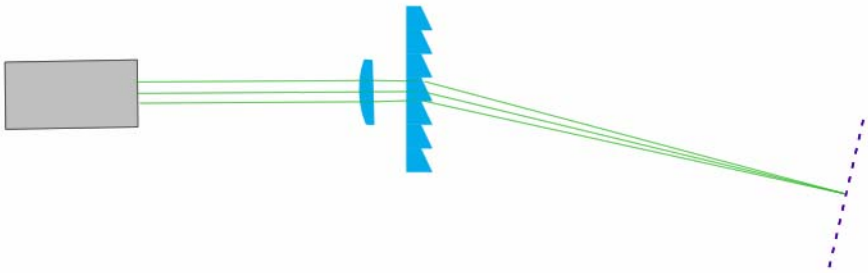

Figure 23. Test setup with Fresnel prism oriented to have grooves facing the image plane

Different orientations of the Fresnel prism will also demonstrate the effect of clearance angle (Figure 22) and groove direction (Figure 23). With a CMOS camera array at the focal plane, the spot size can be captured and compared for the different orientations and different prisms. A control experiment without a prism will be performed to compare the results.

The experimental setup is shown in Figure 24, with the 200 mm focal length lens focusing the 5 mm diameter beam to the location of the camera mount through the Fresnel prism.

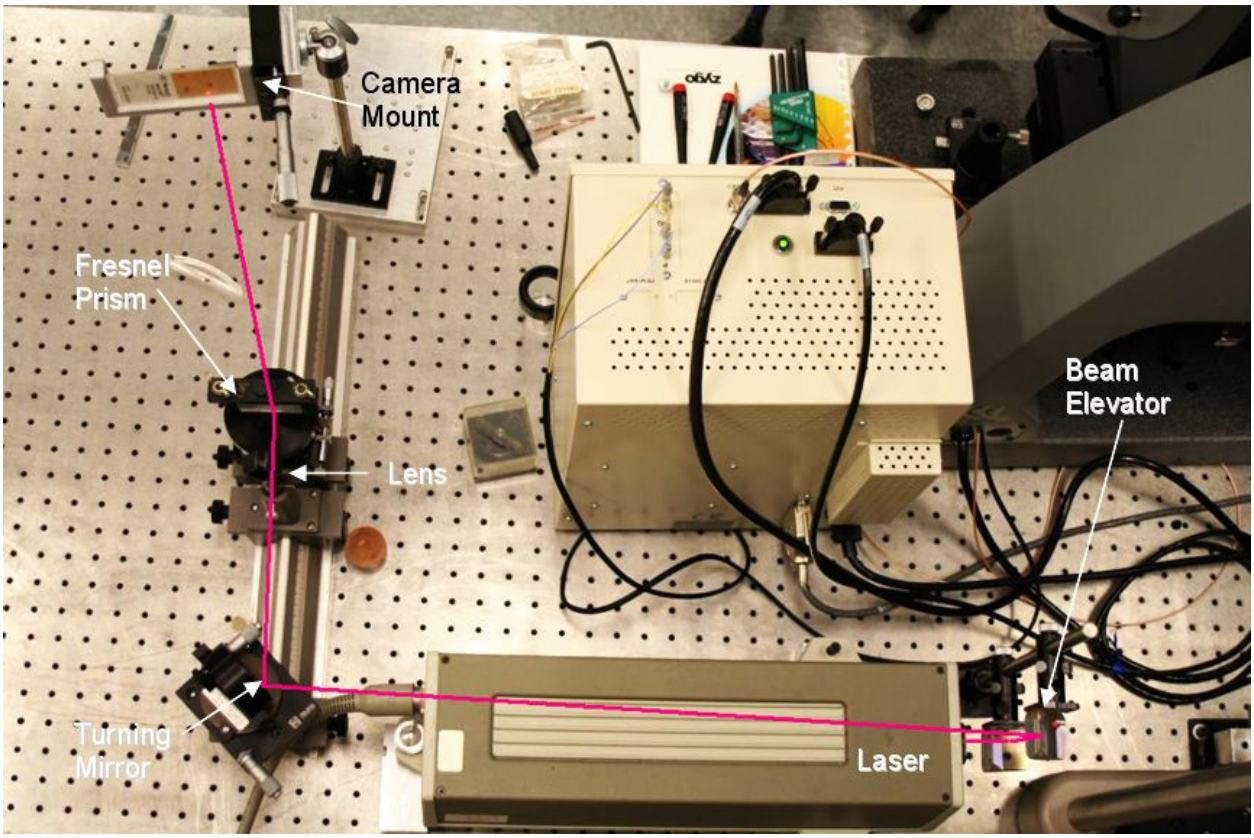

Figure 24. Experimental setup showing beam path through the focusing lens and Fresnel prism for the laser and some beam steering optics.

10.7 CONCLUSION

The goal of this project is to design a Fresnel lens-based scanning system to reduce the cost of the overall scanning system. Little is known about the performance of Fresnel lenses in laser scanning systems of this kind. The groundwork has been laid to solve the challenging problems that lie ahead: Developing design principles for fresnel lenses that will perform as well as existing lenses, finding ways to fabricate these designs and testing the performance of the fabricated lenses.

10.8 REFERENCES

1. http://en.wikipedia.org/wiki/Fresnel_lens
2. http://en.wikipedia.org/wiki/Fresnel_zone_plate

FACULTY

THOMAS A. DOW

Director, Precision Engineering Center
Dean F. Duncan Distinguished University Professor in Mechanical Engineering
Professor, Department of Mechanical and Aerospace Engineering

BS, Mechanical Engineering, Virginia Polytechnical Institute, 1966
MS, Engineering Design, Case Institute of Technology, 1968
PhD, Mechanical Engineering, Northwestern University, 1972

After receiving his PhD degree from Northwestern University in 1972, Dr. Dow joined the Tribology Section of Battelle Columbus Laboratories and worked there for ten years. His research interests were in the areas of friction and wear and included studies on a wide variety of topics from lubrication of cold-rolling mills using oil-in-water emulsions to wet braking effectiveness of bicycle brakes to elastohydrodynamic lubricant film generation in ball and roller bearings. He developed experimental apparatuses, established analytical models, and corroborated those analyses with experimental measurements. Dr. Dow joined the faculty at North Carolina State University in 1982 and was instrumental in developing the academic and research program in precision engineering. His current research interests include the design of precision machining systems, real-time control, and metrology. He was one of the founders of the American Society for Precision Engineering and currently acts as the Executive Director.

GREGORY D. BUCKNER

Associate Professor, Department of Mechanical and Aerospace Engineering

BS, Mechanical Engineering, Louisiana State University, 1986
MS, Mechanical Engineering, Virginia Polytechnic Institute, 1987
PhD, Mechanical Engineering, University of Texas at Austin, 1996

Dr. Buckner is an Associate Professor of Mechanical and Aerospace Engineering at North Carolina State University (NCSU) in Raleigh, NC. His research interests include electromechanical systems, intelligent system identification and control, and precision engineering. Dr. Buckner has researched active and semi-active vehicle suspension systems since 1997, and has demonstrated innovative and effective control strategies for implementations on military HMMWV's and other off-road vehicles. His additional research projects include the development of intelligent control algorithms for active magnetic bearings, medical instruments for robotic surgery, and electromechanical actuators for manufacturing processes. Dr. Buckner is a recipient of the Faculty Early Career Development (CAREER) Award from the National Science Foundation, the New Faculty Research Award from the American Society for Engineering Education, and the Outstanding Teacher Award from NCSU. Prior to his appointment at NCSU, Dr. Buckner was a research engineer at the University of Texas Center for Electromechanics in Austin, TX. He received a Ph.D. in mechanical engineering from the University of Texas at Austin in 1996.

JEFFREY W. EISCHEN

Associate Professor
Department of Mechanical and Aerospace Engineering

BS, Mechanical Engineering, UCLA, 1978
MS, Mechanical Engineering, Stanford University, 1981
PhD, Mechanical Engineering, Stanford University, 1986

Dr. Eischen has been with North Carolina State University since 1986 and his research areas of interest include: linear and nonlinear finite element analysis, multi-body kinematics/dynamics/control, fabric mechanics, and stress analysis in microelectronic devices. He teaches undergraduate courses in strength of mechanical components and mechanical design. His graduate courses include fracture mechanics and advanced machine design. He has collaborated with colleagues in the Precision Engineering Center for several years on computer simulation related projects dealing with precision shape control of disk drive read/write heads, stress and deformation analysis of high energy physics equipment, and contact lens mechanics.

PAUL I. RO

Professor
Mechanical and Aerospace Engineering Department

BS, Mechanical Engineering, University of Minnesota, 1982
MS, Mechanical Engineering, Massachusetts Institute of Technology, 1985
PhD, Mechanical Engineering, Massachusetts Institute of Technology, 1989

Dr. Ro joined the faculty of North Carolina State University in January 1989, as an Assistant Professor in the Mechanical and Aerospace Engineering Department. He became a Professor in July 2001. Dr. Ro has developed two graduate courses in the department (multivariable Control and Robotics) and has taught undergraduate Automatic Control and Dynamics courses. His research covers a wide range of controls and various applications of control theories in precision engineering, robotics, vehicle dynamics and control, and mechatronics.

RONALD O. SCATTERGOOD

Professor
Materials Science and Engineering Department

BS, Metallurgical Engineering, Lehigh University, 1961
MS, Metallurgy, Massachusetts Institute of Technology, 1963
PhD, Metallurgy, Massachusetts Institute of Technology, 1968

R.O. Scattergood is a Professor in the Department of Materials Science and Engineering. He received BS degrees in Mining Engineering and Metallurgical Engineering from Lehigh University. His MS and PhD degrees were obtained in Metallurgy from M.I.T. In 1968 he became a member of the basic research staff in the Materials Science Division at the Argonne National Laboratory. In 1981, he joined the faculty as a Professor of Materials Engineering at North Carolina State University.

Professor Scattergood's major research interests have been focused on the mechanical behavior of solids. He has worked in the areas of strengthening mechanisms in solids, mechanical testing, fracture, tribology, nanocrystaline materials and precision machining processes. He has expertise in He has published over 200 technical papers, books and reports.

STAFF

KENNETH P. GARRARD

Research Assistant
Precision Engineering Center

BS, Computer Science, North Carolina State University, 1979
MS, Computer Studies, North Carolina State University, 1983

As a full-time research assistant, Mr. Garrard is studying the design of systems software that supports the development of high-speed real-time applications for special purpose multiprocessor computer systems. He has several years experience in academia and industry designing and implementing real-time systems. As a Precision Engineering Center staff member, Mr. Garrard's current activities include the design and implementation of software for Diamond Turning Machine and Fast Tool Servo controller projects.

ALEXANDER SOHN

Research Assistant/Lecturer
Precision Engineering Center

B.S., Physics, University of Texas at Arlington, 1992
M.S., Physics, University of Texas at Arlington, 1994

Mr. Sohn joined the Precision Engineering Center in August, 1997 as a member of the technical staff. His current research interests range from machine design and metrology to the design and fabrication of nonimaging optics. Mr. Sohn's varied research activities began in microwave optics and atomic physics as a student at the University of Texas at Arlington and later progressed to precision machine design, design and fabrication of plastic optics as well as automation and machine vision at Fresnel Technologies, Inc. in Fort Worth, Texas.

DONNA IRWIN

Administrative Assistant
Precision Engineering Center

BS, Liberal Studies, Salisbury State University, 1983

Ms. Irwin became a member of the PEC Staff in July 2006. She most recently served as a Technical Information Specialist at Science Applications International Corporation in Falls Church, Virginia. Previously, Ms. Irwin worked as Administrative Manager for numerous law firms in Washington, DC. Ms. Irwin provides the overall administrative support for the Center.

CONSULTANTS

KARL FALTER

Consulting Engineer

BS, Mechanical Engineering, North Carolina State University, 1987
MS, Mechanical Engineering, North Carolina State University, 1989
PhD, Mechanical Engineering, North Carolina State University, 1992

Prior to working as an independent consultant, Dr. Falter was a senior development engineer with Eastman Kodak from 1997 to 2003. He designed and developed electrical and control systems for custom precision machine tools. Dr. Falter also worked for Rank Pneumo from 1994 to 1997.

DAVID YOUDEN

Senior Engineer, Olympic Precision, Inc.
Adjunct Lecturer, Department of Mechanical and Aerospace Engineering

ASME, Central New England College, Worcester, MA, 1965

Prior to joining Olympic Precision's Precision Valley Institute for Advanced Manufacturing in 2006, Mr. Youden was an Applied Research Engineer at Eastman Kodak Company's Manufacturing Systems Technology Division. Between 1984 and 1997 he was Research and Development Manager at Rank Pneumo, a division of Rank Taylor Hobson Inc. Before that, he was Director of Engineering at the Cone Blanchard Machine Company. He has also worked at Ocean Systems, Inc. of Reston, Virginia and the Heald Machine Company, a division of Cincinnati Milacron. During his professional career, Mr. Youden has been granted numerous patents in the field of machine tools, and he has published and presented technical papers on the design and testing of ultra-precision machine tools in the US, Japan, and Germany. In 2006, Mr. Youden received The American Society for Precision Engineering's Lifetime Achievement Award for his contributions to the field of precision engineering.

GRADUATE STUDENTS DURING 2006

DAVID BREHL's extensive industrial career includes a range of design, development, and project engineering roles with AERCO International, BOC Gases, and Babcock & Wilcox. A deepening interest in design of integrated electromechanical systems, along with a desire to focus his career on technology development, led him to pursue a PhD in Mechanical Engineering at NCSU; this follows a recent Master's in ME program at Stevens Institute of Technology (Hoboken, NJ). He joined the PEC in August 2004.

QUNYI CHEN first entered NCSU in 1997. obtaining a MSME in 1998 and a MSEE in 1999. After graduation, Qunyi worked at GE Healthcare to design and develop electro-mechanical subsystems for medical diagnostic X-ray equipment. His passion for technology development in precision electro-mechanical engineering led him to return to NCSU in 2005, where he was able to find an ideal match on the PEC's Fast Long Range Actuator project in June 2006. Qunyi was born and raised in Jiangsu, China. There, he received a BSME in 1993 and a MSME in 1996 before coming to the United States.

TIM KENNEDY was born and raised in Chapel Hill, NC. Tim received his BS from NCSU in May 2004. Before working at the PEC, he worked at the Analytical Instrumentation Facility for two years as an undergraduate research assistant. He started working with the PEC August 2004.

LUCAS LAMONDS interned for RJ Reynolds, AMP and Getrag Gears. He began work at Getrag Gears in July 2002 and held the positions of Quality Engineer, Six Sigma Black Belt, and India-Joint Venture Project Engineer. Most recently, he managed the company's production yields, quality levels, and product launches for India. Lucas is scheduled to complete his master's degree in Spring 2007 and begin working for Micron Technology, Inc. in Boise, ID.

NADIM WANNA was born and raised in Beirut, Lebanon. Nadim received a BS in Mechanical Engineering from NCSU in December 2004. He participated in a research project on object transportation using ultrasonic wave propagation and his prior work experiences include Lebanon Chemical CO. Nadim completed his master's degree in December 2006 and is working for ExxonMobil Corporation in Houston, TX.

ROB WOODSIDE was born and raised in Greenville, NC. He started at UNC-Asheville in 1999 and transferred to NCSU in 2001, where he received his BS in Mechanical Engineering in December 2004. He began work with the PEC in January 2005. Some of his prior work

experience includes MACTEC/PES consulting. Rob completed his master's degree in December 2006 and is working for Harris Corporation in Melbourne, FL.

YANBO YIN received his BS and ME in Precision Instrument and Mechanology from Tsinghua University Beijing in 2000 and 2003, respectively. For his undergraduate thesis, he joined the micro-mechanical lab with experimental research on Micro-jet. For his master's degree, Yin developed a computer-aided system on wireless communication on-base station distribution. Currently, he is pursing his Ph.D. degree in Mechanical Engineering under the guidance of Dr. Ro. His research involves non-contact object transportation using ultrasonic.

GRADUATES OF THE PRECISION ENGINEERING CENTER

Student	Degree	Date	Company/Location
Jeffrey Abler	PhD	December 1994	ETEC Systems, Inc. Tucson, AZ
William Allen	PhD	December 1994	North Carolina State Univ. Raleigh, NC
Kelly Allred	MS	June 1988	
Christopher Arcona	PhD	May 1993	Norton Worcester, MA
Bradford Austin	MS	June 2000	IBM Corporation Fishkill, NY
Markus Bauer	PhD	December 2001	SCYNEXIS Chemistry & Automation, Inc. Research Triangle Park, NC
Tom Bifano	PhD	June 1988	Phillips Automation Pittsburgh, PA
Scott Blackley	MS	May 1990	Motorola Austin, TX
Peter Blake	PhD	December 1988	NASA Goddard Greenbelt, MD
Brett Brocato	MS	June 2005	General Atomics San Diego, CA
Nathan Buescher	MS	May 2005	Consolidated Diesel Rocky Mount, NC
Mark Cagle	MS	June 1986	NASA-Langley Norfolk, VA
John Carroll	PhD	January 1986	Cummins Engine Co. Columbus, IN

Matthew Cerniway	MS	October 2001	Naval Surface Warfare Ctr West Bethesda, MD
Damon Christenbury	MS	June 1985	Michelin Tire Co. Spartanburg, SC
Stuart Clayton	MS	May 2003	Naval Depot Cherry Point
James Cuttino	PhD	December 1994	UNC – Charlotte Charlotte, NC
Bob Day	PhD	July 1998	Los Alamos National Lab Los Alamos, NM
Joseph Drescher	PhD	May 1992	Pratt & Whitney East Hartford, CT
William Enloe	MS	December 1988	ITT Roanoke, VA
Karl Falter	MS	December 1989	Eastman Kodak Company Raleigh, NC
Peter Falter	PhD	May 1990	Lockheed-Martin Orlando, Florida
John Fasick	MS	May 1998	Kodak Rochester, NY
Steven Fawcett	PhD	June 1991	MicroE Natick, MA
Karalyn Folkert	MS	May 2005	Consolidated Diesel Rocky Mount, NC
Andre Fredette	PhD	May 1993	IBM Research Triangle Park, NC
Karl Freitag	MS	August 2004	Northrop Grumman Baltimore, MD
David Gill	PhD	August 2002	Sandia National Laboratories Albuquerque, NM

Jim Gleeson	MS	June 1986	Battelle Columbus Labs Columbus, OH
Mary Smith Golding	MS	May 1990	Harris Corporation Melbourne, FL
David Grigg	PhD	August 1992	Zygo Corporation Middlefield, CT
Hector Gutierrez	PhD	October 1997	Florida Inst. Of Tech. Melbourne, FL.
Christian Haeuber	MS	December 1996	Harris Corporation Melbourne, FL
Simon Halbur	MS	December 2004	
Matias Heinrich	MS	July 2001	Vistakon Jacksonville, FL
Gary Hiatt	PhD	May 1992	Caterpillar Zebulon, NC
David Hood	MS	May 2003	
Peter Hubbel	MS	December 1991	Delco Electronics Kokomo, IN
Konrad Jarausch	PhD	December 1999	Intel Corporation San Jose, CA
Bradley Jared	PhD	December 1999	3M Cincinnati, OH
David Kametz	MS	August 2002	Naval Air Warfare Center Aircraft Division Patuxent River, MD
Jerry Kannel	PhD	June 1986	Battelle Columbus Labs Columbus, OH
Byron Knight	MS	May 1990	US Air Force Washington, DC
Mark Landy	MS	June 1986	Battelle Columbus Labs Columbus, OH

Mike Loewenthal	MS	December 1988	SVG Norwalk, CT
Michael Long	PhD	June 2000	Eastman Kodak Rochester, NY
Bryan Love	MS	May 2001	Virginia Tech
Michael Hung-Tai Luh	MS	June 1989	Proctor and Gamble Cincinnati, OH
Dan Luttrell	MS	1987	Luttrell, Inc. New Boston, NH
Edward Marino	MS	September 1999	Pratt Whitney Hartford, CT
Edward Miller	MS	December 2000	General Electric Greenville, SC
Michele Miller	PhD	December 1994	Michigan Tech. University Houghton, MI
Paul Minor	MS	September 1998	Hartford, CT
Gary Mitchum	MS	June 1987	Harris Corporation Melbourne, FL
Charles Mooney	MS	December 1994	AIF – NC State University Raleigh, NC
Patrick Morrissey	MS	May 2003	
Larry Mosley	PhD	June 1987	Intel Corporation Chandler, AZ
Patrick Moyer	PhD	May 1993	UNC-Charlotte Charlotte, NC
Nobuhiko Negishi	MS	August 2003	
Ayodele Oyewole	MS	October 1997	Barnes Aircraft East Hartford, CT
Hakan Ozisik	PhD	December 1989	

Witoon Panusittikorn	PhD	December 2004	Thailand
John Pellerin	MS	May 1990	Sematech Austin, TX
Travis Randall	MS	August 2004	MBA student NCSU
Ganesh Rao	MS	December 1994	Oak Ridge National Lab Oak Ridge, TN
John Richards	MS	September 1997	Intel Corporation San Jose, CA
Walter Rosenberger	MS	May 1993	The East Group Kinston, NC
Alex Ruxton	MS	December 1996	Pratt &Whitney Palm Beach, Florida
Anthony Santavy	MS	August 1996	Ford Dearborn, MI
Keith Sharp	PhD	May 1998	Morgan Crucible Dunn, NC
Gordon Shedd	PhD	March 1991	
Wonbo Shim	PhD	May 2000	Seagate Inc. Oklahoma City, OK
Robert Skolnick	MS	September 1997	San Diego, CA
Denise Skroch	MS	May 1989	IBM Corporation Raleigh, NC
Elizabeth Smith	MS	April 1989	
Stanley Smith	PhD	May 1993	
Ronald Sparks	PhD	May 1991	Alcoa Corporation Pittsburg, PA
Brent Stancil	MS	December 1996	Harris Corporation Melbourne, FL

Gene Storz	MS	May 1994	
Anand Tanikella	PhD	August 1996	Norton Industrial Ceramics Northboro, MA
Donna Thaus	MS	May 1996	Northern Telecom Research Triangle Park, NC
John Thornton	MS	December 1993	Digital Instruments Santa Barbara, CA
Michael Tidwell	MS	December 1991	
John Tyner	MS	June 1995	Naval Depot Cherry Point
Nadim Wanna	MS	December 2006	ExxonMobil Corporation Houston, TX
Robert Woodside	MS	December 2006	Harris Corporation Melbourne, FL
Tao Wu	PhD	December 2003	

ACADEMIC PROGRAM

Problems and limitations associated with precision manufacturing can originate in the machine, the process, or the material. In fact, most problems will probably be caused by a combination of these factors. Therefore, improvement of current processes and development of new manufacturing methods will require knowledge of a multi-disciplinary array of subjects. The educational goal of the Precision Engineering Center is to develop an academic program which will educate scientists and engineers in metrology, control, materials, and the manufacturing methods of precision engineering.

The graduate students involved in the Precision Engineering Center have an annual stipend as research assistants. They can take up to 3 classes each semester while spending about 20 hours per week on their research projects. These students also work in the Center full-time during the summer months.

The Precision Engineering Center began in 1982 with an emphasis on the mechanical engineering problems associated with precision engineering. As a result, the original academic program proposed was biased toward courses related to mechanical design and analysis. However, as the research program has developed, the need for complementary research in sensors, materials, and computers has become obvious. A graduate student capable of making valuable contributions in the computer area, for example, will require a significantly different academic program than in mechanical engineering. For this reason, the Center faculty has set a core curriculum and each student in the program is required to take at least 3 of these core courses. The remainder of the courses for the MS or the PhD degree are determined by the university or department requirements and the faculty committee of the student.

The required courses are:

- MAE 545 Metrology in Precision Manufacturing
- PY 516 Physical Optics
- MAT 700 Modern Concepts in Materials Science
- CSC (ECE) 714 Real Time Computer Systems

PhD DEGREE PROGRAM

The PhD program in Precision Engineering has been set up as a multi-disciplinary program, drawing upon courses throughout the University to provide background and expertise for the students. It should contain required courses to insure solid grounding in the fundamentals plus electives to prepare the student in his area of specialization. Because Precision Engineering is concerned with an integrated manufacturing process, students interested in computer control, materials, machine structure, and measurement and actuation systems are involved in the program. Student research projects include the wide variety of topics addressed in this report. Each student's thesis should have an experimental component because Precision Engineering is basically a hands-on technology.

MS DEGREE PROGRAM

The Master of Science degree will have a higher percentage of application courses than the PhD degree. The emphasis will be to develop the foundation for involvement in precision engineering research and development. A total of 30 credits, including 6 credits for the MS thesis, are required. The thesis, while less comprehensive than the PhD dissertation, will be directed at important problems in Precision Engineering. Typically, the MS program will take four semesters plus one summer.

UNDERGRADUATE PROGRAM

The undergraduate degree broadly prepares an engineering student for industrial activities ranging from product design and engineering sales to production implementation. Because a large share of engineers only have the BS degree, these will be the people who must implement the new technology developed in research programs like the Precision Engineering Center. Therefore, a way must be found to acquaint engineers at the BS level with the techniques, problems, and potential of precision manufacturing.

In most undergraduate degree programs only limited time is available for technical electives. However, these electives offer the student the opportunity to expand his knowledge in many different directions. Beginning graduate courses (such as metrology) can be used as undergraduate electives.

Undergraduate projects and summer employment have also been utilized to include undergraduate students into the research program of the Center. During the 1998-1999 academic year, four undergraduate students in Mechanical Engineering were involved various projects at the PEC.

STUDY PLANS

Study plans for several example students are given below both for the MS and the PhD degree. Because of the breadth of the field and the wide range of thesis topics, few if any study plans will be exactly the same. The plan will depend upon the student's background, his interests, his thesis topic, the department, and the chairman and members of his committee.

PhD PROGRAM IN MECHANICAL ENGINEERING

Major Courses:

- MAE 740 Advanced Machine Design I
- MAE 741 Advanced Machine Design II
- MAE 706 Heat Transfer Theory & Applications
- MAE 713 Principles of Structural Vibration
- MAE 760 Computational Fluid Mechanics and Heat Transfer
- MAE 545 Metrology in Precision Manufacturing
- MAE 715 Nonlinear Vibrations
- MAE 716 Random Vibration
- MAE 714 Analytical Methods in Structural Vibration
- MAE 742 Mechanical Design for Automated Assembly
- MAE 895 Doctoral Dissertation Research

Minor Courses:

- MA 511 Advanced Calculus I
- MA 775 Mathematical Methods in the Physical Sciences I
- CSC 780 Numerical Analysis II
- PY 516 Physical Optics
- ECE 716 System Control Engineering
- MAT 700 Modern Concepts in Materials Science
- ECE 726 Advanced Feedback Control
- ECE 764 Digital Image Processing

PhD PROGRAM IN MATERIALS ENGINEERING

Major Courses:

- MAT 710 Elements of Crystallography and Diffraction
- MAT 700 Modern Concepts in Materials Science
- MAT 556 Composite Materials
- MAT 715 Transmission Electron Microscopy
- MAT 795 Defect Analysis/Advanced Materials Experiments
- MAT 753 Advanced Mechanical Properties of Materials
- MAT 712 Scanning Electron Microscopy
- MAT 895 Doctoral Dissertation Research

Minor Courses:

- PY 414 Electromagnetism I
- ST 502 Experimental Statistics for Engineers I
- MAE 740 Advanced Machine Design I
- MAE 741 Advanced Machine Design II
- MAE 545 Metrology in Precision Manufacturing
- PY 516 Physical Optics
- MA 401 Applied Differential Equations II

PhD PROGRAM IN ME (FOR STUDENT WITH MS DEGREE)

- ECE 716 System Control Engineering
- ECE 791 Gate Array Design
- MAT 700 Modern Concepts in Materials Science
- PY 516 Physical Optics
- MA 502 Advanced Mathematics for Engineers and Scientists II
- MA 775 Mathematical Methods in the Physical Sciences I
- MA 780 Numerical Analysis II
- MAE 732 Fundamentals of Metal Machining Theory
- MAE 740 Advanced Machine Design I
- MAE 741 Advanced Machine Design II

- MAE 545 Metrology in Precision Manufacturing
- MAE 716 Random Vibration

MS PROGRAM FOR ME STUDENT

- MAE 713 Principles of Structural Vibration
- MAE 740 Advanced Machine Design I
- MAE 545 Metrology in Precision Manufacturing
- MAT 700 Modern Concepts in Materials Science
- PY 516 Physical Optics
- MA 501 Advanced Math for Engineers and Scientists I
- MA 502 Advanced Math for Engineers and Scientists II
- MAE 695 Master's Thesis Research

MS PROGRAM FOR COMPUTER SCIENCE STUDENT

- CSC 501 Operating Systems Principles
- CSC 506 Architecture of Parallel Computers
- CSC 512 Compiler Construction
- ECE 521 Computer Design and Technology
- CSC 715 Concurrent Software Systems
- MAE 545 Metrology for Precision Manufacturing
- MAE 789 Digital Control Systems
- ECE 764 Digital Image Processing

MS PROGRAM FOR MATERIALS SCIENCE STUDENT

- MAT 700 Modern Concepts in Material Science
- MAT 710 Elements of Crystallography and Diffraction
- MAT 715 Transmission Electron Microscopy
- MAT 712 Scanning Electron Microscopy
- MAT 722 Advanced Scanning Electron Microscopy and Surface Analysis
- MAE 545 Metrology for Precision Manufacturing
- PY 516 Physical Optics
- ECE 738 IC Technology and Fabrication
- MAT 695 Master's Thesis Research

MS PROGRAM FOR PHYSICS STUDENT

- PY 516 Physical Optics
- PY 552 Introduction to Structure of Solids I
- PY 753 Introduction to Structure of Solids II
- PY 781 Quantum Mechanics I
- PY 782 Quantum Mechanics II
- PY 783 Advanced Classical Mechanics
- PY 785 Advanced Electricity and Magnetism I
- PY 786 Advanced Electricity and Magnetism II
- MAT 700 Modern Concepts in Material Science
- MAE 545 Metrology for Precision Manufacturing
- PY 695 Master's Thesis Research

SHORT COURSES AND TV COURSES

Six graduate level courses: Scanning Electron Microscopy (MAT 712), Advanced SEM Surface Analysis (MAT 722), Modern Concepts in Material Science (MAT 700), Mechanical Properties of Materials (MAT 705), and Metrology (MAE 545) have been offered as video courses nationwide via National Technological University. In a typical year, approximately 120 students from industry and national laboratories participate in these courses. Future plans call for a MS program in Precision Engineering to be offered via the television network.

TECHNICAL REPORTS

Volume 1 - 1983	December 1983	136 pages
Volume 2 - 1984	January 1985	168 pages
Volume 3 - 1985	January 1986	294 pages
Volume 4 - 1986	January 1987	255 pages
Volume 5 - 1987	December 1987	336 pages
Volume 6 - 1988	December 1988	362 pages
Volume 7 - 1989	March 1990	357 pages
Volume 8 - 1990	March 1991	385 pages
Volume 9 - 1991	March 1992	382 pages
Volume 10 - 1992	March 1993	289 pages
Volume 11 - 1993	March 1994	316 pages
Volume 12 - 1994	March 1995	268 pages
Volume 13 - 1995	January 1996	251 pages

Volume 14 - 1996	January 1997	232 pages
Volume 15 - 1997	January 1998	298 pages
Volume 16 – 1998	January 1999	258 pages
Volume 17 – 1999	January 2000	232 pages
Volume 18 – 2000	January 2001	274 pages
Volume 19 – 2001	January 2002	201 pages
Volume 20 – 2002	January 2003	328 pages
Volume 21 - 2003	January 2004	208 pages
Volume 22 – 2004	February 2005	207 pages
Volume 23 – 2005	February 2006	264 pages
Volume 24 – 2006	March 2007	274 pages

PUBLICATIONS

PAPERS PUBLISHED

1. K. Garrard, T. Dow and K. Folkert, *Ring Gauge for Evaluation of CMM Dynamics*. Proceedings of the Twenty-first Annual Meeting of the ASPE, 39, (2006).
2. Sohn, L. Lamonds and K. Garrard, *Modeling of vibration in single-point diamond turning*. Proceedings of the Twenty-first Annual Meeting of the ASPE, 39, (2006).
3. D. Brehl, T. Dow, K. Garrard and A. Sohn, *Micro-structure fabrication using elliptical vibration-assisted machining (EVAM)*. Proceedings of the Twenty-first Annual Meeting of the ASPE, 39, (2006).
4. D. Brehl and T. Dow, *Review of Vibration-assisted Machining Methods for Precision Fabrication*. Proceedings of the Twenty-first Annual Meeting of the ASPE, 39, (2006).
5. R.K. Guduru, R.O. Scattergood, C.C. Koch, K.L. Murty, S. Guruswamy and M.K. McCarter, *Mechanical Properties of Nanocrystalline Fe-Pb and Fe-Al2O3*. Scripta Mater., 54, 1879, (2006).
6. K.M. Youseff, R.O. Scattergood, K.L. Murty and C.C. Koch, *Nanocrystalline Al-Mg Alloy with Ultrahigh Strength and Good Ductility*. Scripta Mater., 54, 251, (2006).
7. K. Rajulapati, R.O. Scattergood, K.L. Murty, G. Duscher and R.O. Scattergood, *Effect of Pb on the Mechanical Properties of Nanocrystalline Al*. Scripta Mater., 55, 155, (2006).
8. R.K. Guduru, K.A. Darling, R.O. Scattergood, C.C. Koch, K.L. Murty, M. Bakkal and A.J. Shih, *Shear Punch Tests for a Bulk Metallic Glass*. Intermetallics, 14, 1411, (2006).
9. R.K. Guduru, A.V. Nagasekhar, R.O. Scattergood, C.C. Koch and K.L. Murty, *Finite Element Analysis of a Shear Punch Test*. Metall. and Mater. Trans., 37A, 1477, (2006).
10. R.K. Guduru, K.A. Darling, R.O. Scattergood, C.C. Koch and K.L. Murty, *Mechanical Properties of Electrodeposited Nanocrystalline Copper Using Tensile and Shear Punch Tests*, in press, J. Mat. Sci., (2007).
11. Buckner, G.D., Choi, H., and Gibson, N.S., *Estimating Model Uncertainty using Confidence Interval Networks: Applications to Robust Control*. ASME Journal of Dynamic Systems, Measurement, and Control, 128, 3, 626-635, (2006).
12. Pandurangan, P.S. and Buckner, G.D, *Vibration analysis for damage detection in metal-to-metal adhesive joints*. Experimental Mechanics, 46, 5, 601-607, (2006).
13. Lawrence, B., Buckner, G.D., and Mirka, G., *An Adaptive System Identification Model of the Biomechanical Response of the Human Trunk During Sudden Loading*. ASME Journal of Biomechanical Engineering, 128, 2, 235-241, (2006).

14. Lu, B., Choi, H., Buckner, G.D., *LPV Control Design and Experimental Implementation for a Magnetic Bearing System*. Proceedings of the 2006 American Controls Conference, Minneapolis, MN, June (2006).
15. Choi, H., Buckner, G.D., and Gibson, N.S., *Neural Robust Control of a High-Speed Flexible Rotor Supported on Active Magnetic Bearings*. Proceedings of the 2006 American Controls Conference, Minneapolis, MN, June (2006).
16. Pandurangan, P.S. and Buckner, G.D., *Non-destructive evaluation of metal-to-metal adhesive joints using vibration analysis: experimental results*. Nondestructive Evaluation and Health Monitoring of Aerospace Materials, Composites, and Civil Infrastructure V. Edited by Mufti, Aftab A.; Gyekenyesi, Andrew L.; Shull, Peter J. Proceedings of the SPIE, 6176, 103-111, (2006).

REPORTS PUBLISHED

1. T. Dow, K. Garrard, A. Sohn, *Final Report to the Navy ElectroOptics Center on FOCUS*, Freeform Optics Center of the US, (2006).

PAPERS SUBMITTED OR ACCEPTED FOR PUBLICATION AND PRESENTATIONS

1. Eischen, J.W., *A Study of the Relationship Between Buckling and Wrinkling of Membranes*. Proceedings of the Ninth Pan American Congress of Applied Mechanics, Merida, Mexico, January (2006).
2. Jernigan, S., Buckner, G. and Eischen, J.W., *Finite Element Modeling of the Left Atrium to Facilitate the Design of an Endoscopic Atrial Retractor*. Proceedings of BIO2006 2006 Summer Bioengineering Conference, Amelia Island Plantation, Ameilia Island, FL, June 21-25 (2006).

THESES AND DISSERTATIONS

1. Wanna, Nadim, *Design of Reflective Optical Systems*, MS Thesis, North Carolina State University, December 2006.
2. Woodside, Robert, *Metrology of Reflective Optical Systems*, MS Thesis, North Carolina State University, December 2006.